

(i)

THE PERFORMANCE OF AEROFOIL CASCADES
USING CIRCULATION CONTROL

by

CHRISTOPHER IAN HOLLIDAY

A

thesis submitted for

the degree of

DOCTOR OF PHILOSOPHY

in

the

Department of Mechanical Engineering

at

THE UNIVERSITY OF ASTON IN BIRMINGHAM

APRIL 1979

THE PERFORMANCE OF AEROFOIL CASCADES
USING CIRCULATION CONTROL

by

CHRISTOPHER IAN HOLLIDAY

Ph.D.

1979

SUMMARY

The performance of a cascade of two-dimensional, bluff aerofoils employing circulation control by a tangential blowing jet is investigated. Expressions for the lift and drag of such a cascade are derived to eliminate the direct effect of the blowing jet on the measured performance. The cascade characteristics for three cascade geometries over a range of incidences are presented as graphs of lift and drag coefficients and stream deflection plotted as functions of jet blowing momentum coefficient. All cascade tests were performed at a Mach number of 0.3. The cascade performance is found to be influenced strongly by vortex shedding at low jet blowing rates.

A complete numerical solution procedure for calculating the performance of circulation controlled aerofoils, either isolated or in cascade, is presented. The procedure involves the calculation of a blade surface pressure distribution using a potential flow model with a representation of the separated region by the use of a source distribution. Aerofoil surface boundary layer developments are calculated by a finite-difference solution of the parabolic boundary layer momentum equation. The blowing jet development is calculated by the same finite-difference procedure applied to an angular momentum equation, using an intermittency representation of the eddy viscosity distribution.

Results of the solution procedure are compared with experimental results obtained by other workers for an isolated aerofoil and for a cascade. The agreement is satisfactory and encouraging. The solution procedure is applied to two of the cascade configurations tested in the present investigation. The agreement between theory and experiment is excellent in one case, while the poorer agreement in the second comparison is attributed to the experimentally observed changes in wake flow characteristics with cascade geometry.

ACKNOWLEDGEMENTS

From October 1975 to September 1978 the author was in receipt of a Research Studentship awarded by the Science Research Council. The wind tunnel and funds for the construction of the model cascade blades were supplied by Rolls-Royce Limited.

Much of the experimental equipment used in this work was constructed before the author became involved with the project. The credit for this preparatory work is due to Mr.W.L.Flint for the organisation and design and to Mr.D.Green who manufactured most of the components.

A large number of the technical and workshop staff of the Mechanical Engineering Department were called upon to provide services or facilities at some point during the project and the author is indebted to them all for their willing and cheerful assistance. In particular, thanks are extended to Messrs. Botterill and Moss for their practical help and suggestions.

The author is grateful to Professor E. Downham and Mr. A.R. Clark for the loan of recording equipment and aid in the analysis of sound recordings. Gratitude is extended also to Dr.L.H.Hazelwood of the Aston University Computer Centre academic staff for a profitable discussion on aspects of the numerical work. The reception staff of the Computer Centre deserve mention for their unstinting service, often under exceptional work-loads.

Sincere thanks are proffered to Mr.W.L.Flint for his constant encouragement in his capacity as supervisor and to Professor K.Foster, Head of Department and associate supervisor, for his constructive criticism during the writing of this thesis.

<u>CONTENTS</u>	Page
TITLE PAGE	(i)
SUMMARY	(ii)
ACKNOWLEDGEMENTS	(iii)
LIST OF CONTENTS	(iv)
ABBREVIATIONS USED IN TEXT AND REFERENCES	(ix)
NOTE ON LAYOUT OF THESIS	(ix)
NOMENCLATURE	(x)
CHAPTER 1: INTRODUCTION	1
1.1 Origin of Project	1
1.2 The Principle of Incompressible Cascade Analysis	2
1.3 Bluff Bodies and Circulation	3
1.4 Tangential Jets: The Coanda Effect	5
1.5 Boundary Layer Control and Circulation Control	6
CHAPTER 2: SURVEY OF PREVIOUS EXPERIMENTAL WORK	10
2.1 Performance Characteristics of Circulation Controlled Aerofoils	10
2.1.1 Introduction	10
2.1.2 Suitable Correlating Parameters for Circulation Controlled Sections	11
2.1.3 Application of Blowing Parameters to Cascades	14
2.1.4 The Number and Position of Blowing Slots	15
2.1.5 The Effect of Nozzle Shape	18
2.1.6 The Effect of Slot Width and Surface Curvature	18
2.1.7 The Effect of Trailing Edge Shape	20
2.1.8 The Effect of Free-Stream Mach Number	20

	Page
2.2 Testing Considerations	21
2.2.1 Introduction	21
2.2.2 The Effect of Reynolds Number	23
2.2.3 The Effects of Aspect Ratio and Axial Velocity Ratio	25
2.2.4 Tunnel Configuration	27
2.2.5 The Setting of Blade End Suction Levels	27
 CHAPTER 3: EXPERIMENTAL WORK AND DATA REDUCTION	 29
3.1 The Model Blades	29
3.1.1 Design Considerations	29
3.1.2 Construction	30
3.1.3 Spanwise Slot Flow Distribution	31
3.2 Slot Flow Calibration	33
3.2.1 Introduction	33
3.2.2 Calibration Procedure	34
3.2.3 Application of calibration to Blades in External Flow	34
3.2.4 Detailed Treatment of the Slot Velocity Profile	35
3.2.5 Results of Calibration and Comparison with Theory	36
3.2.6 Comments on Calibration of Blades	37
3.3 The Wind Tunnel	38
3.4 The Cascade Assembly and Blowing Air Supply	42
3.5 The Probe Used for Downstream Measurements	44
3.6 Instrumentation	46
3.7 Testing Procedure	48

	Page
3.8 Data Reduction	50
3.8.1 Introduction	50
3.8.2 Standard Analysis Procedure	50
3.8.3 Modification for Blowing	52
3.8.4 The Computer Programmes	53
 CHAPTER 4: RESULTS OF CASCADE PERFORMANCE EXPERIMENTS	 55
4.1 Cascade Characteristics	55
4.1.1 Lift, Drag and Turning Angle	55
4.1.2 Reynolds Number Effects	61
4.1.3 Jet Temperature Effects	61
4.2 Trailing Edge Pressure Distributions	62
4.3 The Nature of Mixing Losses in the Trailing Edge Region	64
4.4 An Investigation of the Cascade Whistle	65
 CHAPTER 5: POTENTIAL FLOW THEORY	 71
5.1 Introduction	71
5.2 The Governing Equations	73
5.2.1 Development of the Equations	73
5.2.2 Equations in Matrix Form	76
5.2.3 Lower Mean Values	77
5.2.4 Treatment of the Separated Region	77
5.3 The Solution Procedure	78
5.3.1 Introduction	78
5.3.2 The Case with no Separation	79
5.3.3 The Case with Separation	81
5.3.4 Calculation of the Incident Flow Angle	84
5.4 Computer Programme Verification	85
5.5 Possible Extensions to the Solution Procedure	87

	Page
CHAPTER 6: BOUNDARY LAYER AND WALL JET THEORY	90
6.1 Introduction	90
6.2 The Boundary Layer Equations	92
6.3 Intermittency	94
6.4 The Effective Viscosity Model	95
6.4.1 Introduction	95
6.4.2 The Near Wall Region	96
6.4.3 The Outer Region of a Conventional Boundary Layer	97
6.4.4 Wall Jets with a Velocity Maximum and Minimum	99
6.4.5 Wall Jets with a Velocity Maximum Only	101
6.5 The Effects of Surface Curvature	102
6.5.1 Survey of Previous Findings	102
6.5.2 The Representation of Curvature Effects	106
6.6 The Solution Procedure	107
6.6.1 General Description of the Procedure	107
6.6.2 Some Particular Details of the Procedure	108
6.6.3 A Test of the Wall Jet Calculation	110
 CHAPTER 7: RESULTS OF THEORY AND COMPARISON WITH EXPERIMENT	 112
7.1 Combination of Potential Flow and Boundary Layer Computer Programmes	112
7.2 Comparison of Theoretical Results with Experiment	113
7.3 Discussion	116

	Page
CHAPTER 8: SUGGESTIONS FOR FURTHER WORK AND CONCLUSIONS	119
8.1 Suggestions for Further Work	119
8.1.1 Experiment	119
8.1.2 Theoretical Work	120
8.1.3 The Practical Application of Circulation Controlled Cascades	121
8.2 Conclusions	121
APPENDIX A: AN INVESTIGATION OF THE DISTRIBUTED PIPE FLOW PROBLEM	123
A.1 Theory	124
A1.1 The Governing Equations	124
A1.2 Equations in Difference Form	126
A1.3 Equations in Functional Form: The Solution Procedure	127
A.2 Description of the Computer Programme	127
A.3 Experimental Method and Results	129
A.4 Theoretical Results and Comparison with Experiment	131
A.5 Prediction of Blowing Slot Performance of the Cascade Blades	134
APPENDIX B: MODIFICATION OF CASCADE PARAMETERS TO TAKE ACCOUNT OF BLOWING	135
B.1 Momentum Considerations	136
B.2 Coefficients of Lift and Drag	139
B.3 The Pressure Loss Term	140
B.4 Summary of Modifications to Cascade Characteristics.	142

	Page
APPENDIX C: THE POTENTIAL FLOW COMPUTER PROGRAMME POTFLO2	143
C.1 Introduction	144
C.2 Preliminary Outline	144
C.3 Description of Programme	146
C.4 Principal Variables and Arrays Used in the Programme	161
C.5 Programme Listing	163
 APPENDIX D: THE BOUNDARY LAYER COMPUTER PROGRAMME BLAYER	 189
D.1 Introduction	190
D.2 Preliminary Outline	190
D.3 Description of Programme	192
D.4 Principal Variables and Arrays Used in the Programme	204
D.5 Programme Listing	207
FIGURES	244
 BIBLIOGRAPHY	 313
TABLES	323
<u>ABBREVIATIONS USED IN TEXT AND REFERENCES</u>	

AIAA	American Institute of Aeronautics and Astronautics
NACA	National Advisory Committee for Aeronautics (USA)
NASA	National Aeronautics and Space Administration (USA)
NGTE	National Gas Turbine Establishment
TASME	Transactions of the American Society of Mechanical Engineers.

NOTE ON LAYOUT OF THESIS

Sketches and plates have been included in the text to facilitate reference to them. All Figures, because of their number, have been arranged together after the Appendices. Symbols are defined on the first reference to them and are listed in the Nomenclature unless used only in the local text. Numerical superscripts in the text refer to the works of other authors, listed in the Bibliography.

NOMENCLATURE

- A Van Driest constant (equation 6.2)
- C_{blc} Boundary layer control parameter (equation 2.1)
- C_d Discharge coefficient (Figure 8)
- C_p Pressure coefficient (equation 5.13)
- C_D Drag coefficient
- C_L Lift coefficient
- C_Q A mass flow coefficient (equation 2.1)
- C_μ Blowing momentum coefficient (equation 2.2)
- H Velocity profile shape factor, δ^*/θ
- K Von Kármán's mixing length coefficient (equation 6.2)
Also, source and vortex influence coefficients (equation 5.1)
- M Mach number
- N Half the number of pivotal points on section surface,
see Figure 33.
- N_s Number of sources distributed around trailing edge
- P Static pressure
- R Longitudinal radius of surface curvature
- R_e Reynolds number based on aerofoil chord
- R_i Richardson number (page 103)
- S Source density. Also Strouhal number (equation 4.1)
- U Local free-stream speed
- U_d Velocity defect (equation 6.1)
- U_j Slot jet exit speed
- U_m Mean cascade flow speed (page 139)
- U_{max} Maximum speed in wall jet profile
- X Blade force acting in the 'x' direction (Figure 60)
- Y Blade force acting in the 'y' direction (Figure 60)
- Y_d Point of departure of velocity profile from law of wall
(equation 6.4).

c	Blade chord
d	Characteristic length in Strouhal number, S
f	Vortex shedding frequency
\dot{m}	Mass flow rate
r	Local radius of curvature of flow
s	Cascade pitch
t	Blowing slot width
u	Local x-direction mean flow velocity
u_τ	Friction velocity $\sqrt{\tau_w/\rho}$
v	Local y-direction mean flow velocity
x	Coordinate parallel to surface
y	Coordinate normal to surface
\bar{y}	Mean position of turbulent front (Equations 6.7, 6.10, 6.11)
α	Flow angle (Figure 4)
β	Constant in curvature correction to v_t
γ	Intermittency factor (page 94). Also surface vortex density
δ	Boundary layer thickness
δ^*	Displacement thickness
ξ	Stagger angle (Figure 4)
θ	Momentum thickness. Also stream turning angle of cascade
μ	Dynamic laminar viscosity
μ_t	Dynamic turbulent (eddy) viscosity
ν	Kinematic laminar viscosity = μ/ρ
ν_t	Kinematic turbulent (eddy) viscosity = μ_t/ρ
ρ	Density

- σ Standard deviation of intermittency profile (equations 6.3, 6.10, 6.11). Also distance around aerofoil surface (Figure 33)
- τ Local shear stress
- τ_w Shear stress at wall
- ϕ Angular measure of distance around section surface

Subscripts

- A line under a symbol denotes a vector quantity
- 1 Upstream of cascade
- 2 Downstream of cascade
- ∞ Free-stream conditions
- x In 'x' direction
- y In 'y' direction
- j At jet exit
- E Outer edge of boundary
- I Inner edge of boundary
- S Induced by source distribution
- sj On section surface at jet exit
- O A stagnation quantity
- γ Induced by vortex distribution.

CHAPTER 1

INTRODUCTION

1.1 Origin of Project

The investigation described herein arose from consideration of the future development of aircraft gas turbine engines. In recent years the pursuit of efficiency and quietness has resulted in the design of high bypass-ratio turbofan engines with reduced jet velocities.

High bypass-ratio engines pose new problems, due primarily to the large diameter of the fan. Two of these problems are:

1. The variation of blade spacing across the fan radius.
2. The high mechanical loading on the blade root section.

One possible solution to the first problem would be to mount an outer ring of blades on the tip circumference of an inner ring of fewer blades, thus maintaining a reasonably uniform blade spacing along the radius. This solution not only exacerbates the root loading problem but also increases the overall length of the compressor, as conventional aerofoils with a long chord have to be used in the heavily stressed inner row.

The above difficulties could be overcome by using thick, bluff sections for the inner blades and controlling their aerodynamic performance by the tangential injection of air through a narrow slot in the blade surface. This principle is known as circulation control.

Another application of circulation controlled bluff blades might be to replace the adjustable inlet guide vanes used on some engines. These vanes create problems of mechanical complexity and alignment. The use of fixed blades, with a turning angle adjustable by a variable blowing jet pressure might well prove advantageous.

1.2 The Principle of Incompressible Cascade Analysis

The application of the aerodynamic theory of circulation to the design of turbomachinery is generally accredited to Griffith who wrote an unpublished paper in 1926, proposing that turbomachinery rings should be analysed on the basis of flow around aerofoils, rather than considering the blades as forming a series of passages⁽¹⁻³⁾.

It is still normal practice to analyse the performance of low speed blading in the same manner as used for isolated aerofoils, the only difference being the modified pressure distribution around a blade in a compressor ring due to the influence of the neighbouring blades.

Where compressibility effects are of significance, channel flow analysis techniques are commonly employed^(4,5). The work considered in this dissertation is confined to cascade flows of a substantially incompressible nature. Much of the discussion on the principles involved in the present investigation, consequently, is concerned with the performance of isolated bodies.

A most comprehensive publication on all aspects of cascade flow analysis has recently become available in the form of a translation by Klein of a German text by Scholz⁽⁵⁾.

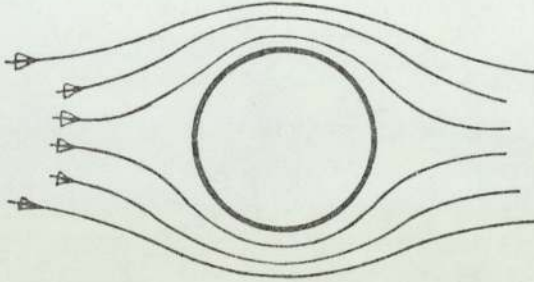
1.3 Bluff Bodies and Circulation

In potential flow about a two-dimensional aerofoil, the flow is indeterminate until the position of one stagnation point is defined: this amounts to a specification of the circulation and hence the lift. In the case of a conventional aerofoil with a pointed trailing edge, the flow is constrained to leave the trailing edge smoothly, an expression of the Kutta-Joukowski condition, and the circulation is thus fixed. If, however, the aerofoil has a blunt trailing edge there is no such constraint and movement of the rear stagnation point around the curved surface causes a variation in the circulation and lift.

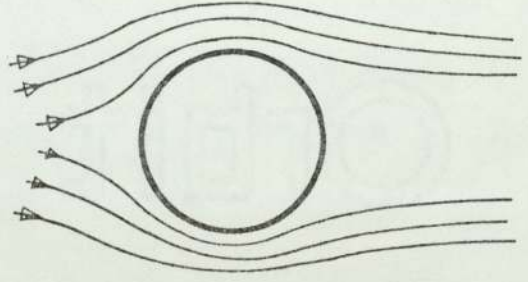
Consider a circular cylinder in a uniform stream. (The circular cylinder is selected merely as a convenience for illustration and the same arguments apply to any bluff body.) In potential flow with no circulation, the streamlines take the symmetrical pattern as in Sketch 1.1a. In real flow separation would occur, but at the same chordwise position on the upper and lower surfaces, as in Sketch 1.1b.

Now consider a wall jet, located at mid-chord on the upper surface. The action of the jet is to re-energise the upper surface boundary layer which is approaching separation and to allow the upper surface flow to remain attached to a point near the 'trailing edge'. The net effect is to distort the flow pattern around the cylinder as in Sketch 1.1d, where it is clear that lift is being developed. The new flow pattern can be approximated by the original potential flow pattern, plus a circulation, as shown in Sketch 1.1c.

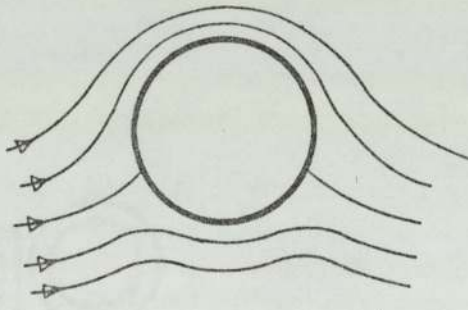
It is seen that tangential blowing is capable not only of suppressing separation but also of generating and controlling lift on sections which would otherwise generate none.



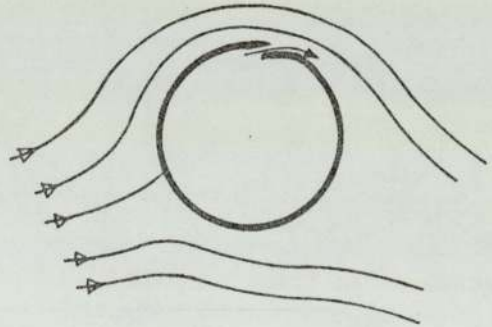
1.1a
Potential Flow
No Circulation



1.1b
Real Flow
No Circulation



1.1c
Potential Flow
With Circulation



1.1d
Real Flow
With Circulation

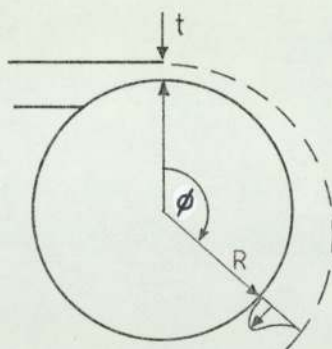
Sketch 1.1

Flow About a Circular Cylinder

1.4 Tangential Jets: the Coanda Effect

The success of the principle described above is clearly dependent upon the tendency of a tangential jet to adhere to a curved surface. It has long been recognised that jets display an inclination to attach and remain attached to a nearby solid surface, even when the surface curves away from the direction of jet injection. This phenomenon is usually associated with Coanda (1932) who exploited fluid jet attachment effects and the accompanying enhanced entrainment rates in many devices to produce, for example, improved scavenging of internal combustion engines and augmented nozzle thrust. However, as early as 1800, Young⁽⁶⁾ commented on the attractive force between a fluid jet and a curved body, while in 1890 Reynolds⁽⁷⁾ discussed the suspension of a ball by a jet of fluid, fully recognising that the stability of the ball was dependent upon the tendency of the flow to remain attached to the curved surface of the ball.

Newman⁽⁸⁾ described the essential features of a jet blown tangentially onto a circular cylinder. Consider Sketch 1.2 which shows a two-dimensional jet of width t , blowing onto the surface of a cylinder, radius R , with the surrounding air at rest at pressure P_∞ . Angular distance, ϕ , is measured round the cylinder from the slot lip. If the flow were inviscid and non-turbulent, then just downstream of the slot exit, the flow would become independent of ϕ , the jet width would be constant, and the jet would remain attached around the whole circumference. The pressure distribution through the jet would be independent of ϕ , but the pressure at the surface of the cylinder would be less than



Sketch 1.2

Tangential Jet on a Circular Cylinder

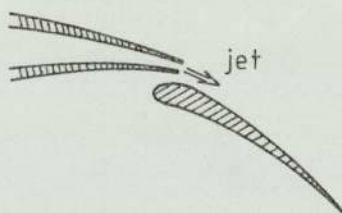
P_{∞} because of the curvature. The real jet continuously entrains fluid from the surroundings, increasing the jet width and reducing the jet velocity with increasing ϕ . Since the fluid near the cylinder surface is retarded, the surface pressure rises and approaches P_{∞} , thus causing separation. Experiment has shown that for high slot blowing Reynolds numbers and small values of t/R , the flow can remain attached for values of ϕ in excess of 180° .

A comprehensive list of references on the Coanda effect may be found in the summary report of Willie and Fernholz⁽⁹⁾.

1.5 Boundary Layer Control and Circulation Control

Experiments on the application of the Coanda effect to aerofoil aerodynamics have been conducted since the 1920's and applications to full size aircraft have been attempted since the 1930's. Some of the historical developments in the application of slot blowing to operational aircraft are described by Attinello⁽¹⁰⁾. In all these applications blowing was used as a boundary layer control on trailing edge flaps,

enabling large flap deflections to be used without stalling, see Sketch 1.3. The primary aim of these systems was to allow take off and landing speeds to be reduced by lift augmentation. Tangential slot blowing may also be used at the leading edge of a main wing to suppress leading edge separation when developing high lift. Experiments on the application of tangential flap blowing to cascades of compressor blades have been performed by Kruger et al.⁽¹¹⁾, Miller and Chapman⁽¹²⁾ and others.

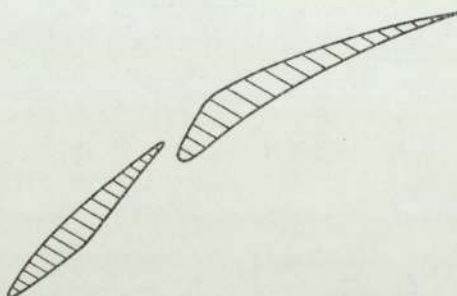


Sketch 1.3

Blown Trailing Edge Flap

Alternative methods to tangential blowing have been devised for the prevention of separation. For example, considerable work has been performed on aerofoils using suction to remove decelerated fluid in the boundary layer, see Schlichting⁽¹³⁾ and Thwaites⁽¹⁴⁾, and was first applied to a circular cylinder by Prandtl in 1904. Blowing is a more practical proposition in the context of compressor blading, however, due to the inherent availability of a high pressure air supply. Slotted sections, as illustrated in Sketch 1.4 have also been employed to increase aerodynamic loadings on wings and turbomachinery blades⁽¹⁵⁻¹⁸⁾. The action of the slot is not simply to create a 'jet' effect on the upper surface boundary layer, a widely held misconception exposed by

Smith⁽¹⁹⁾. The true effect of the slot is more subtle and is discussed in some detail by Smith. In brief, the two sections are better regarded as individual aerofoils in mutual interference.

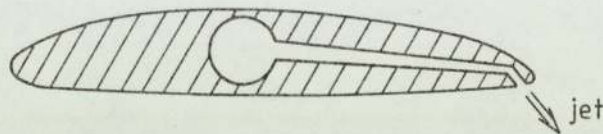


Sketch 1.4

Slotted Cascade Blade

The above techniques have all been used primarily to increase aerodynamic loadings by delaying separation up to a conventional trailing edge and as such fall into the category of boundary layer control rather than circulation control; true circulation control by tangential blowing requires a bluff trailing edge to allow movement of the rear stagnation point. Investigations into the performance of isolated sections with true circulation control have been performed by Kind and Maull⁽²⁰⁾ on an elliptical aerofoil and at the National Gas Turbine Laboratory on elliptical and circular section rotors^(21,22). The only reference which has been found concerning previous experiments on a cascade of bluff blades, employing tangential blowing for circulation control, is a paper by Landsberg and Krasnoff⁽²³⁾. Their work is especially pertinent to the present investigation.

An alternative form of flow control by a jet is obtained by the injection of fluid from a slot in the aerofoil surface but normal or at some large angle to the surface, as illustrated in Sketch 1.5. This arrangement is known as the jet flap and is fundamentally



Sketch 1.5

Aerofoil with Jet Flap

different in its method of operation from the tangential jet, since it is not dependent upon attachment to a surface and is not a direct form of boundary layer control: rather it forms a virtual physical extension of the aerofoil. Since the blowing jet does not act directly on the boundary layer, a reasonably conventional trailing edge is required. The principle is one of true circulation control, however, since a variation in lift or deflection is obtained by a variation in jet blowing rate. Several authors have reported experimental investigations into the performance of jet flap compressor cascades^(23,24). The theory of the jet flap has proved amenable to approximate analytical treatments^(14,25-30).

CHAPTER 2

SURVEY OF PREVIOUS EXPERIMENTAL WORK

2.1 Performance Characteristics of Circulation Controlled Aerofoils

2.1.1 Introduction

This section is a résumé of the findings of previous workers who have performed tests on isolated and cascaded circulation controlled aerofoils. These studies have shown that the lift produced by a circulation controlled aerofoil in cascade is much less than that of the same aerofoil in isolation. However, it is to be expected that general characteristics of isolated circulation controlled sections will apply in broad terms to individual cascaded aerofoils and so the results of isolated aerofoil studies are of interest.

Tangential blowing over a bluff trailing edge is effective in preventing separation in this region and so it might be expected that leading edge separation is a limiting factor on the maximum lift developed by aerofoils with augmented circulation. In commenting on observed characteristics of isolated sections, however, several authors have mentioned the 'saddle' shaped pressure distribution which results from circulation control and the fact that the resulting leading edge suction peak is much less than that of a conventional aerofoil at a corresponding lift coefficient. The effect of circulation control on the pressure distribution over the front portion of a cascade blade

would certainly be expected to be substantially less than that on an isolated aerofoil, a premise supported by numerical examples on a jet flap cascade presented by Starke⁽³¹⁾. Generally speaking, with an effectively designed slot and trailing edge, circulation control by tangential jet is a more efficient method of lift production than the jet flap⁽³²⁾, particularly for cascades⁽²³⁾.

The following sections consider in some detail the reported effects on aerofoil performance of the geometry of the blowing arrangement and the free-stream Mach number. First of all, the suitability of certain performance correlating parameters is discussed.

2.1.2 Suitable Correlating Parameters for Circulation

Controlled Sections.

In 1956, Kelly⁽³³⁾ analysed the typical blowing parameters used in the correlation of blowing type boundary layer control. By considering a control volume encompassing a blowing slot and the upstream and downstream boundary layers, he showed that if the direct effect of the jet upon the external pressure gradient, local skin friction, and the change in mass of fluid flowing across the upstream and downstream control surfaces due to entrainment are neglected, the characteristics of a tangential jet may be defined by a boundary layer control coefficient C_{blc} ;

$$C_{blc} = \frac{t}{c} \frac{P_j - P_{sj}}{\frac{1}{2} \rho_\infty U_\infty^2} + 2C_Q \left(\frac{U_j}{U_\infty} - \frac{U_{sj}}{U_\infty} \right) \quad 2.1$$

where

t = blowing slot width

c = aerofoil chord length

U_∞ = free-stream flow speed

U_j = jet speed at the nozzle exit

U_{sj} = local surface flow speed

C_Q = a mass flow coefficient defined by $C_Q = \frac{\rho_j U_j t}{\rho_\infty U_\infty c}$

ρ_∞ = mainflow density

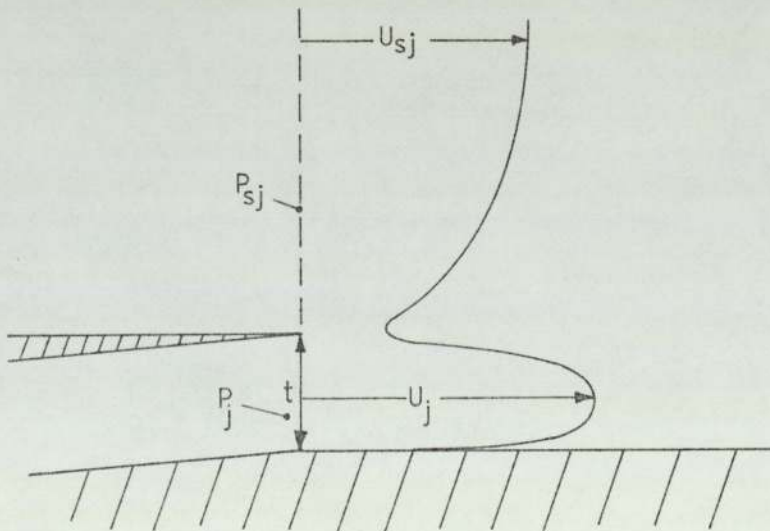
ρ_j = jet density

P_∞ = free-stream static pressure

P_j = pressure immediately inside the nozzle

P_{sj} = aerofoil surface pressure existing at the nozzle exit.

see Sketch 2.1. This equation should correlate the effectiveness of boundary layer control of different jets under the same geometrical arrangements.



Sketch 2.1

Definition of terms used in equation 2.1

For subsonic jet velocities, $P_j = P_{sj}$, so that

$$C_{blc} = 2C_Q \left(\frac{U_j}{U_\infty} - \frac{U_{sj}}{U_\infty} \right)$$

The momentum coefficient, C_μ , is defined by

$$C_\mu = 2C_Q \frac{U_j}{U_\infty} \tag{2.2}$$

Certain previous workers have used a quantity U_j' in the above equation instead of U_j , where U_j' is the velocity resulting from isentropic expansion of the jet from the supply duct total pressure to the free-stream static pressure, rather than the local surface pressure. C_μ can be related to C_{blc} by

$$C_{blc} = C_\mu - 2C_Q \frac{U_{sj}}{U_\infty} \tag{2.3}$$

for incompressible flow through the nozzle.

This result shows that the momentum coefficient, C_μ , will correlate blowing-type boundary layer control results only to the extent that changes in the quantity $2C_Q \frac{U_{sj}}{U_\infty}$ can be neglected. The influence of a velocity dependent term was also discovered in Dunham's analysis of the NGTE results⁽²¹⁾. At high supply duct pressures, the momentum coefficient is an adequate parameter. Kelly⁽³³⁾ and Attinello⁽¹⁰⁾ showed that good correlations of experimental results at low duct pressures are obtained with the parameter C_{blc} as defined by equation 2.3.

For an over-choked convergent nozzle, an approximate jet velocity U_{jc} may be obtained by assuming a non-isentropic free expansion to the

local static pressure. Simple momentum consideration gives for this velocity:

$$U_{jc} = U_j + \frac{P_j - P_{sj}}{\rho_j U_j}$$

if mixing losses at the jet boundary are neglected. The definition of momentum coefficient, equation 2.2. yields:

$$C_\mu = 2C_Q \frac{U_j}{U_\infty} + \frac{P_j - P_{sj}}{\frac{1}{2} \rho_\infty U_\infty^2} \frac{t}{c}$$

and substitution into equation 2.1 gives

$$C_\mu = C_{b1c} + 2C_Q \frac{U_{sj}}{U_\infty}$$

which is the same relationship as that given by equation 2.3 for subsonic jets.

It appears, therefore, that the same correlating parameter is satisfactory for both subsonic and choked blowing nozzle flows. Kelly, in verifying the suitability of the parameter C_{b1c} by comparison with experimental data, commented that there was no apparent significance associated with the attainment of sonic jet velocity.

2.1.3 Application of Blowing Parameters to Cascades

The blowing parameters customarily used for isolated sections employ the aerofoil chord length as a reference length to non-dimensionalise the blowing mass and momentum rates.

As Siestrunk⁽³⁴⁾ pointed out, however, the blade spacing, s , would seem to offer a more appropriate reference length when applying

the coefficients to a cascade because the momentum coefficient C_{μ} , for example, would then relate the jet momentum flux to that through one passage. Such a correlation should give a better guide to the deflecting effect of blowing.

The blade spacing was used by Krasnoff⁽²⁹⁾ as reference length in dealing with cascade jets but as the majority of workers have retained the customary chord length, the usual definitions will be retained in the interests of consistency. For this reason also the blowing coefficients, when applied to cascades, are based on upstream values of flow speed and dynamic pressure.

2.1.4 The Number and Position of Blowing Slots

The purpose of tangential blowing is to prevent separation of the main boundary layer. It is to be expected, therefore, that the most efficient location of a blowing slot is just upstream of the point at which the unblown boundary layer would ordinarily separate. Since an aerofoil or compressor blade is required to operate efficiently over a range of incidence, some degree of compromise is inevitably necessary, so that the blowing slot cannot perform at peak efficiency under all circumstances.

One obvious extension of the principle of tangential blowing is the use of two or more slots, each to reinforce the effect of the previous jet. In such an arrangement, each successive jet would be so located as to re-energise the boundary layer just before the preceding jet was about to lose its effect.

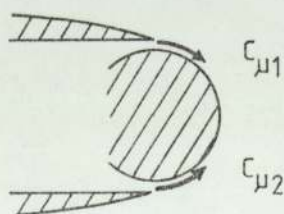
North⁽³⁵⁾ performed some numerical computations to compare the effectiveness of one and two slot blowing arrangements to prevent separation on the wall of a diffuser. Effectiveness was measured in terms of the distance to separation, measured from the first slot. He found that for a given total kinetic energy flux, two slots could be expected to suppress separation for about 1.33 times the distance achieved with only one jet. This result was obtained by postulating that 63% of the total kinetic energy flux should be supplied from the first slot, the apparently optimum distribution. North did not perform full calculations for larger numbers of slots, but he deduced that three slots, with the total kinetic energy flux properly distributed between them, could be expected to give greater separation lengths than the best two-jet arrangement. Certainly, Newman⁽³⁶⁾ was of the opinion that it may be more economical to blow 'little and often' if the engineering complexity is tolerable.

Allcock and Dunham⁽³²⁾ showed that two blowing slots were generally superior to one in terms of lift for a given overall blowing coefficient, when applied to a circular cylinder. The first slot was located at the mid-chord position and the position of the second varied between 30 and 68 degrees from this first slot. With thirty degrees separation, the two slot blowing arrangement was superior at all blowing coefficients. As the jet separation angle was increased so did the blowing coefficient at which two slots became superior, since the minimum blowing coefficient to prevent separation between the slots rose with the separation angle.

NGTE tests on elliptic cylinders⁽³²⁾ showed that two slot models were inefficient compared with single slot models at a free-stream Mach number of 0.2. However, the two slot models showed a much less sudden loss of lift with blowing coefficient and it seemed that two slots became more advantageous with increasing Mach number. It certainly appears that design optimization would show two slots to have major advantages when applied to elliptical sections.

Another form of multi-slot blowing arrangement may be termed 'opposition blowing', as illustrated in Sketch 2.2. With this slot configuration, the position of the rear stagnation point is controlled by differential blowing rates from the two slots. The obvious potential advantage of this arrangement is that the stagnation point position can be controlled while at the same time suppressing separation on both upper and lower surfaces, thus reducing drag more effectively than would only one slot.

Kind and Maull⁽²⁰⁾, in tests on an ellipse, found that for a given difference in blowing momentum from the two slots ($C_{\mu 1} - C_{\mu 2}$), both the lift and the lift/drag ratio decreased with increasing $C_{\mu 2}$. This effect was observed at all positive incidences and it was concluded that single slot blowing, in contrast to the opposition type, was more efficient.



Sketch 2.2

Trailing edge configuration for
opposition blowing.

2.1.5 The Effect of Nozzle Shape

Once the pressure of the air supply to the blowing slot reaches a sufficiently high value, the flow through a convergent nozzle becomes choked. The ideal nozzle for pressure ratios greater than the critical should be convergent-divergent, to obtain the maximum momentum from the emergent jet. Since a different geometry would be required for different supply and exit pressures and since such a nozzle would be inefficient for unchoked flows, the convergent nozzle results in the better performance and fabrication compromise.

Attinello⁽¹⁰⁾ presented a graph of the ratio of jet momentum coefficients for convergent and convergent-divergent nozzle flows. At a pressure ratio of 10, the momentum coefficient attainable with a convergent nozzle is 0.93 that which could ideally be obtained with a convergent-divergent nozzle. At pressure ratios of 2 to 3, the ratio is as high as 0.99, so that the advantages of convergent-divergent nozzles are highly marginal, even if the restricted operating pressure range and fabrication problems were acceptable.

Once the flow through a convergent nozzle becomes choked, a free expansion occurs at the exit which might be expected to reduce jet circulation control efficiency and thus undermine the above conclusion. As commented upon in the earlier section concerning correlating parameters, such an effect is not observed in practice.

2.1.6 The Effects of Slot Width and Surface Curvature

The phenomenon of jet attachment to a curved surface, the Coanda effect, arises because of the normal pressure gradient existing

across a curved flow. For a given blowing jet momentum, an increase in the ratio of slot thickness to surface radius of curvature, t/R , implies a reduced pressure difference across the jet and therefore a decrease in jet attachment effectiveness. However, very thin slots suffer the disadvantages of greater boundary layer blockage, higher blowing pressures for the same C_{μ} and an inability to entrain effectively a thick oncoming boundary layer. There would thus seem to be an optimum slot thickness for any particular application. The existence of an optimum thickness was demonstrated by Allcock and Dunham⁽³²⁾ when using tangential blowing on a circular cylinder.

The general effect of slot width on the NGTE elliptical cylinders is illustrated in Figure 1. It is observed that the finest slot ($t/c = 0.003$) performed well at low blowing rates, but limited the maximum lift available. A large slot width ($t/c = 0.0118$) performed badly since the thick jet was unable to adhere to the trailing edge. These results are not entirely consistent, however, because the trailing edge curvature was not the same for all tests.

Kind and Maul⁽²⁰⁾ reported low speed tests on a blown ellipse, using slot width ratios t/R of 0.0143, 0.0260 and 0.0520 and commented that there was no significant difference in section characteristics over this range of ratios.

Landsberg and Krasnoff⁽²³⁾ performed some tests on an isolated section to investigate the effect of t/R . They found that for values of $t/R = 0.04, 0.08$ and 0.11 , the lift inducing efficiency reduced with increasing slot width, while at $t/R = 0.166$ complete jet detachment occurred at low blowing coefficients.

2.1.7 The Effect of Trailing Edge Shape

Most tangentially blown aerofoils have been equipped with circular trailing edges. Allcock and Dunham⁽³²⁾ reported some results which illustrate the importance of trailing edge shape, even when perfectly smooth. Figure 2 compares the performance of their ellipses with circular-arc and elliptical trailing edges at Mach numbers of 0.2 and 0.6. A circular-arc trailing edge was found to be beneficial at a Mach number of 0.2, above a certain blowing coefficient, but caused a serious loss of performance at a free-stream Mach number of 0.6. This finding proved consistent on both 10% and 20% ellipse models. The effect was apparently related to the absolute value of blowing coefficient, since the C_L was better for the elliptical trailing edge at both $M = 0.2$ and $M = 0.6$ at low values of blowing coefficient.

Clearly, comparisons of different surface shapes are subject to the direct effect of the local magnitude of surface curvature, discussed in the previous section. However, it seems likely that an optimum surface curvature distribution would exist in any particular case. It is known that boundary layer development exhibits a 'lag' effect, whereby the shear layer requires a finite downstream travel distance to react fully to a change in the imposed flow conditions, e.g. surface curvature. It may well be possible to enhance jet turning angles by exploiting this effect.

2.1.8 The Effect of Free-Stream Mach Number

The majority of work on tangentially blown aerofoils has been performed at low incident Mach numbers, where the applied

blowing momentum coefficient C_{μ} and the generated lift coefficient C_L both reached high values. For example, aerofoils tested by Landsberg and Krasnoff⁽²³⁾ reached lift coefficients as high as 5 at blowing coefficients of 0.8. Under these low speed conditions, no peak to the lift curve is observed over the range of blowing coefficients reported. Similarly, cascades tested at low Mach numbers display a continuously increasing C_L with C_{μ} .

The NGTE tests on isolated elliptical cylinders in which Mach number effects were specifically investigated, suggest that Mach number effects can be considerable. Allcock and Dunham⁽³²⁾ found that for an elliptic cylinder, the slope of lift against blowing coefficient increased substantially with free-stream Mach number while the maximum attainable C_L fell rapidly. This effect is illustrated in Figure 3. The phenomenon is clearly due to a characteristic of the jet itself since the maximum lift on a conventional aerofoil does not fall appreciably until the critical Mach number is attained. Figure 3 shows how, at $M = 0.6$, the C_L against C_{μ} curve falls sharply after peaking: it appears that at this Mach number, breakdown of the Coanda effect is sudden and complete.

2.2 Testing Considerations

2.2.1 Introduction

The purpose of wind-tunnel cascade testing is to obtain performance characteristics which allow a prediction to be made of how a particular blade geometry will perform in a turbomachine. Since the range of application of a particular section is likely to be varied and not necessarily specified at the time of testing, it is normal

practice to obtain results under standardized conditions. If required, corrections can be made to results obtained under these standard conditions to predict performance, for example, at a different Reynolds number, although such corrections can only be applied confidently within the range of empirical vindication, primarily because such corrections are themselves usually empirical.

Except where the effects of three-dimensionality are specifically studied, cascade tests are carried out under conditions of two-dimensional flow and the cascade is taken to represent the performance of an infinite row of equally spaced blades.

Figure 4 illustrates the usual British cascade terminology which is used in this work. The performance of a given cascade geometry is sensitive to the flow conditions, namely the Mach number, Reynolds number and axial velocity ratio. Mach number effects are not considered here, because this work deals with flows which can be considered essentially incompressible. The Reynolds number is an important parameter in any flow system and can be expected to exert a considerable influence. In an ideal, incompressible flow, the axial velocity ratio (AVR) is unity, as dictated by continuity. In practice, boundary layer development on the junction between the blade ends and the tunnel wall causes a contraction of the centre-span flow through the cascade resulting in an AVR greater than unity. This effect may be countered by applying suction to the end walls of the wind tunnel to draw off the retarded flow and maintain unit AVR. In addition to these flow considerations there is clearly a limit on the

minimum number of blades arranged in a finite cascade for which the centre blade region adequately represents the performance of an infinitely long cascade.

The above cascade testing considerations are discussed in the following sections under appropriate headings. The majority of results referred to were obtained from extensive investigations by research workers at Liverpool University under the guidance of Professor Horlock.

2.2.2 The Effect of Reynolds Number

Observed effects of Reynolds number upon cascade performance have been reported by Rhoden⁽³⁷⁾, Horlock et al.⁽³⁸⁾, Pollard and Gostelow⁽³⁹⁾, Horlock⁽⁴¹⁾ and Roberts⁽⁴²⁾. Rhoden tested three compressor cascades of camber angles 20, 30 and 40 degrees at Reynolds numbers of 3×10^4 to 5×10^5 based on the inlet air velocity and blade chord. The pitch-chord ratio was maintained at unity and the stagger angles chosen to give an approximately constant outlet angle. The aspect ratio was three and the tests were conducted over a sufficiently wide range of inlet angles to obtain both positive and negative stalling. On the convex surfaces at high Reynolds numbers a few cases of turbulent boundary layer separation occurred, although the turbulent layers were generally able to sustain high pressure rises. As the Reynolds number was reduced, the point of transition moved towards the trailing edge until reaching the point of laminar separation. Further slight reduction of the Reynolds number caused complete laminar separation, the position of separation remaining approximately independent of Reynolds number.

Horlock et al.⁽³⁸⁾ compared some of Rhoden's results with predictions based on the data of Howell who gave a correlation of cascade data for the effect of Reynolds number on deflection. Howell's data did not compare well with Rhoden's results. The results of Horlock et al confirmed the findings of Rhoden that the deviation changes rapidly below a Reynolds number of 1.0×10^5 and varies only slightly above this value. This Reynolds number appears to be a critical value below which laminar separation can occur, although the point of laminar separation is also heavily dependent upon the blade surface pressure distribution.

More recently, Roberts⁽⁴²⁾ presented the results of varying Reynolds number tests on NACA 65 profile cascades. The cascades displayed characteristics similar to those described above. Roberts proposed a method of predicting shear layers across a laminar separation bubble, thus allowing the calculation of low Reynolds number flows.

The above findings applied to cascades of conventional, slender compressor blades. Scholz⁽⁵⁾ commented that Reynolds number effects are considerably less on bluff bodies where pressure drag constitutes a much greater proportion of the total drag. Nash et al.⁽⁴³⁾, in testing a square ended thin wedge section, found that doubling the Reynolds number from 2.25 to 4.5×10^6 caused an increase in the base pressure coefficient of less than one per cent. Since the drag on such a body is almost entirely pressure drag, the drag coefficient can be expected to have changed by a very similar proportion.

2.2.3 The Effects of Aspect Ratio and Axial Velocity Ratio

The effects of aspect ratio and axial velocity ratio are considered together since they are closely related. It is tempting to suppose that a cascade of high aspect ratio would a) give accurate two-dimensional results in the centre span plane, and b) yield an axial velocity ratio very close to unity in this plane. Pollard and Gostelow⁽³⁹⁾ found that for aspect ratios greater than three, the centre span region did indeed exhibit two-dimensional flow over a substantial length of the span. However, even for aspect ratios as high as five, the axial velocity ratio in the centre plane was greater than unity.

These effects occur because of secondary flows at the junction of the tunnel wall and the blade low pressure surfaces. The secondary flows twist the main flow aggravating the corner stalls and producing regions of high loss between the wall and the convex blade surfaces. Pollard and Gostelow showed that a cascade with an aspect ratio as low as two, when tested with solid walls, can cause secondary effects to extend across the whole span, thus invalidating any assumption of two-dimensionality. At higher aspect ratios, the flow may be two-dimensional in the centre region, but the blockage effect of the secondary flows causes a contraction of the flow and an axial velocity ratio greater than unity. The large contraction of flow occurring in cascades of low aspect ratio defers stalling in the mid-span plane but gives a lower deflection than is obtained with two-dimensional results. Studies of the characteristics and prevention of wall stall in compressor cascades have been made by Horlock et al.⁽⁴⁰⁾, Hanley⁽⁴⁴⁾ and by Stratford⁽⁴⁵⁾.

Pollard and Gostelow⁽³⁹⁾ showed that the effect of an increase in axial velocity ratio across a cascade is to reduce the static pressure rise and to cause an increase in deviation. Tests on a cascade of 10C430C50 profiles at a stagger of 36 degrees and space chord ratios of 0.875 and 1.0 exhibited a variation of deviation with AVR which could be approximated by straight lines of the form:

$$\delta = \delta' - 10(\text{AVR} - 1)$$

where δ' is the deviation at AVR = 1.0. Corrections were made for the effects of secondary flows in the results for AVR > 1.0. However, the gradient of $d\delta/d(\text{AVR})$ is expected to be a function of the blade surface pressure distribution and hence of the blade section as pointed out in the reported discussion on Horlock's paper⁽⁴¹⁾.

It is now accepted^(46,47) that the reason for differences between early American and British results on compressor cascades of similar section was due to the British tests being conducted at axial velocity ratios in excess of unity, while the American tests were made in a porous wall tunnel with the AVR maintained at unity.

The AVR was varied in the tests reported by Pollard and Gostelow⁽³⁹⁾ by use of a porous wall tunnel similar to the NACA tunnel reported by Erwin and Emery⁽⁴⁷⁾. The application of suction to the sidewalls enabled good, two-dimensional results to be obtained from a low aspect ratio cascade. The variation of axial velocity ratio through the upstream, downstream and through-cascade regions was measured and it was found that nearly all the change in AVR occurred in the cascade itself, thus validating the practice of setting a cascade to unit AVR based on measuring stations well upstream and downstream.

Felix and Emery⁽⁴⁶⁾, using the NACA porous wall tunnel, found that two-dimensional flow could be established with cascades of aspect ratios as low as unity, provided the suction was applied carefully.

2.2.4 Tunnel Configuration

The NACA instigated an experimental programme to investigate aspects of cascade testing. One of the aspects considered was the minimum number of blades required to obtain conditions representative of the performance of an infinite cascade. Erwin and Emery⁽⁴⁷⁾ found that provided the end and side wall suction was correctly set, the centre blade of a cascade of five blades performed satisfactorily. They also varied the gap between the sidewalls and the end blades of the cascade, but found that this variable had no effect on the centre blade.

2.2.5 The Setting of Blade End Suction Levels

Accepting that suction is necessary to obtain two-dimensional flow in compressor cascade tunnel tests, the obvious question that arises is that of how much suction to apply. Suction on the sidewalls is set to remove the sidewall boundary layers and thus control the inlet flow distribution, which ideally is uniform, and may be set by obtaining the most uniform possible distribution of upstream static pressure. The end suction is applied to remove boundary layers developing in the corner between the blade ends and the tunnel wall and ultimately this suction level can only be determined by trial and error, analysing properties measured downstream of the cascade until unit AVR is obtained.

Horlock⁽⁴⁸⁾ showed that by assuming incompressible flow through the cascade and applying Bernoulli's equation to the flow, the theoretical static pressure rise is given by:

$$\frac{P_2 - P_1}{\frac{1}{2} \rho U_1^2} = \left(1 - \frac{\cos^2 \alpha_1}{\cos^2 \alpha_2}\right) - \frac{\Delta P_o}{\frac{1}{2} \rho U_1^2} \quad 2.4$$

where ΔP_o is the loss in total pressure across the cascade.

Since the static pressure rise is affected by the amount of suction applied, the level may be set by use of this formula. Values of α_2 and ΔP_o are required, but approximations may be obtained from a preliminary test with a 'guessed' suction rate.

This procedure was in fact adopted in the present work for some early tests on a cascade of C4 section blades, performed to gain familiarity with the equipment, and the relationship expressed in equation 2.4 was found to be useful and accurate in setting suction levels. Unfortunately, the procedure is not so simple with a cascade of blown aerofoils, since the blowing air itself affects the static rise and the measured AVR. This problem is dealt with in Chapter 3.

CHAPTER 3

EXPERIMENTAL WORK AND DATA REDUCTION

3.1 Model Blades

3.1.1 Design Considerations

The model blades used in the wind tunnel tests had been designed and cast before the author became involved with this project. The basic philosophy of the design is easily deduced, however, and will be discussed briefly before detailing the blade construction.

The blade profile was based on an ellipse for ease of manufacture. The twenty percent configuration was probably the thinnest section which could be fabricated on the required scale, while being slender enough to avoid critical Mach number effects over a wide range of subsonic incident stream Mach numbers. The slot width was required to be fine enough not to distort the symmetrical blade profile seriously, while allowing the necessary range of blowing momentum coefficients at manageable supply pressures. Consideration of references discussed earlier, suggests that the required upper limit on the C_{μ} values would be between 0.1 and 0.2 at an incident Mach number of 0.3. Figure 5 shows the ratios of jet supply pressure to ambient pressure to give a particular blowing coefficient C_{μ} for a series of values of t/c . The curves of Figure 5 assume full expansion of the jet to the free stream static pressure. Since the loss of momentum coefficient with

use of a convergent nozzle is only about 7% at a jet pressure ratio of 10, the curves are reasonably accurate for convergent nozzles. It is seen that the slot thickness employed ($t/c = 0.006$) requires a slot pressure ratio of about 2.5 to give a C_{μ} of 0.2. Such a slot width is acceptably small from the point of view of profile distortion, without creating undue problems of fabrication or supplying the slot blowing air.

3.1.2 Construction

Drawings of the model blades are presented in Figure 6. The profile was based on a twenty two percent ellipse with a trailing edge formed by a semi-circle, centred on the origin of the ellipse. Each blade was cast from mazak and in two halves, as illustrated. The chord length was 25.4 mm and the geometry of the sections was such that a slot of nominal thickness 0.102 mm would be formed upon joining the blade halves.

Three of the blades were equipped with seven static pressure tappings equally spaced at thirty degree intervals around the trailing edge. They were distributed about the centre twenty per cent of the span, as shown in Figure 6. The tappings were formed by drilling into the trailing edge and inserting lengths of hypodermic stainless-steel tube, the ends being finished flush with the curved trailing edge surface. Experience with the performance of these tappings suggests that it would have been better to leave the ends of the hypodermic tubes below the surface and to join them to the measuring stations with a fine, plain hole. The routing of the static pressure

tubes inside the lower blade halves is shown in Plate 1 on page 32. Two blades were equipped with a single pressure tapping projecting into the slot plenum to record the slot supply pressure.

The blades were joined using ordinary, commercial 'Araldite'. Despite careful surface preparation, the strength of joint obtained was not consistent and instances of parting blades did occur. Some of the blades were originally assembled using a special type of 'Araldite' recommended by the manufacturers but even this adhesive did not prove fully reliable.

Short lengths of stainless-steel tube were inserted into the ends of the slot supply ducts. The tubes projected about 3 mm into each end of the blade and served as blade rear mounting pins. Thin, solid pins were set into the blade ends near the leading edge to act as forward locating points.

3.1.3 Spanwise Slot Flow Distribution

In compressor cascade tests considerable effort is directed towards obtaining two-dimensional flow over the centre span region; hence it was necessary to establish that the flux issuing from the slots did not exhibit a substantial variation along the span of the blades. When the slot is supplied from a large plenum, it can be assumed that a uniform slot width will yield a uniform flux along the whole length of the slot. In the present case, however, size limitations dictated that the blowing slot of each blade should be supplied from a circular duct of diameter 3.175 mm, giving a duct diameter/slot thickness ratio of 20.8 and a ratio of duct diameter/length of 0.125.

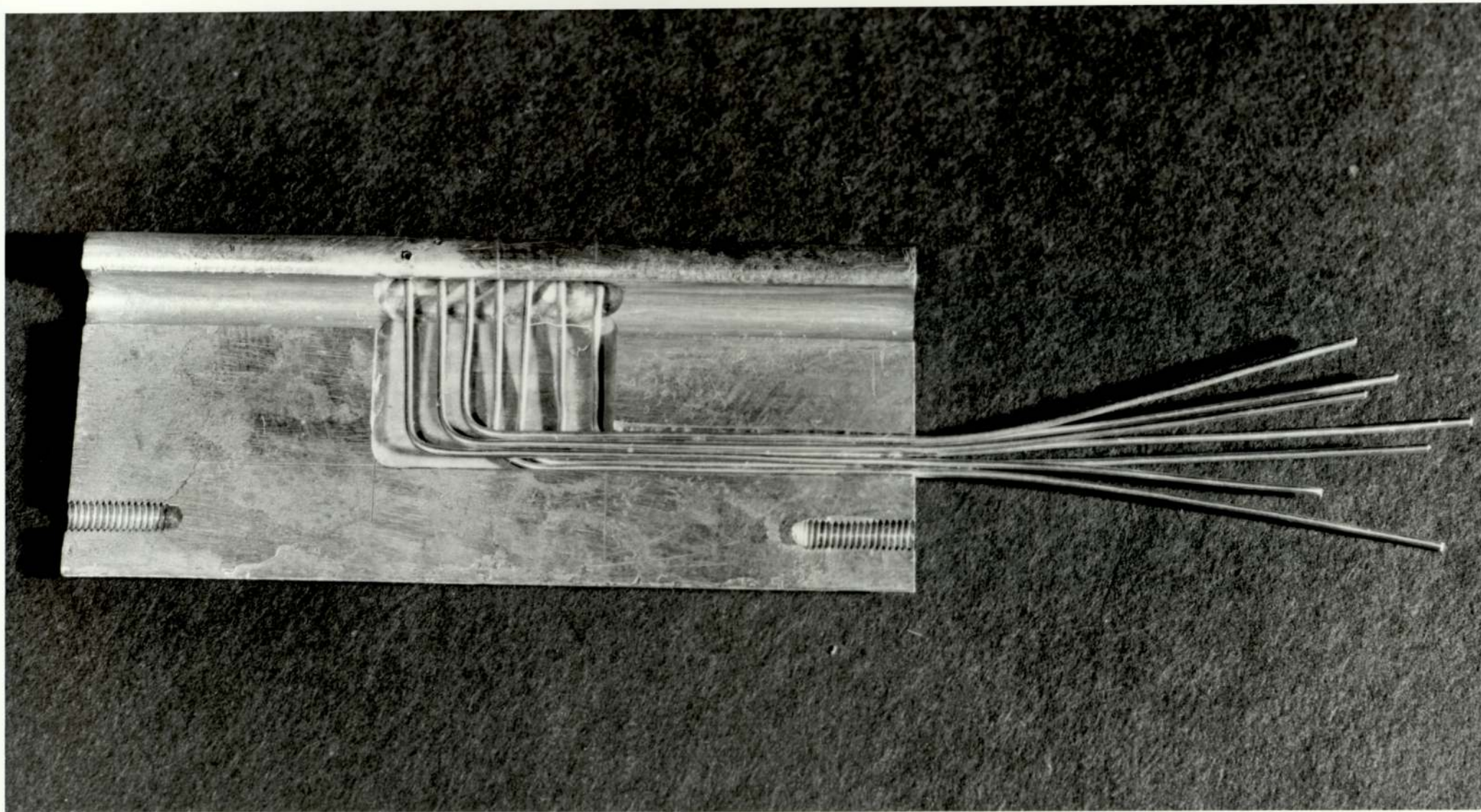


PLATE 1: Routing of Static Pressure Tubes Inside Lower Blade Half.

The latter ratio is obtained by using half the blade length: since the slot supply duct was fed from both ends it can be represented by a pipe of length equal to half the blade span and closed at one end.

Attempts to investigate the slot flow distribution with a fine pitot probe in still air proved difficult and inconclusive. It would have been possible to insert a fine hot-wire anemometer into the slot, but an accurate traverse along the whole length of each slot would probably not have been practical. As an alternative, it was decided to formulate a procedure for predicting the expected flow distribution and then to test the prediction procedure on a larger scale experimental rig. The theory of the method and the experimental comparison are described in Appendix A, together with the application of the procedure to the model compressor blades. The important result is that the maximum predicted variation of blowing momentum over the centre half of the blade span is less than 5% at low blowing pressures and less than 2% for choked flows.

3.2 Blade Slot Flow Calibration

3.2.1 Introduction

Before assembly of the cascade, the flow from each of the tangential blowing slots in the blades was calibrated. There were two reasons for this calibration:

- a) To ensure uniformity in blowing between all the blades.
- b) To avoid the need for metering the supply air to the cascade when under test in the wind tunnel, since any small leaks in the supply apparatus would give false flow readings.

3.2.2 Calibration Procedure

Each of the blades was held in turn in the frame designed for use in the tunnel, with all the air supply holes except those holding the blade blocked off. The air was supplied to both ends of the blade as when in the tunnel.

A flow meter and pressure tapping were included in the supply pipe. A sketch of the apparatus is given in Figure 7. When the fully instrumented blades were tested, the pressure indicated by the static tapping at the slot exit was recorded. When the two blades with a tapping in the slot air supply chamber were tested, this plenum pressure was recorded.

The supply flow was increased in steps over the range of supply pressures used in the tunnel tests. Pressure P_1 marked on Figure 7 was used as the reference pressure for which the same flow was to be expected for all the blades. It was found that all blades could be brought to display the same calibration curve by fine dressing of the slot: either polishing out with a piece of shim or by a gentle rubbing down on the slot lip to close the slot slightly.

Quantitative values for the slot mass flows were obtained by constructing calibration curves for the flow meter at each of the supply pressures used.

3.2.3 Application of Calibration to Blades in External Flow

To enable the calibration to be used for the cascade blades when in the tunnel, it was necessary to express the calibration as a function

of the pressure ratio between the slot plenum and the slot exit plane. The static tappings at the slot lip on the fully instrumented blades were provided to give the exit plane static pressure, but an extra complication arose: due to the curvature of the jet there existed a static pressure gradient across the jet, so that the pressure at the outside of the jet was greater than that at the surface. Thus the mean slot exit pressure would be less than the local external flow pressure and the local surface pressure would be lower still.

The detailed treatment of the slot velocity profile and the static pressure gradient is given in the next section.

3.2.4 Detailed Treatment of the Slot Velocity Profile

The slot exit velocity profile was assumed to conform to a 'power law' and to be of the form illustrated in Figure 8. For such a profile, with the density assumed uniform, the coefficient of discharge C_d is given by

$$C_d = \left(\frac{n}{n+1} \right) \quad 3.1$$

The pressure distribution across a curved flow is given by

$$\frac{\partial P}{\partial y} = \frac{\rho u^2}{R+y}$$

Assumption of the profile shown in Figure 8 gives for the pressure difference across the whole jet

$$\frac{P_E - P_I}{\rho U_j^2} = \left(\frac{2}{t} \right) \left[\int_0^{t/2} \frac{y^{2/n}}{(R+y)} dy + \int_{t/2}^t \frac{(t-y)^{2/n}}{(R+y)} dy \right] \quad 3.2$$

where P_E denotes the pressure at the outer jet flow boundary and P_I that at the surface boundary. For $n \rightarrow \infty$, equation 3.2 gives

$\frac{P_E - P_I}{\rho U_j^2} = \ln\left(\frac{R+t}{R}\right)$. For other values of n , the integrals are easily calculated numerically and Figure 9 shows equations 3.1 and 3.2 plotted as functions of n .

The problem of the spanwise slot flux distribution has already been dealt with. The work presented here assumes uniform conditions along the whole of the slot supply plenum chamber and a constant discharge coefficient of 0.85.

In calculating a theoretical mass flux, another problem arises due to the gradient of static pressure across the slot exit plane. This outlet pressure gradient is not insignificant: Figure 9 shows that for a profile with $n = 7$, the pressure difference across the slot would be expected to have a value of about 9.5% of the dynamic pressure at the centre of the jet. Consequently, it is to be expected that better agreement with experiment would be obtained by assuming the flow to exhaust to an outlet pressure P_m where

$$P_m = \frac{1}{2}(P_E + P_I) \quad 3.3$$

Such a solution requires iteration, since P_I is itself a function of U_j .

3.2.5 Results of Calibration and Comparison with Theory

Figure 10 shows the non-dimensional mass flux from the blade slots plotted as a function of the ratio of slot exit pressure over the pressure at the blade centre. Three curves are given:

1. The curve obtained from experiment.

2. The curve obtained from the assumption that the pressure at the blade centre exists as a total pressure throughout the plenum, and that the flow exhausts to the ambient pressure existing outside the slot.
3. The curve obtained by calculating the exit velocity U_j as in case 2, calculating the associated $P_E - P_I$, then recalculating the exit mass flux taking the exit pressure to be P_m as defined by equation 3.3.

The predictions of the pressure difference across the jet could be compared with experimental values obtained from the pressures indicated by the slot exit tappings, since the pressure at the jet outer surface was known to be atmospheric during calibration. The readings from these tappings were not highly accordant, presumably due to surface imperfections around the ends of the hypodermic tube inserts and the presence of the slot lips. Average values have been used consistently in this work. Figure 11 shows the experimental values of $\frac{P_E - P_I}{\rho U_j^2}$ plotted against the same abscissa as Figure 10. The terms used to non-dimensionalise the measured pressure differences were obtained by considering expansion to P_m , calculated from the measured pressure difference.

3.2.6 Comments on Calibration of Blades

Figure 10 shows the general agreement between the experimental curve and the theoretical curves. Neither of the theoretical curves is significantly better than the other in approximating to the experimental curve. The results suggest that the assumed value of C_d , 0.85, is in fact a little low at pressure ratios below 0.65 and a little high at pressure ratios above 0.65.

This variation in C_d is not unexpected, since the exponent n in the power law is generally a function of Reynolds number for all boundary layer flows. The slot flow Reynolds number at the highest blowing rates used in these tests was about 4×10^3 . It is also quite possible that the slot expanded slightly under the influence of the higher blowing pressures.

Figure 11 shows that the measured values of pressure difference across the jet are somewhat higher than would be expected for a value of n in the region of 6. The fact that the P_I values are consistently high, suggests that the phenomenon is probably a result of the presence of the slot lips: tappings in such a position might be expected to be highly sensitive to minute details of the local flow geometry. The choked flow results showed that the tappings at the slot lip indicated the local external surface pressure, minus the pressure drop across the jet thickness, rather than the choked jet pressure.

In all calculations concerning the cascade performance the slot plenum pressure is assumed uniform at the average of the values indicated by the two blades with tappings in this duct, and a constant discharge coefficient of 0.85 is applied.

3.3 The Wind Tunnel

A sketch of the cascade tunnel is shown in Figure 12. It accepted blades of 57 mm span and 25.4 mm chord. Rows of static tappings were provided at a half chord length upstream of the inlet plane and one chord length downstream of the outlet plane. Incidence was varied by rotation of the turntable and the sidewalls could be adjusted to extend

right up to the cascade inlet plane at any incidence. The sidewalls could also be moved inwards, to contract the tunnel width. The maximum tunnel width (115 mm measured normal to the tunnel axis) was generally used, inward adjustment of the sidewalls only being necessary to align the walls with the end blades when testing at stagger and positive incidence. The sidewalls were extended back to the tunnel inlet by strips of spring steel so that a smooth inlet would be obtained when the tunnel was contracted. A set of 10 static tappings were arranged well upstream of the cascade station to check for flow uniformity when setting the sidewalls. Suction slots were provided on the sidewalls, immediately upstream of the inlet plane, to give control over the distribution of upstream static pressure. The tunnel end walls contained recesses into which were fitted manifolds to supply the blowing air to the cascade. These recesses were used to draw mainflow air from the blade end region, helping to reduce secondary flows and to control the axial velocity ratio. Suction was applied to the blade ends and on the sidewalls by a 30 kW exhaustor. The suction rate from each of the four manifolds could be adjusted independently but a pressure tapping was provided in each of the suction pipes from the blade ends so that these two rates of bleed could be equalised.

The general arrangement of the tunnel and some of the associated equipment is shown in Plate 2, page 40. Plate 3 on page 41 gives a more detailed view of the cascade and the mechanism used to hold and traverse the fixed-direction probe, described in Section 3.5.

The tunnel was supplied with air by a cylindrical settling chamber of 0.46 m diameter and 1.8 m in length. The settling chamber itself was supplied through a steel hose from a 180 kW radial flow compressor.

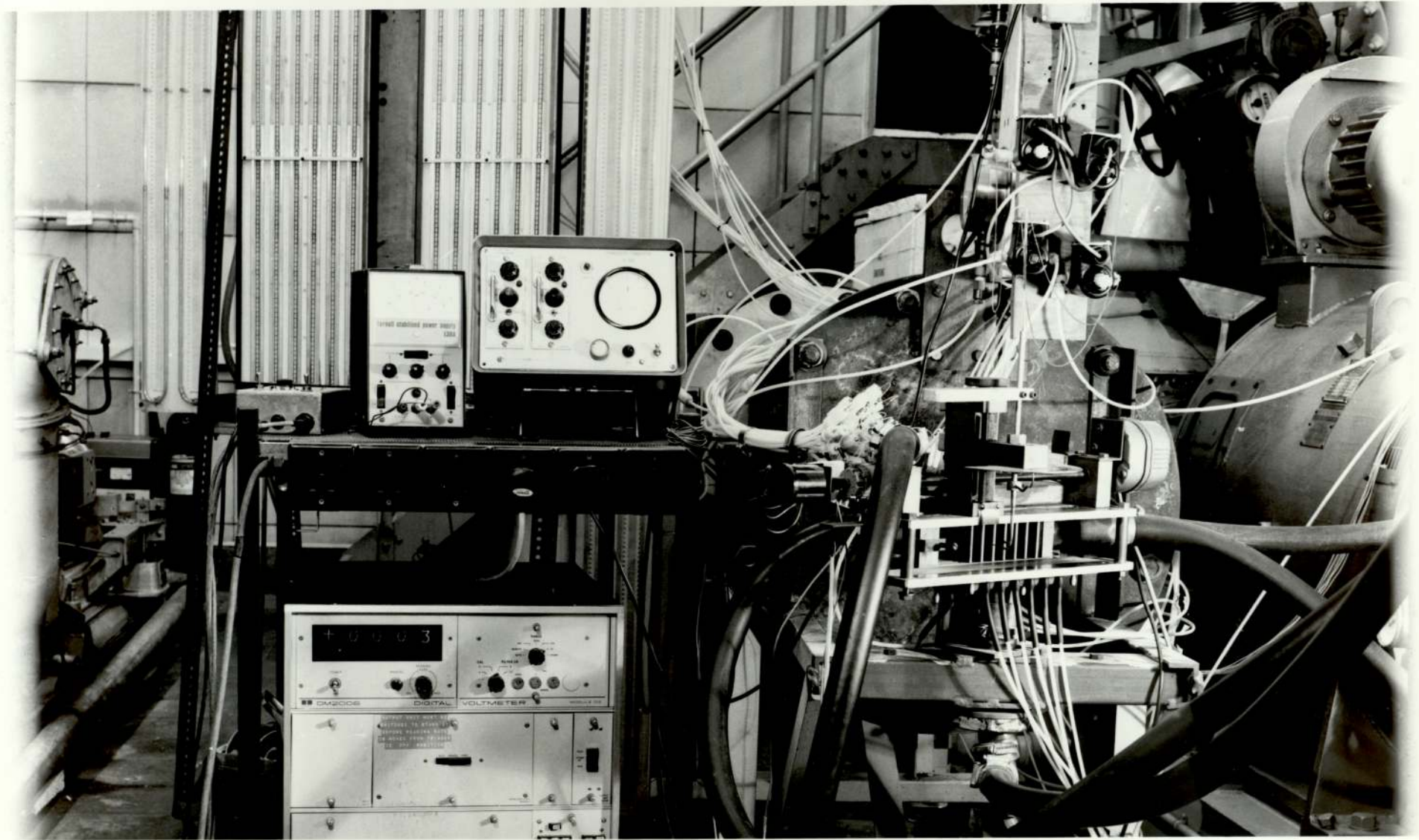


PLATE 2: General Arrangement of Wind Tunnel and Associated Equipment.

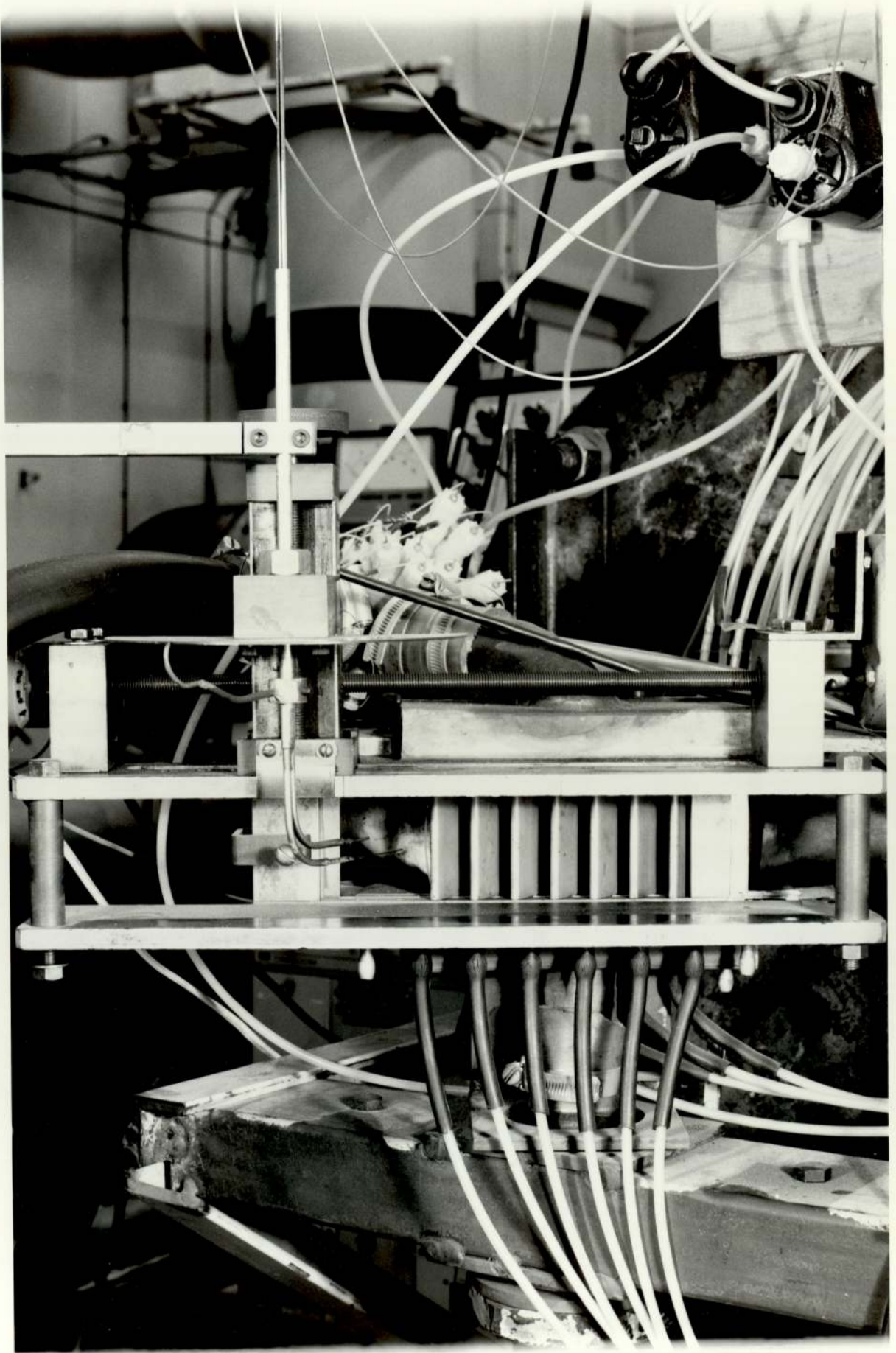


PLATE 3: Detailed View of the Cascade and Probe Traverse Mechanism.

A conical diffusing centre-body was provided at the inlet end of the settling chamber. The wind tunnel end of the chamber was fitted internally with a three-dimensional contraction to smooth the flow into the tunnel. The tunnel flow exhausted to atmosphere.

3.4 The Cascade Assembly and Blowing Air Supply

The cascade was held in a framework, shown in Plate 4, page 43. For the unit space/chord tests, 5 blades could be accommodated within the tunnel width and 7 blades at a space/chord of 0.75. The blowing air supply tubes, projecting from the ends of each blade located in the rear frame, while the forward frame held the small pins set into the blade ends near the leading edge. The cascade stagger could be varied by pivoting the forward and rear blade mounting frames in a parallelogram motion. Packing was clamped between the ends of the two frames to hold the assembly rigid. The blowing air supply manifolds fitted into the blade end suction recesses in the tunnel as sketched in Figure 13. Installation of the cascade necessitated removal of the top of the tunnel so that the rear blade frame could be sealed on the blowing air supply manifolds.

The blowing air was taken from a 1000 kN/m² supply main and passed through a 3 kW heating tube, a filter and a regulating valve. The air was then passed through a drum of silica gel to remove any remaining moisture or oil droplets before dividing into two streams, each to supply one end of the cascade.

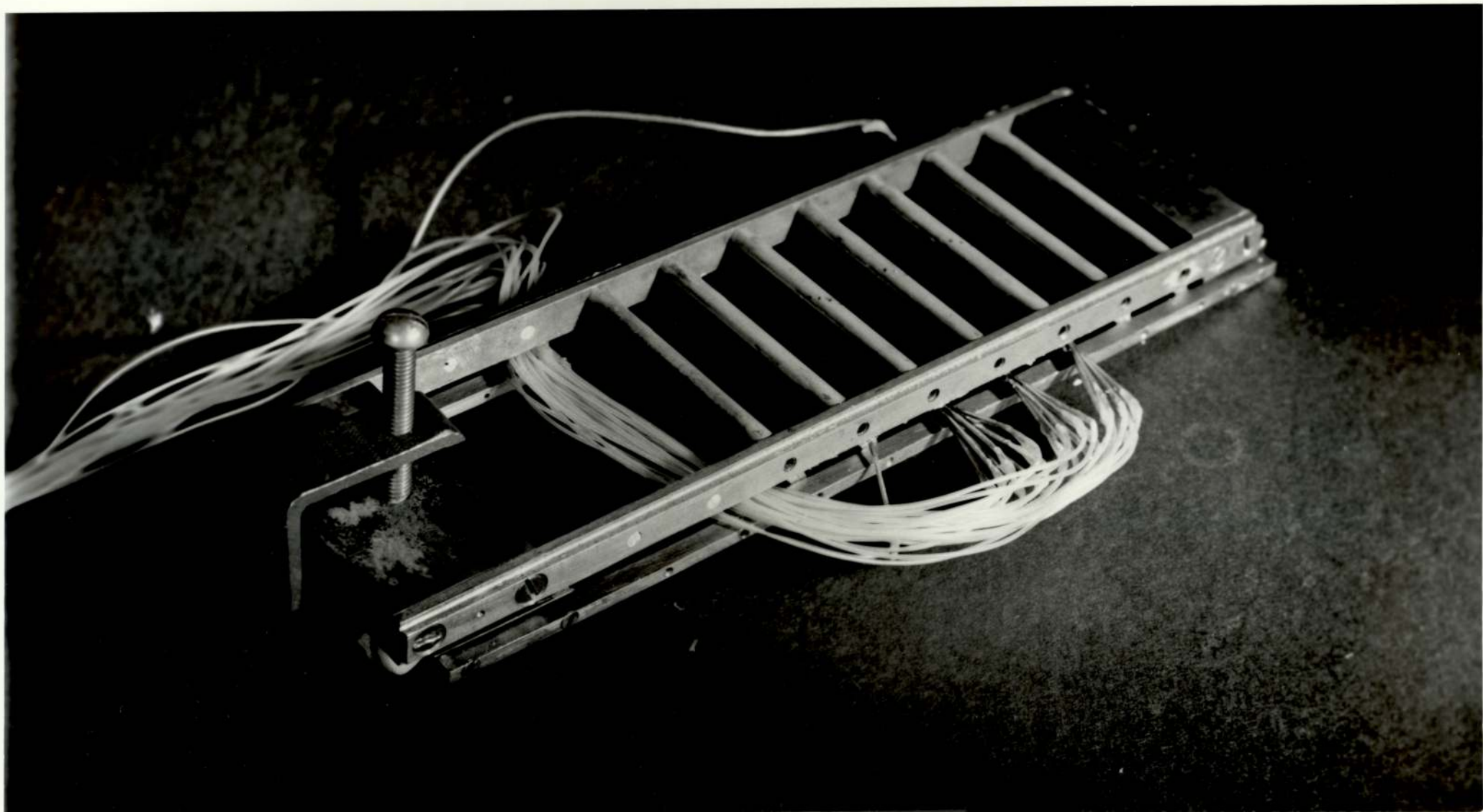


PLATE 4: Cascade held in frame.

3.5 The Probe Used for Downstream Measurements

Downstream readings of total pressure and flow angle were recorded by means of a fixed direction probe which was slowly traversed across the centre-span plane of the cascade. The probe tip was positioned at one chord length downstream of the cascade exit plane, above the static tapings in the tunnel floor. A static pressure probe was not included in the traversing assembly, since Pollard and Gostelow⁽³⁹⁾ found good agreement between probe and wall tapping static pressure measurements.

The probe was of the clustered tube variety, the centre of the three tubes having an orifice plane normal to the probe axis for the measurement of total pressure and the two yaw sensing elements being raked at an angle of forty five degrees. The probe is sketched in Figure 14. The tubing used in the probe assembly was stainless steel and silver solder was used at all joints. The three tubes comprising the probe tip were first joined with silver solder and the top and bottom surfaces of the assembly were ground to a fine, square finish. The cluster was then held in a jig and the tip was ground carefully to the final shape. After polishing, inspection under an eye glass showed a very fine finish with clear, sharp edges. The sharp angles of this type of probe help to maintain independence of the calibration from Reynolds number over a considerable range⁽⁴⁹⁾. The probe tip projected freely for a length of about 35 mm which put the tip well beyond the minimum acceptable distance from the probe support of about three support diameters⁽⁵⁰⁾. To avoid the problem of heat affecting flexible connections, stainless steel tube was used for the whole probe assembly. Flexible connections were then used to join the three outlet tubes to the differential pressure transducers.

The precise volume of the system between the probe tip and the transducer and the transducer volume itself was unknown. Using estimated volumes, an approximate settling time based on an expression given by Larcombe and Petro⁽⁵¹⁾ suggested that a step change in pressure from the highest to lowest pressures likely to be encountered during a cascade scan would give a settling time of about 0.2 seconds. The x-y plotter traces of the downstream total pressure profiles, for example Figures 27 and 28, showed that the pressure recording system was sensitive to local turbulent fluctuations so that mean pressure settling times were clearly negligible in comparison with the speed of the probe traverse.

The probe was calibrated by carefully setting the wind tunnel side walls symmetrically and arranging the probe so that the tip pointed directly along the tunnel axis. The probe elements were connected to U-tube water manometers. The yaw elements were connected differentially across one manometer, while the total pressure element gave readings relative to atmosphere. A pointer was attached to the probe support to indicate probe rotation on a scale which was readable to about $\frac{1}{4}$ degree. The probe was first aligned by obtaining a zero reading on the yaw manometer and adjusting the pointer to indicate zero degrees. The probe was then rotated in increments of $2\frac{1}{2}$ degrees over a range of ± 10 degrees. Since rotation of the probe caused transverse movement of the tip, the probe carriage was traversed after each yaw increment to bring the tip back to the tunnel centre line. At each increment readings were taken from the yaw and total manometers. The readings proved

consistent and repeatable. The calibration was performed at a Reynolds number based on blade chord of about 1.5×10^5 . The calibration has been plotted as the difference in yaw element pressures, non-dimensionalised by the dynamic pressure. The original calibration curve and later checks are plotted in Figure 15.

The characteristics and sensitivity of this design of probe have been investigated by Dudzinski and Krause⁽⁵⁰⁾. They concluded that flow direction is measurable to within one degree provided that the probe is individually calibrated. They also found that the centre tube gives correct readings of total pressure over yaw or pitch angles of about ten degrees. The calibration performed on the probe used in the present tests, suggests that the accuracy figure of one degree quoted by Dudzinski and Krause is conservative, and that flow direction measurement at a particular flow speed is realisable to an accuracy better than $\frac{1}{2}$ degree.

3.6 Instrumentation

All the tunnel static tapings were connected to multitube banks of water manometers, reading relative to atmosphere. A pressure tapping in the side of the settling cylinder was connected to a water manometer in the room from which the main compressor was controlled. This manometer was taken to indicate the total pressure at the cascade inlet since tests showed no discernable loss between the settling chamber and the centre region of the tunnel at the cascade station. The mainstream flow total temperature was measured by a thermometer inserted into the settling cylinder.

The centre element of the downstream probe was connected to one side of a differential, half bridge pressure transducer ($\pm 34.5 \text{ kN/m}^2$), the other side being connected to the settling cylinder. Thus, this transducer indicated directly the loss in total pressure across the cascade. The two yaw elements were connected differentially across a second pressure transducer. The three pressure leads to the transducers were also connected, through solenoid valves, to water U-tube manometers. This arrangement allowed easy checks to be made on the transducer calibrations. The transducers were connected to a converter unit to give a direct voltage output. Calibration of the transducers showed a good linear response over the whole range of pressures encountered during the tests.

The probe traverse was driven by a twelve volt motor. Readings of probe position were output in terms of a voltage measured across a multi-turn potentiometer which was driven by the traverse lead-screw.

The total and yaw transducer outputs and the probe position signal were all input to a data logging system which could scan at the rate of ten channels per second. Once a probe traverse across the rear of the cascade was commenced the data logging system would continuously monitor the input channels, recording the readings on punched tape. Successive groups of ten input signals were read in the following format:

4 total pressure readings,
1 yaw reading
4 total readings
1 probe displacement reading.

The reading rate was sufficient to yield approximately 20 such blocks of data across each blade pitch at a pitch/chord ratio of 0.75. The output from the total pressure loss transducer was also connected to an x-y plotter, thus giving an immediate visual record of the downstream total pressure distribution. This facility proved particularly useful during cascade tests.

The twenty one static pressure tapings arranged around the trailing edges of the three instrumented blades were connected to multi-tube manometer banks. Tappings 1 and 2 on each blade were connected to a tilting mercury manometer bank and the others to water manometers. At low blowing pressures, the two tapings provided to measure the slot plenum pressure were connected to the mercury manometer bank and at high blowing pressures to gauges. The calibrations of the gauges were checked on a dead-weight tester. A thermocouple was inserted into one of the blowing air supply hoses and connected in series with another in the main settling cylinder. Knowledge of the mainflow total temperature thus enabled the blowing air supply temperature to be determined.

3.7 Testing Procedure

Tests were performed at a nominal Mach number of 0.3. The required settling chamber pressure was set by regulating the proportion of total compressor flow fed to the tunnel. It has already been mentioned that the setting of blade end suction levels to attain unit axial velocity ratio was complicated by the use of blade blowing. In early tests, readings were taken for two or three different suction rates with the aim of spanning the unit axial velocity ratio condition. It was found,

however, that the blade end suction level had little effect on the results and in later tests, the suction rate was set by judgement based on experience.

The setting of sidewall suction rates was adjusted by referring to the distribution of upstream static pressure. The objective was to obtain as uniform a distribution as possible. The distribution became more difficult to control with increasing cascade incidence and blowing rate but the variation in upstream static pressure along the cascade was generally no greater than 2.5% of the inlet dynamic pressure.

The probe was aligned with the outlet flow direction at mid-passage: the centre of a passage flow was most easily found by obtaining a preliminary downstream total pressure distribution on the x-y plotter. The data logging system was then started and a traverse was made across the rear of the cascade in the centre span plane. All traverses and movements of the probe saddle during probe calibration were made in the same direction, since there was some backlash in the traversing system. Immediately after the traverse, readings of settling chamber total pressure and temperature, upstream and downstream static pressure distributions, the blowing air supply pressure and the trailing edge pressures of the three centre blades were recorded.

After each testing session, spot checks on the transducer calibrations were made. Such checks never yielded a discrepancy from the original calibrations of more than 2.5%. It was found that some degree of zero drift in the transducer converter always occurred during

a testing session. The total drift at the end of a session was recorded and a proportion of this total drift was apportioned to each set of results. The analysis of the total pressure records allowed this zero drift to be accounted for.

The pressure leads were tested periodically for leakage and the probe calibration was checked when the cascade was removed from the tunnel for changes in pitch-chord ratio or stagger.

3.8 Data Reduction

3.8.1 Introduction

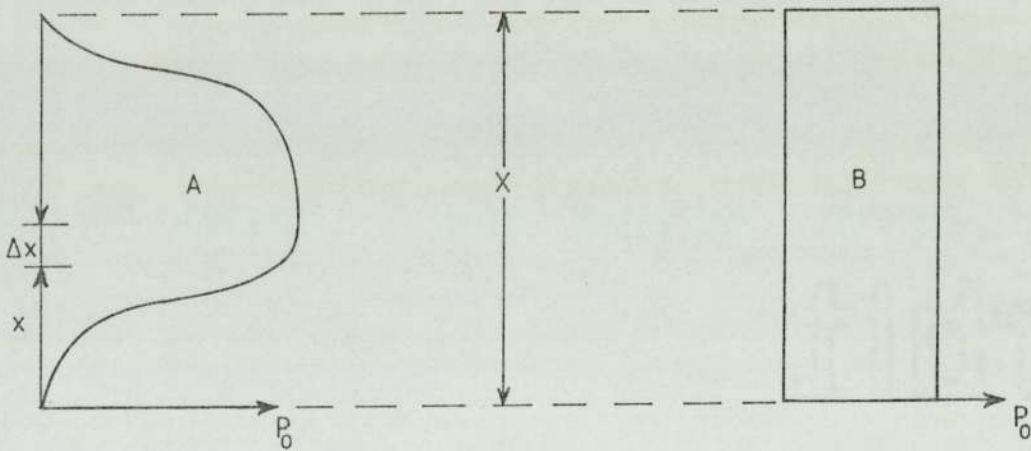
It was required to determine the usual cascade performance parameters, lift coefficient C_L , drag coefficient C_D , total pressure loss and static pressure rise for the blown cascade. All these terms are conventionally inferred by applying energy and momentum considerations to flow through a control volume encompassing one blade. When blowing is applied, modifications to the standard calculations are clearly necessary since a proportion of the downstream flow originates from the blowing slot: otherwise, for example, a negative drag would be calculated at high blowing rates. The reduction of results, therefore, was performed with the intention of eliminating the direct contribution of the blowing jets to the flow measurements recorded behind the cascade.

3.8.2 Standard Analysis Procedure

The downstream total pressure records consisted of many readings of total pressure at closely spaced positions across the rear of the cascade. The total pressure profile displays a marked periodicity for large downstream distances: Pollard and Gostelow⁽³⁹⁾

illustrate the decay of such a profile. The momentum analysis applied to a control volume assumes uniform flow conditions along the upstream and downstream boundaries. Thus, the application of the momentum analysis requires the deduction of properties existing at some hypothetical station so far downstream that the individual blade wakes have become fully mixed with the high energy passage flows.

Consider Sketch 3.1 which shows one pitch length of a total pressure profile, A, recorded a short distance downstream of the cascade outlet plane and the equivalent fully mixed profile, B, at a hypothetical station infinitely far downstream.



Sketch 3.1

Real and Fully Mixed Total Pressure Profiles

Application of momentum and energy conservation equations yields the following implicit expression for the Mach number at Station B:

$$\frac{1 + \gamma M_B^2}{M_B [1 + (\frac{\gamma-1}{2}) M_B^2]^{\frac{1}{2}}} = \frac{\Sigma (1 + \gamma M_A^2) \Delta x}{\Sigma M_A [1 + (\frac{\gamma-1}{2}) M_A^2]^{\frac{1}{2}} \Delta x} \quad 3.4$$

Numerical integration of the right hand side of equation 3.4, across one pitch length, with values of M_A calculated from the total pressure readings allows M_B to be found by iteration. The corresponding fully mixed static pressure may then be calculated from the momentum equation.

Having found the fully mixed flow conditions, the expressions given by Horlock⁽⁴⁸⁾ for lift and drag may be applied. These formulae, for a conventional, unblown cascade, may be obtained from those given in Appendix B if the slot blowing terms are ignored.

3.8.3 Modification for Blowing

It was required to subtract from the experimental results the direct contribution of slot blowing to the cascade performance characteristics. The necessary modifications to the results obtained from the conventional analysis described above are derived from first principles in Appendix B.

In calculating jet momentum coefficients, a peak jet velocity was deduced from the measured jet supply pressure and the slot exit pressure, the latter corrected for the normal pressure gradient across the jet. The entire jet flow was assumed to emerge with this velocity. While this definition of jet momentum coefficient is simple and in accord with previous practice, for example Kind⁽⁵²⁾, it may suggest a poor performance if results are compared with others in which the loss

of momentum in the slot boundary layer has been accounted for. This is particularly so in the present case, where the slot discharge coefficient is quite low.

3.8.4 The Computer Programmes

Two computer programmes were written to perform the data reduction described above. The programmes were written in BASIC computer language and were run on a Hewlett-Packard 9830 computer, coupled to a tape reader. The first programme read the data from the cascade outlet traverse directly from the punched tape and other data were manually supplied. The results output consisted of values of inlet Reynolds and Mach numbers, outlet angle, lift and drag coefficients, total pressure loss and axial velocity ratio. The outlet angle was taken to be the average of all values recorded over a pitch length. It is recognised that the yaw probe readings would tend to be inaccurate in regions of total pressure gradient, but as the probe was carefully aligned with the mid-passage flow, the adjustments to this nominal outlet angle made by the yaw probe readings were only small.

All the above results were calculated as for a conventional cascade. Due to computer memory limitations, the total pressure profile integration was only performed over one pitch length. Such an integration was generally repeated four times over different sections of the outlet profile so that good, average results would be obtained, representing the performance of several blades.

In addition to the fully mixed solutions described earlier, the programme also calculated results obtained from area and mass flow averaged values of downstream total pressure.

The second programme modified the fully mixed results to take account of the slot blowing effect, using the expressions presented in Appendix B.

CHAPTER 4

RESULTS OF CASCADE PERFORMANCE EXPERIMENTS

4.1 Cascade Characteristics

4.1.1 Lift, Drag and Turning Angle

Table 4.1, page 56, summarizes the cascade geometries tested. The majority of tests were performed at a space-chord ratio of 0.75 so that more blades could be accommodated within the tunnel. With a larger number of blades in the tunnel a better distribution of flow over the centre passages could be obtained at high blowing rates. Figures 16 to 26 show the lift and drag coefficients and the turning angles of the cascade over all the geometries tested. These characteristics have been plotted against the customary blowing coefficient, C_{μ} . The values of lift and drag coefficient have been corrected as described earlier, to subtract the direct effect of the jet on the downstream measurements.

Most of the lift coefficient and turning angle curves display a characteristic shape. Below a blowing coefficient of about 0.01, the slope is generally very small or zero. The curves then rise sharply to a blowing coefficient of approximately 0.03, beyond which the curves are roughly linear. The most striking characteristic, however, is the inflexion which occurs in the majority of these curves for the $s/c = 0.75$ results at a blowing coefficient of between 0.025 and 0.06.

s/c	Stagger ξ	Inlet Angle α_1
1.0	0°	0°, +5°, +10°
0.75	0°	-5°, 0°, +5°, +10°
0.75	35°	+25°, +30°, +35°, +40°, +45°

TABLE 4.1

Summary of Cascade Geometries Tested

These inflexions in the lift and turning angle curves are accompanied by a discontinuous fall in drag coefficient by about 50%. This phenomenon is not observed in the unit solidity results, although the drag is seen to fall as soon as blowing is applied in these cases.

The discontinuities in the $s/c = 0.75$ results were generally associated with the cessation of a loud, piercing whistle which was heard at low and zero blowing rates. An investigation of this whistle is described in Section 4.3, the conclusion being that it was the result of vortex shedding from the bluff trailing edges. The axial velocity ratio was also found to be influenced strongly by this phenomenon. In the unit solidity tests, results spanning the unit axial velocity ratio condition were readily obtained by varying the blade end suction rate, at all blowing coefficients. With the cascade set to $s/c = 0.75$, however, the low blowing results yielded axial velocity ratios below unity, even at very low or zero blade end suction rates. The axial velocity ratio in these cases could be as low as 0.91 with no slot blowing at all. The sudden drop in drag coincided with a general rise of axial velocity ratio such that varying suction would allow the unit axial velocity ratio point to be spanned. As might be expected with such a sudden change in characteristics, hysteresis in the position of this change was noticed, the blowing coefficient at which it occurred being generally higher when increasing C_{μ} than when reducing C_{μ} . Between these limits the flow was inclined to jump from one mode to the other.

Any expansion or contraction of the downstream flow between the trailing edge plane and the probe position, one chord downstream, would

give rise to an inaccurate analysis and erroneous axial velocity ratios. Inspection of the traverse displacement record and the associated total pressure profile, however, showed that there was no consistent expansion or contraction of the distance between total pressure minima. It would appear that the vortex shedding at low blowing rates causes a vigorous mixing action behind the cascade, effecting such large energy losses that the downstream axial velocity is lowered.

Figures 27 and 28 show downstream total pressure profiles recorded on the x-y plotter. The traces show a very marked change in total pressure profile with stagger angle. At 35° stagger, Figure 28, the downstream flow was more fully mixed at all blowing coefficients. Figure 23 indicates that a discontinuous fall in drag did not occur for the results at $\xi = 35^\circ$, $\alpha_1 = 40^\circ$ but at the same stagger where such a drop did occur, such as at $\alpha_1 = 35^\circ$, the total pressure profiles at low blowing coefficients were very similar to those at $\alpha_1 = 40^\circ$: that is, very much more mixed than at zero stagger. This fundamental difference in total pressure profiles between the two stagger angles was observed at all incidences. Consequently, it may be deduced that the wake flow characteristics were substantially different at the two stagger angles, even though well defined vortex motion was present in both cases below a certain blowing coefficient. In general, the whistle accompanying the vortex creation was found to be more sensitive to the slot blowing rate and to the amount of suction applied to the blade ends and tunnel walls, at $\xi = 35^\circ$. It was also observed that under this cascade configuration the whistle sometimes became slightly higher pitched and displayed a tendency to 'twitter' intermittently when the slot blowing rate was close to that at which

the whistle vanished altogether. This region of instability was associated with an increased local 'jaggedness' of the local pressure trace, such as in Figure 28b. Comparison of the traces for the two cascade staggers shows that a slightly more jagged profile is displayed for all the 35° stagger results, implying a more violent turbulence structure. This greater turbulence was presumably the reason for the greater mixing behind the staggered cascade.

The lift coefficient and turning angle curves at zero stagger, zero incidence, do not pass through the origin. At unit solidity the turning angle is -0.5 deg., with no blowing and at $s/c = 0.75$ it is about +1.0 deg. It is accepted that imperfections in the cascade assembly probably limited the accuracy of individual blade alignment to about 0.5 deg. Additionally, the typical accuracy of outlet angle measurement is considered to have been about 0.5 deg. The zero blowing values of turning angle, therefore, probably represent the general accuracy limits of the curves. It is likely, however, that the presence of the slot just before the upper surface boundary layer would ordinarily separate with no blowing, would cause a slight asymmetry of the blade wakes, so that curves passing exactly through the origin are not necessarily to be expected.

It is interesting to observe that the drag coefficient curves all start at a value of between 0.15 and 0.25 at zero blowing and after the drop in drag tend to a constant value of about 0.1. This behaviour is in contrast with the results of Kind and Maull⁽²⁰⁾ for an isolated, tangentially blown ellipse. They also applied an analysis to subtract the direct effect of the blowing jet from the results of a wake-traverse,

but obtained drag values which increased continuously with blowing coefficient. A clue to this behaviour is to be found in the pressure distributions measured around the trailing edges of the three centre blades. This will be discussed further in Section 4.1.5.

Certain curves, for example Figure 22 with $\alpha_1 = 45$ deg., are terminated at a blowing coefficient well below 0.15. This is because the downstream total pressure profile, outlet angle, and the upstream static pressure distribution varied considerably across the centre blade passages at high blowing coefficients and the data reduction was deemed to be unacceptably inaccurate. In no test was there any evidence of a breakdown of the Coanda effect or stall as would be signified by a peak in the turning angle and lift coefficient curves.

Figure 29 shows the variation of boundary layer control coefficient, C_{blc} , and jet velocity ratio, U_j/U_{sj} with momentum coefficient for one set of results. The point where $U_j/U_{sj} = 1.0$ is significant, since it is here that the blowing jet begins to take real effect. Other workers have found that for values of this ratio below unity, the jet has little effect and may, under certain circumstances, be detrimental. Reference to Figures 17 and 25 shows that the unit velocity ratio occurs in the region where the turning angle and lift are increasing most rapidly, so that the jet is effective even for ratios less than unity. This is because the boundary layer is very close to separation at the slot position, so that even low blowing rates impart more energy to the boundary layer than it would have in the absence of blowing. The position of unit slot velocity ratio was found to lie in the region of most rapid turning angle increase for all the curves.

4.1.2 Reynolds Number Effects

It was considered desirable to determine whether Reynolds number variation had a great effect on the cascade performance. It had been noticed in particular that the position of the discontinuity in characteristics was sensitive to the inlet total pressure and hence the test Reynolds number. The Reynolds number could not be varied very much: evidence discussed earlier shows that conventional cascade performance becomes sensitive to Reynolds number as the Re is reduced towards 1.0×10^5 but it was not believed advisable to raise the inlet velocity due to concern about the strength of the blade joints. Figures 18, 23 and 26 include points obtained at a Reynolds number of 1.27×10^5 . The corresponding 'standard' results were obtained at a Reynolds number of approximately 1.45×10^5 . The associated inlet Mach numbers were 0.26 and 0.30. The most notable effect of the reduced Reynolds number is the shift in the position of the discontinuity in drag to a higher blowing coefficient. Beyond this point, it appears that the two sets of characteristics tend to converge. On the basis of this limited evidence, it might be expected that tests conducted at generally higher Reynolds numbers, say $Re > 2 \times 10^5$, would be entirely free from vortex shedding and the associated inflexions and discontinuities in characteristics: it is well known that vortex shedding is a low Reynolds number phenomenon.

4.1.3 Jet Temperature Effects

Figures 18, 23 and 26 show three sets of experimental points obtained with the slot blowing air heated to a total temperature which was within 2 K of the mainstream temperature. These tests were performed last of all for fear that the high jet temperature in

combination with a high blowing pressure might cause the blades to part. It was considered necessary to establish whether the cascade performance was noticeably affected by the difference in jet and mainstream total temperatures existing in all earlier tests because certain previous workers in the wall-jet field have taken trouble to equalise these temperatures⁽⁵³⁾. The limited number of experimental points was due to the difficulty in maintaining the jet temperature constant over the time required to record a full set of readings.

It is seen that the first two sets of results coincide well with the original results, obtained at a jet total temperature about 60 K below that of the mainflow. The third result does not correspond so well but in this one case problems with the punched tape record severely limited the analysis of the downstream total pressure profile. This result, therefore, is not expected to be fully consistent with those obtained from a normal analysis. The important finding is that the previous results do not appear to have been influenced substantially by the difference in jet and mainstream total temperatures.

4.2 Trailing Edge Pressure Distributions

Figures 30 and 31 show typical trailing edge pressure distributions measured at two space-chord ratios and at the same inlet angle and stagger. It can be seen that in the case of the unit solidity cascade, at zero blowing, there is no sign of the negative pressure peak which occurs at 90° on the lesser pitched cascade. Neither did such a peak manifest itself at low blowing rates. Beyond a low blowing coefficient the pressure distribution on the smaller pitched cascade becomes similar

to that on the unit pitch configuration: high negative pressures at the slot exit and at 30° from this position, then a sudden rise in pressure to an almost constant value.

It is instructive to compare the corresponding drag curves, Figures 19 and 20. The relatively flat drag curve at unit pitch reflects the fact that the static pressure is fairly uniform around the majority of the trailing edge at all blowing rates, save for the peak near the blowing slot. At the smaller pitch, a greater drag at low blowing rates can be predicted from the observed higher negative pressures. The loss of the suction peak at 90° on this cascade, with the abrupt increase in trailing edge pressures to an almost constant value of about -0.45, coincides with the discontinuous fall in drag.

The observed behaviour of the trailing edge static pressure distribution explains the marked difference in drag characteristics between the cascade and the isolated ellipse tested at low speed by Kind⁽⁵²⁾. In the latter case, the drag coefficients rose continuously with slot blowing momentum because the trailing edge suction peak was maintained over the whole range of blowing rates.

Unfortunately, the relative sparsity of static tappings between the slot exit and the 60° station makes it impossible to observe the changing position of jet separation with blowing coefficient. The results represented in Figures 30 and 31 indicate that the jet separated before the 60° station over the whole range of blowing coefficients.

It was commented earlier that there appeared to be a marked difference in wake characteristics between the staggered and unstaggered cascades at a pitch of 0.75. The absence of the negative pressure peak at 90° on the trailing edge of the unit pitch cascade at low blowing rates, in contrast with the 0.75 pitch configuration, yet again implies a substantial dissimilarity in wake characteristics. Clearly, cascade geometry exerts considerable influence on flow in the trailing edge region.

4.3 The Nature of Mixing Losses in the Trailing Edge Region

The characteristics of the mixing process and associated losses in the wall jet flow around the trailing edge of a circulation controlled aerofoil were considered in some detail by Kind⁽⁵²⁾, based on the works of Stratford⁽²⁵⁻²⁷⁾. Stratford showed that the net momentum flux excess of a jet which mixes with a parallel stream in a region of low static pressure exceeds that of a jet which does not mix, in a subsequent region of higher static pressure. The converse is true if the jet mixes in a region of high pressure and flows to a lower pressure region. Mixing losses also occur if the mixing streams are not parallel.

Kind argued that over the attached portion of a trailing edge blowing jet the static pressure is lower than the free stream static pressure and that the local external flow is reasonably parallel to the jet flow. Thus, over this attached region, a mixing gain is to be expected. However, in the region of jet separation, the local velocity is lower than the free stream velocity and the angle between the jet and the local external stream becomes large. Thus mixing losses are expected to be

high in the region where the blowing jet separates. These tendencies were verified experimentally by Kind.

The mixing losses induce drag by two mechanisms: first, the mixing losses inhibit the ability of the jet sheet to induce an upwash at the leading edge. In an ideal flow this upwash would counteract the form drag created by the low pressure region around the trailing edge, which exists due to the centrepetal acceleration of the wall jet. Second, the mixing process causes a lowering of the static pressure around the trailing edge by virtue of the 'sink' effect as discussed by Stratford. Simply, the mixing effect of the jet requires the drawing of surrounding flow into the jet mixing region, so creating a suction around the jet boundary in a manner similar to a sink distribution.

Kind considered that the primary contributor to drag in his tests, with high jet inclination angles, was the reduced form thrust and this is likely to be so in the present case, once the blowing jet is sufficiently strong to close the wake.

4.4 An Investigation of the Cascade Whistle

During the course of tests on the cascade at a pitch chord ratio of 0.75, a loud, high pitched whistle was sometimes heard. The appearance and disappearance of this whistle generally accompanied a notable change in cascade characteristics and so it was decided to investigate this phenomenon.

At first, it was not entirely clear whether the whistle was caused by the shedding of vortices at the bluff trailing edges of the blades

or by the presence of the slot, causing a resonance within the slot air supply chamber. It was even possible that the presence of the slots might have caused a standing wave to be set up between blades.

The noise was not created by the jet flow itself, a phenomenon treated theoretically by Baker and Manhardt⁽⁵⁴⁾, because it was present when no slot blowing was applied. It was decided to measure the frequency of the whistle and determine whether the associated wavelength or some meaningful aliquot part of the wavelength corresponded to a physical dimension of the cascade assembly. With the cascade set to zero incidence, 35° stagger and at a typical test Reynolds number the blowing air was set to a pressure just above that at which the whistle disappeared. A tape recording of this background noise was taken as a reference base. The blowing air supply pressure was then reduced slightly to produce the whistle, and another recording was taken. The recording system comprised a Brüel and Kjoar condenser microphone connected to a Racal Store 4 recorder, giving a frequency response of up to about twenty kiloHertz. The recordings were analysed on a Spectral Dynamics Real Time Analyser and the resulting frequency distributions are shown in Figure 32. The effect of the whistle is most marked, the first harmonic occurring at about 6 kHz. The second and third harmonics are clearly visible. The wavelength corresponding to this frequency is about 60 mm which bore no obvious relationship to any dimension of the cascade except, perhaps, the span (57 mm). This did raise the possibility of the suction slots at the blade ends being a cause of resonance, but since the effect was not noticed with a different blade spacing or, indeed, with variously pitched cascades of conventional blades, the suction slots seemed an unlikely cause.

It became clear that the audible frequency was generated by the shedding of vortices from the bluff trailing edges and this view was strengthened by the observation that the downstream total pressure profiles recorded on the x-y plotter displayed high fluctuations from the mean when the whistle was present as demonstrated in Figure 28b.

The most common manifestation of vortex shedding in the audible range is the well known Aeolian tone produced by a wind blowing over a wire. This sound is produced by the formation of a Kármán vortex street behind the wire. For circular cylinders vortices continue to be shed regularly up to a Reynolds number of 4×10^5 to 5×10^5 , beyond which complete turbulent mixing occurs and vortex formation is suppressed^[55]

A dimensionless quantity known as the Strouhal number is used to characterise vortex shedding phenomena. The Strouhal number, S , is defined by

$$S = \frac{fd}{U} \quad 4.1$$

where f = the shedding frequency

d = a characteristic length, usually the maximum width presented to the oncoming flow.

U = a characteristic flow speed, usually the free-stream speed.

Roshko⁽⁵⁶⁾ studied the shedding frequencies of variously shaped bluff cylinders and found that by forming a Strouhal number from values of d and U characteristic of the wake flow and relating this to a Reynolds number again obtained from wake characteristics, a 'universal' empirical relationship could be established. The combination of this



result with free streamline theory allows drag to be calculated simply from a measurement of the shedding frequency for a particular section shape. The calculation requires a value for the width of the wake which is a function of the overall shape of the bluff section, so the calculation procedure is restricted to sections for which empirical data concerning the wake width is available.

The majority of work on vortex shedding has been performed on circular cylinders, although square, rectangular, triangular and other geometries of cylinder have also been reported^(56,57). Modi and Wiland⁽⁵⁸⁾ performed tests on isolated elliptic cylinders of two thicknesses, 80% and 60%, measuring the fluctuating pressures and vortex shedding frequencies over a range of incidences. The Reynolds numbers of their tests varied between 2×10^4 to 10^5 based on the major ellipse axis and they found that the Strouhal number varied linearly with flow speed. They showed that the variation of Strouhal number with incidence was much less when based on the projected cylinder height than when based on the minor axis. At zero incidence, the Strouhal number for both ellipses was about 0.215 which corresponds to the asymptotic value given by Roshko⁽⁵⁶⁾ for circular cylinders in the Reynolds number range 10^3 to 10^4 .

Nash et al⁽⁴³⁾ investigated the variation of Strouhal number with Mach number for a wedge shape of 10% thickness, at zero incidence and with a square trailing edge. The Strouhal number remained constant at a value of 0.25 between Mach numbers of 0.2 and 0.9, the corresponding chord Reynolds numbers being 0.77×10^6 and 2.5×10^6 .

The Strouhal number obtained from the cascade test using the measured frequency, the downstream flow speed and the maximum blade thickness was 0.25. The corresponding Reynolds number based on the blade chord was about 1.5×10^5 . This Strouhal number compares well with the values quoted above, especially as a slightly higher value is to be expected as a result of the wake contraction caused by the cascade effect. The tendency for the whistle to disappear with the application of blowing is easily understood: the jet moves the upper surface separation point round the trailing edge contracting the wake and suppressing the formation of vortices. What is not so clear is the reason for the absence of the whistle during the unit space-chord ratio experiments. During these tests no whistle was noticed and none of the downstream total pressure traces displayed the large fluctuations noticed when the whistle was present in the 0.75 space-chord tests. However, when the whistle did occur, it was found to be highly sensitive to the slot blowing rate, the wind tunnel end and sidewall suction rates and the mainstream flow speed. It is not altogether surprising, in view of this sensitivity, that the whistle was not present in the unit space-chord tests. It is to be expected that the vortex formation would be heavily dependent upon the blade surface boundary layer development and hence upon the blade pressure distribution.

None of the previous works studied, concerning the application of tangential blowing to either cascades or isolated sections, have mentioned vortex created audible noise. This is most probably because circulation control tests on circular cylinders have been performed at higher Reynolds numbers than the tests described here, while the

elliptical sections previously used have been less bluff. The present findings are of considerable interest and show the importance of considering the possible creation of aerodynamic noise by bluff sections.

CHAPTER 5

POTENTIAL FLOW THEORY

5.1 Introduction

Historically, there have been two principal methods of calculating the incompressible flow past aerofoils or through cascades: the classical method of transformation and the distributed singularity approach.

The classical method of transformation is capable of giving mathematically exact results for certain sections which can be mapped onto a complex plane by conformal transformation. It is also possible to accomplish approximate transforms of shapes for which there is no exact transformation. The primary disadvantage of the application of this technique to general shapes is the considerable operator interaction required with the computations. Where exact transformations are possible, however, 'reference' results can be obtained with which other, approximate methods can be compared. This procedure has been accomplished by Gostelow⁽⁵⁹⁾ who extended the theory of Merchant and Collar⁽⁶⁰⁾ to obtain a standard for comparison with approximate methods.

The principle now most generally used is that of distributed singularities. These modern methods are founded upon the works of Schlichting⁽⁶¹⁾ and of Martensen⁽⁶²⁾. The techniques represent the

aerofoil(s) or cascade by a distribution of singularities, which on being combined with the incident flow, create a streamline which follows the profile of the desired aerofoil shape.

The Schlichting method involves distributing sources, sinks and vortices along the chord line of each blade. This method was used by Pollard and Wordsworth⁽⁶³⁾ and by Gostelow⁽⁵⁹⁾, the distribution of singularities matching the profile at between fifteen and twenty points. Some of the assumptions involved in Schlichting's method and the importance of data presentation have been investigated by Lewis and Pennington⁽⁶⁴⁾.

A more sophisticated distributed singularity approach was developed by Martensen⁽⁶²⁾, who distributed vorticity around the profile perimeter. This method, with variations, is now very widely used⁽⁶⁵⁻⁶⁹⁾ and can be applied to isolated sections, multiple section aerofoils and to cascades with an accuracy comparable with experimental data.

It is the Martensen distributed vortex method, with an extension to allow simulation of a wake by the use of sources, which has been used to calculate the pressure distribution about the aerofoils and cascades treated theoretically in this dissertation. The distribution of vortex elements about the section surface follows the method of Wilkinson⁽⁶⁹⁾ and of Jacob and Riegels⁽⁶⁶⁾, while the use of source distributions in the trailing edge region is an approach briefly outlined by Geller⁽⁶⁵⁾.

5.2 The Governing Equations

5.2.1 Development of the Equations

The section is represented by a continuous distribution of vortices around the perimeter of strength $\gamma(\sigma)$ per unit length. Where separation is present at a bluff trailing edge, a source distribution $S(\sigma)$ is added in this region, (Figure 33). The boundary condition is that the sum of the effects of the freestream flow, the vortex distribution and the source distribution should yield zero internal tangential velocity at all points on the section perimeter. Equating the sum of these components to zero at a point σ_m gives:

$$\begin{aligned}
 - \frac{\gamma(\sigma_m)}{2} + \frac{1}{2\pi} \oint \gamma(\sigma) K_\gamma(\sigma_m, \sigma) d\sigma + \frac{1}{2\pi} \int_{\sigma_{nL}}^{\sigma_{nu}} S(\sigma) K_S(\sigma_m, \sigma) d\sigma \\
 = - U_\infty \left(\cos\alpha \frac{dx}{d\sigma_m} + \sin\alpha \frac{dy}{d\sigma_m} \right) \qquad 5.1
 \end{aligned}$$

The first term on the left hand side represents the local velocity discontinuity, the second the integrated effect of the vortex distribution and the third the integrated effect of the source distribution between points σ_{nL} and σ_{nu} . $K_\gamma(\sigma_m, \sigma)$ and $K_S(\sigma_m, \sigma)$ are influence coefficients. The right hand side of equation 5.1 represents the contribution of the free stream resolved parallel to the surface at σ_m .

A new variable, ϕ , is defined which varies continuously from zero at the trailing edge to 2π moving anti-clockwise around the complete perimeter. The section can then be represented in parametric form:

$$x = x(\phi), \qquad y = y(\phi)$$

Transformed vortex and source distributions are defined by

$$\gamma(\phi)d\phi = \gamma(\sigma)d\sigma$$

and

5.2

$$S(\phi)d\phi = S(\sigma)d\sigma$$

Equation 5.1 becomes

$$\begin{aligned} -\frac{\gamma(\phi_m)}{U_\infty c} + \frac{1}{2\pi} \int_0^{2\pi} \frac{\gamma(\phi)}{U_\infty c} K_\gamma(\phi_m, \phi) d\phi + \frac{1}{2\pi} \int_{\phi_L}^{\phi_u} \frac{S(\phi)}{U_\infty c} K_S(\phi_m, \phi) d\phi \\ = -(\cos\alpha x'_m + \sin\alpha y'_m) \end{aligned} \quad 5.3$$

where $x' = \frac{dx}{d\phi}$, $y' = \frac{dy}{d\phi}$, c is a reference length,

and $\phi_u = \phi$ at separation on the upper surface,

$\phi_L = \phi$ at separation on the lower surface.

The γ function is represented by $2N$ discrete points, termed pivotal points, and the integration in equation 5.3 is performed by the trapezium rule:

$$-\frac{\gamma(\phi_m)}{U_\infty c} + \frac{1}{2\pi} \int_0^{2\pi} \frac{\gamma(\phi)}{U_\infty c} K_\gamma(\phi_m, \phi) d\phi = \frac{1}{2N} \sum_{n=1}^{2N} \gamma_n K_{\gamma mn} \quad 5.4$$

where

$$\gamma_n = \frac{\gamma(\phi_n)}{U_\infty c}, \quad \phi_n = \frac{n\pi}{N}, \quad (n = 0, 1, 2, \dots, 2N)$$

and the local discontinuity term has been absorbed into element K_{mm} .

In the case of the source distribution, the integration covers only the points within the separated region:

$$\frac{1}{2\pi} \int_{\phi_L}^{\phi_u} S(\phi) K_S(\phi_m, \phi) d\phi = \frac{1}{2N} \sum_{n=(n_L+1)}^{(n_u-1)} S_n K_{S mn} \quad 5.5$$

where

$$S_n = \frac{S(\phi_n)}{U_\infty c}$$

and it is implicit that $S_{nL} = S_{nu} = 0$, i.e. that the source distribution vanishes on the separation points.

The influence coefficients are defined by:

$$K_{\gamma mn} = \frac{(x_m - x_n)y_m' - (y_m - y_n)x_m'}{(x_m - x_n)^2 + (y_m - y_n)^2},$$

$$K_{\gamma mm} = \frac{1}{2} \frac{(x_m' y_m'' - y_m' x_m'')}{x_m'^2 + y_m'^2} - N,$$

$$K_{S mn} = \frac{(y_m - y_n)y_m' + (x_m - x_n)x_m'}{(x_m - x_n)^2 + (y_m - y_n)^2}, \quad 5.6$$

$$K_{S mm} = 0$$

for an isolated section. For the case of an infinite cascade, the influence coefficients of isolated vortices and sources are replaced by expressions for the influence of infinitely long rows, spacing s :

$$K_{\gamma mn} = \frac{\pi}{s} \frac{\sinh \frac{2\pi}{s}(x_m - x_n)y_m' - \sin \frac{2\pi}{s}(y_m - y_n)x_m'}{\cosh \frac{2\pi}{s}(x_m - x_n) - \cos \frac{2\pi}{s}(y_m - y_n)},$$

$$K_{S mn} = \frac{\pi}{s} \frac{-\cot \frac{\pi}{s}(y_m - y_n) [1 - \coth^2 \frac{\pi}{s}(x_m - x_n)] y_m' + \coth \frac{\pi}{s}(x_m - x_n) [1 + \cot^2 \frac{\pi}{s}(y_m - y_n)] x_m'}{\coth^2 \frac{\pi}{s}(x_m - x_n) + \cot^2 \frac{\pi}{s}(y_m - y_n)}$$

5.7

and $K_{\gamma mm}$, $K_{S mm}$ are as for the isolated section.

It is important to note that with the presence of source elements, the coefficient matrix is not square.

5.2.3 Lower Mean Values

The trapezium integration is fairly accurate at all points except where two vortices lie opposite each other on the upper and lower surfaces, near a cusped trailing edge. At this point, the integration curve has a high and narrow peak. Following Wilkinson, a lower mean value of $K_{\gamma m, 2N-m}$ is used, derived from the condition of irrotationality. Each column, n , of the matrix $K_{\gamma mn}$ represents the effect of one vortex at each point $m_1, m_2, m_3, \dots, m_{2N}$ on the section surface. From the condition of irrotationality, the integral of the surface velocity component induced by any one vortex around the closed section, not including that vortex, is zero:

$$\sum_{m=1}^{2N} K_{\gamma mn} = 0$$

This allows the $K_{\gamma m, 2N-m}$ element to be replaced by a lower mean value:

$$K_{\gamma m, 2N-m} = - \sum_{\substack{p=1 \\ p \neq m}}^{2N} K_{\gamma p, 2N-m} \quad 5.10$$

5.2.4 Treatment of Separated Region

The inclusion of source terms in equation 5.9 is to simulate the separated region and wake of a bluff section. It has been well established, experimentally, that the surface pressure in a separated region is uniform and this fact allows a set of relationships to be deduced between the vortex and source strengths in this region.

At each point on the section surface, the vortex density is identical with the tangential velocity and the source density is identical with the normal velocity on the outer edge of the sheet. The condition of constant pressure, equivalent to the condition that the geometric sum of tangential and normal velocities should be equal on the surface in the separated region, therefore gives rise to a set of quadratic equations of the form:

$$\gamma^2(\sigma_n) + S^2(\sigma_n) = A^2 \quad 5.11$$

where n refers to all points within the separated region and A is a constant. Since the source distribution vanishes on the separation points,

$$|A| = |\gamma(\sigma_{nu})| = |\gamma(\sigma_{nL})| \quad 5.12$$

and

$$\gamma(\sigma_{nu}) = -\gamma(\sigma_{nL})$$

5.3 The Solution Procedure

5.3.1 Introduction

Two potential flow programmes were constructed. The first directly follows the work of Wilkinson in dealing with the unseparated flow about cusped or bluff aerofoils, either isolated or in cascade. The second programme is an extension of the first, allowing consideration of the wake effect on the pressure distribution about a bluff section. Although calculations concerning circulation controlled aerofoils and cascades require a representation of the wake effect due to the formation of a separation bubble on the trailing edge, the first of the two programmes proved useful in verifying the accuracy of the general procedure. Also, the second programme is applicable, strictly, to bluff sections only, so that the two programmes together form a package

capable of calculating flow over two-dimensional sections, isolated or in cascade, with a cusped or bluff trailing edge and no separation, and bluff sections with separation. The only restriction placed on profile shape is that it should be of finite thickness.

The solution of the general matrix, equation (5.9), is quite different in the two cases and so each is described separately. The description of the solution for the first case, with no separation, is brief and affords a useful introduction to an outline of the second procedure.

5.3.2 The Case with No Separation

Consider equation 5.9 but without the source terms K_{smn} and S_n . The coefficient matrix $K_{\gamma mn}$ is then square. This matrix is singular, since by equation 5.10 any one row is a linear sum of all the others. This situation arises due to the well known result that the potential flow about any body is indeterminate until the circulation is specified. Wilkinson eliminated row and column $2N$ from the system of equations 5.9, implying $\gamma_{2N} = 0$ and thus that the trailing edge point is a stagnation point. This is an expression of the Kutta Joukowski condition that the velocity at the trailing edge is zero. However, Wilkinson showed that for sections with a cusped trailing edge the resulting $(2N-1) \times (2N-1)$ matrix may still be singular. This is a consequence of the use of the angular variable ϕ and the fact that setting $\lim_{\phi \rightarrow 0} \gamma(\phi) = 0$ leaves $\lim_{\sigma \rightarrow 0} \gamma(\sigma)$ indeterminate unless the trailing edge angle $\tau = \pi$. Wilkinson solved this problem by setting $\gamma_{2N-1} = -\gamma_1$ which imposes a 'zero trailing edge loading'.

By subtracting column 2N-1 of equation 5.9 from column 1 and eliminating row and column 2N-1 the result is a non-singular matrix of dimensions (2N-2)x(2N-2). This specification of zero loading at the trailing edge has been used by other workers^(67,68) as a convenient device for defining circulation.

The matrix in the first programme, POTFLO1, is reduced in the manner described above. The equations are then solved for two separate right hand sides, -2Nx' and -2Ny'. Consideration of equation 5.8 shows that these two solutions may be combined after factoring by $\cos\alpha$ and $\sin\alpha$ respectively, to yield a solution for the vortex densities at any incidence(s). These values for γ_n must then be converted back into functions of σ by equation 5.2 to give the local surface velocities and hence the pressure coefficients:

$$C_{p_n} = 1 - \frac{U_n^2}{U_1^2} = 1 - \frac{\gamma_n^2}{x_n'^2 + y_n'^2} \quad 5.13$$

When dealing with a cascade, the set of infinite vortex rows comprising each surface point of the section induce a resultant velocity at infinity upstream and downstream. This velocity combines with the specified incident flow to create a net inlet velocity which is different in both magnitude and direction from the incident flow. Solutions for the two right hand sides enable an incident flow angle to be calculated such that the required inlet angle is obtained. The resultant inlet velocity magnitude may then be determined so that the pressure and force coefficients can be based upon the required flow velocity.

5.3.3 The Case With Separation

When source terms are present in equation 5.9 the solution procedure is complicated by the need to solve simultaneously the matrix equation and the set of quadratic equations 5.11. The procedure adopted is as follows:

Consider equation 5.9 with the left hand side of the coefficient matrix reduced to an upper triangular form by Gaussian reduction to produce

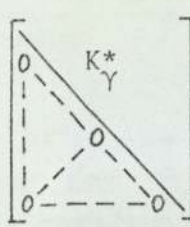
$$\left[\begin{array}{c|c} \begin{array}{c} \text{O} \\ \text{O} \\ \text{O} \end{array} & \begin{array}{c} K_Y^* \\ \text{O} \\ \text{O} \end{array} \\ \hline \begin{array}{c} \text{O} \\ \text{O} \\ \text{O} \end{array} & \begin{array}{c} \text{O} \\ \text{O} \\ \text{O} \end{array} \end{array} \right] \begin{array}{c} K_S^* \\ \underline{Y} \\ \underline{S} \end{array} = \begin{array}{c} \underline{\text{RHS}^*} \end{array}$$

where the superscript* refers to a quantity modified by the Gauss reduction. Rearranging and writing out the right hand side in its two components gives

$$\left[\begin{array}{c|c} \begin{array}{c} \text{O} \\ \text{O} \\ \text{O} \end{array} & \begin{array}{c} K_Y^* \\ \text{O} \\ \text{O} \end{array} \\ \hline \begin{array}{c} \text{O} \\ \text{O} \\ \text{O} \end{array} & \begin{array}{c} \text{O} \\ \text{O} \\ \text{O} \end{array} \end{array} \right] \begin{array}{c} \underline{Y} \\ \underline{S} \end{array} = \begin{array}{c} (-2Nx'_m)^* \cos\alpha \\ (-2Ny'_m)^* \sin\alpha \\ K_S^* \end{array} \begin{array}{c} \underline{S} \end{array}$$

5.14

Now, for the reason given in consideration of the case with no separation, the K_Y^* matrix is singular with a rank of $(2N-1)$ for a bluff section. A more general expression of equation 5.14 is given by



$$\begin{bmatrix} \text{---} \\ \text{---} \\ \text{---} \end{bmatrix} K_Y^* \begin{bmatrix} \text{---} \\ \text{---} \\ \text{---} \end{bmatrix} = \begin{bmatrix} (-2N_{x'_m})^* \end{bmatrix} \cos\alpha + \begin{bmatrix} (-2N_{y'_m})^* \end{bmatrix} \sin\alpha + \begin{bmatrix} 0 \\ \text{---} \end{bmatrix} C - \begin{bmatrix} K_S^* \\ \text{---} \end{bmatrix} \begin{bmatrix} \text{---} \\ \text{---} \\ \text{---} \end{bmatrix} \begin{bmatrix} \text{---} \\ \text{---} \\ \text{---} \end{bmatrix}$$

①
②
③
④

5.15

where the new term on the right hand side, ③ represents an homogeneous system and C is an arbitrary constant. Non-trivial solutions of the homogeneous system exist by virtue of the singularity of the matrix K_Y^* . In hydrodynamic terms, the homogeneous system corresponds to a pure circulation.

The solution of the $\underline{\gamma}$ vector may be regarded as the sum of the solutions for the four terms on the right hand side of 5.15:

$$\underline{\gamma} = \underline{\gamma}_1 \cos\alpha + \underline{\gamma}_2 \sin\alpha + C \underline{\gamma}_3 - \underline{\gamma}_4$$

Particular solutions to the first two terms, excluding factors $\cos\alpha$ and $\sin\alpha$, may be determined immediately by back substitution, having set $\gamma_{2N} = 0$. Similarly, a non-trivial solution to the homogeneous system ③ is obtained by setting $\gamma_{2N} = 1$. The remainder of the solution procedure is an iterative process. A first approximation to \underline{S} is made and a solution for $\underline{\gamma}_4$ obtained. Taking a first value for α , solutions $\underline{\gamma}_1 \cos\alpha$, $\underline{\gamma}_2 \sin\alpha$ and $\underline{\gamma}_4$ are summed. It then remains to determine the factor C by which the circulatory solution $\underline{\gamma}_3$ is multiplied before addition. Factor C is calculated from the condition expressed by equation 5.12:

$$(\underline{\gamma}_1 \cos\alpha + \underline{\gamma}_2 \sin\alpha - \underline{\gamma}_4)_{nL} + C \underline{\gamma}_3_{nL} = -(\underline{\gamma}_1 \cos\alpha + \underline{\gamma}_2 \sin\alpha - \underline{\gamma}_4)_{nu} - C \underline{\gamma}_3_{nu} \quad 5.16$$

Since this relationship expresses equal and opposite surface velocities at the separation points, it is necessary to factor the summed solution and $\underline{\gamma}_3$ by $\left(\frac{d\phi}{d\sigma}\right)$ before applying equation 5.16, thus converting the vortex densities to speeds. Once the factor C is found, the full solution is obtained in adding $C\underline{\gamma}_3$ to the existing summation.

Now that a solution for $\underline{\gamma}$ has been obtained, the assumed values of \underline{S} can be checked by equations 5.11 and 5.12. If these equations are not satisfied to the required degree of accuracy, a new approximation to \underline{S} can be obtained from them and the above cycle repeated. If a cascade is considered, the necessary incident flow angle θ to produce the required inlet angle, α_1 is calculated in each cycle, since this angle α_1 is a function of the solved set of vortex and source strengths.

Once convergence to a solution of sufficient accuracy is obtained, the pressure coefficients are calculated according to equation 5.13 with an allowance for the sources in the separated region.

It was mentioned in Section 5.3.2 that the imposition of $\gamma_{2N} = 0$ does not necessarily leave the K_Y matrix non-singular for sections with a cusped trailing edge. For this reason the procedure here is applicable, strictly, to bluff sections only. However, it seems likely that a minor smoothing of the trailing edge point of a cusped section, with separation just before the trailing edge, would make little difference to the resulting pressure distribution. The procedure is probably, therefore, of very general applicability.

A more detailed description of the mechanics of the programme and a listing are given in Appendix C.

5.3.4 Calculation of the Incident Flow Angle

It is easily shown that the velocities induced at $x = -\infty$ by the infinite rows of vortices and sources along the y -axis, representing the cascade, are

$$\left(\frac{v}{U_{\infty} c}\right)_{x=-\infty} = -\frac{1}{2s} \frac{\pi}{N} \sum_{n=1}^{2N} \gamma_n$$

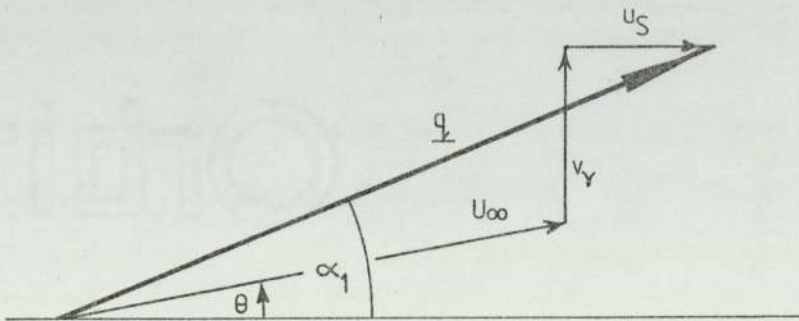
$$\left(\frac{u}{U_{\infty} c}\right)_{x=-\infty} = 0$$

$$\left(\frac{v}{U_{\infty} c}\right)_{x=-\infty} = 0$$

$$\left(\frac{u}{U_{\infty} c}\right)_{x=-\infty} = -\frac{1}{2s} \frac{\pi}{N} \sum S_n$$

5.17

Consider such components which, in combination with the incident flow, are to yield the required inlet angle. The problem is most clearly expressed by drawing the components in vector form



Sketch 5.1

Composition of Inlet Velocity Vector \underline{q}

From Sketch 5.1 the following expression for θ is obtained

$$A \cos\theta - \sin\theta = B \quad 5.18$$

where $A = \tan\alpha_1$

$$B = v_{\gamma} - u_S \tan\alpha_1$$

Solutions to equation 5.18 are given by

$$\sin\theta = \frac{-B \pm A\sqrt{1-B^2+A^2}}{(1+A^2)}$$

The two solutions for $\sin\theta$ may be substituted back into equation 5.18 to find which is correct. The magnitude of the inlet velocity is given by

$$q = \sqrt{(u_S + U_{\infty} \cos\theta)^2 + (v_{\gamma} + U_{\infty} \sin\theta)^2} \quad 5.19$$

The magnitude and direction of the outlet velocity is found from similar expressions in which $v_{\gamma} = -v_{\gamma}$ and $u_S = -u_S$
 $x=+\infty \quad x=-\infty \quad x=+\infty \quad x=-\infty$

5.4 Computer Programme Verification

Since the potential flow programmes are quite complex, it was decided to test for correct working and accuracy by applying them to a series of flows for which exact or accurate results were available. Because most exact or accurate solutions pertain to unseparated flows, the first potential flow programme, POTFLO1, was used for the majority of tests. The two potential flow programmes have identical profile building routines so these tests served as a check of a large part of both programmes. The cascade nomenclature used in the Figures referred to below is defined in Figure 4.

Figures 34 and 35 show results for the simplest two-dimensional cylinder of all; the circular cylinder. Figure 34 shows the exact and predicted pressure distributions about a circular cylinder for two magnitudes of circulation, zero and 4π . Figure 35 is a comparison of the variation of lift coefficient with incidence for a fixed rear stagnation point. With this simple geometry, incidence can be applied either by varying the position of the rear stagnation point or by keeping it fixed and varying the true incidence of the free-stream flow. A comparison of the exact and computed variation of lift coefficient with incidence for a very thin ellipse of only 5% minor chord is given in Figure 36. Considering the extremely high negative pressure coefficients developed around the leading edge at large incidence, these results are remarkably good and show that very thin sections pose no problems for this solution procedure.

Figures 37 and 38 show comparisons of predicted results with the exact values given by Gostelow⁽⁵⁹⁾ for a cascade obtained by conformal transformation. Thus, this calculation provides a direct test of the programme against exact results for a conventionally shaped aerofoil with a finely cusped trailing edge and in cascade. The accuracy of the prediction is seen to be very good even although the pivotal point distribution in the trailing edge region was not modified: a closer point spacing near the trailing edge can be used to reduce inaccuracies introduced by the zero trailing edge loading assumption.

It is hardly fair to compare directly predictions made by the potential flow programme alone with experimental results, since the potential flow programme POTFLO1 does not pretend to take account of

the viscous effect existing in real flows. However, Wilkinson⁽⁶⁹⁾ found that good predictions of experimental results were obtained for the flow about cascades of NACA primary turbine blades. These blades might be expected to give reasonable agreement between theory and experiment, since the pressure gradient through turbine blades is favourable and boundary layer development only slight. Figures 39 and 40 show comparisons between theory and experiment for cascades of these blades at different staggers and agreement is again seen to be good.

A test of the programme POTFLO2 was performed by comparing a predicted pressure distribution with that measured Patel⁽⁷⁰⁾ on a circular cylinder. The reported separation points, which defined the extent of the source distribution in the computer programme, were represented to an accuracy of 2° . The comparison is shown in Figure 41. The prediction is seen to be a great improvement on the exact, unseparated potential flow solution. This example represents an extreme case with the flow attached over only about $3/5$ of the entire surface. It may be concluded that the use of source distributions to represent separated regions yields a good portrait of the effect of separation on the surface pressure distribution.

5.5 Possible extensions to the Solution Procedure

The inclusion of a wake effect in the calculation of blade surface pressure distributions adds considerable realism to the basic, pure vortex solution when a bluff section is considered. There are further ways in which greater flexibility or accuracy might be obtained, but which have not been attempted in the present work. Two of the more obvious potential extensions of the calculation procedure are briefly discussed below.

Perhaps the most obvious extension of the present method would be the inclusion of further source elements on the surface points to simulate the displacement effect of the boundary layer. This procedure would not necessitate a corresponding increase in the number of unknowns, since the source strengths could be defined from a knowledge of the displacement thickness, δ^* , at each surface point. These sources would therefore form an extra right hand side of the matrix equation. However, it would seem that on bluff bodies in particular, the wake effect has a greater effect on the pressure distribution than does the main surface boundary layer⁽⁶⁵⁾. This is why the extra sources have not been added in the present work.

The second extension would be the inclusion of compressibility effects. Such effects can be predicted by linear theory, based on the assumption that all perturbations on the inlet velocity vector are small⁽¹⁰⁵⁾. It follows that it is inaccurate for any but very thin blades at low incidence. The simplest application of this theory is direct use of the Prandtl-Glauert rule, factoring the pressure coefficients obtained from an incompressible flow analysis by $1/\sqrt{1-M^2}$. Mikolajczak et al⁽¹⁵⁾ used the Prandtl-Glauert factor to transform the blade surface coordinates, stagger angle, flow angle and gap between slotted compressor blades. The incompressible pressure distribution on the transformed aerofoil was then assumed to be that on the untransformed aerofoil in compressible flow. Minassian⁽⁶⁷⁾ applied the semi-empirical method of Labrujere et al⁽¹⁰⁶⁾ to include the nonlinear influence of surface slopes. This procedure again involves the calculating of the incompressible flow about transformed profiles. The resulting surface velocities are related to the compressible flow about the original profile and isentropic relationships are used to determine the pressure coefficients from the compressible flow velocities.

The present work is confined to the consideration of flows at or below a Mach number of 0.3, which is about the upper limit of Mach number for which compressibility effects may reasonably be neglected.

CHAPTER 6

BOUNDARY LAYER AND WALL JET THEORY

6.1 Introduction

The attempt to model theoretically the cascade performance required calculation of boundary layer development on the upper and lower blade surfaces and also of the wall jet blown onto the curved trailing edge. While the former part of the calculation is accomplished relatively easily, the wall jet calculation, especially with severe curvature and pressure gradient effects, represents an extreme and difficult case.

Wall jets are merely one particular variety of the general turbulent wall boundary layer; however, they merit particular attention because they display more extreme variations in flow properties across the thickness of the boundary layer. When used to suppress separation of an external flow, the resulting profile incorporates features of a conventional boundary layer in the outer region with the wall jet creating a high energy inner region. Figure 42 shows the ways in which a boundary layer can develop downstream of a blowing slot, dependence being on the slot geometry, the blowing momentum, the thickness of the upstream boundary layer, the local surface curvature and the pressure gradient. When a wall jet develops without a minimum in the velocity profile the wall jet is said to entrain completely the

upstream boundary layer. The physical properties of wall jets have been studied by many researchers and various calculation approaches have been presented^(53, 71-75).

Integral techniques have been applied frequently to the calculation of wall jets: Allcock and Dunham⁽³²⁾ used Spalding's Unified Theory⁽⁷⁶⁾ for the wall jet calculation in their investigation of a circulation controlled circular cylinder. Kind⁽⁷⁷⁾ followed the approach of Allcock and Dunham in analysing his circulation controlled ellipse, but introduced extensive modifications to their method, since the earlier analysis had proved inaccurate. Gartshore and Newman⁽⁷⁸⁾ described an integral method of calculating a turbulent wall jet in an arbitrary pressure gradient. Their method involved a two-part representation of the velocity profile by functions of distance from the surface and the use of a turbulent viscosity to calculate shear stresses at three points across the profile. This method, however, like the majority of wall jet calculation procedures, is applicable to profiles with a velocity maximum only.

When calculating wall jet development by solution of the usual boundary layer momentum equation, the problem becomes one of defining an 'effective' or 'eddy' viscosity. The distribution of eddy viscosity through a wall jet profile is known to be complex. Dvorak⁽⁷⁹⁾ attempted to represent the nature of turbulence by employing an intermittency model of eddy viscosity, which is described later in this Chapter, in a finite difference calculation procedure. Using empirical functions, he deduced expressions for calculating the eddy viscosity distribution

across conventional boundary layers, wall jets with a maximum and minimum point in the velocity profile and wall jets with a maximum velocity only. The general shapes of the resulting eddy viscosity profiles are illustrated in Figure 43.

It is Dvorak's work which has been used in the present study to calculate the development of blowing jet profiles. For computational efficiency, main blade surface boundary layer calculations have been performed using a simple mixing length representation of the eddy viscosity.

The boundary layer equations, the concept of intermittency and the eddy viscosity model are described in the following sections. An outline of the finite-difference procedure used for solving the boundary layer equations is presented in Section 6.6.

6.2 The Boundary Layer Equations

In calculating boundary layer flows with small longitudinal curvature most authors have applied a plane surface boundary layer equation with curvature effects incorporated into a modified mixing or other length scale. The justification for this is discussed in Section 6.5.1.

Because it was required to calculate flows with fairly severe curvature, it was decided to use an angular momentum equation for the mean motion as well as modifying the Reynolds stress term. This approach was adopted by Dvorak⁽⁷⁹⁾, Wilson and Goldstein⁽⁹⁷⁾ and

others. The full boundary layer equations for curved flow in curvilinear coordinates are given by Schlichting⁽¹³⁾, p.112. The angular momentum equation used in the present work is

$$\rho u \frac{\partial(ur)}{\partial x} + \rho v \frac{\partial(ur)}{\partial y} = -r \frac{\partial P}{\partial x} + \frac{1}{r} \frac{\partial}{\partial y} [r^3 \mu_t \frac{\partial}{\partial y} (\frac{u}{r})]$$

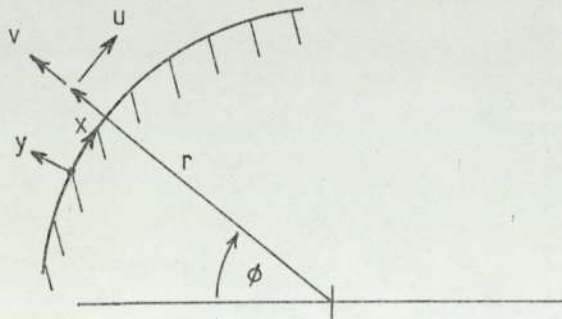
with the associated continuity and radial equilibrium equations

$$\frac{\partial(ur)}{\partial x} + \frac{\partial(vr)}{\partial y} = 0,$$

$$\frac{\partial P}{\partial y} = \frac{\rho u^2}{r} .$$

Distance x is measured along the surface as indicated in Sketch 6.1. The above equations are those used by Launder⁽⁸⁰⁾ et al. in calculating curved flows with a kinetic energy model of turbulence, except that they replaced dx by $r d\phi$.

Once values for the eddy viscosity, μ_t , are provided, the above equations may be solved. The representation of the eddy viscosity term and the adopted solution procedure are discussed in the following sections.



Sketch 6.1

Nomenclature for Flow over a Curved Surface

6.3 Intermittency

In a fully developed turbulent shear flow the inner region, near the wall, is generally fully turbulent, while at the free boundary the flow fluctuates strongly with time between that of a turbulent and that of a substantially irrotational nature. Hot wire investigations of turbulent boundary layers⁽⁸¹⁻⁸³⁾ have shown that the outer region turbulence is instantaneously confined within a sharp boundary, termed the turbulence front. This front is highly irregular in shape and varies continuously with time. Such turbulence occurs also in jets, wakes and in pipe flows over the transition region and is a fundamental feature of turbulent flow.

The degree of intermittency at a point in a turbulent shear layer is defined by the intermittency factor, γ , which is a function of position and represents the fraction of total time during which the flow is turbulent. Hence, $\gamma = 1$ corresponds to continuously turbulent flow and $\gamma = 0$ to continuously laminar flow. Experiments have shown that the distribution of intermittency through the thickness of a boundary layer can be represented accurately by the expression

$$\gamma(y) = \frac{1}{\sigma\sqrt{2\pi}} \int_y^\infty \exp\left[-\frac{(y-\bar{y})^2}{2\sigma^2}\right] dy$$

where \bar{y} is the value of y for which $\gamma = 0.5$ and represents the mean position of the turbulent front. The standard deviation of the measured intermittency profile, σ , is a measure of the width of the intermittency distribution and as such characterizes the size of the large eddies. Formally, σ is defined by

$$\sigma = \sqrt{(Y - \bar{y})^2} = \sqrt{\bar{y}^2 + 2 \int_0^{\infty} (y - \bar{y}) \gamma \, dy}$$

where Y is the instantaneous position of the turbulence front.

6.4 The Effective Viscosity Model

6.4.1 Introduction

The model employed is basically that due to Dvorak⁽⁷⁹⁾ but with slight modifications where the work of other authors suggests that superior results are obtainable by simple extensions.

In the near wall region, Dvorak applied the very widely used Van Driest⁽⁸⁴⁾ modification to Prandtl's mixing length theory. The outer region model is based on the results of an experimental study by Wagnanski and Fiedler⁽⁸⁵⁾. They showed that by considering the instantaneously turbulent fluid only, an eddy Reynolds number, C , could be formed where

$$C = \frac{U_d \sigma}{v_{t\ell}} \tag{6.1}$$

$v_{t\ell}$ is the local eddy viscosity in the turbulent fluid only and U_d is a velocity defect representative of the outer or wake portion of the boundary layer. Wagnanski and Fiedler found C to lie between 14 and 15 in a zero pressure gradient turbulent boundary layer, while Dvorak showed that measurements by Bradshaw and Ferriss⁽⁸⁶⁾ in an adverse pressure gradient gave an eddy Reynolds number in the same range. He assumed this Reynolds number to be applicable to general turbulent shear layer flows, including wall jets.

The values of U_d and σ are heavily dependent upon the present state and the history of the boundary layer. Dvorak proposed three different correlations for these quantities depending on whether the boundary layer is of the conventional type, a wall jet profile with velocity maximum and minimum or a wall jet profile with a velocity maximum only. An outline of the treatment of each flow is given in the following sections,

Although the intermittency representation of a conventional boundary layer is included in the computer programme described in Appendix D, it has not been used in the present work, since the classical mixing length approach is able to cope with this relatively simple case and is considerably more efficient in terms of computer time. Because part of the wall jet intermittency model uses aspects of the conventional layer model, however, this latter work is described.

6.4.2 The Near Wall Region

All turbulent boundary layers exhibit a region near to the wall where the flow is fully turbulent and response to changes in the energy supply is immediate. Following Dvorak and many other workers, Prandtl's mixing length theory as modified by Van Driest is used,

$$v_t = K^2 y^2 \left[1 - \exp\left\{-\frac{y u_T}{\Lambda v}\right\} \right]^2 \left| \frac{\partial u}{\partial y} \right| \quad 6.2$$

where $u_T = \sqrt{\frac{\tau_w}{\rho}}$ (τ_w = wall shear stress)

$$K = 0.435$$

$$A = 26.$$

While the value of K has been assigned values varying between 0.40 and 0.45 by various authors, it has been found to remain constant even in low Reynolds number flows^(100,101). The Van Driest parameter A has also been shown to be independent of Reynolds number⁽¹⁰¹⁾, although a proposal has been made by Horstman⁽¹⁰²⁾ to express A as a function of pressure gradient.

In the present work, following usual practice, both A and K are taken to be constants of the values quoted above.

6.4.3 The Outer Region of a Conventional Boundary Layer

A value for σ , the standard deviation of the intermittency profile, is calculated from

$$\sigma/\delta^* = 0.245 + 0.189/(H-1.176) \quad 6.3$$

which is an empirical relationship for developing boundary layers, deduced from the results of Fiedler and Head⁽⁸¹⁾. H is the boundary layer shape factor, the ratio of displacement thickness, δ^* , to the momentum thickness, θ .

The velocity defect, U_d is the difference between the local freestream velocity and the velocity in the boundary layer at the point where the mean velocity profile departs from the law of the wall. The point of departure, $y = Y_d$ was tabulated as a function of H and δ^* by Dvorak for developing and mildly relaxing flows. This tabulation is well represented by the following function

$$Y_d/\delta^* = 0.018 + 0.157/(H-1.227) \quad 6.4$$

Once σ and U_d have been deduced, equation 6.1 may be applied to obtain the local maximum turbulent viscosity, $\nu_{t\ell}$.

Dvorak applied a diffusion equation to account for the effect of upstream history on this value of $\nu_{t\ell}$ giving a modified value,

$$\nu_{t_{\max}} \cdot X \frac{\partial \nu_{t_{\max}}}{\partial x} = K_1 (\nu_{t\ell} - \nu_{t_{\max}}) \quad 6.5$$

where $K_1 = 0.02$, $X = \delta^*$.

If $\nu_{t\ell}$ were independent of x , then equation 6.5 could be integrated to show that $\nu_{t_{\max}}$ approached $\nu_{t\ell}$ in an exponential manner. In practice a difference formulation was used to approximate to equation 6.5, so that $\nu_{t_{\max}}$ is found from:

$$\nu_{t_{\max}} = \frac{K \, dx}{X} (\nu_{t\ell} - \nu_{-}) + \nu_{-} \quad 6.6$$

where $\nu_{-} = \nu_{t_{\max}}$ on the previous step.

The mean position of the turbulent front, \bar{y} , which is the value of y where $\gamma = 0.5$, is found from

$$\bar{y}/\delta^* = 2.226 + 0.962/(H-1.158) \quad 6.7$$

which Dvorak again deduced from the results of Fiedler and Head.

The intermittency distribution can be calculated from an error function:

$$\gamma(y) = 0,5(1 - \operatorname{erf} \frac{\delta^*}{\sigma\sqrt{2}} [\frac{y}{\delta^*} - \frac{\bar{y}}{\delta^*}]) \quad 6.8$$

where $\operatorname{erf}(x) = \frac{2}{\sqrt{\pi}} \int_0^x \exp(-u^2) du,$

A tabulation of values of this error function by Kreyszig⁽¹⁰³⁾ shows that the error function can be represented closely by the polynomial

$$\operatorname{erf}(x) = 1.1061x + 0.1557x^2 - 0.7635x^3 + 0.44x^4 - 0.1056x^5 + 0.0095x^6$$

Finally, the distribution of turbulent viscosity through the outer layer is found by factoring the local maximum value by the intermittency distribution

$$v_t(y) = v_{t_{\max}} \gamma(y) \quad 6.9$$

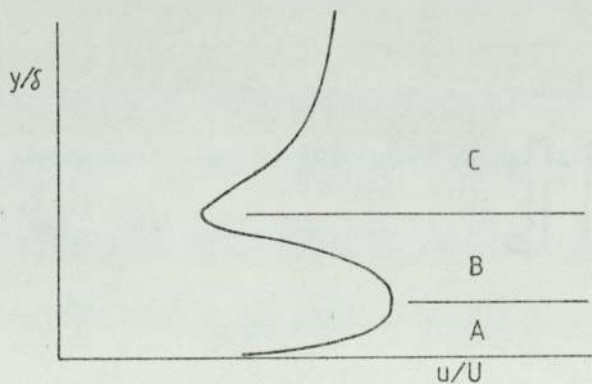
6.4.4 Wall Jets with a Velocity Maximum and Minimum

Wall jets with a maximum and minimum in velocity occur because the jet is unable to entrain the upstream boundary layer. Dvorak treated the inner region, marked A in Sketch 6.2 by the same two layer model as for a conventional boundary layer except that the effect of intermittency was excluded as the flow is fully turbulent. Because the calculation of eddy viscosities in area A outside the 'near wall region' by this method is complex and was found to be computationally time consuming, a conventional mixing length model was applied in this region. The eddy viscosities thus calculated were found to be very similar to those computed from Dvorak's more complex model.

The outer region, C in Sketch 6.2 represents the remnant of the upstream boundary layer and has a large value of shape factor, H. The measurements of Fiedler and Head indicate that the standard deviation σ and the mean position of the turbulent front, \bar{y} , approach asymptotic values at large shape factors. Dvorak reported similar behaviour for the velocity defect U_d . The asymptotic values are

$$\sigma/\delta = 0.127, \quad \bar{y}/\delta = 0.93, \quad \frac{U_d}{U} = 0.76 \quad 6.10$$

Equation 6.6 is applied again to express the effect of upstream history but the displacement thickness δ^* is replaced by the actual boundary layer thickness δ as a more appropriate length scale. The constant K_1 is also changed, to 0.2. The behaviour of v_t in region B, Sketch 6.2, is complex and uncertain. Following Dvorak a cosine fairing is used to join regions A and C.



Sketch 6.2

Division of Wall Jet Profile.

6.4.5 Wall Jets with a Velocity Maximum Only

Wall jets with only a maximum in velocity occur when the blowing jet has sufficient momentum to entrain completely the upstream boundary layer within a short distance of the blowing slot. The inner region eddy viscosity profile is calculated in the same manner as described in the previous section.

The velocity defect in this case is simply $U_d = U_{\max} - U$. Dvorak plotted profiles of σ/x and \bar{y}/x against a jet shape parameter from the measured intermittency profiles of Gartshore⁽⁸²⁾. However, the present work has suggested that more general relationships are to be obtained by non-dimensionalising σ and \bar{y} by a length typical of the local velocity profile. The results of Gartshore suggest the use of y_m , the distance to the velocity maximum. The following representations have been used

$$\begin{aligned}\bar{y}/y_m &= 9.53/(UMD + 0.823) - 0.726 \\ \sigma/y_m &= 1.35 - 0.281 UMD \quad UMD > 0.5 \\ \sigma/y_m &= 1.06 + 0.091/(UMD + 0.104) \quad UMD \leq 0.5\end{aligned}\tag{6.11}$$

where $UMD = U/(U_{\max} - U)$

The effect of upstream history is represented by equation 6.5. A cosine fairing is used as previously to join the inner and outer region viscosity profiles.

6.5 The Effects of Surface Curvature

6.5.1 Survey of Previous Findings

Surface curvature has an appreciable influence on the development of both conventional boundary layers and on wall jets. Reyleigh⁽⁸⁷⁾, in 1916 showed that for flow on a convex surface, an increase in angular momentum of the fluid with distance from the centre of curvature is required for stability. By this criterion, the outer region of a wall jet which does not fully entrain the upstream boundary layer on a convex surface will be unstable.

Traditionally, boundary layers developing on curved surfaces have been treated as flat wall layers developing in the appropriate pressure gradient and the specific effects of curvature have been neglected. However, it is well known that the entrainment rate of a wall jet flowing over a surface of convex curvature exceeds that of a flat wall jet. Bradshaw^(88,89) showed that even for values of δ/R as small as $1/300$, turbulence characteristics may be altered significantly. He pointed out that at such a low degree of curvature, the static pressure change across a typical boundary layer is less than one half percent of the free stream dynamic head, so that the effect of curvature on turbulence greatly exceeds the effect on the mean motion. Further, in his comprehensive review of experimental data and theoretical models concerning curved boundary layers, Bradshaw⁽⁸⁹⁾ found that the effect of curvature on the turbulent stresses was greater by a factor of about ten than would be expected from the addition of curvature terms in the equations of mean motion.

The parameter governing curvature effects is $(u/R)/(du/dy)$ which is half the Richardson number, Ri , as discussed by Bradshaw. Basically, curvature increases the turbulent shear stress when $Ri < 0$ and decreases it when $Ri > 0$. Thus, the effect of curvature depends upon the local velocity gradient as well as the surface curvature.

Experiments on channel flow round curved ducts have been performed by So and Mellor⁽⁹⁰⁾ and by Ramaprian and Shivaprasad⁽⁹⁸⁾. The order of the ratio of boundary layer thickness to local surface radius of curvature (δ/R) was 0.1 in the former case and 0.013 in the latter. Both experiments showed that the inner region of flow, usually characterised by a logarithmic variation of u with y , was unaffected by convex curvature, although Ramaprian and Shivaprasad observed that the extent of the region in which the logarithmic law was valid was reduced by the curvature. They found that the logarithmic law applied for $25 < \frac{yU_{\tau}}{\nu} < 250$, which is in general agreement with So and Mellor's upper limit for the logarithmic profile ($\frac{yU_{\tau}}{\nu} < 200$) under stronger curvature. It was found that the outer region of the boundary layer was affected significantly by wall curvature, convex curvature increasing the relative strength of the wake component. Bradshaw suggested that the logarithmic law should be valid in the inner region of curved wall jets, as well as boundary layers for all practicable flows.

The concept of a Richardson number correction to turbulent length scales has been applied by many authors and some have investigated theoretically the dependence of turbulence parameters on the Richardson number. Irwin and Smith⁽⁹²⁾ deduced that for negative Ri ,

turbulence becomes less sensitive to curvature with increasing curvature, the shear stress becoming virtually independent of Ri for $Ri < -0.3$. For $Ri > 0$, the opposite was found to be true, there being an upper limit of $Ri \approx 0.2$ beyond which turbulence cannot exist which can be compared with the experimental findings of So and Mellor, who obtained a value of $Ri = 0.3$ as the Richardson number beyond which turbulence cannot sustain itself.

Richardson number corrections to turbulent length scales have generally been applied in a linear form

$$l' = l_0(1.0 - \beta Ri)$$

where l_0 is the length scale of the corresponding plane flow. The linear form of this correction has been shown by Sawyer⁽⁹³⁾ to be deducible from mixing length arguments. The value assigned to β has varied somewhat: Bradshaw advocated $\beta = 4.5$ for unstable flows ($Ri < 0$) and $\beta = 7.0$ to 10.0 in stable conditions. He used a value $\beta = 7$ to modify a dissipation length parameter in calculating the flow over the aerofoil of Schaubert and Klebanoff⁽⁹⁴⁾, and obtained better agreement with experiment than by ignoring curvature effects. Johnson and Eide⁽⁹⁵⁾ tried various values of β in modifications to a mixing length to obtain the best fit with experiment for four sets of curved wall experimental data. A value of $\beta = 6$ was generally found to give best agreement. Other authors^(96,79) have assumed a direct analogy between the molecular and eddy viscosities, which yields $\beta = 1.0$. Wilson and Goldstein⁽⁹⁷⁾ suggest that $\beta = 1$ is valid only for isotropic turbulence and this value certainly seems low in comparison with the findings of other authors.

The effects of curvature cannot be modelled precisely by application of the simple Richardson number correction: the effects of curvature are highly complex and any useable correction, especially in the context of a mixing length can be, at best, only a crude approximation.

Ramaprian and Shivaprasad described the observed characteristics of the boundary layer passing over a transition from a straight wall to a section of uniform curvature. They found that although the convex wall boundary layer had a strong wake component, the rate of growth of momentum thickness Reynolds number R_θ diminished initially and then later grew at a faster rate than the corresponding flat plate layer. The skin friction initially increased, then fell continuously, being lower than the flat plate value for the majority of the curved section. They concluded that the effects of curvature could be divided into three constituents:

1. The initial effect of the application of curvature ("dR/dx effect").
2. The effect of the local normal pressure gradient brought into existence by curvature ("dR/dn effect").
3. The effect of sustained curvature ("R effect").

Constituents 1 and 2 were considered to be dominant in the region immediately following the start of curvature,

The findings described above illustrate the way in which curvature influences the turbulence structure and thus displays considerable effects of development history. Bradshaw suggested

the use of a lag equation of the form

$$X \frac{d Ri_{eff}}{dx} = Ri - Ri_{eff} \quad 6.12$$

where Ri_{eff} is the effective curved flow Richardson number and Ri is the calculated local value. X represents the time constant of the lag effect: Bradshaw recommended $X = 10\delta$ for a conventional boundary layer and about 2δ for a wall jet with no external stream.

6.5.2 The Representation of Curvature Effects

The earlier discussion of curvature effects on the development of shear layers demonstrated the complexity of this influence. Bradshaw argued that there is little justification in using any correction to a length scale or eddy viscosity more sophisticated than a simple linear function, F , of the Richardson number:

$$F = 1 - \beta Ri \quad 6.13$$

which was to be considered valid for the approximate range $0.5 < F < 1.5$. For conventional boundary layers, the corresponding limit of curvature is about $|\delta/R| < 0.015$. Following many previous workers, the F -factor is applied here to flows of considerably more severe curvature with large values of Ri .

The wide variation of values assigned to β has already been mentioned. If the linear form of equation 6.13 is assumed to apply up to the point at which turbulence is suppressed, the predicted results of Irwin and Smith and the experimental results of So and Mellor give values for β of 5 and 3 respectively. The values of β

for negative Richardson numbers appear to be generally less than for positive Ri . In the present work the following values of β have been used:

$$\beta = 4 \quad Ri > 0,$$

$$\beta = 2 \quad Ri < 0,$$

with the obvious limit $F \nrightarrow 0$, and the somewhat more arbitrary limit $F \nrightarrow 2$.

A lag equation for curvature effects is also applied, as recommended by Bradshaw. The lag equation used is equation 6.12, using the same lag constants as were used to express the effects of flow history on v_{tl} .

6.6 The Solution Procedure

6.6.1 General Description of the Procedure

The solution procedure adopted is that due to Patankar and Spalding⁽⁹⁹⁾. Their finite-difference method was specially developed for the solution of the two dimensional boundary layer equations and is highly efficient as a result. The cross-stream variable y is abandoned in favour of a dimensionless stream function ω , which allows the grid to expand with the growth of the calculated boundary-layer. To allow economy in treating the steep gradients which occur near walls special 'wall function' formulae are used. These equations are derived by integrating simplified boundary layer equations to obtain algebraic expressions relating conditions at the wall to those in the fluid adjacent to the wall. The finite difference

equations are obtained by expressing each term of the momentum equation as an integrated average over a small control volume with the assumption that the unknown, u_r , varies linearly with ω between grid points.

Full details of the procedure are provided by Patankar and Spalding. Their complete procedure allows solution of equations for conservation of chemical species and stagnation enthalpy in addition to momentum. The present work is concerned primarily with momentum calculations, although the equations for conservation of stagnation enthalpy are included in the solution procedure to allow consideration of varying jet temperatures. Various other simplifications to the method presented in reference 99 have been adopted for greater efficiency: for example, it is assumed that the boundary layer is always on a solid surface adjacent to a free stream, so that the outer boundary of the grid can be treated more expeditiously. The central core of the numerical solution procedure has been taken directly from the computer programme listing given by Patankar and Spalding. This section comprises only a small proportion of the whole programme: the majority is concerned with ancillary routines for providing the effective viscosities, calculating the pressure gradient, generating starting profiles and the like.

6.6.2 Some Particular Details of the Procedure

The wall jet calculation proved to be the most difficult part of all the computing performed in the present study. Many problems arose during the development of this procedure and the measures employed to overcome some of them are outlined below.

With the type of wall jet flow being considered, the jet usually entrains the upstream boundary layer rapidly so the profile changes from being one with both a maximum and a minimum velocity to one with a maximum only. Once the upstream boundary layer has become almost fully entrained the profile may be regarded as falling into either category. In the present work, the change in eddy viscosity calculation was triggered when the quantity $(U - \bar{u})/U$ fell below 0.1.

Once the upstream boundary layer had become entrained, the predicted eddy viscosities fell to low values in the outer region where the velocity gradient was small. It was found that in strongly adverse pressure gradients a new velocity minimum tended to form in this outer region and in very strong gradients a stalling of the flow in the outer region was predicted. This effect was unrealistic because it was simply a consequence of the definition of the outer edge of the shear layer which at this stage of the calculation was quite arbitrary. To correct this behaviour, the velocity-radius product ur was not allowed to fall below that at the outer edge of the shear layer once the entrainment criterion given above was satisfied.

In certain cases, the calculated velocity at the outer edge of the boundary layer fell to a very low value as separation was approached. As the outer region flow retarded, so the overall thickness of the calculated boundary layer rapidly increased and it was felt that the pressure gradients calculated in the inner jet region, being dependent upon integration from the outer edge, tended to become inaccurate. To prevent this, the outer edge velocity of the shear layer was not allowed to fall below one half of the free stream velocity.

6.6.3 A Test of the Wall Jet Calculation

It was decided to test the computer programme on the most complex flow that it would be required to calculate when later incorporated into the overall solution procedure, namely a wall jet development. The experimental data of Kind⁽⁵²⁾ were the obvious choice for the test, because his wall jet flows were measured in detail and it was for the prediction of precisely this type of flow, involving large pressure gradients and curvature, that the programme was to be used.

The wall pressure distribution measured by Kind (Flow II) was supplied as input data and the subroutine used to calculate the variation in $\frac{\partial p}{\partial x}$ across the layer thickness was accordingly modified, see Appendix D. The measured upstream boundary layer profile was supplied to the programme and the calculation was started at the blowing slot by allowing the programme to generate a jet profile. The profile was assumed to be of the form depicted in Figure 8 and on the basis of jet slot momentum loss curves given by Kind, the index n of the power law profile was set to 25.

The resulting jet development is compared with the measurements of Kind in Figure 4 4. The programme predicted rapid entrainment of the upstream boundary layer which is in agreement with the measured results. Beyond an angular distance of 32° from the blowing slot, the predicted profile is seen to develop a rather unrealistically sharp peak. The shape and size of this peak was found to be sensitive to the geometry of the fairing used to join the inner and outer jet regions. Fortunately, gross features of the flow such as separation

distance, were not found to alter substantially with modification of the fairing, so no great trouble was taken to prevent the persistence of this peak. The prediction of negative $\frac{\partial u}{\partial y}$ values towards the outer region of the jet profile is a consequence of preventing the product ur from falling below that at the outer edge of the profile as discussed earlier. The measured profiles show that this product actually grows with increasing r .

Kind does not specify a separation point for his measured flows but examination of the pressure distribution suggests separation at about 107° around the trailing edge. The programme predicted an earlier separation at 101° : experience with the theoretical model shows that the rate of change of separation distance with blowing coefficient increases as the 'correct' separation point, corresponding to the pressure distribution is approached. On the basis of later work, the 6° difference in separation positions would be reduced to zero by increasing the blowing coefficient in the computer programme by less than 10%. Thus, for the purpose of predicting a blowing coefficient, given a trailing edge pressure distribution and an upstream boundary layer profile, the programme may be considered to have yielded a satisfactory result for the case considered.

The suitability of the wall jet model will be discussed later in the light of predictions made by the complete solution procedure. The example described above served to illustrate that the model would at least give a qualitatively satisfactory prediction of the gross features of the type of wall jet flow to which the calculation procedure was to be applied.

CHAPTER 7

RESULTS OF THEORY AND COMPARISON WITH EXPERIMENT

7.1 Combination of Potential Flow and Boundary Layer Programmes

The overall solution procedure was constructed so that a full calculation could be performed for any particular blade geometry without user interaction. By a "full calculation" is meant the prediction of the blowing coefficient required to produce a particular lift. By solving for the blowing coefficient at several lift coefficients, the lift-blowing momentum characteristic could be established.

Figure 45 is a flow chart of the macro used to run the potential flow and boundary layer programmes. The position of the upper trailing edge separation point is supplied with the geometrical details of the section. Iteration between the potential flow and boundary layer programmes is required to establish the position of the lower separation point. Once convergence is obtained, the upper surface boundary layer development is calculated up to the blowing slot lip. A blowing jet profile is then added below the incident boundary layer, using a first approximation to the jet momentum coefficient. The jet is calculated to separation and this point is compared with the position of separation specified in the potential flow programme. The blowing jet momentum is altered by an amount dependent upon the distance between these separation points and the wall jet development re-calculated. The jet calculation is repeated until convergence to the correct separation position is obtained.

The potential flow and boundary layer programmes used in the solutions presented here are those listed in Appendices C and D respectively. The macro also ran two small link programmes which were used to manipulate data files. All computations were performed on an I.C.L. 1904A digital computer and 64 pivotal points were used to represent each aerofoil surface in POTFLO2.

7.2 Comparison of Theoretical Results with Experiment

The solution procedure was tested on the experimental results of Kind⁽⁵²⁾ and of Landsberg and Krasnoff⁽²³⁾ before applying it to the experimental data obtained in the present investigation. It is emphasised that the testing of circulation controlled sections and cascades is extremely difficult and that experimental results should be viewed with some caution if a quantitative comparison with the predictions of a theoretical model is to be made. For example, Kind corrected his results for the effect of downwash induced by three-dimensional effects. The correction was made by calculating the effective incidence at which the aerofoil was operating, deduced from the measured pressure distribution. The difference in blowing coefficient required to give a particular lift at the same geometric and corrected "effective" incidences was of the order of fifty percent. Although Kind considered the effective incidences to be correct to within about $\pm \frac{1}{2}^\circ$, the above observation illustrates the magnitude of inaccuracy that can occur in experimental results.

In Figure 46, predicted values of blowing coefficient are compared with experimental curves given by Kind. The experimental curves are those corresponding to Kind's corrected incidences. Although only

three points were obtained for each incidence, the agreement with experiment is seen to be good. The changing gradient of the experimental curves is not reflected but the theoretical points indicate a realistic average rate of change of C_L with C_{μ} over the range of C_L considered. The theory also predicts realistically the effect of incidence, which Kind's theory failed to do. An attempt was made to obtain theoretical results for a lower value of C_L at each incidence. However, the boundary layer model predicted that the upper surface boundary layer contained insufficient momentum to allow entrainment by the jet and stalling of the outer region flow was predicted before separation of the jet. This prediction may have been a true reflection of reality: Kind did not measure wall jet profiles at such low blowing rates so it is not possible to expand this point further.

Figure 47 compares computed solutions with the experimental curve of Landsberg and Krasnoff for a cascade of unstaggered elliptical aerofoils. Once again, attention is directed to the general accuracy of the experimental results. For example, Figure 6 in reference 23 shows that the flow deflection varied by 4° or 16% across the outlet stream of the cascade when operating in the jet flap configuration. The turning angles of the tangentially blown configuration were considerably larger and so the corresponding variation in outlet angle across the width of the cascade was presumably greater. Landsberg and Krasnoff do not appear to have recorded any static pressures on the aerofoil surfaces and so it is assumed that the blowing coefficients were calculated by considering jet expansion to mainstream conditions. The jet air was metered, however, so the correction made to the computed C_{μ} values was based on a modified U_j rather than U_j^2 : in fact, the

necessary corrections were found to be small. The theoretical treatment of their tests was additionally complicated by the need to allow the boundary layer programme to predict transition of the upper and lower surface boundary layers, since no transition device was used. Their tests were also conducted at the rather low Reynolds number of about 1.6×10^5 . These problems were not undesirable, however, because the same difficulties applied to the prediction of results obtained in the present research. The computed results are seen to compare well with experiment and the changing gradient of the curve is predicted. An effort was made to obtain a result at a blowing coefficient of about 0.8, but the calculation of pressure gradient around the trailing edge became unstable due to the extreme variation in pressure coefficient from point to point in this region at such a high blowing coefficient. It is believed that this problem could be overcome simply by increasing the number of pivotal points used in the potential flow programme. This would be more costly in terms of computing but is probably inevitable where high lift coefficients and the associated sharp surface pressure gradients are to be considered.

The solution procedure was applied to two configurations of the cascade tested in the present investigation. Figure 48 shows a comparison between theoretical and experimental turning angles for the staggered cascade at a pitch-chord ratio of 0.75. The agreement is apparently excellent in this case, in contrast to the much poorer agreement displayed in Figure 49 for the unstaggered, unit pitch geometry. These results will be discussed further in the following section.

Figure 50 shows a comparison between measured and predicted pressure distributions around the trailing edge of Kind's ellipse. The particular case shown was chosen because the theoretical results happened to coincide reasonably well with specific experimental conditions under which a full set of surface static pressure readings were recorded. The sparsity of measured pressures at the outer boundary of the wall jet, $C_{p\delta}$, gives a rather ill-defined curve, but the theoretical curve is seen to be a good approximation to this outer boundary pressure distribution.

7.3 Discussion

The results presented above illustrate the general suitability of the calculation procedure for predicting the performance of tangentially blown aerofoils and cascades. The agreement between theory and experiment for the results of Kind and of Landsberg and Krasnoff is probably as good as is possible for a complete solution procedure: Allcock and Dunham⁽³²⁾ point out that changes in the shape of the jet blowing slot can cause changes in lift of as much as fifty percent on a circular cylinder. In view of this evidence, little more than order of magnitude agreement with experiment can be expected from any solution procedure of the flexibility aimed at in the present study.

The agreement between theory and experiment for the cascade tested in the present investigation is not consistently good. In the staggered configuration the agreement probably is better than the accuracy of the theoretical model. For the unstaggered cascade, the agreement is worse than the previous results would lead one to expect.

The experimental drag curve, Figure 19, shows that vortex shedding was a predominant influence at low blowing rates, while the drag curve for the staggered geometry, Figure 23, indicates that where the agreement between theory and experiment was good, vortex shedding was not in evidence even at low C_{μ} . This leads to the suspicion that even when vortex shedding had apparently been suppressed by the wake closing effect of the jet, the wake flow of the unstaggered cascade was still not behaving in a manner similar to that of the staggered cascade. The fundamental difference in wake flow characteristics between the staggered and unstaggered cascades has already been commented upon in Chapter 4. A detailed experimental investigation of the flow behind circulation controlled bodies of comparable bluntness would be necessary to clarify this point. However, it is gratifying to reflect that the theoretical model gives grounds for such surmise.

The comparison of theoretical and experimental pressure distributions around the trailing edge of Kind's ellipse shows that the potential flow theory, with the representation of a separation bubble, realistically models the effect of circulation induced by a tangential jet. It is pleasing to note the very accurate prediction of separation pressure which exists throughout the separation bubble, Figure 50. The development of this flexible potential flow model greatly increases the extent of possible theoretical investigations of circulation controlled aerofoils or cascades: previous work has been confined to circular or elliptical sections so that theoretical surface pressure distributions could easily be calculated. With the present model, this restriction is lifted.

The boundary layer calculations on the upper and lower aerofoil surfaces is considered to be quite adequate: some trials on Kind's ellipse showed that changes in both the thickness of the starting boundary layer velocity profile and in the position of the start of the calculation, made very little difference to the predicted position of lower surface separation. In this case, however, the boundary layer was assumed turbulent from the start because Kind used trip wires near the leading edge of his ellipse. The need to predict transition in the other cases considered, introduced an extra degree of uncertainty, particularly in view of the relatively low test Reynolds numbers. The wall-jet calculation is believed to be the least satisfactory part of the present theoretical model, although it coped well in the present study. This section of the model proved by far the most difficult to commission and it requires relatively large amounts of computing time. Because the use of an eddy viscosity model or the usual parabolic boundary layer equation becomes highly dubious in the case of wall-jet flows, it is believed that a simpler model may well be capable of yielding comparable results. The employment of an integral technique for the wall-jet calculation would appear attractive, although the use of such methods in the past have not met with very great success when applied to problems of circulation control. Moreover, the current finite-difference method has the advantage of flexibility, allowing the calculation of heat transfer and chemical reaction phenomena by relatively simple extensions of the computer programme. It was largely because of this potential flexibility that the present model was adopted. If these extra facilities are not required, then a thoughtfully constructed integral approach could be more efficient.

CHAPTER 8

SUGGESTIONS FOR FURTHER WORK AND CONCLUSIONS

8.1 Suggestions for further work

8.1.1 Experiment

The purpose in developing any numerical calculation procedure of the type presented in this dissertation is primarily to avoid the need for extensive experimentation during aerofoil design stages. Once sufficient empirical data are available to test new calculation procedures, attention is better directed to the development of better theoretical models. At present, there are few data available on the performance of circulation controlled cascades and further, carefully obtained experimental results would be of use in testing theoretical models. Quite apart from the obtaining of general data on such cascades, it is felt that two distinct investigations are called for.

First, the dependence of vortex shedding phenomena on Reynolds number for circulation controlled sections. This relationship is a function of the section bluntness and in the case of cascades, probably strongly influenced by the cascade pitch and stagger. Secondly, it was mentioned in Chapter 2 that mainflow Mach number has been found to influence substantially the performance of isolated circulation controlled sections: a similar effect is to be anticipated for cascades and may prove to be of considerable importance since the maximum attainable turning angle is likely to fall rapidly with increasing Mach number.

8.1.2 Theoretical Work

The solution procedure developed during the present work has been only cursorily tested and much computational work is necessary to determine the full potential of this model. Apart from the testing of the procedure on further circulation controlled aerofoil experimental results, it would be of interest to discover how well the model performs when applied to problems concerning blown trailing edge flaps, where the large separation bubble present on the bluff trailing edge of circulation controlled aerofoils does not exist. Additionally, the capacity of the boundary layer procedure to solve problems of heat transfer has not yet been explored.

At a more detailed level, the complete solution procedure may be used to investigate the likely effects of varying the position and width of the blowing slot(s) on circulation controlled aerofoils, since substantial improvements in blowing efficiency may be obtained by optimising these variables. The calculation of the blowing jet development, however, is believed to be the least satisfactory part of the present solution procedure, simply because of its complexity and the need to generalise several empirical relationships. It may well be that a simpler model, perhaps of the integral type, could yield comparably accurate results with considerably reduced computing times.

The usefulness of the potential flow model without a blowing jet calculation should not be overlooked: the programme can be used to optimise profile shape by viewing the blade surface pressure distributions resulting from various geometries, while only a relatively crude boundary layer calculation is necessary to establish the approximate position of lower blade surface separation.

8.1.3 The Practical Application of Circulation Controlled Cascades

The above discussion has centred on the possible direction of future experimental and theoretical research. Ultimately, the usefulness of the principle involved is determined by the feasibility of applying it to practical situations. The potential applications of circulation controlled cascades were outlined in Chapter 1. There are now sufficient experimental data to consider in broad terms the practicability of using such cascades at low Mach numbers. The deciding factor is the necessary quantity and supply pressure of the blowing air: the bleeding of high pressure air from late compressor stages is generally a wasteful process and requires careful design to minimise power loss.

8.2 Conclusions

The experimental characteristics obtained for the cascades of bluff, circulation controlled compressor blades were influenced strongly by vortex shedding at low jet blowing rates. The experimental evidence suggests that even when a degree of wake closing has been achieved by the action of the blowing jet, the nature of the wake flow is sensitive to cascade geometry. This phenomenon is likely to be a common feature of the low Reynolds number performance of aerofoils with a comparable degree of bluntness and is thus an important design consideration.

In no test was an upper limit to the turning effectiveness of the blowing jet reached. The limits in the present investigation, at a Mach number of 0.3, were imposed by considerations of pitch to pitch flow uniformity.

The complete solution procedure has been shown to be capable of producing realistic predictions of the performance of circulation controlled aerofoils and cascades. The potential flow model, with its allowance for the separation bubble which occurs on circulation controlled sections, is likely to be useful on its own in preliminary design stages where knowledge of likely surface pressure distributions is required.

APPENDIX A

AN INVESTIGATION OF THE DISTRIBUTED PIPE FLOW PROBLEM

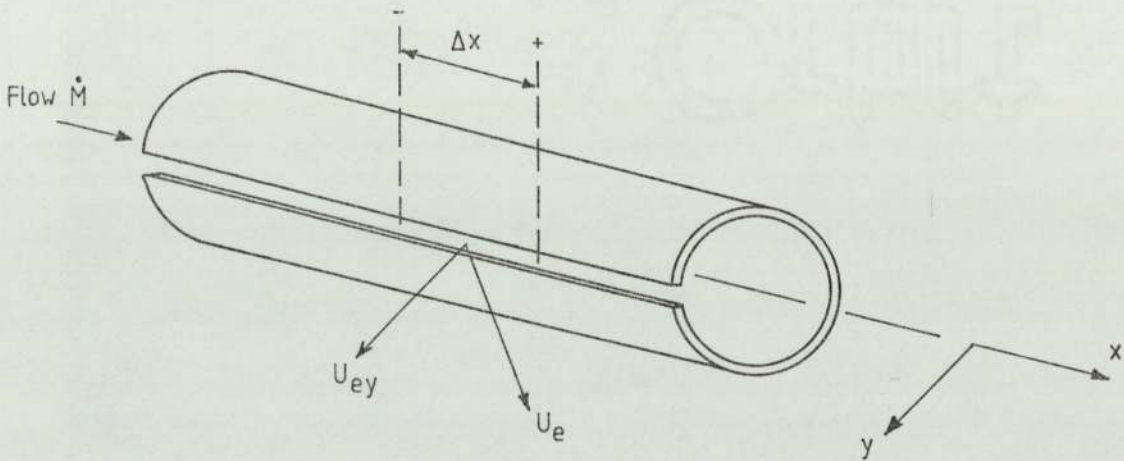
NOTE

The nomenclature in this Appendix differs slightly from that used in the main text. Definitions are provided as necessary.

A1. Theory

A1.1 The Governing Equations

Consider an element of pipe length, Δx , as illustrated below in Sketch A1, with some quantity of the pipe flow $\dot{m}_y \Delta x$ exhausting through the element of slot, width h :



Sketch A1

Flow from Slotted Pipe

Application of the energy equation to flow from the interior of the pipe, "i", to the slot outlet at "e", gives

$$\frac{\gamma}{\gamma-1} \left[\frac{P_i}{\rho_i} - \frac{P_e}{\rho_e} \right] = \frac{U_e^2 - U_i^2}{2}$$

where γ is here the ratio of specific heats of the gas in question, and if the flow through the slot can be considered isentropic:

$$U_e^2 = U_i^2 + \frac{2\gamma}{\gamma-1} \frac{P_i}{\rho_i} \left[1 - \left(\frac{P_e}{P_i} \right)^{\frac{\gamma-1}{\gamma}} \right]$$

It is assumed that the flow emerging from the slot retains its momentum in the direction of the pipe axis. Thus, the component of velocity of the emerging flow, normal to the pipe axis, U_{ey} , is:

$$U_{ey} = \sqrt{\frac{2\gamma}{\gamma-1} \frac{P_i}{\rho_i} \left[1 - \left(\frac{P_e}{P_i}\right)^{\frac{\gamma-1}{\gamma}} \right]} \quad A1$$

and the mass flow rate per unit length of the slot is:

$$\dot{m}_y = \rho_i h \left(\frac{P_e}{P_i}\right)^{\frac{1}{\gamma}} \sqrt{\frac{2\gamma}{\gamma-1} \frac{P_i}{\rho_i} \left[1 - \left(\frac{P_e}{P_i}\right)^{\frac{\gamma-1}{\gamma}} \right]} \quad A2$$

Consideration of equations A1 and A2 shows that the momentum flux in a direction normal to the pipe axis is

$$\frac{2\gamma}{\gamma-1} P_i h \left(\frac{P_e}{P_i}\right)^{\frac{1}{\gamma}} \left[1 - \left(\frac{P_e}{P_i}\right)^{\frac{\gamma-1}{\gamma}} \right]$$

per unit length of the pipe.

The equation of continuity for flow along the pipe is

$$\frac{d\dot{M}}{dx} = -\dot{m}_y \quad A3$$

while the energy equation can be expressed as

$$d\left(\frac{U^2}{2}\right) + \frac{\gamma}{\gamma-1} d\left(\frac{P}{\rho}\right) = 0 \quad A4$$

for the main pipe flow.

It is easily shown that provided the main pipe flow is large in comparison with the local slot flow, an obvious condition in any case, the momentum equation for pipe flow with friction retains its usual form:

$$dP + 2f\rho U^2 \frac{dx}{D} = -\rho U dU \quad A5$$

where f is the pipe friction factor, and D is the pipe diameter.

A1,2 Equations in Difference Form

Considering the element of pipe length shown in Sketch A1, properties at the upstream end of the element are denoted by the subscript "-" and the properties at the downstream end by the subscript "+".

The equation of continuity, A3, may then be written as

$$\rho_+ U_+ = \rho_- U_- - \frac{\dot{m}_y}{A} \Delta x$$

where A is cross-sectional pipe area.

The momentum equation, A5, can be expressed as

$$A(P_+ - P_-) = \dot{M}(U_- - U_+ - 2f\bar{U} \frac{\Delta x}{D})$$

and the energy equation for the main pipe flow, A4:

$$U_+^2 - U_-^2 = \frac{2\gamma}{\gamma-1} \left[\frac{P_-}{\rho_-} - \frac{P_+}{\rho_+} \right] \tag{A6}$$

Quantities which do not specifically pertain to one end or the other of the element are set to a mean value over the interval.

Denoting mean values by a bar, the continuity and momentum equations become

$$\frac{\dot{M}}{A} = \frac{1}{2}(\rho_+ U_+ + \rho_- U_-) \tag{A7}$$

and

$$P_+ - P_- = \frac{\dot{M}}{A} (U_- - U_+ - 2f\bar{U} \frac{\Delta x}{D}) \tag{A8}$$

A1.3 Equations in Functional Form; The Solution Procedure

The unknown "U₊" may be eliminated by use of equation A7 with A8:

$$P_+ - P_- = \frac{\bar{M}}{A} \left\{ U_- - \frac{2\bar{M}}{A_+} + \left(\frac{\rho_-}{\rho_+} \right) U_- - f \frac{dx}{D} \left[U_- + \frac{1}{\rho_+} \left(\frac{2\bar{M}}{A} - \rho_- U_- \right) \right] \right\} \quad A9$$

The quantity ρ_+ is found from equations A7 and A6:

$$\rho_+ = \frac{P_+ \pm \sqrt{P_+^2 + 4 \left(\frac{\rho_-}{\rho_+} + \frac{\gamma-1}{2\gamma} U_-^2 \right) \left(\frac{\gamma-1}{2\gamma} \right) \left(\frac{2\bar{M}}{A} - \rho_- U_- \right)^2}}{2 \left(\frac{\rho_-}{\rho_+} + \frac{\gamma-1}{2\gamma} U_-^2 \right)} \quad A10$$

Now, $\frac{2\bar{M}}{A} > \rho_- U_-$ so the expression under the square root is always $> P_+$. Thus, the negative root solution is of no consequence.

Over a small step, dx, equations A9 and A10 may be solved iteratively. Initial assumptions for downstream values are used to calculate \dot{m}_y , the flow through the slot over the interval. The solution for P_+ from equation A9 is applied in equation A10 to give ρ_+ . New mean values over the interval can be calculated and the cycle repeated to give convergence.

A2. Description of the Computer Programme

The computer programme utilising the expressions presented in the previous section will solve for any of three cases:

1. It will solve for the exit mass flux, momentum flux and pipe pressure distributions corresponding to a specified pipe and slot geometry.

2. It will solve for the momentum flux, pressure and slot width distributions for a specified constant exit mass flux and pipe geometry.
3. It will solve for the exit mass flux, pressure and slot width distributions for a specified constant exit momentum flux and pipe geometry.

The solution procedure is of the forward stepping variety, with iteration necessary in cases 1 and 3 to establish the mass flow at inlet to the pipe.

As basic input data, the pipe length, diameter and, where appropriate, slot width distribution are specified, together with the inlet static pressure and temperature and the pressure at the slot exit.

If the ratio of external pressure to the local total pressure falls below the critical ratio, the local slot flow will be choked. At each step, the local total pressure is calculated and if the pressure ratio is below the critical value, the local slot exit pressure is set to $(\frac{2}{\gamma+1})^{\frac{\gamma}{\gamma-1}}$ times the local total pressure.

The effect of a slot discharge coefficient is included very simply by multiplying the calculated exit mass flux by the coefficient in the cases of specified slot width distribution and specified momentum flux, or by dividing the calculated slot width by the coefficient in the case of a specified mass flux. The discharge coefficient can be defined as any function of local conditions or, of course, as a constant.

Units of the Système International are used throughout and all pressures and temperatures are absolute. The computer programme is written in BASIC and at present up to 50 step lengths can be taken. The results presented in this Appendix were obtained with either ten or twenty steps, larger numbers being found to make little difference.

A3. Experimental Method and Results

The slotted pipe, constructed to test the prediction procedure, was designed to allow variation of the slot width and length, although only the slot width was varied in the tests described herein. Illustrations of the slotted pipe and the air supply apparatus are shown in Figure 51.

The slot width could be varied by the use of different shim thicknesses and the slot length was defined by the depth of insertion of the supply pipe and the blanked-off stub pipe. These pipes were secured with silver solder. In the tests reported here, the slot length was maintained at 127 mm and slot widths of 0.762 mm and 1.397 mm were used. The slotted pipe was of 15 mm diameter with a 0.762 mm shim and the slot lip thickness was 0.79 mm. The supply pipe, of length 1 m to ensure a fully developed turbulent profile at inlet to the slotted pipe, was chamfered to give a smooth inlet flow, although some degree of step was inevitable with the larger of the two shim thicknesses.

Five static pressure tappings were drilled at intervals of 25.4 mm along the slotted pipe and a further tapping was situated in the blanked-off stub pipe.

The flow to the settling pipe was supplied through a 50.8 mm diameter pipework including a Rotameter to allow measurements of flow rate. A seventh static tapping was provided a short distance from the rotameter outlet to allow calibration and a thermocouple for measurement of total temperature was positioned near the contraction to the settling pipe.

The seven static pressure tappings were connected to a seven way pressure switch, enabling each one to be connected in turn to a 0-100 kN/m² transducer, giving an output display on a digital voltmeter. Static tapping 7 was also connected to a mercury U-tube manometer allowing calibration of the transducer.

Measurements of flow rate and pipe pressure distribution were recorded for three different flow rates at each of the two slot thicknesses. The slot flow was sonic for the third test on the narrower of the two slots.

A calibration chart was drawn up for the rotameter at each of the six supply pressures, and the mass flow rates calculated. It was suspected, and subsequent examination of the results confirmed, that the pressure readings given by the first static tapping were all low, since the end of the supply pipe projected virtually to this hole. These readings, therefore, have been ignored.

The pressure profiles have been plotted as distributions of

$\frac{P_x - P_e}{P_L - P_e}$ against fraction of distance along the pipe, where P_L

represents the pressure at the closed end of the pipe. Thus, the solid curves of Figures 52 to 57 depict the distribution of pressure drop across the slot.

A4. Theoretical Results and Comparison with Experiment

The primary difficulty in calculating the theoretical results was the specification of unknown quantities. In the interests of realism, the calculation procedure allowed the inclusion of a pipe friction factor and a slot discharge coefficient. However, these factors are applied here to a complex flow and it is not altogether reasonable to assume that they retain their usual relationships with the properties normally used to non-dimensionalise their characteristics. For example, the friction factor, normally employed to express the influence of shear stress at the pipe walls for conventional flow, must here also represent the effect of redistribution of flow within the pipe as the main pipe flow is continuously reduced. Similarly, the local discharge coefficient is likely to be a function of the local main pipe flow velocity as well as the usual parameters of pressure drop across the slot and slot geometry.

The majority of computing trials were conducted on the first three sets of results, obtained with the narrower slot width. First of all, a fourth order polynomial was fitted to the experimental curve, to give an extrapolated value for the pressure at the start of the slot. This was the pressure specified in the programme. As a first approximation, a friction factor was selected, based on the inlet Reynolds number and a roughness ratio typical of steel, using a conventional friction factor chart. This gave a value for f of about

0.007 and it was assumed to be a constant along the whole pipe length. Having defined the inlet static pressure and friction factor in this manner, the discharge coefficient was assumed to be constant and was determined by trial and error, altering the value until the predicted pressure at the closed end of the pipe corresponded closely with the measured value.

This procedure yielded the results marked by triangles on Figures 52, 53 and 54. Although the resulting pressure distributions are in good agreement with experiment, the predicted mass flows were of the order of 10% too low, see Table A1, on page 133. As a result, and because of anticipated effects of flow redistribution on the effective friction factor, the factor was raised to 0.015 and the coefficients of discharge found again by trial and error. The new distributions are marked by dashed lines on Figures 52, 53 and 54. The pressure distributions are only marginally worse than those predicted using the lower value of f but the disagreement between measured and predicted flow rates was considerably reduced, that at the highest flow rate being only 2.5%, within the usual limit of accuracy of the type of flowmeter used.

The comparison of experiment and theory for the larger slot width is generally less satisfactory. On the basis of the earlier experiences, the friction factor was set to 0.015, since the range of inlet Reynolds numbers covered by all the tests was not large. It was found that the pressure distribution curves could not satisfactorily be fitted by a polynomial as before and so the inlet static pressure together with the discharge coefficient were selected by trial and

	Result					
	1	2	3	4	5	6
Slot Width/Pipe Diameter	0.051	0.051	0.051	0.091	0.091	0.091
Slot Width/Pipe Length	0.0059	0.0059	0.0059	0.011	0.011	0.011
Measured Flow (kg/s) x 10 ³	11.5	22.0	38.7	11.3	33.3	49.0
Predicted Flow (kg/s) x 10 ³ f = 0.007	10.1	20.0	35.8	-	-	-
Predicted Flow (kg/s) x 10 ³ f = 0.015	10.6	21.1	37.7	11.0	34.2	51.3

TABLE A1
Measured and Predicted Mass Flow Rates in Slotted Pipe Experiments

error to obtain reasonable agreement with the measured values of end pressure and inlet mass flow rate. It can be seen from Figures 55, 56 and 57 that the resulting predicted inlet pressures appear to be somewhat high and the general agreement of curve shape is not as good as for the narrower slot.

A5. Prediction of Blowing Slot Performance of the Cascade Blades

The blowing slot geometry of the model compressor blades was supplied to the programme and the theoretical pressure, mass flux and momentum distributions calculated for a range of supply pressures. A friction factor of 0.010 was specified and on the basis of the experimental slot flow calibration, the discharge coefficient was set to a constant 0.85.

Figure 58 shows the slot pressure drop distribution for four supply pressures while Figure 59 illustrates the corresponding distributions of momentum deviation. It can be seen that the uniformity of both the pressure and momentum distributions improves continuously with increasing supply pressure. Figure 59 forms the focus of this Appendix. It can be seen that even at the lowest blowing supply pressure, the maximum predicted variation of blowing momentum over the centre half of the blade span is less than 5% and the variation for choked flow is less than 2%.

APPENDIX B

MODIFICATION OF CASCADE PARAMETERS TO TAKE ACCOUNT OF BLOWING

B.1. Momentum Considerations

Consider flow through a cascade of bluff aerofoils, as illustrated in Figure 60a. From the trailing edge of each blade a mass of air, \dot{m}_j , is ejected. A control volume is drawn, encompassing a full blade, the blade surface constituting an inner boundary of the control volume. Stations 1 and 2 indicate planes sufficiently far upstream and downstream that flow conditions can be considered uniform. The control volume is considered in more detail in Figure 60b.

Forces X and Y represent the components of force exerted on the control volume by the blade. Incompressible flow through the cascade is assumed.

Considering momentum in the x direction gives:

$$(P_1 - P_2)s + X = \dot{m}_2 U_{2x} - \dot{m}_j U_{jx} - \dot{m}_1 U_{1x}$$

Now, $\dot{m}_2 = \dot{m}_j + \dot{m}_1$

$$(P_1 - P_2)s + X = \dot{m}_1 (U_{2x} - U_{1x}) - \dot{m}_j (U_{jx} - U_{2x}) \quad \text{B.1.}$$

With the addition of the nozzle flow, the axial continuity equation becomes:

$$U_{2x} = U_{1x} (1 + R) \quad \text{B.2.}$$

where

$$R = \frac{\dot{m}_j}{\rho s U_{1x}}$$

On substitution of the above in equation B.1, the axial component of blade force is given by:

$$X = (P_2 - P_1)s + [(2+R) - \frac{U_{jx}}{U_{1x}}] \rho s U_{1x}^2 R \quad \text{B.3}$$

Consideration of momentum in the y direction gives:

$$Y = \dot{m}_1 U_{1y} - \dot{m}_2 U_{2y} + \dot{m}_j U_{jy}$$

which can be written

$$Y = \rho s U_{1x} (U_{1y} - U_{2y}) - [(1+R) \tan \alpha_2 - \frac{U_{jy}}{U_{1x}}] \rho s U_{1x}^2 R \quad \text{B.4.}$$

by use of equation B.2.

The term $(P_2 - P_1)s$ in equation B.3. can be replaced by:

$$\frac{1}{2} \rho s (U_1^2 - U_2^2) - \Delta P^* s \quad \text{B.5.}$$

where ΔP^* represents a loss in total pressure across the cascade and will be discussed later. Substitution into B.3. gives:

$$X = \frac{1}{2} \rho s U_{1x}^2 [\tan^2 \alpha_1 - (1+R)^2 \tan^2 \alpha_2 - 2R - R^2] - \Delta P^* s + [2+R - \frac{U_{jx}}{U_{1x}}] \rho s U_{1x} R$$

and if R^2 can be neglected in comparison with R , then

$$X \approx \frac{1}{2} \rho s U_{1x}^2 [\tan^2 \alpha_1 - \tan^2 \alpha_2 + 2R(1 - \tan^2 \alpha_2 - \frac{U_j}{U_{1x}} \cos \alpha_j)] - \Delta P^* s \quad \text{B.6.}$$

The term $\rho U_{1x} s (U_{1y} - U_{2y})$ in equation B.4, can be replaced by $\rho U_{1x}^2 s (\tan \alpha_1 - (1+R) \tan \alpha_2)$ to give:

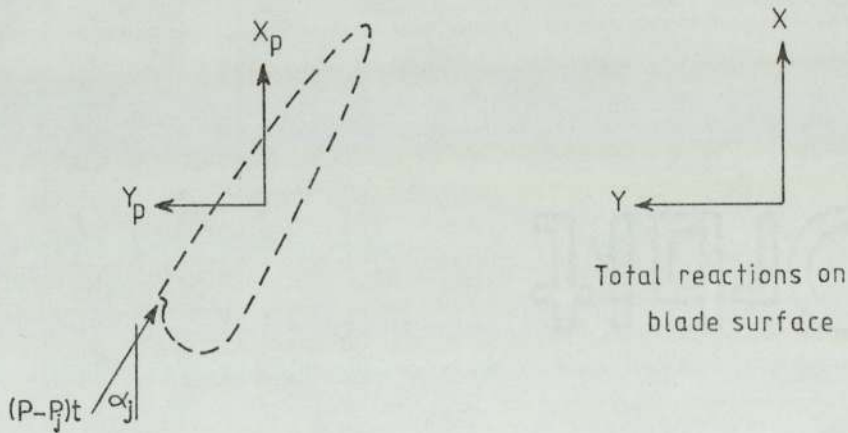
$$Y = \rho s U_{1X}^2 [\tan\alpha_1 - (1+R)\tan\alpha_2] - \rho s R U_{1X}^2 [(1+R)\tan\alpha_2 - \frac{U_j Y}{U_{1X}}]$$

or

$$Y \approx \rho s U_{1X}^2 [\tan\alpha_1 - (1+2R)\tan\alpha_2 + R \frac{U_j}{U_{1X}} \sin\alpha_j] \quad \text{B.7.}$$

by neglecting terms in R^2 as before.

The expressions derived above, give the total force exerted on the control volume by each blade, there being an equal and opposite reaction on the blades. The blade around which the inner control surface of Figure 60 was drawn is considered in Sketch B1 below



Sketch B1

Forces Acting on Cascade Blades

The total force acting on this control surface is comprised of two components: the profile drag (skin friction plus form drag), and the force resulting from any pressure drop at the blowing slot exit. This latter force will only occur when the slot flow is choked.

Consideration of Sketch B1 shows that

$$X_p = X - (P - P_j)t \cos\alpha_j$$

and

$$Y_p = Y + (P - P_j)t \sin\alpha_j$$

where X_p and Y_p are the x and y components of profile drag.

B.2. Coefficients of Lift and Drag

The coefficients of lift and drag are conventionally the lift and drag forces (perpendicular and parallel to the mean velocity vector) divided by the mean dynamic pressure and blade chord ($\frac{1}{2}\rho U_m^2 c$). In the case of blown blades, the "mean velocity" does not have quite the same significance, due to the addition of mass from the blade nozzles and the resulting increased downstream velocity. The "mean velocity" is here defined as

$$U_m = U_{1x} \sec\alpha_m$$

where $\tan\alpha_m = \frac{1}{2}(\tan\alpha_1 + \tan\alpha_2)$ as usual.

Using this definition of the mean velocity, the coefficient of lift can be written:

$$C_L = \frac{1}{\frac{1}{2}\rho c U_m^2} \{X_p \sin\alpha_m + Y_p \cos\alpha_m\}$$

$$C_L = 2\frac{S}{c} \cos\alpha_m (\tan\alpha_1 + \tan\alpha_2) - \frac{\Delta P^* s \sin\alpha_m \cos^2\alpha_m}{\frac{1}{2}\rho c U_1^2 \cos^2\alpha_1}$$

$$+ 2R\frac{S}{c} \cos^2\alpha_m [(1-\tan^2\alpha_2)\sin\alpha_m - 2\tan\alpha_2 \cos\alpha_m - \frac{U_j}{U_{1x}} \sin(\alpha_m - \alpha_j)]$$

$$+ \frac{(P - P_j)t}{\frac{1}{2}\rho c U_{1x}^2} \sin(\alpha_j - \alpha_m) \cos^2\alpha_m$$

and the coefficient of drag

$$C_D = \frac{1}{\frac{1}{2}\rho c U_m^2} \{Y_P \sin\alpha_m - X_P \cos\alpha_m\}$$

$$C_D = \frac{\Delta P^* s \cos^3\alpha_m}{\frac{1}{2}\rho c U_1^2 \cos^2\alpha_1}$$

$$- 2R\frac{S}{c} \cos^2\alpha_m [2\tan\alpha_2 \sin\alpha_m + (1-\tan^2\alpha_2)\cos\alpha_m - \frac{U_j}{U_{1x}} \cos(\alpha_j - \alpha_m)]$$

$$+ \frac{(P - P_j)t}{\frac{1}{2}\rho c U_{1x}^2} \cos(\alpha_j - \alpha_m) \cos^2\alpha_m$$

These expressions for lift and drag are identical with those given by Horlock⁽⁴⁸⁾ if the terms multiplied by "R" and the slot pressure drop terms are neglected.

B.3. The Pressure Loss Term

With a conventional cascade, the term ΔP^* equals ΔP_0 , the loss in total pressure across the cascade. When blowing is applied, the term is complicated by the effect of the blowing air. If incompressible flow is assumed everywhere, including the slot flow, then:

$$L_p = \dot{m} \left(\frac{P_1}{\rho} + \frac{U_1^2}{2} - \frac{P_2}{\rho} - \frac{U_2^2}{2} \right) + \dot{m}_j \left(\frac{P_{0j}}{\rho} - \frac{P_2}{\rho} - \frac{U_2^2}{2} \right)$$

where L_p is the total pressure energy loss of both the main flow and the blowing slot flow. Rearranging gives:

$$P_2 - P_1 = \frac{1}{2} \rho (U_1^2 - U_2^2) - R \left(P_2 + \frac{\rho U_2^2}{2} - P_{0j} \right) - \frac{\rho L_p}{\dot{m}} \quad \text{B.8.}$$

where the total pressure loss has been expressed as an energy loss per unit mass of the mainstream flow. Equation B.8. shows that the term ΔP^* , introduced in equation B.5., is given by:

$$\Delta P^* = R \left(P_2 + \frac{\rho U_2^2}{2} - P_{0j} \right) + L_m \quad \text{where } L_m = \frac{\rho L_p}{\dot{m}}$$

L_m is a pressure loss term which absorbs the effects of both the conventional pressure loss and the extra blowing air mixing losses. It is not possible to resolve these two components of the pressure loss in terms of overall cascade characteristics.

B.4. Summary of Modifications to Cascade Characteristics

Parameter	Usual expression	Modification necessary if blowing employed
AVR	$\frac{U_{2x}}{U_{1x}}$	Divide by (1 + R)
Total Pressure Pressure loss coefficient	$\frac{\Delta P_0}{\frac{1}{2}\rho U_1^2}$	Add A
C_L	$\frac{2\frac{S}{c}[\tan\alpha_1 - \tan\alpha_2]\cos\alpha_m}{\frac{1}{2}\rho U_1^2} \frac{s}{c} \frac{\sin\alpha_m \cos^2\alpha_m}{\cos^2\alpha_m}$	Add B + C sin($\alpha_j - \alpha_m$)
C_D	$\frac{\Delta P_0}{\frac{1}{2}\rho U_1^2} \frac{s}{c} \frac{\cos^3\alpha_m}{\cos^2\alpha_1}$	Add -D + C cos($\alpha_j - \alpha_m$)

$$A = \frac{R(P_{0j} - P_{02})}{\frac{1}{2}\rho U_1^2}$$

$$B = 2R\frac{S}{c}\cos^2\alpha_m [(1 - \tan^2\alpha_2)\sin\alpha_m - 2\tan\alpha_2 \cos\alpha_m - \frac{U_j}{U_{1x}} \sin(\alpha_m - \alpha_j)]$$

$$C = \frac{(P - P_j)t}{\frac{1}{2}\rho c U_{1x}^2} \cos^2\alpha_m$$

$$D = 2R\frac{S}{c} \cos^2\alpha_m [(1 - \tan^2\alpha_2)\cos\alpha_m + 2\tan\alpha_2 \sin\alpha_m - \frac{U_j}{U_{1x}} \cos(\alpha_j - \alpha_m)]$$

APPENDIX C

THE POTENTIAL FLOW COMPUTER PROGRAMME

POTFLO2

C.1. Introduction

The theory on which this programme is based was outlined in Chapter 5. This Appendix presents details of the computer programme written in FORTRAN IV, with sufficient information for a potential user to implement calculations readily and with confidence.

Basically the programme progresses in a stepwise fashion, from block to successive block, so that the sequence of operations is easily followed. For this reason, the programme has been divided into Chapters, each Chapter corresponding to a significant operation. Chapter 10 is the longest and the only one in which a loop of significant size and complexity is employed.

C.2. Preliminary Outline

The FORTRAN programme was constructed with maximum flexibility as a prime objective. Two alternative data input sections are available:

1. The section may be specified by camber and half-thickness values at various fractions of chord length. This is the form of profile definition used by the NACA.
2. Alternatively, the section may be defined by providing surface coordinates of an already cambered section. This method of input is used, for example, when surface coordinates are generated by conformal transformation.

All the necessary variable quantities are specified in the input data, together with the stagger and pitch if a cascade is considered, and up to twenty incidences/inlet angles. The positions of the upper and lower separation points are defined.

For each incidence/inlet angle, the corresponding pressure coefficients are calculated and the resulting force coefficients, C_x and C_y , are determined by Simpson's integral method. If required, the programme then calculates distances around the section of each pivotal point from the forward stagnation position, in preparation for a boundary layer calculation.

So that all geometrical details concerning a section can be input together, the geometry of any tangential blowing arrangements are input to this programme. These details concern the positioning and thickness of the blowing slots and the position and curvature of the bluff trailing edge. Up to ten blowing slots on the upper and lower surfaces can be accommodated.

Figure 61 is an outline flowchart of the whole programme.

C.3. Description of Programme

Chapter 1

All preliminary data is read in this Chapter. The precise order and format of the required data is given in Figure 62 and the meaning of all the terms in Section C4. The input data is also printed out in Chapter 1 for checking. At the end of the Chapter, various quantities are defined for use later in the programme. The more important quantities are defined in Section C.4.

Chapter 2

In this Chapter, the remainder of the input data is read, this data comprising the detailed definition of the section shape. Depending on the value of ICAMB, subroutine CAMPROF or CAMTHIK is called, the first being used when coordinates of a ready cambered section are supplied and the latter when a camber-thickness distribution is specified. These subroutines are described later. On return to the main programme, arrays XSURF and YSURF contain the 2N surface coordinates of the unstaggered profile. Using arrays DXDFI and DYDFI for temporary storage, the surface coordinates are smoothed using

$$f_0 = \frac{1}{12}(-f_{-2} + 4f_{-1} + 6f_0 + 4f_1 - f_2)$$

which is equivalent to fitting a least squares parabola through five points and replacing the centre point by the coordinate of the parabola at the centre. The surface points corresponding to subscripts -2, -1, 1, 2 are determined by a small subroutine I1234, briefly described later. The smoothed surface coordinates are then written out.

Chapter 3

If a cascade is being considered, this Chapter staggers the profile coordinates by an amount STAG (ξ):

$$x' = x \cos \xi - y \sin \xi$$

$$y' = y \cos \xi - x \sin \xi$$

If slots and trailing edge limits have been specified in the input data, the x-coordinates of these are staggered. The y-coordinates do not need to be adjusted, since the positions of these points in terms of distance around the surface are later defined by interpolation in x.

The staggered surface coordinates are output.

Chapter 4

Arrays containing $\frac{dx}{d\phi}$, $\frac{dy}{d\phi}$, $\frac{d^2x}{d\phi^2}$, $\frac{d^2y}{d\phi^2}$ are constructed using:

$$f'_0 = \frac{1}{12h} (f_{-2} - 8f_{-1} + 8f_1 - f_2), \quad h = \frac{\pi}{N}$$

Chapter 5

An array BOT is built, which contains conversion factors from vortex and source densities to surface speeds, e.g.

$$U_{\text{surface}_i} = \frac{\gamma_i}{\text{BOT}(i)} \quad \text{where } \text{BOT}(i) = \sqrt{\left(\frac{dx}{d\phi}\right)^2 + \left(\frac{dy}{d\phi}\right)^2}$$

An array NSOU is then constructed, where NSOU(i) contains the number of the surface point on which source number (i) lies, see Figure 63.

Both of these arrays prove useful in later Chapters.

Chapter 6

At the beginning of this Chapter, the calculation is directed to one of two blocks, depending upon whether an isolated section or a cascade is being considered. In the relevant block, the K matrix is constructed, using the terms defined in equations 5.6 for $K_{\gamma mn}$ and $K_{S mn}$. The matrix is constructed in the manner depicted in equation 5.9, the source terms occupying the last NS columns.

Chapter 7

Lower mean values are first substituted for the $K_{\gamma m, 2N-m}$ matrix elements.

The two incident flow vectors, terms (1) and (2) in equation 5.15, are added to the K matrix. Their inclusion in the matrix simplifies the Gaussian reduction implemented in the next Chapter.

Chapter 8

In a very short loop, the left hand side of the K matrix, i.e. the K_{γ} component, is reduced to an upper triangular form by Gaussian reduction. Equations 5.6 show that the $K_{\gamma mn}$ terms are considerably larger in modulus than the off-diagonal elements, so row interchange is unnecessary.

Chapter 9

The matrix is solved for the right hand sides (1), (2) and (3) in equation 5.15. The back substitution is carried out in Subroutine SOLVE, described later. On return to the main segment, the three solution vectors are contained in GAMA(1-2N,i), $i = 1, 2, 3$.

Chapter 10

This is the longest Chapter and the most complex. There is one "DO" loop covering the whole Chapter, which is repeated for each incidence. Within this Chapter there is an iterative loop, required for convergence on a solution at a particular incidence. The Chapter has been sub-divided into the sections below.

10/A

The incidence/inlet angle ALPH1 is set and preliminary values are assigned to the outlet angle and the upstream and downstream flow speeds. All these quantities remain unchanged if an isolated section is considered.

10/B

This is the start of the iterative loop. The first approximation to all the source strengths is zero, so values are not assigned initially to array SOU. The right hand side (4) of equation 5.15 is constructed using the latest values contained in SOU.

10/C

Subroutine SOLVE is called to obtain a solution vector GAMA(i,4) for the right hand side due to the sources, constructed in 10/B.

10/D

Solutions (1), (2) and (4) in equation 5.15 are summed to give a particular solution to γ_n , contained in GAMA(i,5).

10/E

To impose the condition implied by equation 5.14, solutions contained in GAMA(i,3), GAMA(i,5) and SOU(i) need to be converted into surface speeds. This is effected by calling Subroutine SPEED.

10/F

Equation 5.14 is applied to yield a value for C, the factor by which the circulatory solution is to be multiplied before adding to the existing sum of solutions, GAMA(i,5). This addition is performed.

10/G

At this point, a test is applied to determine whether sufficient convergence on a solution has been achieved. The test is simply one of the degree of uniformity of pressure in the separated region. If all points within the separated region satisfy the limit imposed, the trigger quantity IENDIT is set to unity.

10/H

If convergence has not been attained, new source strengths are calculated using equations 5.11 and 5.12.

10/I

The values in SOU(i), GAMA(i,3) and GAMA(i,5) at this point still represent surface speeds. In this section, subroutine SPEED is called again to re-convert these quantities to source and vortex densities.

10/J

This section is only traversed if a cascade is being considered. With every new set of surface vortex and source strengths, the incident flow angle, θ , necessary to yield the required inlet angle, α_1 , has to be re-calculated and thus forms part of the iterative process. The value of θ (THETA) is calculated according to equation 5.18 and the resultant upstream speed by 5.19.

10/K

This is an output section, traversed on every iterative cycle and it writes out the latest approximations to the source strength.

If IENDIT has not been set to unity, representing convergence, the programme jumps back to section 10/B. An upper limit is set on the allowable number of iterations. If this limit is exceeded due to some error, the programme terminates with an appropriate comment.

10/L

This section is encountered once convergence has been achieved, but is bypassed if an isolated section is being considered. The outlet angle, α_2 (ALPH2) and the downstream speed are calculated.

10/M

The pressure coefficients for the converged vortex solution are calculated with the source components added in the separated region. The force coefficients C_x and C_y are then obtained by integrating the pressure components using Simpson's method.

The pressure and force components are based on the upstream flow speed. It would be a very simple matter to arrange for, say, the mean flow speed to be used as the reference value.

10/N

The flow angles and pressure and force coefficients for the particular inlet angle/incidence are written out. If the trigger value NSTOR is set to unity, Subroutine DISTANCE is called to calculate distances around the section surface.

At the end of this segment, control returns to the start of Chapter 10 to loop for the next inlet angle/incidence.

Chapter 11

After solving for the last inlet angle/incidence, the programme is terminated.

Subroutine CAMTHICK

This Subroutine is called in Chapter 2 if the profile is to be built from a given camber and thickness distribution. The Subroutine has been divided into segments to aid comprehension.

Since the thickness of a section is added normal to the camber line, it is necessary to calculate gradients of and distances along the camber line. To avoid difficulties in gradient calculations at the ends of the camber line, extra points are added at each end, to give an odd function about $x/L=0$ and $x/L=1.0$.

CT/A

The data is read according to the format detailed in Figure 62. The values read into arrays CHORD and YCAMB start at element 5, to allow inclusion of the "dummy" points for gradient calculations. The four dummy values at each end of arrays CHORD and YCAMB are then added and the input data is written out.

The data is read starting at the trailing edge point.

CT/B

Gradients of the camber-line at each of the input data points are calculated by taking the quotient $\frac{dy_c}{dx} = \frac{dy_c}{di} / \frac{dx_c}{di}$. Second derivatives are also found, D2YCDX. At the end of this segment, all arrays to be used in future calculations are arranged such that the quantity contained in each element pertains to the corresponding point in the input data.

CT/C

The distance along the camber line, l , of each input point is calculated and each distance is then divided by the total camber line length, L . Distances are measured from the leading edge.

CT/D

Values of ϕ at the input points are calculated, using

$$l'/L = \frac{1}{2}(1 + \cos\phi)$$

where

$$l' = l(1.0 + (1.0 - k)l(1.0 - l))$$

This latter expression, given by Wilkinson, allows a modification of the pivotal point spacing near the trailing edge. In general, the value of k is set to unity which leaves the point spacing unchanged.

Wilkinson suggested that there is a minimum allowable value, $k \geq 0.03N$.

CT/E

Arrays XFI, YCFI, YTFI, and DYDXFI are constructed for equal increments of ϕ ; $\phi = \frac{i\pi}{N}$, $i = 0, 1, 2, \dots, N$. For each ϕ -value, Subroutine LAGINT is called to interpolate in terms of ϕ . The first element of each of the arrays corresponds to the trailing edge point, so that a total of $N+1$ points are defined.

CT/F

It remains to add the calculated half-thicknesses, YTFI, to the camber line to yield the final $2N$ surface coordinates XSURF, YSURF. This final numbering system corresponds to that shown in Figure 33.

Control returns to the main programme segment.

Subroutine CAMPROF

This Subroutine is called in Chapter 2 if the profile is input in a cambered form, that is, as a set of actual surface points.

New surface points are obtained by interpolation, and care is taken to arrange that points m and $2N-m$ should lie approximately opposite each other on the normal to the mean line. This condition improves the accuracy of the lower mean values calculated in the main programme segment.

CP/A

The data is read according to the format detailed in Figure 62. The data consists of pairs of x,y values for the upper and lower surfaces, starting at the trailing edge point. Although the first and last pairs of coordinates should be $(1,0)$ and $(0,0)$ respectively, for both the upper and lower surfaces, it is permissible for these points to be slightly inexact. This flexibility has been allowed since profiles obtained by conformal transformation can exhibit small numerical inaccuracies.

The input data is written out.

CP/B

Equal increments of ϕ , $\frac{i\pi}{N}$, $i=1,2,3\dots N-1$ are taken and the corresponding x -coordinates calculated from $x = \frac{1}{2}(1 + \cos\phi)$. Interpolation for each y -coordinate is performed by a four point Lagrange interpolation, effected in Subroutine LAGINT. This procedure is carried out first for the upper surface and then the lower surface to yield a set of y -coordinates in array YSURF. The x -coordinates are

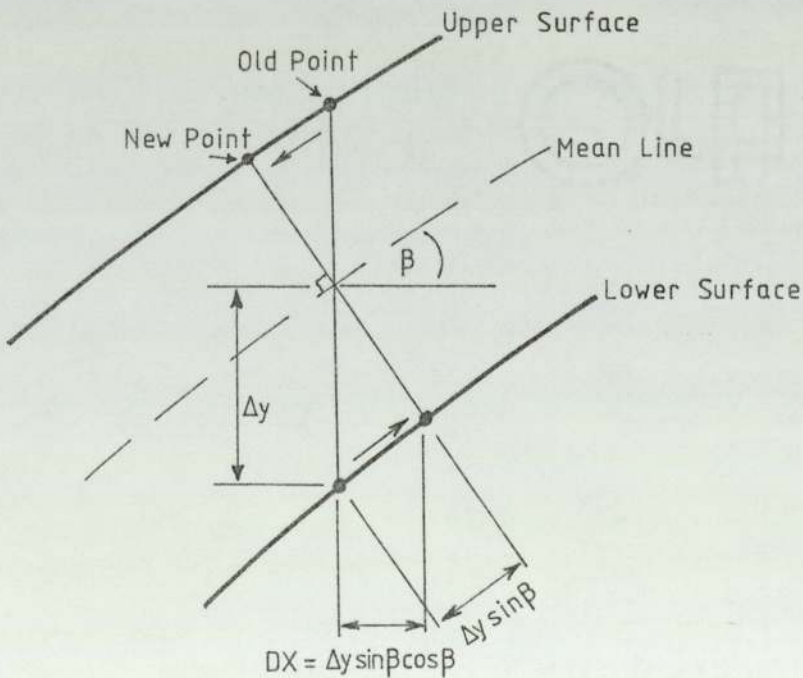
stored in XFI but while point 1, at $\phi = \frac{\pi}{N}$, corresponds to the first element in YSURF, it corresponds to the third element in XFI. This shift is employed to facilitate mean-line gradient calculations. XFI is treated as an odd function about $\phi = 0$ and $\phi = \pi$.

CP/C

Gradients of the mean-line are calculated. Array MEAN is built to correspond with array XFI, with an extra point at the leading and trailing edges. Gradients DYDXFI are calculated and the elements in this array correspond to the surface point numbering system, Figure 33.

CP/D

The x-coordinates of the upper and lower surface points are then moved by an amount DX to lie opposite each other on the normal to the mean-line, see Sketch C1 below.



Sketch C1

Movement of Surface Points in Section CP/D

CP/E

The corrected x-values, contained in XSURF, are used to re-interpolate for y-coordinates, YSURF, using the original input data. Thus, any inaccuracies introduced in the above sections do not affect the accuracy of the final profile.

Control is returned to the main programme segment.

Subroutine DISTANCE

This Subroutine calculates distances around the section surface of each pivotal point in order to create a data file suitable for access by a boundary-layer programme. The Subroutine is called from Chapter 10/N if the trigger value NSTOR is set to unity.

Distances are calculated around the upper and lower section surfaces, starting from points M-1 and M+1 respectively, where M is the point nearest to the position of forward stagnation. If blowing slots and a curved trailing edge have been specified in the input data, the positions of these are also recorded in terms of surface distances.

The "upper" and "lower" surfaces are defined here as shown in Figure 63. The geometrical upper and lower surfaces, of course, are those separated by the camber line.

The following assumptions are made:

1. Any slot input as lying on the geometrical lower surface, but which lies on the upper surface as defined above, is assumed to blow in a clockwise direction.
2. The start of the trailing edge curvature does not lie between points 1 and 2N,
3. The upper separation point does not lie beyond the start of the curved trailing edge on the lower surface.

DS/A

The point which lies nearest to the front stagnation position, M is found.

DS/B

This section is comprised of one large DO loop. The first half of the loop considers the upper surface, starting at point M-1. The distance DLU between adjacent surface points is calculated. A check is made to see whether the start of a curved trailing edge or a blowing slot has been stipulated to lie between the surface points being considered. If so, a linear interpolation in x is made to define their position in terms of surface distance. A similar procedure is carried out for the lower surface in the second half of the loop.

To allow accurate pressure gradient calculations in the boundary layer programme, lower surface distances are calculated as far as the geometrical trailing edge, point 2N, or to the upper separation point if this lies below point 2N. The calculations of upper surface distances is extended as far as the lower separation point.

DS/C

If the upper separation point lies beyond the trailing edge, in a clockwise sense as in Figure 63, then some of the geometrical lower surface points lie on what is, for the present purposes, the upper surfaces. This section of the Subroutine considers points lying in this region. Whatever the location of the upper separation point, this section is necessary to allow the calculation of upper surface distances right around to the lower separation point. Any slots that are encountered before the upper separation point, having been defined originally as lying on the lower surface, are included on the new "upper surface".

DS/D

Surface gradients and distances are written out. Data necessary for a boundary layer calculation are then stored in a data file. The format of these output data is shown in Figure 64. Control is returned to the main programme segment.

Subroutine SOLVE

This Subroutine is called in Chapters 9 and 10 to perform back substitution in matrix K. When called to solve the right hand sides numbered (1), (2) and (3) in equation 5.15, the right hand side, array RHS, is transferred from the appropriate column in ARAY. For the source solution, right hand side 4 in equation 5.15, the RHS array is built in Chapter 10 and transferred to the Subroutine.

Subroutine SPEED

This Subroutine converts vortex and source densities into tangential and normal surface speeds, or vice-versa, according to the value of subscript NTRIG. The conversion factors are contained in array BOT, built in Chapter 5.

Subroutine LAGINT

This is an interpolation Subroutine employing the standard Lagrange method, for four points. The Subroutine is called by Subroutine CAMTHIK and CAMPROF for interpolation in ϕ or in x respectively. Hence the use of FIORX for the array name in LAGINT.

Subroutine I1234

This very short Subroutine called to determine the points to be used for the calculation of surface gradients in Chapter 4. The routine is only necessary because of the discontinuity in numbering at the trailing edge.

C.4. Principal Variables and Arrays Used in the Programme

DEDTE	Distance, along lower surface, to start of trailing edge curvature.
DSTTE	Distance, along upper surface, to start of trailing edge curvature.
ICAMB	1 if a cambered section is input, 0 if a camber-thickness distribution is input.
ISEC	1 for an isolated section, 2 for a cascade.
M	Surface point lying nearest to leading edge stagnation.
N	Half the number of pivotal points on the section surface.
NI	Number of chord positions at which data is input in the case of camber-thickness input, OR, Number of upper and lower surface points given, in the case of a ready-cambered section input.
NINC	Number of incidences to be solved for.
NS	Number of source elements in separated region.
NSEPL	Lower separation point in terms of final surface point numbering.
NSEPU	Upper separation point in terms of final surface point numbering.
NSL	Number of lower surface slots.
NSTOR	1 is data for boundary layer calculation is to be stored, 0 if not.
NSU	Number of upper surface slots.
NXL	Number of points on lower surface.
NXU	Number of points on upper surface.
RK	Factor to control point spacing at trailing edge. $RK < 1.0$ for closer spacing.
STAG	Cascade stagger (Radians).
T	Cascade pitch (Fraction of chord).
XEDTE YEDTE	X-Y coordinates of end of trailing edge curvature.
XSTTE YSTTE	X-Y coordinates of start of trailing edge curvature.

Arrays

CHORD Chord fractions at data input points for camber-thickness data input.

CPL Lower surface pressure coefficients.

CPU Upper surface pressure coefficients.

DSL Distance of lower surface slots along lower surface.

DSU Distance of upper surface slots along upper surface.

GAMA Two-dimensional array containing vortex density solutions.

KARAY Two-dimensional coefficient matrix.

RINC Incidences for which the pressure distributions are to be found
(Radians).

SOU Densities of sources in separated region.

TSL Thickness of lower surface slots.

TSU Thickness of upper surface slots.

XL Distances of lower surface points along lower surface.

XU Distances of upper surface points along upper surface.

XLS Lower surface input coordinate for cambered section data input.
YLS

XUS Upper surface input coordinates for cambered section data input.
YUS

XSL X-Y coordinates of lower surface slots.
YSL

XSU X-Y coordinates of upper surface slots.
YSU

YCAMB Camber values at data input points for camber-thickness data input.

YTHICK Half-thickness values at data input points for camber-
thickness data input.


```

135  FORMAT(6I3)
      WRITE(2,150)NSEPU,NSEPL
150  FORMAT(' ', 'SEPARATED REGION BETWEEN POINTS', I4, ', ', I4)
      IF(NSU.EQ.0)GOTO175
      READ(1,180)(XSU(I),YSU(I),TSU(I),I=1,NSU)
      DO170I=1,NSU
        WRITE(2,188)XSU(I),YSU(I),TSU(I)
170  CONTINUE
175  IF(NSL.EQ.0)GOTO184
      READ(1,180)(XSL(I),YSL(I),TSL(I),I=1,NSL)
180  FORMAT(3F8.0)
      DO182I=1,NSL
        WRITE(2,188)XSL(I),YSL(I),TSL(I)
182  CONTINUE
184  READ(1,186)TERAD,XSTTE,YSTTE,XEDTE,YEDTE
186  FORMAT(5F8.0)
188  FORMAT(' ', 'SLOT AT X=', F8.6, 2X, 'Y=', F8.6, 4X, 'THICKNESS=', F8.6)
      WRITE(2,190)TERAD,XSTTE,YSTTE,XEDTE,YEDTE
190  FORMAT(' ', 'TRAILING EDGE RADIUS =', F8.4/
*      ' ', 'STARTING AT X =', F8.4, 3X, 'Y =', F8.4/
*      ' ', 'ENDING AT X =', F8.4, 3X, 'Y =', F8.4/
*      ' ', 'ON UNSTAGGERED SECTION')
      REALN=FLOAT(N)
      NT2=2*N
      NM1=N-1
      NT2M2=NT2-2
      RNT2=FLOAT(NT2)
      PI=3.141592654
      PD3N=PI/(3.0*REALN)
      DNPI =REALN/PI.
      NT2M1=NT2-1
      NS=NSEPU-NSEPL+1
      IF(NSEPU.LT.N)NS=NSEPU+NT2M1-NSEPL
      NTOT=NT2+NS
      NTOTM1=NTOT-1
      NTOTP1=NTOT+1
      NZM=NT2-NSEPU

```

```
NMP1=NTOT=NSEPU+1
NM=NT2-NSEPL
NSUM1=NSEPU-1
NSLP1=NSEPL-1
```

```
C
C*****CHAPTER 2
C BUILD UP PROFILE AND SMOOTH SURFACE COORDINATES
C
```

```
IF(ICAIB.EQ.1)CALL CAMPROF(REALN,N1,RK,NT2)
IF(ICAIB.EQ.0)CALL CANTHIK(REALN,N1,RK,NT2)
C---USE DXDFI AND DYDFI AS TEMPORARY STORAGE
DO200I=1,NT2
  DXDFI(I)=XSURF(I)
  DYDFI(I)=YSURF(I)
200 CONTINUE
DO205I=1,NT2
  CALL I1234(NT2,I,I1,I2,I3,I4)
  XSURF(I)=(-DXDFI(I1)+4.0*DXDFI(I2)+6.0*DXDFI(I)
    +4.0*DXDFI(I3)-DXDFI(I4))/12.0
  YSURF(I)=(-DYDFI(I1)+4.0*DYDFI(I2)+6.0*DYDFI(I)
    +4.0*DYDFI(I3)-DYDFI(I4))/12.0
205 CONTINUE
WRITE(2,210)
210 FORMAT('0','UNSTAGGERED SURFACE COORDINATES'//25X,'X',15X,'Y'//)
DO215I=1,NT2
  WRITE(2,220)I,XSURF(I),YSURF(I)
215 CONTINUE
220 FORMAT(13,17X,F9.6,8X,F9.6)
C---ADJUSTMENT OF SLOT AT TRAILING EDGE (IF ANY)
IF(NSU.EQ.0)GOTO300
IF(XSU(NSU).NE.-1.0)GOTO300
XSU(NSU)=XSURF(NT2)
YSU(NSU)=YSURF(NT2)
```

```
C
C*****CHAPTER 3
C APPLY STAGGER
```

C---ROTATE PROFILE ABOUT LEADING EDGE FOR STAGGER

C
C

300 IF((ISEC.EQ.1),OR.(STAG.EQ.0.0))GOTO400

CS=COS(STAG)

SN=SIN(STAG)

DO305I=1,NT2

X1=XSURF(I)*CS-YSURF(I)*SN

Y1=YSURF(I)*CS+XSURF(I)*SN

XSURF(I)=X1

YSURF(I)=Y1

305 CONTINUE

C---STAGGER SLOT X-COORDS AND TRAILING EDGE LIMITS

DO310I=1,NSU

XSU(I)=XSU(I)*CS=YSU(I)*SN

310 CONTINUE

DO315I=1,NSL

XSL(I)=XSL(I)*CS=YSL(I)*SN

315 CONTINUE

XSTTE=XSTTE*CS=YSTTE*SN

XEDTE=XEDTE*CS=YEDTE*SN

C---PRINTOUT STAGGERED SURFACE COORDINATES

320 WRITE(2,325)

325 FORMAT('0','STAGGERED SURFACE COORDINATES'//25X,'X',15X,'Y'//)

DO330I=1,NT2

WRITE(2,220)I,XSURF(I),YSURF(I)

330 CONTINUE

C

C*****CHAPTER 4

C

DXDFI,DYDFI,D2XDFI2,D2YDFI2

C

C

400 DO405I=1,NT2

CALL I1234(NT2,I,I1,I2,I3,I4)

DXDFI(I)=(DNPI/12.0)*(XSURF(I1)+8.0*XSURF(I2)+8.0*XSURF(I3)
-XSURF(I4))

1

DYDFI(I)=(DNPI/12.0)*(YSURF(I1)+8.0*YSURF(I2)+8.0*YSURF(I3)


```

1
405 CONTINUE
DO410I=1,NT2
CALL I1234(NT2,I,I1,I2,I3,I4)
D2XDFI(I)=(DNPI/12.0)*(DXDFI(I1)+8.0*DXDFI(I2)+8.0*DXDFI(I3)
1
1
1 D2YDFI(I)=(DNPI/12.0)*(DYDFI(I1)+8.0*DYDFI(I2)+8.0*DYDFI(I3)
-DXDFI(I4))
-DYDFI(I4))
410 CONTINUE

```

```

C
C*****CHAPTER 5
C CONVERSION FACTORS RELATING SOURCE AND VORTEX
C DENSITIES TO SURFACE SPEEDS
C AND SURFACE POINT IDENTIFICATION OF SOURCES
C BUILD ARRAY FOR CONVERSION FROM VORTEX DENSITIES TO SPEEDS
C
C

```

```

C
C DO500I=1,NT2
C BOT(I)=SQRT(DXDFI(I)*DXDFI(I)+DYDFI(I)*DYDFI(I))
500 CONTINUE
C RECORD POSITIONS OF SOURCES IN NSOU
C*****NOTE ORDERING OF SOURCE ELEMENTS*****
C** ACW AROUND SURFACE; STARTING **
C** AT POINT 1 **
C
C J=0
C DO510I=1,NT2
C IF(I,LE.NSEPL.AND.I,GE.NSEPU)GOTO510
C IF(I,GE.NSEPL.AND.I,GE.NSEPU.AND.VSEPU,GT.N)GOTO510
C IF(I,LE.NSEPL.AND.I,LE.NSEPU.AND.NSEPU,GT.N)GOTO510
C J=J+1
C NSOU(J)=I
510 CONTINUE

```

```

C
C*****CHAPTER 6
C MATRIX ELEMENTS
C
C

```

```

      GOTO(600,625),ISEC
C---ISOLATED SECTION
600  DO620I=1,NT2
      J1=NT2
      DO615J=1,NT2
          IF(I.EQ.J)GOTO605
          R1=XSURF(I)-XSURF(J)
          R2=YSURF(I)-YSURF(J)
          IF(J.EQ.NT2-I)GOTO610
          ARAY(I,J)=(R1*DYDFI(I)-R2*DXDFI(I))/(R1*R1+R2*R2)
          GOTO610
605  R3=DXDFI(I)*D2YDFI(I)-DYDFI(I)*D2XDFI(I)
          ARAY(I,J)=(0.5*R3/(DXDFI(I)*DXDFI(I)+DYDFI(I)*DYDFI(I)))
          *                                     =REALN
610  IF(J.NE.NSOU(J1-NT2+1))GOTO615
          J1=J1+1
          IF(I.EQ.J)GOTO615
          ARAY(I,J1)=(R2*DYDFI(I)+R1*DXDFI(I))/(R1*R1+R2*R2)
615  CONTINUE
620  CONTINUE

```

GOTO 650

```

C---INFINITE CASCADE
625  PDT=PI/T
      PDNT=PI/(REALN*T)
      PD2NT=PDNT*0.5
      PT2DT=PDT*2.0
      DO645I=1,NT2
          J1=NT2
          DO640J=1,NT2
              R1=(XSURF(I)-XSURF(J))*PT2DT
              R2=(YSURF(I)-YSURF(J))*PT2DT
              IF(J.EQ.NT2-I)GOTO635
              IF(I.EQ.J)GOTO630
              R3=EXP(R1)
              R4=1.0/R3
              R5=0.5*(R3+R4)
              R6=0.5*(R3-R4)

```

```

R7=PD7*(R5*DYDFI(I)-DXDFI(I)*SIN(R2))
ARAY(I,J)=R7/(R6-COS(R2))
GOTO635
630 R8=0.5*(DXDFI(I)*D2YDFI(I)-DYDFI(I)*D2XDFI(I))
ARAY(I,J)=R8/(DXDFI(I)*DXDFI(I)+DYDFI(I)*DYDFI(I))-REALN
635 IF(J.NE.NSOU(J1=NT2+1))GOTO640
J1=J1+1
IF(I.EQ.J)GOTO640
S1=0.5*R1
S2=0.5*R2
IF(ABS(SIN(S2)).LT.1.0E-30)S2=1.0E+30
S3=EXP(S1)
S4=1.0/S3
S5=0.5*(S3+S4)
IF(ABS(S5).LT.1.0E+30)S5=1.0E+30
S6=0.5*(S3+S4)
S7=S6/S5
S8=S7*S7
S9=COS(S2)/SIN(S2)
S10=S9*S9
S11=PD7*(S9*(1.0+S8)*DYDFI(I)+S7*(1.0+S10)*DXDFI(I))
ARAY(I,J1)=S11/(S8+S10)
640 CONTINUE
645 CONTINUE
650 CONTINUE

```

```

C
C*****CHAPTER 7
C---LOWER MEAN VALUES
C
DO710I=1,NT2
REP=0.0
DO700I1=1,NT2
IF((I.EQ.NT2).AND.(I1.EQ.NT2))GOTO700
IF(I1.EQ.NT2-I)GOTO700
REP=REP+ARAY(I1,I)
700 CONTINUE
IF(I.EQ.NT2)GOTO705

```



```

      IF(I, EQ, NT2) GOTO 705
      ARAY(NT2-1, I) = REP
      GOTO 710
705  ARAY(NT2, NT2) = REP
710  CONTINUE
C      BUILD U VECTORS INTO ARRAY
      DO 715 I=1, NT2
      ARAY(I, NTOT+1) = -RNT2 * DXDFI(I)
      ARAY(I, NTOTP1+1) = -RNT2 * DVDFI(I)
715  CONTINUE
C
C*****CHAPTER 8
C---UPPER TRIANGULARISE LHS OF MATRIX
C  ROW INTERCHANGE UNNECESSARY SINCE LEADING DIAGONAL
C      ALWAYS LARGE
C
      DO 810 I=1, NT2M1
      IP1=I+1
      DO 805 J=IP1, NT2
      RMULT=ARAY(J, I)/ARAY(I, I)
      DO 800 K1=I, NTOTP1+2
      ARAY(J, K1)=ARAY(J, K1)-ARAY(I, K1)*RMULT
800  CONTINUE
805  CONTINUE
810  CONTINUE
C
C*****CHAPTER 9
C---SOLVE FOR TWO INCIDENT FLOW RHS'S AND HOMOGENEOUS SOLN
C
      DO 900 I4=1, 3
      CALL SOLVE(I4)
900  CONTINUE
C
C*****CHAPTER 10
C
      DAMP=0.7
      WRITE(2, 950) DAMP

```

```

950  FORMAT(1,1,DAMPING FACTOR =1,F6.4)
C
C
C-----10/A
C---THIS CHAPTER LOOPED FOR EACH INCIDENCE
C
      DO1088I2=1,NINC
C
      ALPH1=RINC(I2)
      THETA=ALPH1
      ALPH2=ALPH1
      VELUS=1.0
      VELDS=1.0
C
      IT=0
C
C-----10/B
1000  IT=IT+1
C      BUILD RHS DUE TO SOURCES
C---LET FIRST APPROX TO SOURCES BE ZERO
      DO 1010I=1,NT2
          RHS(I)=0.0
          DO1005J=NT2+1,NTOT
              RHS(I)=RHS(I)-ARRAY(I,J)*SOU(J-NT2)
1005  CONTINUE
1010  CONTINUE
C
C-----10/C
C
C      SOLVE FOR THIS RHS
      CALL SOLVE(4)
      SNTA=SIN(THETA)
      CSTA=COS(THETA)
C
C-----10/D
C

```

```

C      SUM SOLUTIONS 1,2 AND 4
      DO1015 I=1,NT2
          GAMA(I,5)=GAMA(I,1)*CSTA+GAMA(I,2)*SNTA+GAMA(I,4)
1015  CONTINUE
C
C-----10/E
C
C      CONVERT SOLUTIONS 3 AND 5 AND SOURCES INTO SPEEDS
      CALL SPEED(1)
C
C-----10/F
C
C---FIND CIRCULATION TO BE ADDED
      C=-(GAMA(NSEPL,5)+GAMA(NSEPU,5))/(GAMA(NSEPU,3)+GAMA(NSEPL,3))
      DO1020 I=1,NT2
          GAMA(I,5)=GAMA(I,5)+C+GAMA(I,3)
1020  CONTINUE
C
C-----10/G
C
C---TEST FOR CONVERGENCE
      IENDIT=0
      DO1025 I=1,NS
          IF(ABS(GAMA(NSOU(I),5)**2+SOU(I)**2-GAMA(NSEPU,5)**2)
            *
            .GT.0.001)GOTO1030
1025  CONTINUE
      IENDIT=1
      GOTO1040
C
C-----10/H
C      NEW APPROX TO SOURCE STRENGTHS
1030  DO1035 I=1,NS
          DIF=GAMA(NSEPU,5)**2-GAMA(NSOU(I),5)**2
          IF(DIF.LT.0.0)DIF=0.0
          SOU(I)=DAMP+SOU(I)+(1.0-DAMP)*SQRT(DIF)
1035  CONTINUE
C

```



```

C-----10/I
C---RECONVERT SOURCES AND GAMAS 3,5 INTO VORTEX DENSITIES
1040 CALL SPEED(2)
C---CALCULATE NEW INLET ANGLE
IF(ISEC.EQ,1)GOTO1050
J=0
SSUM=0.0
GSUM=0.0
DO1045I=1,NT2
  GSUM=GSUM+GAMA(I,5)
  IF(I.NE.NSOU(J+1))GOTO1045
  J=J+1
  SSUM=SSUM+SOU(J)
1045 CONTINUE
VGAMU=-PD2NT*GSUM
USQUU=-PD2NT*SSUM
TNAL1=TAN(ALPH1)
TNAL1S=TNAL1*TNAL1
UTTMV=VGAMU-TNAL1*USQUU
TERM=1.0-UTTMV*UTTMV+TNAL1S
IF(TERM.GE.0.0)GOTO1046
THETA=THETA-PI/10.0
IF(THETA.GT.PI/2.0)GOTO1090
SNTH=SIN(THETA)
GOTO1049
1046 TERM=TNAL1*SQRT(TERM)
SNTH1=(=UTTMV+TERM)/(1.0+TNAL1S)
SNTH2=(=UTTMV-TERM)/(1.0+TNAL1S)
RESID1=TNAL1*SQRT(1.0-SNTH1*SNTH1)-SNTH1-UTTMV
RESID2=TNAL1*SQRT(1.0-SNTH2*SNTH2)-SNTH2-UTTMV
IF(ABS(RESID1).GT.ABS(RESID2))GOTO1047
RESID=RESID1
SNTH=DAMP*SIN(THETA)+(1.0-DAMP)*SNTH1
GOTO1049
1047 RESID=RESID2
SNTH=DAMP*SIN(THETA)+(1.0-DAMP)*SNTH2
1049 THETA=ASIN(SNTH)

```

```
CSTH=SQRT(1.0-SNTH*SNTH)
VELUS=SQRT((SNTH+VGAMU)**2+(CSTH+USOUU)**2)
```

```
C-----10/K
```

```
C
1050 WRITE(2,1051)IT
1051 FORMAT(1 1,'ITERATION',15,5X,'POINT',10X,'SOURCE STRENGTHS')
DO1055I=1,NS
WRITE(2,1060)NSOU(I),SOU(I)
1055 CONTINUE
1060 FORMAT(1 1,20X,13,13X,F10.6)
THETAD=THETA*180.0/PI
WRITE(2,1062)THETAD,VGAMU,USOUU
1062 FORMAT(1 1,'INCIDENT FLOW ANGLE THETA =',F8.4/
* 1 1,'VGAMU =',F8.4,3X,'USOUU =',F8.4)
WRITE(2,1063)C
1063 FORMAT(1 1,'CIRCULATION CONSTANT C =',F8.4)
IF(IT.GT.30)GOTO1064
IF(IENDIT.EQ.0)GOTO1000
GOTO1068
1064 WRITE(2,1066)
1066 FORMAT(1 1,'MORE THAN THIRTY ITERATIONS ATTEMPTED')
GOTO1090
```

```
C-----10/L
```

```
C
C OUTLET ANGLE
1068 IF(ISEQ.EQ.1)GOTO1072
TNAL2=(SNTH-VGAMU)/(CSTH-USOUU)
ALPH2=ATAN(TNAL2)
VELDS=SQRT((SNTH+VGAMU)**2+(CSTH-USOUU)**2)
WRITE(2,1070)
1070 FORMAT(1 1,'COEFFICIENTS BASED ON U.S. VELOCITY')
```

```
C-----10/M
```

```
C
C---SOLVE FOR CP'S AND FORCES
```

```

1072 J=0
      DO1076 I=1,NT2
        GAMA(I,5)=GAMA(I,5)/VELUS
        CPFACT=GAMA(I,5)*GAMA(I,5)
        IF(NS.EQ.0)GOTO1074
        IF(I.NE.NSOU(J+1))GOTO1074
        J=J+1
        SOU(J)=SOU(J)/VELUS
        CPFACT=CPFACT+SOU(J)*SOU(J)
1074   CPFACT=CPFACT/(BOT(I)*BOT(I))
        CP(I)=1.0-CPFACT
1076   CONTINUE
        S1=0.0
        S2=0.0
        S3=0.0
        S4=0.0
        DO1078 I=2,NT2,2
          S1=S1+CP(I)*DXDFI(I)
          S2=S2+CP(I-1)*DXDFI(I-1)
          S3=S3+CP(I)*DYDFI(I)
          S4=S4+CP(I-1)*DYDFI(I-1)
1078   CONTINUE
        CX=-PD3N*(2.0*S3+4.0*S4)
        CY= PD3N*(2.0*S1+4.0*S2)
C-----10/N
C---WRITE CPIS, FORCES, ANGLES
C
      ALPH1D=ALPH1*180.0/PI
      ALPH2D=ALPH2*180.0/PI
      WRITE(2,1080)ALPH1D,ALPH2D,VELUS,VELD3,CX,CY
1080   FORMAT('0','ALPHA1 =',F8.3,1X,'DEG'/ ' ', 'ALPHA2 =',F8.3,1X,'DEG'/
*         ' ', 'UPSTREAM SPEED =',F9.4,5X,'DOWNSTREAM SPEED =',F9.4/
*         ' ', 'CX =',F8.4/' ', 'CY =',F8.4/)
      WRITE(2,1082)
1082   FORMAT(' ',10X,'POINT',15X,'CP',16X,'S(=1-CP)')

```



```

      S=1.0-CP(1)
      WRITE(2,1086)I,CP(1),S
1084  CONTINUE
1086  FORMAT(1 1,8X,15,2(13X,F8.4))
      IF(NSTOR.EQ.1)CALL DISTANCE
1088  CONTINUE
C
1090  STOP
      END

```

C
C
C

```

SUBROUTINE SPEED(NTRIG)
COMMON/A/NT2M1,ARAY(64,90),NTOTM1,NT2,GAMA(64,5),
*      NT2M2,NSEPU,NSEPL,JP,BOTP,BOT(64),RHS(64)
COMMON/B/NSOU(30),SOU(30)
J=0
DO10I=1,NT2
  FACT=BOT(I)
  IF(NTRIG.NE.0.1)FACT=1.0/FACT
  GAMA(I,5)=GAMA(I,5)*FACT
  GAMA(I,3)=GAMA(I,3)*FACT
  IF(I.NE.NSOU(J+1))GOTO10
  J=J+1
  SOU(J)=SOU(J)*FACT
10  CONTINUE
      RETURN
      END

```

C
C
C

```

SUBROUTINE SOLVE(I5)
COMMON/A/NT2M1,ARAY(64,90),NTOTM1,NT2,GAMA(64,5),
*      NT2M2,NSEPU,NSEPL,JP,BOTP,BOT(64),RHS(64)
      IF(I5.EQ.4)GOTO25
      NTOT=NTOTM1+1
      DO20I=1,NT2

```

```

      RHS(I)=ARAY(I,NTOT+15)
20  CONTINUE
C   SPECIFY GAMMA VALUE AT POINT 2N
25  GAMA(NT2,15)=0.0
      IF(15.EQ.3.OR.15.EQ.4)GAMA(NT2,15)=1.0
C   BACK SUBSTITUTION FOR GAMMA VALUES
      DO40 I=1,NT2M1
        I1=NT2-I
        SUM=0.0
        DO30 I2=I1+1,NT2
          SUM=SUM+ARAY(I1,I2)*GAMA(I2,15)
30  CONTINUE
        SUM=RHS(I1)=SUM
        GAMA(I1,15)=SUM/ARAY(I1,I1)
40  CONTINUE
      RETURN
      END

```

C
C
C

```

      SUBROUTINE DISTANCE
C---SUBROUTINE TO CALCULATE DISTANCES ALONG
C---UPPER AND LOWER SURFACES
C

```

```

      DIMENSION XU(60),XL(60),CPU(60),CPL(60),DSU(10),DSL(10)
      COMMON XSURF(64),YSURF(64),PI,N
      COMMON/A/NT2M1,ARAY(64,90),NTOTM1,NT2,GAMA(64,5),
*          NT2M2,NSEPU,NSEPL,JP,BOTP,BOT(64),RHS(64)
      COMMON/C/CP(64),DXDFI(64),DYDFI(64),D2XDFI(64),D2YDFI(64),
1          XSU(10),XSL(10),TSL(10),TSU(10),
2          REALN,NM1,XSTTE,XEDTE,TERAD,NSL,NSU

```

C
C-----DS/A
C

```

      NSLC=0
      NSUC=0
      DISTU=0.0

```

```

DISTU=0.0
DISTL=0.0
DO1030M=NM1,NT2M2
  IF((CP(M).GT.CP(M-1)).AND.(CP(M).GT.CP(M+1)))GOTO1035
1030 CONTINUE
C---CP(M) IS NEAREST TO STAGNATION
1035 CPU(1)=CP(M-1)
  CPL(1)=CP(M+1)
C-----DS/B
C---UPPER SURFACE
C
  DFI=PI/REALN
  DO1060I=2,M
    JU=M+I+1
    D1=DXDFI(JU)*DXDFI(JU)+DXDFI(JU)*D2XDFI(JU)*DFI
1      +0.25*D2XDFI(JU)*D2XDFI(JU)*DFI*DFI
    D2=DYDFI(JU)*DYDFI(JU)+DYDFI(JU)*D2YDFI(JU)*DFI
1      +0.25*D2YDFI(JU)*D2YDFI(JU)*DFI*DFI
    DLU=DFI*SQRT(D1+D2)
      IF(JU.GT.N)GOTO1050
      IF((TERAD.EQ.0.0).OR.(DSTTE.NE.0.0))GOTO1037
      IF(XSURF(JU-1).LT.XSTTE)GOTO1037
1037  DSTTE=DISTU+(XSTTE-XSURF(JU))*DLU/(XSURF(JU-1)-XSURF(JU))
      IF(NSUC.EQ.NSU)GOTO1050
      IF(JU.EQ.1)GOTO1040
      IF(XSURF(JU-1).LT.XSU(NSUC+1))GOTO1050
      NSUC=NSUC+1
1      DSU(NSUC)=DISTU+(XSU(NSUC)-XSURF(JU))*DLU/
        (XSURF(JU-1)-XSURF(JU))
      GOTO1037
C-----DEAL WITH ANY UPPER SURFACE SLOT BETWEEN 1 AND 2N.
1040  NSUC=NSUC+1
1      DSU(NSUC)=DISTU+(XSU(NSUC)-XSURF(1))*DLU/
        (XSURF(NT2)-XSURF(1))
      GOTO1037
1050  DISTU=DISTU+DLU
      XU(I)=DISTU

```



```

      IF(JU.EQ,1)JU=NT2+1
      CPU(I)=CP(JU=1)
C---LOWER SURFACE
      JL=M+I-1
      IF((JL.GE.NSEPU.AND.NSEPU.GT.N).OR.JL.GE.NT2)GOTO1060
      D1=DXDFI(JL)*DXDFI(JL)+DXDFI(JL)*D2XDFI(JL)*DFI
      1      +0.25*D2XDFI(JL)*D2XDFI(JL)*DFI*DFI
      D2=DYDFI(JL)*DYDFI(JL)+DYDFI(JL)*D2YDFI(JL)*DFI
      1      +0.25*D2YDFI(JL)*D2YDFI(JL)*DFI*DFI
      DLL=DFI*SQRT(D1+D2)
      IF((TERAD.EQ.0.0).OR.(DEDTE.NE.0.0))GOTO1053
      IF(XSURF(JL+1).LT.XEDTE)GOTO1053
      DEDTE=DISTL+(XEDTE-XSURF(JL))*DLL/(XSURF(JL+1)-XSURF(JL))
      1053  IF(NSLC.EQ.NSL)GOTO1055
      IF(XSURF(JL+1).LT.XSL(NSLC+1))GOTO1055
      NSLC=NSLC+1
      DSL(NSLC)=DISTL+(XSL(NSLC)-XSURF(JL))*DLL/
      1      (XSURF(JL+1)-XSURF(JL))
      GOTO1053
      1055  DISTL=DISTL+DLL
      XL(I)=DISTL
      CPL(I)=CP(JL+1)
      1060  CONTINUE
C-----DS/C
      NSLU=0
C---CONSIDER UPPER SURFACE BEYOND T.E.,
      DO1070I=1,NT2-NSEPL
      NS=NT2-I+1
      D1=DXDFI(NS)*DXDFI(NS)+DXDFI(NS)*D2XDFI(NS)*DFI
      1      +0.25*D2XDFI(NS)*D2XDFI(NS)*DFI*DFI
      D2=DYDFI(NS)*DYDFI(NS)+DYDFI(NS)*D2YDFI(NS)*DFI
      1      +0.25*D2YDFI(NS)*D2YDFI(NS)*DFI*DFI
      DLU=DFI*SQRT(D1+D2)
      1063  IF(NSL.EQ.(NSLC+NSLU))GOTO1065
      IF(XSURF(NS-1).GT.XSL(NSL=NSLU))GOTO1065
      NSUC=NSUC+1
      DSU(NSUC)=DISTU+(XSURF(NS)-XSL(NSL=NSLU))*DLU/

```

```

          DSU(NSUC)=DISTU+(XSURF(N5)-XSL(NSL-NSLU))*DLU/
1          (XSURF(N5)-XSURF(N5-1))
          TSU(NSUC)=TSL(NSL-NSLU)
          NSU=NSU+1
          NSLU=NSLU+1
          GOT01063
1065     DISTU=DISTU+DLU
          XU(M+I)=DISTU
          CPU(M+I)=CP(N5-1)
1070     CONTINUE
          NSL=NSL-NSLU
          NXU=M+NT2-NSEPL
          NXL=NT2-M
          IF(NSEPU.GT.N)NXL=NSEPU-M
          ISEPU=M-NSEPU
          IF(NSEPU.GT.N)ISEPU=M+NT2-NSEPU
          ISEPL=NSEPL-M
          WRITE(2,1080)
1080     FORMAT('0',1,'SURFACE DISTANCES'/1,' ',18X,'XU',10X,'CPU',15X,
*          'XL',10X,'CPL'/)
          DO1110 I=1,NXU
          WRITE(2,1120) I,XU(I),CPU(I),XL(I),CPL(I)
1110     CONTINUE
1120     FORMAT(' ',2X,13,10X,F8.4,5X,F8.4,10X,F8.4,5X,F8.4)
          WRITE(6,1130)NXL,NSL,ISEPL
          WRITE(6,1140)(XL(I),I=1,NXL),(CPL(I),I=1,NXL),(DSL(I),I=1,NSL),
*          (TSL(I),I=1,NSL)
          WRITE(6,1140)TERAD,DSTTE,DEDTE
          WRITE(6,1130)NXU,NSU,ISEPU
          WRITE(6,1140)(XU(I),I=1,NXU),(CPU(I),I=1,NXU),(DSU(I),I=1,NSU),
*          (TSU(I),I=1,NSU)
1130     FORMAT(' ',3I3)
1140     FORMAT(' ',5F10.6)
          RETURN
          END

```

C

```

SUBROUTINE I1234(NT2,I,I1,I2,I3,I4)
IF((I.NE.1).AND.(I.NE.2))I1=I-2
IF(I.EQ.1)I1=NT2-1
IF(I.EQ.2)I1=NT2
IF(I.NE.1)I2=I-1
IF(I.EQ.1)I2=NT2
IF(I.EQ.NT2)I3=1
IF(I.NE.NT2)I3=I+1
IF((I.NE.NT2).AND.(I.NE.NT2-1))I4=I+2
IF(I.EQ.NT2)I4=2
IF(I.EQ.NT2-1)I4=1
RETURN
END

```

C
C
C

C FOR INPUT OF PROFILES DEFINED BY CAMBER AND THICKNESS

```

SUBROUTINE CAMTHIK(REALN,N1,RK,NT2)
COMMON XSURF(64),YSURF(64),PI,N
DIMENSION CHORD(58),YCAMB(58),YTHICK(50),DXCDN(54),DYDXFI(33),
1 DYCDX(54),D2YCDX(50),CAMBL(50),PHIIN(50),YCFI(33),YTFI(33),
2 XFI(33)

```

```

NP1=N+1
N1P2=N1+2
N1P4=N1+4
N1P6=N1+6
READ(1,110)(CHORD(I),I=5,N1P4)
READ(1,110)(YCAMB(I),I=5,N1P4)
READ(1,110)(YTHICK(I),I=1,N1)

```

110

```

FORMAT(5F12.0)
DO120I=1,4
CHORD(I)=2.0-CHORD(10-I)
CHORD(N1P4+I)=-CHORD(N1P4-I)
YCAMB(I)=-YCAMB(10-I)
YCAMB(N1P4+I)=-YCAMB(N1P4-I)

```

120

```

CONTINUE

```



```

C---LIST INPUT COORDINATES
      WRITE(2,130)
130  FORMAT(12X,'X',20X,'CAMBER',8X,'1/2-THICKNESS',/)
      DO140I=1,N1
      WRITE(2,150)CHORD(I+4),YCAMB(I+4),YTHICK(I)
140  CONTINUE
150  FORMAT(F17.6,F23.6,F17.6)
C---CAMBER GRADIENTS AT INPUT POINTS
      DO160I=3,N1D6
      DXCDN(I-2)=CHORD(I-2)-8*CHORD(I-1)+8*CHORD(I+1)-CHORD(I+2)
      DYCDN      =YCAMB(I-2)-8*YCAMB(I-1)+8*YCAMB(I+1)-YCAMB(I+2)
      DYCDX(I-2)=DYCDN/DXCDN(I-2)
160  CONTINUE
      DO170I=3,N1D2
      G= DYCDX(I-2)=8*DYCDX(I-1)+8*DYCDX(I+1)-DYCDX(I+2)
      D2YCDX(I-2)=G/DXCDN(I)
170  CONTINUE
      DO180I=1,N1
      DYCDX(I)=DYCDX(I+2)
      CHORD(I)=CHORD(I+4)
      YCAMB(I)=YCAMB(I+4)
180  CONTINUE
C---CALCULATE LENGTHS ALONG CAMBER LINE AT INPUT POINTS
      RL=0.0
      DO190I=1,N1
      J=N1-I+1
      IF(J.NE.N1)GOTO183
      DX=0.0
      DL=0.0
      GOTO185
185  DX=CHORD(J)-CHORD(J+1)
      DL=1.0+DYCDX(J+1)**2+DX*DYCDX(J+1)+D2YCDX(J+1)
      DL=DL*0.25+DX*DX*D2YCDX(J+1)+D2YCDX(J+1)
      DL=DX*SQRT(DL)
      RL=RL+DL
185  CAMBL(J)=RL
190  CONTINUE

```

```

DO200I=1,N1
  CAMBL(I)=CAMBL(I)/RL
200 CONTINUE
C--=CALCULATE VALUES OF PHI AT INPUT POINTS
DO220I=1,N1
  CAMBL(I)=CAMBL(I)*(1.0+(1.0-RK)*CAMBL(I)*(1.0-CAMBL(I)))
  CSPHI=2.0*CAMBL(I)-1.0
  IF(CSPHI.NF.=1.0)GOTO210
  PHIIN(I)=PI
  GOTO220
210 PHIIN(I)=ATAN(ABS((SQRT(1.0-CSPHI*CSPHI))/(CSPHI+1.0E-50)))
  IF(CSPHI.GE.0.0)GOTO220
  PHIIN(I)=PI-PHIIN(I)
220 CONTINUE
C--=INTERPOLATE IN PHI FOR YC,YT,DYDX,X
DO255I=1,NP1
  PHI=FLOAT(I-1)*PI/REALN
  DO245I1=2,N1
    IF(PHIIN(I1-1).NE.PHI)GOTO230
    XFI(I)=CHORD(I1-1)
    YCFI(I)=YCAMB(I1-1)
    YTFI(I)=YTHICK(I1-1)
    DYDXFI(I)=DYCDX(I1-1)
    GOTO255
230 IF(PHIIN(I1).NE.PHI)GOTO240
    XFI(I) =CHORD(I1)
    YCFI(I) =YCAMB(I1)
    YTFI(I) =YTHICK(I1)
    DYDXFI(I)=DYCDX(I1)
    GOTO255
240 IF(PHIIN(I1).LT.PHI.OR.PHIIN(I1-1).GT.PHI)GOTO245
    CALL LAGINT(I1,PHIIN,PHI,S1,S2,S3,S4,N1,L)
    XFI(I) =S1*CHORD(L-4)+S2*CHORD(L-3)+S3*CHORD(L-2)
    +S4*CHORD(L-1)
    YTFI(I) =S1*YTHICK(L-4)+S2*YTHICK(L-3)+S3*YTHICK(L-2)
    +S4*YTHICK(L-1)
    YCFI(I) =S1*YCAMB(L-4)+S2*YCAMB(L-3)+S3*YCAMB(L-2)

```

```

1          DYDXFI(I)=S1*DYCDX(L-4)+S2*DYCDX(L-3)+S3*DYCDX(L-2)
1          +S4*DYCDX(L-1)
1          +S4*YCAMB(L-1)
1          GOT0255
245         CONTINUE
255         CONTINUE
C-->ADD THICKNESS NORMAL TO CAMBER
DO260I=2,N
  ATN=ATAN(DYDXFI(I))
  XSURF(I=1)=XFI(I)-YTFI(I)*SIN(ATN)
  XSURF(NT2-I+1)=2.0*XFI(I)-XSURF(I-1)
  YSURF(I=1)=YCFI(I)+YTFI(I)*COS(ATN)
  YSURF(NT2-I+1)=2.0*YCFI(I)-YSURF(I-1)
260        CONTINUE
  XSURF(N)=0.0
  YSURF(N)=0.0
  YSURF(NT2)=0.0
  XSURF(NT2)=1.0
  RETURN
  END
C
C
C
C-->INPUT OF CAMBERED SURFACE COORDINATES
SUBROUTINE CAMPROF(REALN,N1,RK,NT2)
COMMON XSURF(64),YSURF(64),PI,N
DIMENSION XUS(50),YUS(50),XLS(50),YLS(50),YMEAN(37),XFI(35),
*         DYDXFI(32)
  NM1=N-1
  READ(1,10)(XUS(I),YUS(I),I=1,N1)
  READ(1,10)(XLS(I),YLS(I),I=1,N1)
10  FORMAT(2F12.0)
  WRITE(2,12)
12  FORMAT('0','INPUT DATA','0',11X,'XU',10X,'YU',15X,'XL',10X,'YL'/)
  DO14I=1,N1
    WRITE(2,14)XUS(I),YUS(I),XLS(I),YLS(I)
14  CONTINUE

```



```

16  FORMAT(1,2(7X,F10.8,2X,F10.8))
    NP1=N+1
    NP2=N+2
    DO55 I=1,NM1
      PHI=FLOAT(I)*PI/REALN
      X=0.5*(1+COS(PHI))
      XFI(I+2)=X
      DO40 I1=2,N1
        IF(XUS(I1-1).NE.X)GOTO20
        YSURF(I)=YUS(I1-1)
        GOTO55
20    IF(XUS(I1).NE.X)GOTO30
        YSURF(I)=YUS(I1)
        GOTO55
30    IF((XUS(I1).GT.X).OR.(XUS(I1-1).LT.X))GOTO40
        CALL LAGINT(I1,XUS,X,S1,S2,S3,S4,N1,L)
        YSURF(I)=S1*YUS(L+4)+S2*YUS(L+3)+S3*YUS(L+2)+S4*YUS(L+1)
        GOTO55
40    CONTINUE
55  CONTINUE
    DO90 I=1,NM1
      X=XFI(I+2)
      DO80 I1=2,N1
        IF(XLS(I1-1).NE.X)GOTO60
        YSURF(N+2-I)=YLS(I1-1)
        GOTO90
60    IF(XLS(I1).NE.X)GOTO70
        YSURF(N+2-I)=YLS(I1)
        GOTO90
70    IF((XLS(I1).GT.X).OR.(XLS(I1-1).LT.X))GOTO80
        CALL LAGINT(I1,XLS,X,S1,S2,S3,S4,N1,L)
        YSURF(N+2-I)=S1*YLS(L+4)+S2*YLS(L+3)+S3*YLS(L+2)+S4*YLS(L+1)
        GOTO90
80    CONTINUE
90    CONTINUE
    XFI(2)=XUS(1)
    XFI(NP2)=XUS(N1)

```

```

XFI(NP2)=XUS(N1)
XFI(1)=2.0*XFI(2)-XFI(3)
XFI(N+3)=2.0*XFI(NP2)-XFI(NP1)
YSURF(NT2)=YUS(1)
YSURF(N)=YUS(N1)
C---MEAN LINE GRADIENTS
DO100I=1,N
  YMEAN(I+2)=0.5*(YSURF(I)+YSURF(NT2-I))
100 CONTINUE
  YMEAN(N+3)=2.0*YMEAN(NP2)-YMEAN(NP1)
  YMEAN(1)=2.0*YMEAN(2)-YMEAN(3)
  YMEAN(2)=YSURF(NT2)
DO110I=3,NP1
  DXDN=XFI(I-2)-8.0*XFI(I-1)+8.0*XFI(I+1)-XFI(I+2)
  DYDN=YMEAN(I-2)-8.0*YMEAN(I-1)+8.0*YMEAN(I+1)-YMEAN(I+2)
  DYDXFI(I-2)=DYDN/DXDN
110 CONTINUE
DO120I=1,NM1
  ALF=ATAN(DYDXFI(I))
  DX=(YMEAN(I+2)-YSURF(NT2-I))*SIN(ALF)*COS(ALF)
115 XSURF(I)=XFI(I+2)-DX
  XSURF(NT2-I)=XFI(I+2)+DX
C---CHECK THAT DX DOES NOT MOVE THE POINT TOO FAR
IF((XSURF(I).GT.XFI(I+3)).AND.(XSURF(I).LT.XFI(I+1)))GOTO120
DX=0.75*DX
GOTO115
120 CONTINUE
XSURF(N)=XUS(N1)
XSURF(NT2)=XUS(1)
C---RE-INTERPOLATE FOR Y'S
DO160I=1,NM1
  X=XSURF(I)
DO150I1=2,N1
  IF(XUS(I1=1),NE,X)GOTO130
  YSURF(I)=YUS(I1-1)
  GOTO160
130 IF(XUS(I1),NE,X)GOTO140

```

```

        YSURF(I)=YUS(I1)
        GOTO160
140     IF((XUS(I1).GT.X).OR.(XUS(I1-1).LT.X))GOTO150
        CALL LAGINT(I1,XUS,X,S1,S2,S3,S4,N1,L)
        YSURF(I)=S1*YUS(L=4)+S2*YUS(L=3)+S3*YUS(L=2)+S4*YUS(L=1)
        GOTO160
150     CONTINUE
160     CONTINUE
        DO200I=1,NM1
            X=XSURF(NT2=I)
            DO190I1=2,N1
                IF(XLS(I1-1).NE.X)GOTO170
                YSURF(NT2=2)=YLS(I1-1)
                GOTO200
170     IF(XLS(I1).NE.X)GOTO180
                YSURF(NT2=I)=YLS(I1)
                GOTO200
180     IF((XLS(I1).GT.X).OR.(XLS(I1-1).LT.X))GOTO190
                CALL LAGINT(I1,XLS,X,S1,S2,S3,S4,N1,L)
                YSURF(NT2-I)=S1*YLS(L=4)+S2*YLS(L=3)+S3*YLS(L=2)+S4*YLS(L=1)
                GOTO200
190     CONTINUE
200     CONTINUE
        RETURN
        END

```

```

C
C
C
C---LAGRANGE INTERPOLATION FOR DATA INPUT SECTIONS
SUBROUTINE LAGINT(I1,FIORX,VAR,S1,S2,S3,S4,N1,L)
DIMENSION FIORX(50)
M=2
IF(I1.NE.2)GOTO10
M=3
GOTO20
10  IF(I1.NE.N1)GOTO20
M=1

```



```

20  S=1.0
    S1=1.0
    S2=1.0
    S3=1.0
    S4=1.0
    L=I1+M
    DO30 J=1,4
        S=S*(VAR-FIORS(L+J-S))
30  CONTINUE
    DO40 J=1,4
        IF(J.EQ.4)GOTO32
        S1=(FIORS(L-4)-FIORS(L-J))*S1
32  IF(J.EQ.3)GOTO34
        S2=(FIORS(L-3)-FIORS(L-J))*S2
34  IF(J.EQ.2)GOTO36
        S3=(FIORS(L-2)-FIORS(L-J))*S3
36  IF(J.EQ.1)GOTO40
        S4=(FIORS(L-1)-FIORS(L-J))*S4
40  CONTINUE
    S1=(S/S1)/(VAR-FIORS(L-4))
    S2=(S/S2)/(VAR-FIORS(L-3))
    S3=(S/S3)/(VAR-FIORS(L-2))
    S4=(S/S4)/(VAR-FIORS(L-1))
    RETURN
    END
    FINISH

```

APPENDIX D

THE BOUNDARY LAYER COMPUTER PROGRAMME

BLAYER

D.1. Introduction

This Appendix describes the computer programme constructed to implement the boundary layer calculation method outlined in Chapter 6. The programme, written in FORTRAN, was constructed specifically to calculate boundary layer development on aerofoil surfaces, although the model is flexible and could readily be applied to other flows.

D.2. Preliminary Outline

An outline flowchart of the boundary layer calculation procedure is given in Figure 65. The FORTRAN programme relies heavily on the use of subroutines, the section controlling the process depicted in Figure 65 being quite short. Units of the Système International are used throughout.

All details concerning the surface pressure distribution, starting conditions, surface curvature and the position of any tangential blowing slots are input as data. The pressure distribution under which the boundary layer develops is defined by a set of discrete pressure coefficients and the associated distances along the surface. The calculation of pressure gradients is performed in the programme. If a tangential blowing slot is present, an iterative calculation is performed to find the blowing momentum necessary to maintain flow attachment up to the specified separation point.

A starting velocity profile is generated using the wake function of Coles⁽¹⁰⁷⁾: values of boundary layer thickness and displacement thickness at the starting position need to be provided in the input data, although the resulting boundary layer development is not usually very sensitive to the starting profile.

When the computer programme was constructed, the facility to calculate stagnation enthalpies was included. This would enable, for example, the prediction of heat transfer from a hot boundary or the effect of using a hot blowing jet. The expressions for wall functions and the solution of the stagnation enthalpy conservation equation which are included in the programme have been taken from or constructed with reference to the text of Patankar and Spalding⁽⁹⁹⁾. It is stressed, however, that this aspect of the programme has not been tested and may yet require development. No further reference to the sections of programme dealing with this calculation will be made in this Appendix.

The programme controlling segment and the subroutines are described in the following sections.

D.3 Description of Programme

MAIN

This main section controls the overall programme operation as depicted in Figure 65. Data is read according to the format of Figure 66 and definitions of the variables are included in Section D4. Flow conditions in the free-stream are defined by the Reynolds number (RE), Mach number (RMACH) and total temperature (TO). The Reynolds number and surface distances contained in array XS are based on unit chord. The free stream speed on which the pressure coefficients are based is given by $U_{\infty} = M\sqrt{\gamma RT_{\infty}}$ and various other quantities, T_{∞} , ρ_{∞} , P_{∞} are calculated from normal compressible flow expressions. When interpolating for certain fluid properties from tabulated values, it is assumed that the flow temperature T_{∞} lies in the range $300 < T_{\infty} < 400$ K. The free-stream laminar viscosity, VISCL, is calculated from Sutherland's equation, see Schlichting⁽¹³⁾, p.339.

The free-stream properties are written out and values are assigned to the slot blowing momentum coefficient, CMEW (a first approximation), and the slot air total temperature, SLTTO. The pressure coefficients are converted into pressures. Headings are then printed to define quantities printed out on each step forward if these values are required. The overall thickness and displacement thickness, Y(NM1) and DISPT, of the starting profile is read. These values are later used in Subroutine COLES to generate a starting profile. The variable NPOS defines the current position of the calculation within the set of input data. Values of distance along the surface have already been input in array XS and the starting value of x (XST) has been specified. NPOS is the element of array XS which lies closest to x, with the condition $XS(NPOS) \leq x$.

The initial value of NPOS is found in MAIN, and is updated in Subroutine PGDT when the calculation reaches the next data input point. The starting value of pressure coefficient, CPST, is calculated by linear interpolation in XS and CPST is then used to obtain the local surface flow speed, USTART.

Subroutine COLES is called, to generate a starting profile. Subroutine DMS is then called to calculate integral profile parameters: displacement and momentum thicknesses and the shape factor, H.

The next section is looped on each forward step. The step length DX is governed by a factor DXF provided in the input data:

$$dx = \frac{Y(N-1) DXF}{1+10 \left| \frac{\tau_{W-} - \tau_W}{\tau_{W-}} \right|}$$

τ_W = latest calculated wall stress,

τ_{W-} = previously calculated wall stress.

Thus, the step length is linked to the overall boundary layer thickness, Y(NM1). This in itself is not sufficient, however, since the layer thickness increases rapidly near separation where small step lengths are required because of the rapidly changing layer properties. Therefore the step length is also factored by a term dependent upon the magnitude of change in the wall shear stress.

The trigger value IPOINT is set to zero or unity: the latter value is assigned if the step length is such as to carry the calculation

beyond the next input data position, $XS(NPOS+1)$. If IPOINT is unity, the step length is modified so that the step brings the calculation to the next input data point.

A test is then made to see if the selected step length brings the calculation to a blowing slot. If so, Subroutine SLOT is called to set the new profile. Subroutine PGDT is called to calculate the longitudinal pressure gradient over the forward step. A test is made to check if the surface is curved at the downstream station, i.e. if $X + DX \geq DCURV$. If so, Subroutine NORPRES is called to calculate the variation of pressure and of longitudinal pressure gradient across the shear layer thickness. A call is made to Subroutine SOLVE which takes the forward step and sets all the boundary layer properties to their new values. If the new position of the calculation coincides with an input data point, i.e. if IPOINT=1, Subroutine DMS is called to calculate the profile integral parameters. This subroutine is called on every step if the intermittency representation of effective viscosity is being used.

The final section comprises a series of tests on whether separation has occurred and the resulting course of action to be taken. In cases where high flow accelerations and decelerations occur, such as on the leading edge of an aerofoil developing high lift, separation may be predicted in this region. If this occurs, the whole calculation is re-started at the predicted separation point. This final section is best described by a flowchart, sketched in Figure 67.

Subroutine SOLVE

This subroutine performs the actual forward step, solving the finite difference equations which govern the boundary layer development. Before the step, however, various ancillary calculations are performed and subroutines are called to supply quantities required for the step.

The first section is concerned with predicting transition and is only accessed if the boundary layer is currently laminar ($LT = 1$) and transition is to be allowed ($NTRIG3 = 2$). The prediction of transition utilizes data given by Schlichting⁽¹³⁾. First, a shape factor, Λ (SHAPEA) is calculated $\Lambda = \frac{\delta^2}{\mu U} \frac{dP}{dx}$. The local critical Reynolds number, $RCRIT$, is plotted as a function of this shape factor by Schlichting. The relationship has been represented by a polynomial for the present purposes. The actual local Reynolds number, RBL , is calculated, where $RBL = \frac{U\delta^*}{\nu}$. The point of laminar instability, $XINST$, is taken to be the first point at which $RBL \geq RCRIT$. The distance between the point of instability and transition is represented by the difference between the momentum thickness Reynolds numbers at the two stations. Schlichting gives a plot of this difference as a function of the parameter \bar{K} where

$$\bar{K} = \frac{1}{x_{tr} - x_i} \int_{x_i}^{x_{tr}} \frac{\theta^2}{\mu U} \frac{dP}{dx} dx,$$

$x_i = XINST$ and x_{tr} is the position of transition. The integral \bar{K} is added to on each forward step after the point of instability has been reached and the corresponding value of momentum thickness Reynolds number at transition calculated. If the actual local value exceeds this transition value then transition is assumed to occur.

Velocity gradients are calculated and the subroutine for calculating laminar viscosities, LAMFLO, is called. Provided the flow is turbulent, one of the two effective viscosity routines, MLH or TURB is called. The viscosities in array EMU are then factored by r/dy and transferred into array EMURDY.

The entrainment rate, characterised by the quantity $r_{E\dot{m}E}''$ in the nomenclature of Patankar and Spalding is calculated from the expression

$$r_{E\dot{m}E}'' = \frac{-\mu_{N-1}}{(y_N - y_{N-1})} \left(\frac{r_N}{r_E}\right) - \frac{\mu_{N/2}}{(2y_N - y_{N/2} - y_{N/2+1})} \left(\frac{r_{N/2}}{r_E}\right)$$

which is of a form suggested by the above authors. Since it is convenient to be able to treat grid line N-1 as characterising properties at the outer edge of the boundary layer, i.e. where $y = \delta$, the entrainment is factored by

$$\left(0.99 + \left|\frac{U_N - U_{N-1}}{U_N}\right|\right)^2$$

This arrangement maintains the condition $U_{N-1} = 0.99 U_N$ fairly well.

A call is made to Subroutine WF which supplies the wall functions used as boundary conditions to the main calculation. The remainder of the subroutine deals with the solution of the finite difference equations. Almost all the nomenclature in this section has been taken directly from the listing given by Patankar and Spalding who provide a comprehensive programme description. The only changes of significance

which have been made to their solution procedure concern modifications to certain coefficients. These modifications arise because the equations being solved here concern angular rather than linear momentum and the unknown radius \times velocity product ur is being solved for, rather than the velocity u . The necessary changes to the finite-difference coefficients correspond to those given by Patankar and Spalding for the solution of the equation governing the swirl velocity of an axi-symmetrical flow. Other minor alterations occur as a logical consequence of the change of variable and are best appreciated by reference to the text quoted above.

Subroutine WF

This subroutine supplies wall functions to be used as boundary conditions for the main solution procedure. The functions used are quite simple and pertain to a smooth wall. Two alternative sections are provided, depending on whether the outer boundary of this wall region extends into the turbulent flow or if the flow can be considered wholly laminar. Experience shows that better results are obtained by grouping the grid lines sufficiently densely near the wall that laminar functions can be used.

The magnitude of the local couette flow Reynolds number, RE , is used to decide whether laminar functions are used, or if the logarithmic law for turbulent flow is to be employed. The expressions used to calculate the wall functions may all be found in the text by Patankar and Spalding.

Subroutine PGDT

This subroutine calculates the longitudinal pressure gradient from the discrete pressures supplied as input data. The gradient is calculated from four Taylor expansions about the mean position over the step, that is at $x + \frac{1}{2}dx$. The four data points used are comprised of two on either side of the station $x + \frac{1}{2}dx$ except near the start or end of the input data, when it becomes necessary to use three points on one side of $x + \frac{1}{2}dx$ and one on the other. The resulting 4×4 matrix of the simultaneous equations is solved by Gauss reduction to give P and dP/dx at $x + \frac{1}{2}dx$.

If IPOINT has been set to unity in MAIN, signifying that the step will bring the calculation to the next data point, NPOS is incremented by one.

Subroutine NORPRES

The longitudinal pressure gradient corresponding to the input pressure data is calculated in subroutine PGDT, described above. Subroutine NORPRES calculates the distribution of pressure and longitudinal pressure gradient across a curved boundary layer. The expressions used are

$$\frac{\partial P}{\partial y} = \frac{\rho U^2}{r} \quad \text{and} \quad \left(\frac{\partial P}{\partial x}\right)_i = \left(\frac{\partial P}{\partial x}\right)_E - \frac{\partial}{\partial x} \int_E^i \frac{\rho U^2}{r} dy$$

or

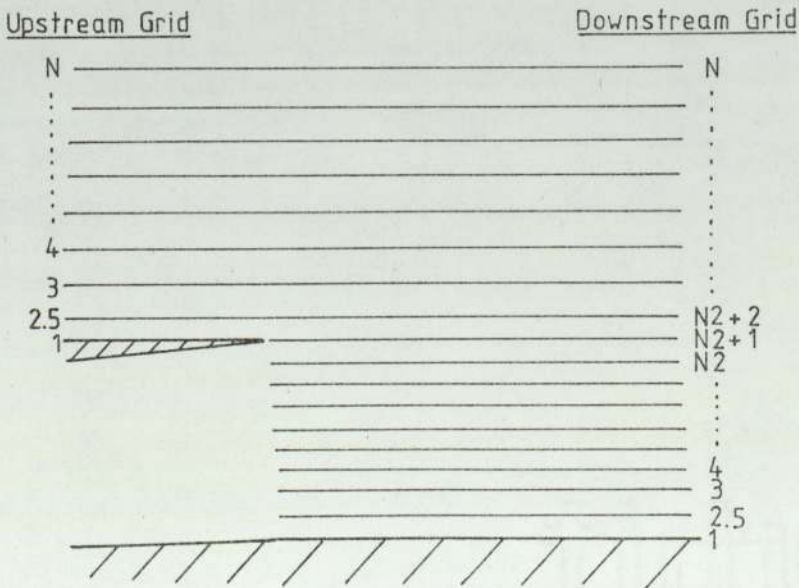
$$P_i = P_E - \int_E^i \frac{\rho U^2}{r} dy$$

where subscript 'E' refers to conditions at the outer flow boundary.

On the first occasion that this subroutine is accessed, preliminary array values are set and the opportunity is taken to set the values of r , the radius of curvature of each grid line. On the first call to this subroutine, therefore, no gradient of pressure is calculated.

Subroutine SLOT

This subroutine is provided to generate a tangential blowing jet profile and to add this profile underneath the oncoming boundary layer. Because the required blowing rate generally is not known in advance and this routine is used several times in an iterative loop, the oncoming boundary layer profile has to be stored on the first cycle. This storage is performed in the first section of this subroutine, the stored values being suffixed by '0'. N_2 is the number of grid lines to be used for the blowing jet profile, so that the total number of grid lines become $N = N_0 + N_2$ where N_0 is the number of grid lines used to calculate the upstream boundary layer. The grid line numbering system is sketched below.



Sketch D1

Grid Line Numbering at a Blowing Slot

The blowing jet profile is set according to a power law, as shown in Figure 8. In the programme, Q represents the exponent, n, and is supplied in the input data. The grid spacing across the slot width is set by a cosine profile to group the grid lines most closely near the regions of large velocity gradient.

The remainder of the subroutine is concerned with re-assigning all the variables to their new grid lines. One forward step is made from within the subroutine so that all the boundary layer properties are calculated for each grid line ready for the printing out of properties in the call to Subroutine OUTPUT.

Subroutine COLES

The starting profile is generated in this subroutine. Values of boundary layer thickness and displacement thickness have already been read from the input data and the surface speed at the starting position of the calculation, USTART, has been derived in MAIN. These quantities are used to generate a starting profile using the function derived by Coles⁽¹⁰⁷⁾.

The remainder of the subroutine assigns starting values to all the necessary variables.

Subroutine MLH

This subroutine calculates an eddy viscosity distribution using a simple mixing length representation. In the near-wall region, Van Driest's damping factor is applied. If the surface is curved locally, Subroutine CURVE is called to factor the eddy viscosities by a curvature correction.

Subroutine TURB

This subroutine can be used to calculate the distribution of eddy viscosity across a conventional boundary layer or across a wall jet profile. At present it is only used for wall jet profiles, since ordinary boundary layers are coped with quite adequately by the mixing length model which is also more computationally efficient.

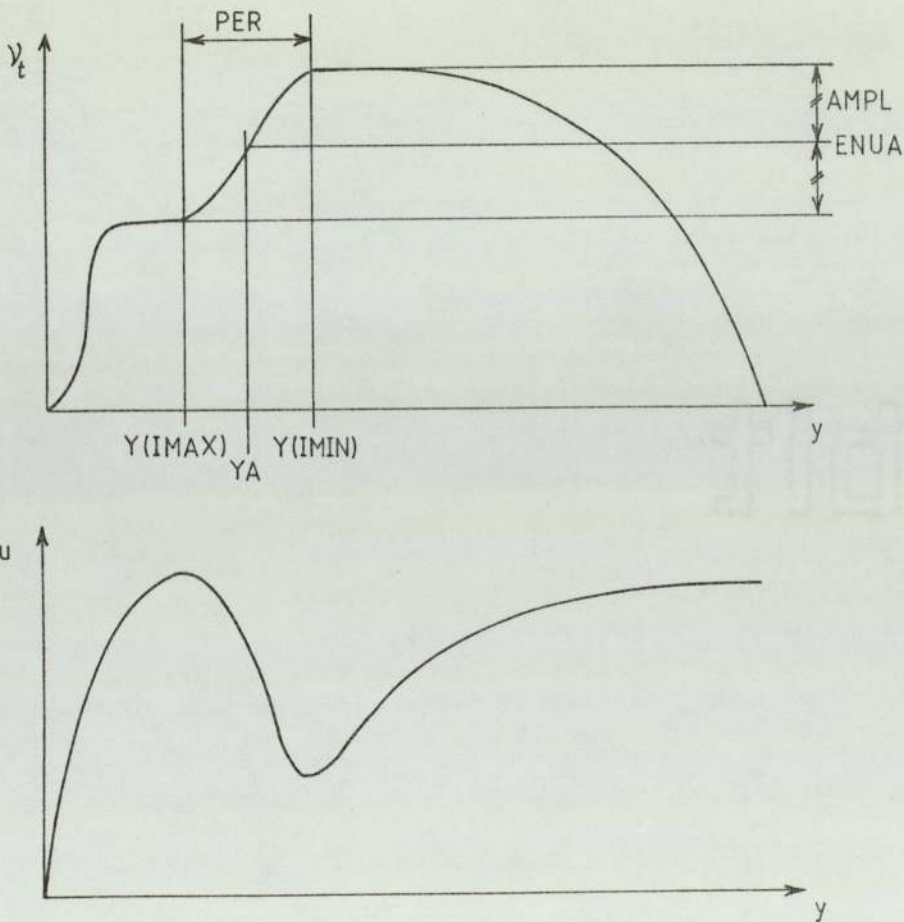
First, the type of velocity profile is identified, JET being set to 0, 1 or 2 depending on whether the profile is a conventional boundary layer, a wall jet with a maximum only in velocity or a wall jet with a maximum and a minimum in velocity.

The velocity defect, U_d , is then found for the relevant profile. For a conventional boundary layer, the point of departure from the law of the wall, YD , is found first. All the expressions used are given in Chapter 6. The inner region viscosities are calculated using the mixing length model with the Van Driest damping factor. Values are assigned to σ , SIGMA, the standard deviation of the intermittency profile. The diffusion equation parameters, K and X in equation 6.5 are set. These quantities are defined by RK1 and DEL respectively in this subroutine. The position of the mean turbulent front, \bar{y} , is calculated from the relevant equation, 6.7, 6.10 or 6.11.

The error function defined by equation 6.8 is calculated at each grid point in the appropriate region. A polynomial representation of the error function is used. The effective viscosities are then set according to equation 6.9. If the surface is curved, Subroutine CURVE is called to factor the calculated eddy viscosities by a curvature correction,

If JET = 1 or 2, a cosine fairing is used to join the inner and outer eddy viscosity profiles. Sketch D2 below illustrates the nomenclature used to 'fair' in the JET=2 profile. The procedure used for the Jet=1 profile is very similar.

Finally, some of the quantities generated in the subroutine are printed out.



Sketch D2

Cosine Profile Used to Join Inner and Outer Eddy Viscosity Regions

Subroutine CURVE

The curvature correction described in Chapter 6 is applied to a calculated eddy viscosity when this subroutine is called from MLH or TURB. A lag equation is applied to the curvature effect, using the same lag equation constants as are applied in TURB to the development of the maximum eddy viscosity. The curvature factor itself is limited to an obvious limit of zero when reducing the eddy viscosity and a limit of 2.0 when increasing the eddy viscosity.

Subroutine DMS

Integral profile parameters are calculated in this subroutine. The displacement thickness, DISPT, and momentum thickness, TMTM, are obtained by numerical integration across the latest profile. The shape factor, SHAPE, is the quotient of these two quantities.

Subroutine LAMFLO

This subroutine simply assigns laminar viscosities to each grid point, using Sutherland's equation. The values are then modified so that $EMU(i)$ represents the mean viscosity between grid points i and $i+1$.

Subroutine OUTPUT

This subroutine is called from various points within the programme to provide an output of current variables. If the argument NTRIG is set to zero, one line of values is output. If $NTRIG = 1$, a full output of the current profile properties is given. There is also an automatic full output every twenty five steps.

D.4. Principal Variables and Arrays Used in the Boundary Layer Programme

Variables

CMEW	Jet momentum coefficients.
CPST	Pressure coefficient at starting position of boundary layer calculation.
DCURV	Distance along surface of start of curvature.
DISPT	Displacement thickness of boundary layer.
DX	Step length.
DXF	Factor to control step length.
IENTH	1 for solution of heat transfer equations, 0 for no calculation.
IPOINT	1 if step brings calculation to next data point, otherwise 0.
ISEP	Position of specified separation in input data (for blowing jet calculation).
N	Number of grid lines.
NM1	N-1.
NPOS	Position of calculation in input data (see discussion of MAIN).
NS	Number of blowing slots (currently assumed to be 1 or 0).
NTRIG1	1 for use of mixing length representation of eddy viscosity, 2 for intermittency.
NTRIG2	Currently unused.
NTRIG3	1 for calculation of laminary boundary layer only, 2 to allow transition.
NTRIG4	1 for storage of displacement at each data input point, 0 for no storage.
NTRIG5	1 for laminar start to calculation, 2 for turbulent start.

NX Number of input data points at which pressure coefficients
 and surface distances are given.

Q Exponent n in power law representation of blowing jet profile.

RE Mainstream flow Reynolds number.

RMACH Mainstream flow Mach number.

SLTTO(zero) Total temperature of blowing jet.

TO(zero) Mainstream flow stagnation temperature.

TERAD Radius of curvature of surface
 (set to zero if no curvature).

U Local free-stream flow speed at start of calculation.

VISCL Laminar viscosity in free-stream.

X Current x-direction position of calculation.

XST Starting position of calculation.

Arrays

CP Pressure coefficients at data input points.

DPDX Pressure gradient at each grid point.

DS Distance of each slot along surface.

DUDY Velocity gradient at each grid point.

EMU Effective viscosity at each grid point.

HO(H zero) Stagnation enthalpy at each grid point.

OM Omega value at each grid point.

P Static pressure at each grid point.

PREF Effective Prandtl number at each grid point.

R Radius of curvature of streamline at each grid point.

RHO Fluid density at each grid point.

RUR Product of radius of curvature, flow speed and density
 at each grid point.

TS Width of each blowing slot.

U Flow speed in x-direction at each grid point.

- UR Product of flow speed and radius of curvature at each
 grid point,
- XS Distance along surface of each blowing set.
- Y Distance, normal to surface, of each grid point.

```

MASTER BLAYER
C
C
C*****SEGMENT MAIN
C
C
C      DIMENSION DS(10),TS(10),XS(70),PS(70),
1      DELT(70),CP(70)
C      COMMON/A/DUDY(75),EMU(75),HO(75),OM(75),PREF(75),RHO(75),RU(75),
C      TEMP(75),U(75),Y(75),EMURDY(75),TAU(75),R(75),UR(75),
C      BPI,OMI,PEI,TAUI,YI,R25,KRAD,IRAD
C /B/DPDX(75),P(75),CAIR,DX,HOINIT,IENTH,LT,N,NM1,NPOS,NSTEP,
C      PI,PR,RUS,TERAD,VISCL,X,DCURV,SLTX,SLTY,NSCAN,LAG
C /G/DISPT,SHAPE,TMTM
C /D/AK,ALMG,FR
C /E/NTRIG1,NTRIG2,NTRIG3
C*****PROGRAMME CONTROL*****
C      CONSTANTS AND DATA INPUT
C
C-----1-REYNOLDS NO. BASED ON UNIT CHORD
C      ASSUMED TEMP RANGE = 300-400 K.
C
C      FR=0.01
C      ALMG=0.09
C      AK=0.435
C--=READ STORED DATA
C      READ(1,17)NX,NS,ISEP
C      READ(1,10)(XS(I),I=1,NX),(CP(I),I=1,NX),(DS(I),I=1,NS),
C      *      (TS(I),I=1,NS)
C      READ(1,10)TERAD,DCURV
C      READ(1,10)XST
C      READ(1,10)DXF,RE,TO,RMACH
C      IF(NS.NE.0)READ(1,10)Q
10      FORMAT(5F10.6)
C      NTRIG1=1 FOR ML, 2 FOR INTERMITTENCY
C      3=1 FOR LAMINAR LAYER ONLY, 2 TO ALLOW TRANSITION
C      4=1 FOR STORAGE OF DISPTS, 0 FOR NO STORAGE
C      5=1 FOR LAMINAR START, 2 FOR TURBULENT START

```

```

17 READ(1,17)N,IENTH,NTRIG1,NTRIG2,NTRIG3,NTRIG4,NTRIG5
   FORMAT(7I3)
   NM1=N-1
   TINF=T0/(0.2*RMACH*RMACH+1.0)
   VEL=RMACH*SQR(1.4*287.0*TINF)
   VISCL=0.0001962*((325.0+110.0)/(TINF+110.0))*(TINF/325.0)**1.5
   RO=VISCL*RE/VEL
   RUSQH=0.5*VEL*VEL*RO
   PINF=RO*287.0*TINF
   PO=PINF*(1.0+0.2*RMACH*RMACH)**0.2857
   PR=0.707*(0.688-0.707)*(TINF-300.0)/100.0
C-----TAKE TURBULENT PRANDTL NO. = 0.9
   PRT=0.9
   CAIR=1004.9+(1013.5-1004.9)*(TINF-300.0)/100.0
   HOINIT=CAIR*T0
   EMU(1)=VISCL
20 WRITE(6,20)RE,T0,RMACH,TINF,VEL,RO,PINF,PR,PRT,CAIR
   FORMAT(' ',RE=' ',F10.0,'/ ',T0=' ',F6.1,'/ ',RMACH NO=' ',F6.3,
1      '/ ',TSTATIC=' ',F6.1,'/ ',UPSTREAM VEL=' ',F6.2,
2      '/ ',DENSITY=' ',F6.3,'/ ',STATIC PRESSURE=' ',F8.0,
3      '/ ',PRANDTL NO=' ',F6.4,5X,TURBULENT VALUE=' ',F6.4,
4      '/ ',CP=' ',F8.1)
   IF(NTRIG1.EQ.2)GOTO24
   WRITE(6,22)
22  FORMAT('0','MIXING LENGTH USED FOR TURBULENT FLOW')
   GOTO28
24  WRITE(6,26)
26  FORMAT(' ','INTERMITTENCY USED FOR TURBULENT FLOW')
C----SLOT BLOWING MOMENTUM COEFFICIENT AND TOTAL TEMP
28  CMEW=0.05
   SLTTO=T0
C
C----CONVERT CP VALUES INTO SURFACE PRESSURES
   DO30I=1,NX
   IF(I.GT.5.AND.I.LT.NX-3)GOTO29
   PS(I)=PINF+RUSQH*CP(I)
   GOTO30

```



```

29     PS(I)=PINF+RUSQH*(-CP(I-2)+4.0*CP(I-1)+6.0*CP(I)+4.0*CP(I+1)
*       -CP(I+2))/12.0
30     CONTINUE
      WRITE(6,35)
35     FORMAT('0','SURFACE PRESSURES'//10X,'X',9X,'PI)
      DO40I=1,NX
        WRITE(6,50)I,XS(I),PS(I)
40     CONTINUE
50     FORMAT(' ',I2,3X,F7.4,4X,F10.1)
      WRITE(6,55)TERAD,DCURV
55     FORMAT('0','SURFACE CURVATURE =',F6.4,2X,'AT',F6.4,2X,
1       'ALONG SURFACE')
      IF(NS.EQ.0)GOTO58
      DO58I=1,NS
        WRITE(6,62)DS(I),TS(I)
58     CONTINUE
62     FORMAT('0','SLOT AT X =',F8.4,5X,'WIDTH =',F8.6)
C
C-----WRITE OUT HEADINGS
C
      WRITE(2,65)
65     FORMAT('0','NSTEP',5X,'X',8X,'DX',7X,'TAUI',6X,'DPDX',6X,'PEI',
1       5X,'SHAPE',5X,'DISPTC',/!' ',55X,'JET',3X,'HI',4X,'UDI',
2       5X,'YDC',3X,'SIGHAC',2X,'YDIC',4X,'UDI',1X,'SIGMAIC',
3       2X,'HI',4X,'PEI')
C
C---SET SURFACE STARTING VELOCITY PROFILE
      READ(1,10)Y(N),DISPT
      EMU(1)=VISCL
      LT=1
      X=XST
      IF(X.GE.DCURV)KRAD=1
      R(1)=TERAD
      IF(R(1).EQ.0.0)R(1)=1.0
      IF(NTRIG5.EQ.2)LT=2
70     DO75I=2,50
        IF(XS(I).GT.X)GOTO80

```

```

75  CONTINUE
80  NPOS=I-1
    CPST=CP(NPOS)+(X-XS(NPOS))*(CP(NPOS+1)-CP(NPOS))
    / (XS(NPOS+1)-XS(NPOS))
85  USTART=VEL*SQRT(1.0-CPST)
    U(N)=USTART
    CALL COLES(TINF,PS,NX,XS)
    CALL DMS
    DELT(1)=DISPT
    WRITE(2,90)
90  FORMAT('0',' STARTING PROFILE')
C---STEP LENGTH TO COINCIDE WITH SURFACE POINTS
C
C          *****
C  THIS SECTION LOOPED FOR EACH FORWARD STEP
C          *****
C
95  DX=(Y(N)*DXF)/(1.0+10.0*ABS((TAUO=TAUI)/TAUI))
    IF(NSTEP.EQ.0)DX=DISPT
    TAUO=TAUI
    IPOINT=0
    IF((X+DX).LT.XS(NPOS+1))GOTO100
    DX=XS(NPOS+1)-X
    IPOINT=1
100  IF(ISLT.EQ.NS)GOTO105
    IP1=ISLT+1
    IF((X+DX).LT.DS(IP1))GOTO105
    SLTX=DS(IP1)
    SLTT=TS(IP1)
    UJMIN=0.5*VEL
    CALL SLOT(VEL,CHEW,ISLT,SLTTO,RO,DXF,Q)
105  CALL PGDT(PS,NX,XS,IPOINT)
C    IF TERAD IS A FUNCTION OF X, INSERT FUNCTION HERE
C
C
    IF((X+DX).GE.DCURV.AND.TERAD.NE.0.0)CALL NORPRES

```

```

CALL SOLVE(0,UJMIN)
IF(NSTEP.EQ.1)CALL OUTPUT(1)
IF(IPOINT.EQ.1.OR.NTRIG1.EQ.2)CALL DMS
IF(IPOINT.EQ.1)DELT(NPOS)=DISPT
IF(TAUI.LE.0.0)GOTO115
CALL OUTPUT(0)
IF(ABS(X-XS(ISEP)).GT.1.0E-08)GOTO95

```

C
C
C

C-----DECISION TO BE MADE WHEN SEPARATION PREDICTED
C-----OR END OF SURFACE REACHED

```

WRITE(6,110)
110 FORMAT('0','NO SEPARATION')
IF(ISLT.EQ.0)GOTO135
CMEW=CMEW-0.0075
IF(CMEW.LT.0.005)GOTO135
X=DS(ISLT)
ISLT=ISLT-1
GOTO100
115 PSEP=P(1)
DXSEP=XS(ISEP)-X
WRITE(6,120)PSEP,X,NSTEP
120 FORHAT('0','SEPARATION PRESSURE =',F8.4,5X,'AT X =',F8.4,
1 5X,'NSTEP=',I4)
CALL OUTPUT(1)
IF(ISLT.EQ.0)GOTO125
IF(ABS(DXSEP).LT.0.001)GOTO125
CMEW=CMEW*(1.0+25.0*DXSEP)
X=DS(ISLT)
ISLT=ISLT-1
GOTO100
125 IF(DXSEP.LT.0.8.AND.LT.EQ.2)GOTO135
WRITE(6,130)X
130 FORMAT('0','PREMATURE SEPARATION PREDICTED',5X,
1 'CALCULATION RESTARTED AT X =',F8.4)
LT=2

```



```

GOTO70
135 NDEL=NPOS
    IF(NTRIG4.NE.1)GOTO160
    WRITE(4,140)NDEL
    WRITE(4,150)(DELT(I),I=1,NDEL)
140  FORMAT(' ',13)
150  FORMAT(' ',5F10.6)
160  STOP
    END

```

C
C
C
C
C

SUBROUTINE TO TAKE FORWARD STEP

```

SUBROUTINE SOLVE(NTR,UJMIN)
DIMENSION AU(75),BU(75),CU(75),SU(75),SD(75),
1      AH(75),BH(75),CH(75)
COMMON/A/DUDY(75),EMU(75),HO(75),OH(75),PREF(75),RHO(75),RU(75),
C      TEMP(75),U(75),Y(75),EMURDY(75),TAU(75),R(75),UR(75),
C      BPI,OMI,PEI,TAUI,YI,R25,KRAD,IRAD
C /B/DPDX(75),P(75),CAIR,DX,HOINIT,IENTH,LT,N,NM1,NPOS,NSTEP,
C      PI,PR,RU3,TERAD,VISCL,X,DCURV,SLTX,SLTT,NSCAN,LAG
C /C/DISPT,SHAPE,TMTM
C /E/NTRIG1,NTRIG2,NTRIG3
IF(NTR.EQ.1)GOTO267

```

C-----TRANSITION CRITERION

```

130 IF(LT.EQ.2.OR.NTRIG3.EQ.1)GOTO150
    CALL DMS
    DEL=Y(NM1)
    IF(XINST.NE.0.0)GOTO134
    SHAPEA=-DEL*DEL*DPDX(N)/(U(N)*EMU(1))
    RCRIT=10.0**(2.8203+0.2454*SHAPEA+0.0049*SHAPEA**2
1      -0.0022*SHAPEA**3)
    IF(SHAPEA.GT.8.0)RCRIT=12000.0
    IF(SHAPEA.LT.-6.0)RCRIT=100.0
    RBL=U(N)*DISPT*RHO(N)/EMU(1)
    IF(RBL.LT.RCRIT)GOTO138

```

```

WRITE(6,133)X,SHAPEA
133 FORMAT('0','START OF INSTABILITY X =',F6.4,3X,'SHAPEA=',F8.4)
XINST=X
RTHETI=U(N)*TMTM*RHO(N)/EMU(1)
134 SUMK=SUMK-DX*TMTM*TMTH*DPDX(N)/(U(N)+EMU(1))
IF(XINST.EQ.X)GOTO138
BARK=SUMK/(X-XINST)
DELTKX=837.1+28834.2*BARK+684720.3*BARK*BARK+5.44E06*BARK**3
DELTX=U(N)*TMTH*RHO(N)/EMU(1)-RTHETI
IF(DELTX.LT.DELTKX)GOTO138
LT=2
WRITE(6,136)X
136 FORMAT('0','TRANSITION AT X =',F6.4)
138 CONTINUE
C-----DU/DY.
150 DO160I=2,NM1
      DUDY(I)=(U(I+1)-U(I))/(Y(I+1)-Y(I))
160 CONTINUE
C-----VISCOSITY AND PRANDTL NO.
C---CALCULATE SHEAR STRESSES
DO165I=2,NM1
      TAU(I)=EMU(I)*DUDY(I)
165 CONTINUE
      CALL LAMFLO
      IF(LT.EQ.1)GOTO170
      IF(NTRIG1.EQ.2)CALL TURB(RME)
      IF(NTRIG1.EQ.1)CALL MLH(RME)
C-----MODIFY EMU ARRAY.
170 DO180I=2,NM1
      EMURDY(I)=EMU(I)/(Y(I+1)-Y(I))
      EMURDY(I)=EMURDY(I)*0.5*(R(I)+R(I+1))
180 CONTINUE
C-----ENTRAINMENT CONTROL.
C*****ENTRAINMENT CONTROL SPECIFIED HERE*****
RME=-EMURDY(NM1)-0.5*EMU(N/2)*R(N/2)/(Y(N)-Y(N/2))
RME=RME*(0.99+ABS((UR(N)-UR(NM1))/UR(N)))**2
IF(LT.EQ.1)RME=-EMURDY(NM1)*(1.99+UR(NM1)/UR(N))**2

```

```

C-----WALL FUNCTIONS
  CALL WF(T1,FDIFI,T1F)
  IF(IENTH.EQ.0)GOTO206
C-----SOURCE TERMS FOR ENTHALPIES
C-----USE SD FOR TEMPORARY STORAGE
  DO203I=2,NM1
    S5=U(I)*U(I)
    S6=U(I+1)*U(I+1)
    S D(I)=EMURDY(I)*(S6-S5)
203  CONTINUE
    S D(1)=0.0
  DO205I=2,NM1
    T=(1.0-1.0/PREF(I))*0.5
    SU(I)=(S D(I)-S D(I=1))*T
205  CONTINUE
  DO206I=2,NM1
    SD(I)=0.0
206  CONTINUE
C
C-----PRELIMINARIES FOR COEFFICIENTS.
  PX=PEI/DX
  G=RME
  PD8=0.125*PX
  PD4=0.25*PX
  PG=PX+G
  PGD8=0.125*PG
  PGD4=PGD8+PGD8
  GD4=0.25*G
  BOMP=OM(3)=OM(2)
  PGOMP=PGD4*BOMP
  P4OMP=PD4*BOMP
  TPGD4=0.75*PG
C-----BOUNDARY COEFFICIENTS FOR VELOCITY.
  HLP=-GD4*(OM(2)+OM(3))
  AHLP=ABS(HLP)
  THLP=HLP+HLP
  TP=EMURDY(2)

```



```

TTP=TP+AHLP+ABS(TP-AHLP)
AD=TTP*(R25/R(3))**2-THLP-T1*(R(1)/R25)**2=PGOMP
BD=2.0*T1
CD=P4OMP*(3.0*UR(2)+UR(3))=DPDX(2)*0.5*YI*(R(1)+R25)
1      *(R(1)+R25)
DU=TTP*(R25/R(1))**2+T1+THLP+3.0*PGOMP
RP=R25
AU(2)=AD/DU
BU(2)=BD/DU
CU(2)=CD/DU
IF(IENTH.EQ.0)GOTO207

```

```

C-----BOUNDARY COEFFICIENTS FOR ENTHALPY
C-----FOR ZERO ENTHALPY FLUX ACROSS SURFACE

```

```

TPF2=TP/PREF(2)
TTPF=TTPF+AHLP+ABS(TPF2-AHLP)
ADF=TTPF-THLP-PGOMP+0.5*SD(2)
DF=ADF+PX*BOMP-2.0*SD(2)
TT=3.0*H0(2)+H0(3)
CDF=P4OMP*TT+2.0*SU(2)
AH(2)=ADF/DF
BH(2)=0.0
CH(2)=CDF/DF

```

```

C-----GENERAL COEFFICIENTS.
C-----VELOCITIES

```

```

207 DO208I=3,NM1
      BOMM=BOMP
      BOMP=OM(I+1)-OM(I)
      BOM=BOMM+BOMP
      BOMT3=BOM*3.0
      PGOMM=PGOMP
      PGOMP=PGD4*BOMP
      PBOM=PX*BOM
      THLM=THLP
      HLP=-GD4*(OM(I+1)+OH(I))
      THLP=HLP+HLP
      AHLP=ABS(HLP)

```

```

TTM=TPP
TP=EMURDY(I)
TTP=TP+AHLP+ABS(TP-AHLP)
RM=RP
RP=0.5*(R(I)+R(I+1))
AD=TTP*(RP/R(I+1))*2-THLP-PGOMP
BD=TTM*(RM/R(I-1))*2+THLM-PGOMM
CD=PD4*(BOMT3*UR(I)+BOMP*UR(I+1)+BOMM*UR(I-1))-
1      DPDX(I)*(Y(I+1)-Y(I-1))*R(I)*R(I)
DU=TTP*(RP/R(I))*2+TTM*(RM/R(I))*2+THLP-THLM+TPGD4*BOM
AU(I)=AD/DU
BU(I)=BD/DU
CU(I)=CD/DU
IF(IENTH.EQ.0)GOTO208

```

C-----ENTHALPIES

```

TTMF=TTPF
TPF=EMURDY(I)/PREF(I)
TTPF=TPF+AHLP+ABS(TPF-AHLP)
AD=TTPF-THLP-PGOMP
BD=TTMF+THLM-PGOMM
CD=PD4*(BOMT3*HO(I)+BOMP*HO(I+1)+BOMM*HO(I-1))
CD=CD+2.0*SU(I)
DF=AD+BD+PBOM-2.0*SD(I)
AH(I)=AD/DF
BH(I)=BD/DF
CH(I)=CD/DF

```

208 CONTINUE

C-----SOLVE FOR D/S U'S

```

UR(N)=UR(N)-DPDX(N)*R(N)*R(N)*DX/RU(N)
IF(UR(N).LT.UJMIN*R(N))UR(N)=UJMIN*R(N)
BU(2)=BU(2)+UR(1)+CU(2)
DO210I=3,NM1
  T=1.0-BU(I)*AU(I-1)
  AU(I)=AU(I)/T
  BU(I)=(BU(I)+BU(I-1)+CU(I))/T

```

210 CONTINUE

NEGV=0

```

DO220J=2,NM1
  I=N=J+1
  UR(I)=AU(I)*UR(I+1)+BU(I)
  IF(UR(I).GE.0.0.OR.I.EQ.2)GOTO220
  WRITE(6,215)I
215  FORMAT(' ', 'NEGATIVE VELOCITY, I=', I3)
      NEGV=1
      UR(I)=UR(I+1)
220  CONTINUE
      IF(NEGV.EQ.0)GOTO240
      WRITE(6,230)
230  FORMAT('0', 'TAUI SET NEGATIVE TO TERMINATE CALCULATION')
      TAUI=-1.0
240  IF(IENTH.EQ.0)GOTO265
C-----SOLVE FOR D/S ENTHALPIES
      BH(2)=BH(2)+HO(1)+CH(2)
      DO250I=3,NM1
          T=1.0-BH(I)*AH(I-1)
          AH(I)=AH(I)/T
          BH(I)=(BH(I)*BH(I-1)+CH(I))/T
250  CONTINUE
      DO260I1=2,NM1
          I2=N=I1+1
          HO(I2)=AH(I2)+HO(I2+1)+BH(I2)
260  CONTINUE
C-----ADJUST HO(1)
      HO(1)=FDIFI+0.5*(HO(2)+HO(3))
265  PEI=PEI-RME*DX
C-----CALCULATE RHO*U*R,S
267  DO270I=1,N
      RU(I)=RHO(I)*UR(I)
270  CONTINUE
      RU3=RU(3)
      DO280I=2,NM1
          RU(I)=0.5*(RU(I)+RU(I+1))
280  CONTINUE
C

```



```

IF(RU(2).NE.0.0)GOTO300
WRITE(2,290)
290  FORMAT('0', 'RU(2)=0.0. JUMP TO END OF SOLVE')
      RETURN
300  CONTINUE
C
C-----NORMAL DISTANCES.
C      NOTE THAT NORMAL DISTANCES ARE CORRECT WHETHER
C      FLOW IS CURVED OR NOT
      YI=PEI+OMI/(BPI+RU(2))
      Y(3)=YI+PEI+OM(3)/(RU(2)+RU3)
      Y(2)=2.0*YI-Y(3)
      DO310 I=4,N
          Y(I)=Y(I-1)+PEI*(OM(I)-OM(I-1))/RU(I-1)
310  CONTINUE
      IF(KRAD.EQ.0)GOTO330
      DO320 I=2,N
          R(I)=R(1)+Y(I)
320  CONTINUE
      R25=R(1)+YI
C-----SOLVE FOR D/S TEMPS AND DENSITIES
330  DO340 I=1,N
          U(I)=UR(I)/R(I)
          ENTH=HO(I)-0.5*U(I)*U(I)
          TEMP(I)=ENTH/CAIR
          RHO(I)=P(I)/(287.0*TEMP(I))
340  CONTINUE
      NSTEP=NSTEP+1
      X=X+DX
      RETURN
      END
C
C

```

```

C      SUBROUTINE TO SUPPLY WALL FUNCTIONS
C
      SUBROUTINE WF(T1,FDIFI,T1F)
      COMMON/A/DUDY(75),EMU(75),HO(75),OH(75),PREF(75),RHO(75),RU(75),
C          TEMP(75),U(75),Y(75),EMURDY(75),TAU(75),R(75),UR(75),
C          BPI,OH1,PEI,TAUI,YI,R25,KRAD,IRAD
C /B/DPDX(75),P(75),CAIR,DX,HOINIT,IENH,LT,N,NM1,NPOS,NSTEP,
C      PI,PR,RU3,TERAD,VISCL,X,DCURV,SLTX,SLTT,NSCAN,LAG
C /D/AK,ALMG,FR
      DATA SHALF,EWALL/0.04,9.0/
      RHOREF=0.5*RHO(1)+0.25*(RHO(2)+RHO(3))
      YREF=YI
      UREF=0.5*(U(2)+U(3))
      F=0.5*(DPDX(2)+DPDX(3))*YI/(RHOREF*UREF*UREF)
      RE=UREF*RHOREF*YREF/EMU(1)
      IF(RE.LT.120.0)GOTO195
C-----LOG LAW
      ER=RE*EWALL
      NIT=0
191  SHALF1=SHALF
      SHALF=AK/ALOG(ER*SHALF)
      IF(ABS(SHALF-SHALF1).LT.0.0001.OR,NIT.GT.10)GOTO192
      NIT=NIT+1
      GOTO191
192  S=SHALF*SHALF
      BPI=1.0-SQRT(S+F)/AK
      EMURDY(2)=0.25*RHOREF*ABS(U(3)-U(2))*(AK/BPI)**2
      WRITE(6,190)X,NSTEP,RE
190  FORHAT(' ',NON LAMINAR WALL FLOW AT X=',F6.4,INSTEP=',I4,
      'RE=',F6.2)
      GOTO196
C-----LAMINAR FLOW
195  S=1.0/RE-0.5*F

```

```

      BPI=0.5-RE*F/12.0
      IF(KRAD.EQ.1)BPI=0.08333*(3.0+R(1)/R25)
      EMURDY(2)=EMU(1)*R25/ABS(Y(3)-Y(2))
196  T1=S*RU(2)
      TAU1=T1*UREF/R(1)
      IF(TAU1.GT.0.0)GOTO198
      WRITE(6,197)TAU1,UREF,RE,F
197  FORMAT('0','TAU1 NEGATIVE',F8.4,2X,'UREF =',F8.4,2X,'RE =',F8.4,
1      2X,'F =',F8.4)
C-----WALL FUNCTIONS FOR ENTHALPIES
198  IF(IENTH.EQ.0)GOTO201
      H=PREF(2)
      IF(RE.LT.120)GOTO200
C-----TURBULENT FLOW
      PRRAT=PR/PREF(2)
      PJAYS=3.68*(PRRAT-1.0)/PRRAT**0.25
      RES=AK*AK*RE
      SS0=1.0/RES-0.1561/RES**0.45+0.08723/RES**0.3
1      +0.03713/RES**0.18
      SS10=SS0/(1.0+PJAYS*SS0**0.5)
      FD=0.25*RES*F/(AK*AK*(1.0+0.0625*RES))
      SS1S=(1.725/RES**0.3333)/(PJAYS+6.8)**1.165
      SS1=SS10*(1.0-FD)+FD*SS1S
      S=SS1*AK*AK
      FDIFI=(H-1.0)*0.5*UREF**2
      T1F=S*RU(2)
      GOTO201
C-----LAMINAR FLOW
200  S=1.0/(RE*PR)
      FDIFI=(H-1.0)*0.5*UREF*UREF
      T1F=S*RU(2)
201  RETURN
      END

```


C
C
C
C
C
C

THIS ROUTINE USES THE POWER LAW TO REPRESENT THE BLOWING PROFILE
AT EXIT FROM THE SLOT

```

SUBROUTINE SLOT(VEL,CHEW,ISLT,SLTTO,RO,DXF,Q)
COMMON/A/DUDY(75),EMU(75),HO(75),OM(75),PREF(75),RHO(75),RU(75),
C      TEMP(75),U(75),Y(75),EMURDY(75),TAU(75),R(75),UR(75),
C      BPI,OMI,PEI,TAUI,YI,R25,KRAD,IRAD
C /B/DPDX(75),P(75),CAIR,DX,HOINIT,IENTH,LT,N,NM1,NPOS,NSTEP,
C      PI,PR,RU3,TERAD,VISCL,X,DCURV,SLTX,SLTT,NSCAN,LAG
C /C/DISPT,SHAPE,TMTM
C /D/AK,ALMG,FR
C /E/NTRIG1,NTRIG2,NTRIG3
DIMENSION HOO(50),OMO(50),RHOO(50),
1      RUO(50),TEMPO(50),UO(50),YO(50),DPDXO(50),PSI(75)
ISLT=ISLT+1
NIT=NIT+1

C
IF(NIT.LT.5)GOTO5
WRITE(6,3)
3  FORMAT('0','ITERATION STOPPED')
STOP

C
5  IF(NIT.GT.1)GOTO 13
LT=2
NPSS=NPOS
DX=SLTX-X
CALL SOLVE(0,0,0)
WRITE(2,10)
10  FORMAT(' ','UPSTREAM PROFILE AT SLOT')
CALL OUTPUT(1)
DO1SI=1,N
HOO(I)=HO(I)
OMO(I)=OM(I)
RHOO(I)=RHO(I)
```

```
TEMPO(I)=TEMP(I)
UO(I)=U(I)
YO(I)=Y(I)
DPDXO(I)=DPDX(I)
```

```
15 CONTINUE
```

```
BPIO=BPI
```

```
OMIO=OMI
```

```
PEIO=PEI
```

```
PIO=PI
```

```
YIO=YI
```

```
NO=N
```

```
NOM1=N-1
```

```
NOP1=N+1
```

```
NOP2=N+2
```

```
NSTEP0=NSTEP
```

```
PEO=PE
```

```
RU3O=RU3
```

```
C
```

```
18 HSLTT=0.5*SLTT
SLTHTM=0.5*CMEW*RO*VEL*VEL
SLTRO=RO
CPSLT=1005.0
SLTHO=CPSLT*SLTTO
SLTUMX=SQRT(0.5*VEL*VEL*CMEW/SLTT)
NPOS=NPSS
NSLT=NO+40
N=NSLT
NM1=N-1
N2=NSLT-NO
NZP1=N2+1
NZP2=N2+2
NZP3=N2+3
NZH1=N2-1
```

```
C-----TRANSFER EXISTING VALUES TO OUTER PART OF NEW GRID
```

```
DO20I=2,NOP1
```

```
J=NOP2-1
```

```
JPN2=J+N2
```

```
Y(JPN2)=Y0(J)+SLTT
U(JPN2)=U0(J)
RHO(JPN2)=RHO0(J)
H0(JPN2)=H00(J)
TEMP(JPN2)=TEMP0(J)
DPDX(JPN2)=DPDX0(J)
P(JPN2)=PIO
```

```
20 CONTINUE
```

```
C-----SET VELOCITY PROFILE ACROSS SLOT ACCORDING TO POWER LAW
```

```
D0301=3,N2
```

```
FACT=0.5*(1.0-COS(3.1416*FLOAT(I)/FLOAT(N2P1)))
```

```
FACT=FACT*(FLOAT(I)/FLOAT(N2P1))**0.5
```

```
Y(I)=FACT*Y(N2P1)
```

```
YA=Y(I)
```

```
IF(Y(I).GT.HSLTT)YA=SLTT=Y(I)
```

```
U(I)=SLTUMX*(YA/HSLTT)**(1.0/Q)
```

```
RHO(I)=SLTRO
```

```
DPDX(I)=DPDX(N2P1)
```

```
P(I)=PIO
```

```
H0(I)=SLTH0
```

```
TEMP(I)=(SLTH0-0.5*U(I)*U(I))/CPSLT
```

```
30 CONTINUE
```

```
YI=0.6*Y(3)
```

```
U25=SLTUMX*(YI/HSLTT)**(1.0/Q)
```

```
C VALUES AT NEW GRID LINES 1 AND 2
```

```
U(2)=2.0*U25-U(3)
```

```
RHO(2)=SLTRO
```

```
Y(2)=2.0*YI-Y(3)
```

```
DPDX(2)=DPDX(N2P1)
```

```
P(2)=PIO
```

```
H0(2)=SLTH0
```

```
TEMP(2)=(SLTH0-0.5*U(2)*U(2))/CPSLT
```

```
RHO(1)=SLTRO
```

```
DPDX(1)=DPDX(N2P1)
```

```
P(1)=PIO
```

```
H0(1)=SLTH0
```



```

TEMP(1)=SLTH0/CPSLT
IRAD=0
KRAD=0
IF(X.GE.DCURV.AND.TERAD.NE.0.0)GOTO36
DO34I=1,N
  R(I)=1.0
34 CONTINUE
  R25=1.0
  GOTO39
36 KRAD=1
  DO37I=1,N
    R(I)=TERAD+Y(I)
37 CONTINUE
  R25=TERAD+YI
  RU(2)=0.5*(R(2)*U(2)*RHO(2)+R(3)*U(3)*RHO(3))
  CALL WF(T1,FDIFI,T1F)
C-----CALCULATE DISTRIBUTION OF OMEGA VALUES ACROSS WHOLE GRID
39 PSI1=BPI*YI*U25*SLTRO*R25
  PSI(3)=0.25*(U25+U(3))*(R25+R(3))*(Y(3)-YI)*SLTRO*PSI1
  DO40I=4,N
    PSI(I)=PSI(I-1)+0.125*(R(I)+R(I-1))*(U(I)+U(I-1))*(Y(I)-Y(I-1))
    * (RHO(I)+RHO(I-1))
    1
40 CONTINUE
  PEI=PSI(N)
  DO60I=3,N
    OM(I)=PSI(I)/PEI
60 CONTINUE
  OM1=0.5*OM(3)
  RU(2)=0.5*(RHO(2)*U(2)+RHO(3)*U(3))*R25
  DO74I=1,N
    UR(I)=U(I)*R(I)
74 CONTINUE
  DX=0.01*Y(N)

```

```
CALL SOLVE(1,0.0)
X=SLTX
NTRIG1=2
NSCAN=0
LAG=1
SLTP0=PI/(1.0-0.1429*SLTUMX*SLTUMX/(287*SLTT0))**3.5
WRITE(6,75)NIT
75  FORMAT(' ', 'ITERATION', I4)
WRITE(6,80)CMEW,SLTP0,SLTT0,ISLT
80  FORMAT(' ', 'BLOWING COEFFICIENT =', F8.6, /' ',
1     'ISENTROPIC P0 =', F8.0, '4X, 'T0 =', F6.1, /' ',
2     'SLOT', I3)
CALL DMS
CALL OUTPUT(1)
DXF=0.04
RETURN
END
```

C
C

C
C
C
C

SUBROUTINE TO CALCULATE NORMAL PRESSURE GRADIENT
RESULTING FROM SURFACE CURVATURE

```
SUBROUTINE NORPRES
DIMENSION OMDIF(75), ARINT(75), PSI(75)
COMMON/A/DUDY(75), EMU(75), HO(75), OM(75), PREF(75), RHO(75), RU(75),
C      TEMP(75), U(75), Y(75), EMURDY(75), TAU(75), R(75), UR(75),
C      BPI, OMI, PEI, TAU1, Y1, R25, KRAD, IRAD
C  /B/DPDX(75), P(75), CAIR, DX, HOINIT, IENTH, LT, N, NM1, NPOS, NSTEP,
C      PI, PR, RU3, TERAD, VISCL, X, DCURV, SLTX, SLTT, NSCAN, LAG
IF(X=SLTX.LT.0.001)GOTO90
NM3=N-3
IF(IRAD.EQ.1)GOTO25
KRAD=1
IRAD=1
DO10I=1,N
  R(I)=TERAD+Y(I)
  UR(I)=U(I)*R(I)
  RU(I)=RHO(I)*UR(I)
10  CONTINUE
DO15I=2,NM1
  RU(I)=0.5*(RU(I)+RU(I+1))
15  CONTINUE
R25=R(1)+Y1
U25=0.5*(U(2)+U(3))
BPI=0.08333*(3.0+R(1)/R25)
PSI1=BPI*Y1+U25*RHO(2)*R25
PSI(3)=0.25*(U25+U(3))*(R25+R(3))*(Y(3)-Y1)+RHO(2)*PSI1
DO22I=4,N
  PSI(I)=PSI(I-1)+RU(I-1)*(Y(I)-Y(I-1))
22  CONTINUE
PEI=PSI(N)
DO24I=1,NM3
  J=N-I
  OMDIF(J)=OM(J+1)-OM(J)
```



```

RM=0.5*(R(J)+R(J+1))
RMSQ=RM*RM
ARINT(J)=ARINT(J+1)+PEI*0.5*(U(J)+U(J+1))+OMDIF(J)/RMSQ
24 CONTINUE
OMI=0.5*OH(3)
GOTO90
25 IF(DX0.LT.0.000005)GOTO90
DO30I=1,NM3
J=N-I
RM=0.5*(R(J)+R(J+1))
RMSQ=RM*RM
RINT=ARINT(J+1)+PEI*0.5*(U(J)+U(J+1))+OMDIF(J)/RMSQ
DPDXJ=DPDX(N)-(RINT-ARINT(J))/DX0
DPDX(J)=DPDX(J)+(DPDXJ-DPDX(J))*1000.0*DX0
P(J)=P(N)-RINT
ARINT(J)=RINT
30 CONTINUE
P(2)=P(3)
DPDX(2)=DPDX(3)
P(1)=P(3)
DPDX(1)=DPDX(3)
PI=P(1)
90 DX0=DX
RETURN
END

```

C

C
C
C

SUBROUTINE TO CALCULATE LONGITUDINAL PRESSURE GRADIENTS

```
SUBROUTINE PGDT(PS,NX,XS,IPOINT)
COMMON /B/DpDX(75),P(75),CAIR,DX,H0INIT,IENTH,LT,N,NM1,NPOS,NSTEP,
C      PI,PR,RU3,TERAD,VISCL,X,DCURV,SLTX,SLTT,NSCAN,LAG
DIMENSION A(4,5),XS(70),PS(70)
XM=X+0.5*DX
10  H1=XS(NPOS+1)-XM
    IF(H1/(XS(NPOS+1)-XS(NPOS)).LT.0.015)GOTO70
    P1=PS(NPOS+1)
    IF(NPOS.NE.1)GOTO20
        H2=XS(NPOS+2)-XM
        H3=XS(NPOS+3)-XM
        H4=XS(NPOS)-XM
        P2=PS(NPOS+2)
        P3=PS(NPOS+3)
        P4=PS(NPOS)
        GOTO40
20  IF(NPOS.NE.(NX-1))GOTO30
        H2=XS(NPOS)-XM
        H3=XS(NPOS-1)-XM
        H4=XS(NPOS-2)-XM
        P2=PS(NPOS)
        P3=PS(NPOS-1)
        P4=PS(NPOS-2)
        GOTO40
30  H2=XS(NPOS+2)-XM
    H3=XS(NPOS)-XM
    H4=XS(NPOS-1)-XM
```

P2=PS(NPOS+2)
P3=PS(NPOS)
P4=PS(NPOS-1)

```
40  DO50 I=1,4  
    J=4-I  
    A(1,I)=H1**J  
    A(2,I)=H2**J  
    A(3,I)=H3**J  
    A(4,I)=H4**J  
50  CONTINUE  
    A(1,5)=P1  
    A(2,5)=P2  
    A(3,5)=P3  
    A(4,5)=P4  
    DO60 K=2,4  
        DO60 I=K,4  
            DO60 J=K,5  
                A(I,J)=A(I,J)-A(K-1,J)*A(I,K-1)/A(K-1,K-1)  
60  CONTINUE  
    PI=A(4,5)/A(4,4)  
    DPDX1=(A(3,5)-A(3,4)*PI)/A(3,3)  
    DO70 I=1,N  
        DPDX(I)=DPDX1  
        P(I)=PI  
70  CONTINUE  
    IF(IPUINT.EQ.1)NPOS=NPOS+1  
    RETURN  
    END
```

C


```

C
C   SUBROUTINE FOR GENERATION OF VELOCITY PROFILE USING
C   COLES WAKE FUNCTION
SUBROUTINE COLES(TINF,PS,NX,XS)
DIMENSION PSIL(75),XS(70),PS(70)
COMMON/A/DUDY(75),EMU(75),H0(75),OH(75),PREF(75),RHO(75),RU(75),
C   TEMP(75),U(75),Y(75),EMURDY(75),TAU(75),R(75),UR(75),
C   BPI,OMI,PEI,TAUI,YI,R25,KRAD,IRAD
C /B/DPDX(75),P(75),CAIR,DX,HOINIT,IENTH,LT,N,NM1,NPOS,NSTEP,
C   PI,PR,RU3,TERAD,VISCL,X,DCURV,SLTX,SLTT,NSCAN,LAG
C /C/DISPT,SHAPE,TMTM
C /D/AK,ALMG,FR
WRITE(2,10)
10  FORMAT(' ', 'COLES WAKE FUNCTION USED FOR STARTING PROFILE')
XST=X
NSTEP=0
DX=0.1*Y(NM1)
CALL PGDT(PS,NX,XS,IPOINT)
ROI=PI/(287.0*TINF)
C=5.1
PIF=0.5
UTAU=3.0
25  TRY=U(N)/(4.598+PIF+C*2.3*ALOG(Y(N)*UTAU*ROI/VISCL))
IF(ABS(UTAU-TRY)/TRY.LT.0.001)GOTO30
UTAU=TRY
GOTO25
30  WRITE(6,50)PIF,UTAU
50  FORMAT(' ', 'PI=', F6.4, 5X, 'UTAU=', F10.8)
RLN=FLOAT(N)
DO60I=1,N
Y(I)=Y(N)*(FLOAT(I)/RLN)**2

```

```

R(I)=R(1)+Y(I)
IF(KRAD.EQ.0)R(I)=1.0
YDD=Y(I)/Y(N)
YWALL=Y(I)*UTAU*ROI/VISCL
IF(YWALL.GE.10.0)GOTO53
U(I)=UTAU*YWALL
GOTO55
53 WAKF=0.005298-0.459549*YDD+7.31577*YDD*YDD-4.85816*YDD*YDD*YDD
IF(YDD.GE.1.0)WAKF=2.0
U(I)=UTAU*((ALOG(YWALL))/AK+C+PIF*WAKF/AK)
55 RHO(I)=ROI
TEMP(I)=TINF
PREF(I)=PR
HO(I)=HOINIT
60 CONTINUE
YI=0.7*Y(3)
R25=R(1)+YI
IF(KRAD.EQ.0)R25=1.0
BPI=0.5
70 U25=U(3)*(Y(3)-YI)/((2.0*BPI+1)*YI-Y(3))
IF(YI*U25*ROI/VISCL.LT.120.0.OR.BPI.HE.0.5)GOTO80
YI=0.6*Y(3)
BPI=0.8
GOTO70
80 U(1)=0.0
Y(1)=0.0
Y(2)=2.0*YI-Y(3)
R(2)=R(1)+Y(2)
U(2)=2.0*U25-U(3)
DO84I=1,N
UR(I)=U(I)*R(I)

```

```

      RU(I)=RHO(I)*UR(I)
84  CONTINUE
      RU3=RU(3)
      DO86I=2,NM1
          RU(I)=0.5*(RU(I)+RU(I+1))
86  CONTINUE
      EMU(1)=VISCL
      CALL WF(T1,FDIFI,T1F)
      PSI25=ROI*BPI*U25*YI+R25
      PSIL(3)=PSI25+ROI*0.25*(R25+R(3))*(U25+U(3))*(V(3)-YI)
      DO90I=4,N
          PSIL(I)=PSIL(I-1)+RU(I-1)*(Y(I)-Y(I-1))
90  CONTINUE
      PEI=PSIL(N)
      DO100I=3,N
          OM(I)=PSIL(I)/PEI
100 CONTINUE
      CALL PGDT(PS,NX,XS,IPOINT)
      OM1=0.5*OM(3)
      OM(1)=0.0
      OM(2)=0.0
      CALL SOLVE(1,0.0)
      NSTEP=0
      X=XST
      RETURN
      END

```

C
C

C SUBROUTINE TO CALCULATE EDDY VISCOSITIES USING
C MIXING LENGTH HYPOTHESIS
C

SUBROUTINE MLH(RME)
COMMON/A/DUDY(75), EMU(75), HO(75), OH(75), PREF(75), RHO(75), RU(75),
C TEMP(75), U(75), Y(75), EMURDY(75), TAU(75), R(75), UR(75),
C BPI, OMI, PEI, TAUI, YI, R25, KRAD, IRAD
C /B/DPDX(75), P(75), CAIR, DX, HOINIT, IENTH, LT, N, NM1, NPOS, NSTEP,
C PI, PR, RU3, TERAD, VISCL, X, DCURV, SLTX, SLTT, NSCAN, LAG
C /D/AK, ALMG, FR
NM2=N-2
DIF=U(N)*FR

C -----FIND POSITION AND INTERPOLATE LINEARLY FOR CHARACTERISTIC LENGTH

J=N
110 J=J-1
UJ1=U(N)-U(J)
IF(UJ1.GE.DIF)GOTO120
GOTO110
120 YL=Y(J)+(Y(J+1)-Y(J))*(U(N)-DIF-U(J))/(U(J+1)-U(J))

```

C-----CALCULATE EFFECTIVE VISCOSITIES USING MIXING
C-----LENGTH THEORY
C-----APPROXIMATION TO VAN DRIEST FACTOR
C-----EMU(1) ALWAYS LAMINAR
      UTAU=SQRT(TAUI/RHO(1))
      DO150I=2,NM1
        AL=ALMG*YL
        RHOM=0.5*(RHO(I)+RHO(I+1))
        YM=0.5*(Y(I)+Y(I+1))
        IF(YM.LT.AL/AK)AL=AK*YM
        D=(YM*RHOM*UTAU/(EMU(I)*26.0))
        IF(D.GT.5.0)GOTO130
        AL=AL*(1.0-EXP(-D))
130      EMUTY=RHOM*AL*AL*ABS(DUDY(I))
C-----APPLY CURVATURE CORRECTION TO EMU'S
      IF(X.GT.DCURV.AND.TERAD.NE.0.0)CALL CURVE(U,Y,R,DUDY(I),
1          EMUTY,I,0.1,Y(NM1))
      EMU(I)=EMU(I)+EMUTY
150    CONTINUE
      RETURN
      END

```

SUBROUTINE FOR TURBULENT VISCOSITIES
USING DVORAK'S INTERMITTENCY REPRESENTATION

```

C
C
C
C
C
SUBROUTINE TURB(RME)
DIMENSION GAMA(75)
COMMON/A/DUDY(75), EMU(75), HO(75), OM(75), PREF(75), RHO(75), RU(75),
C      TEMP(75), U(75), Y(75), EMURDY(75), TAU(75), R(75), UR(75),
C      BPI, OMI, PEI, TAUI, YI, R2S, KRAD, IRAD
C /B/DPDX(75), P(75), CAIR, DX, HOINIT, IENTH, LT, N, NM1, NPOS, NSTEP,
C      PI, PR, RU3, TERAD, VISCL, X, DCURV, SLTX, SLTT, NSCAN, LAG
C /C/DISPT, SHAPE, TMTM
C /D/AK, ALHG, FR

```

```

C
C-----SHAPE FACTOR H IS USED IN THIS ROUTINE
C

```

```

      NSCAN=NSCAN+1
      H=SHAPE

```

```

C
C-----DETERMINE FORM OF VELOCITY PROFILE
C

```

```

      JET = 0 FOR PLAIN B.L.

```

```

      JET = 1 FOR MAXIMUM IN PROFILE

```

```

      JET = 2 FOR MAXIMUM AND MINIMUM IN PROFILE

```

```

3      NM2=N-2

```

```

      JET=0

```

```

      MAX=0

```

```

      MIN=0

```

```

      IMAX=0

```

```

      IMIN=0

```

```

      DO 10 I=3, NM2

```

```

          IF (DUDY(I).LT.0.0.OR.DUDY(I+1).GE.0.0.

```

```

          * OR.MAX.EQ.1)GOTO5

```

```

          UMAX=U(I+1)

```

```

          MAX=1

```

```

          IHAX=I+1

```

```

          YMAX=Y(I+1)

```



```

      OMAX=OM(I+1)
5      IF(DUDY(I).GT.0.0.OR.DUDY(I+1).LE.0.0.
*      OR.MIN.EQ.1)GOTO10
      IF(I-IMAX.LT.5)GOTO10
      IMIN=I+1
      MIN=1
      UMIN=U(I+1)
      YMIN=Y(I+1)
10     CONTINUE
      IF(MAX.EQ.1)JET=1
      IF(MAX.EQ.1.AND.MIN.EQ.1)JET=2
      IF(ABS(IMAX-IMIN).LE.3)JET=0
      CRIT=(U(N)-UMIN)/U(N)
      IF(JET.EQ.2.AND.CRIT.LT.0.1)JET=1
      IF(JET.EQ.2.AND.JETO.EQ.1.AND.NSCAN.NE.1)JET=1
25     TLMAYER=Y(NM1)
C-----CALCULATE VELOCITY DEFECT AND POINT OF DEPARTURE FROM LAW OF WALL
      IF(JET.NE.1)GOTO40
      UD=UMAX-U(N)
      UMD=U(N)/UD
      IF(U(N)/UD.GT.4.5)JET=0
40     IF(JET.EQ.0)YD=(0.136/(H-1.269))*DISPT
      IF(H.GT.2.1.AND.JET.EQ.0)YD=0.15*DISPT
      IF(H.LT.1.4.AND.JET.EQ.0)YD=(6.935-4.212*H)*DISPT
      IF(JET.EQ.2)UD=0.76*U(N)
      JP1=JET+1
      GOTO(45,78,78),JP1
C
C---PLAIN BOUNDARY LAYER
45     DO50I=3,N
      IF(Y(I).GE.YD)GOTO60
50     CONTINUE
60     UD=U(N)-(U(I-1)+(U(I)-U(I-1))*(YD=Y(I-1))/(Y(I)-Y(I-1)))
C
C-----CALCULATE INNER REGION VISCOSITIES
C-----VAN DRIEST MODEL

```

```

78  UTAU=SQRT(TAUI/RHO(1))
    DIF=UMAX*FR
    J=IMAX
80  J=J-1
    UJ1=UMAX-U(J)
    IF(UJ1.GE.DIF)GOTO82
    GOTO80
82  YL=Y(J)+(UMAX-U(J)-DIF)*(Y(J+1)-Y(J))/(U(J+1)-U(J))
    DO85I=2,NM1
        YM=0.5*(Y(I+1)+Y(I))
        RHOM=0.5*(RHO(I)+RHO(I+1))
        AL=ALMG*YL
        IF((JET.EQ.0.AND.YM.GT.YD).OR.(JET.NE.0.AND.I.GT.IMAX))GOTO90
        IF(AL.GT.AK*YM)
            *   AL=AK*YM*(1.0-EXP(-YM*RHOM*UTAU/(EMU(I)*26.0)))
            EMUTY=RHOM*AL*AL*ABS(DUDY(I))
            EMU(I)=EMU(I)+EMUTY
            IF(EMU(I).LT.EMU(I-1))EMU(I)=EMU(I-1)
85  CONTINUE
90  IDEPT=I
C-----SIGMA VALUES
    IF(JET.EQ.0)SIGMA=(0.245+0.189/(H-1.176))*DISPT
    IF(JET.EQ.1.AND.UMD.GT.0.5)SIGMA=(1.35-0.281*UMD)*YMAX
    IF(JET.EQ.1.AND.UMD.LE.0.5)SIGMA=(1.06+0.091/(UMD*0.104))*
1      YMAX
    IF(JET.EQ.2)SIGMA=0.127*TLAYER
    ENUTL=UD*SIGMA/15.0
C      LOCATION OF HEAN TURBULENT FRONT
95  IF(JET.EQ.0)YBAR=(2.226+0.962/(H-1.158))*DISPT
    IF(JET.EQ.1)YBAR=(9.53/(UMD+0.823)-0.726)*YMAX
    IF(JET.EQ.2)YBAR=0.93*TLAYER
C-----GAMMA DISTRIBUTION
C
    IG=0
    UMP=0.5*(UMAX+U(N))
C-----APPROXIMATION TO ERROR FUNCTION AT GRID POINTS
    DO100I=IDEPT,N

```

```

      EX=ABS(Y(I)-YBAR)/(SIGMA*1.414)
      ERF=1.1061*EX+0.1557*EX*EX-0.7635*EX**3+0.44*EX**4
1      -0.1056*EX**5+0.0095*EX**6
      IF(ABS(EX).GE.3.0)ERF=1.0
      IF(Y(I).LT.YBAR)ERF=-ERF
      GAMA(I)=0.5*(1.0-ERF)
      IF(GAMA(I).LT.0.0)GAMA(I)=0.0
      IF(GAMA(I).GT.1.0)GAMA(I)=1.0
      IF(U(I).LE.UMP.AND.I.GT.IMAX.AND.IG.EQ.0)IG=I
100  CONTINUE
C-----DIFFUSION EFFECT
C      AND SETTING OF INITIAL TURBULENCE LEVEL
      IF(NSCAN.EQ.1.OR.JET.NE.JETO)ENUMX=ENUTL
      RK1=0.02
      DEL=DISPT
C-----ALTERNATIVE DELTA AND K1 FOR JET=1,2 PROFILES
      IF(JET.EQ.0)GOTO105
      RK1=0.2
      IF(JET.EQ.1)RK1=0.5
      DEL=TLAYER
      IF(JET.EQ.1)DEL=2.0*Y(IG)
105  ENUMX=RK1*DX*(ENUTL-ENUMX)/DEL+ENUMX
C-----EFFECTIVE VISCOSITY DISTRIBUTION
      DO120I=IDEPT,NM1
      RHOM=0.5*(RHO(I)+RHO(I+1))
      GAMM=0.5*(GAMA(I)+GAMA(I+1))
      EMUTY=ENUMX*GAMM*RHOM
      IF(X.GT.DCURV.AND.TERAD.NE.0.0)CALL CURVE(U,Y,R,DUDY(I),
1                                     EMUTY,I,RK1,DEL)
C-----PREVENT GROWTH OF LAMINAR OUTER LAYER
      IF(UR(I).LT.UR(N).AND.JET.EQ.1.AND.I.GT.IMAX)
*      UR(I)=UR(N)
118  EMU(I)=EMU(I)+EMUTY
120  CONTINUE
C-----COSINE FAIRING TO JOIN REGIONS FOR JET=1 OR JET=2
      GOTO(150,126,136),JP1
C

```



```

126 FACT=0.8
128 YJOIN=FACT*(Y(IG)-YMAX)+YMAX
    J=IMAX
130 J=J+1
    IF(Y(J).GE,YJOIN)GOTO132
    GOTO130
132 IG1=J
    IF(GAMA(IG1).GT.0.9.OR.FACT.LE.0.1)GOTO134
    FACT=FACT-0.1
    GOTO128
134 ENUA=0.5*(EMU(IG1)/RHO(IG1)+2.0*EMU(IMAX)/RHO(IMAX))
    PER=Y(IG1)-Y(IMAX)
    YA=Y(IMAX)+0.5*PER
    LIML=IMAX
    LIMU=IG1
    AMPL=EMU(IG1)/RHO(IG1)-ENUA
    GOTO138

C
136 ENUA=0.5*(ENUMX+2.0*EMU(IMAX)/RHO(IMAX))
    PER=Y(IMIN)-Y(IMAX)
    YA=Y(IMAX)+0.5*PER
    LIML=IMAX
    LIMU=IMIN
    AMPL=ENUMX-ENUA
138 DO140 I=LIML,LIMU
    RHOM=0.5*(RHO(I)+RHO(I+1))
    EMU(I)=(ENUA+AMPL*SIN(3.142*(Y(I)-YA)/PER))*RHOM
140 CONTINUE
150 YDC=YD*1000.0
    YDIC=YDI*1000.0
    SIGIC=SIGMAI*1000.0
    SIGHAC=SIGMA*1000.0
    WRITE(2,200)JET,H,UD,YDC,SIGMAC,YDIC,UDI,SIGIC,HI,PEI
200 FORMAT(' ',56X,I1,F6.2,F7.3,F8.5,F7.4,F8.5,F6.2,F7.4,F5.2,F8.5)
    JETO=JET
    RETURN
    END

```

C
C
C
C
C

THIS SUBROUTINE FACTORS EDDY VISCOSITIES BY A
CURVATURE CORRECTION
A LAG EQUATION IS ALSO APPLIED

```
SUBROUTINE CURVE(U,Y,R,DUDYI,EMUTY,I,RK1,DEL)
DIMENSION U(75),Y(75),RIO(75),R(75)
COMMON/B/DPDX(75),P(75),CAIR,DX,H0INIT,IENTH,LT,N,NM1,NPOS,NSTEP,
1 PI,PR,RU3,TERAD,VISCL,X,DCURV,SLTX,SLTT,NSCAN,LAG
DUDY=DUDYI
UM=0.5*(U(I)+U(I+1))
RM=0.5*(R(I)+R(I+1))
IF(ABS(DUDY).LT.10.0)DUDY=10.0
RI=2.0*(UM/RM)/DUDY
IF(RI.GT.0.25)RI=0.25
IF(RI.LT.-0.5)RI=-0.5
IF(LAG.EQ.0)RIO(I)=RI
IF(NSCAN.EQ.1)RIO(I)=0.0
RI=RIO(I)+(RI-RIO(I))*DX*RK1/DEL
RIO(I)=RI
BETA=4.0
IF(RI.LT.0.0)BETA=2.0
FACT=1.0-BETA*RI
EMUTY=EMUTY*FACT
LAG=1
RETURN
END
```

C
C
C
C
C
C
C

THIS SUBROUTINE CALCULATES DISPLACEMENT AND MOMENTUM
THICKNESSES AND SHAPE FACTOR

```
SUBROUTINE DMS
COMMON/A/DUDY(75),EMU(75),HO(75),OM(75),PREF(75),RHO(75),RU(75),
C      TEMP(75),U(75),Y(75),EMURDY(75),TAU(75),R(75),UR(75),
C      BPT,OMI,PEI,TAUI,YI,R25,KRAD,IRAD
C /B/DPDX(75),P(75),CAIR,DX,HOINIT,IENTH,LT,N,NM1,NPOS,NSTEP,
C      PI,PR,RU3,TERAD,VISCL,X,DCURV,SLTX,SLTT,NSCAN,LAG
C /C/DISPT,SHAPE,TMTM
SUM1=0.0
SUM2=0.0
DO10I=3,NM1
  DY=Y(I+1)-Y(I)
  RHOM=0.5*(RHO(I+1)+RHO(I))
  UM=0.5*(U(I+1)+U(I))
  S1=RHOM*UM*DY
  SUM1=SUM1+S1
  SUM2=SUM2+S1*UM
10 CONTINUE
RHO25=0.5*(RHO(2)+RHO(3))
U25=0.5*(U(2)+U(3))
SUM1=SUM1+0.333*RHO25*U25*YI
SUM2=SUM2+RHO25*U25*U25*YI*0.2
S1=0.25*(RHO25+RHO(3))*(U25+U(3))*(Y(3)-YI)
SUM1=SUM1+S1
SUM2=SUM2+S1*(U25+U(3))*0.5
S1=RHO(N)*U(N)
DISPT=Y(N)=SUM1/S1
TMTM=SUM1/S1-SUM2/(S1*U(N))
SHAPE=DISPT/TMTM
RETURN
END
```


C
C
C
C
C

LAMINAR VISCOSITIES AND PR FOR CELL BOUNDARIES

```
SUBROUTINE LAMFLO
COMMON/A/DUDY(75),EMU(75),HO(75),OH(75),PREF(75),RHO(75),RU(75),
C      TEMP(75),U(75),Y(75),EMURDY(75),TAU(75),R(75),UR(75),
C      EPI,OMI,PEI,TAUI,YI,R2S,KRAD,IRAD
C /B/DPDX(75),P(75),CAIR,DX,HOINIT,IENTH,LT,N,NM1,NPOS,NSTEP,
C      PI,PR,RU3,TERAD,VISCL,X,DCURV,SLTX,SLTT,NSCAN,LAG
DO100I=1,N
  EMU(I)=0.00001962*(435.0/(TEMP(I)+110.0))*(TEMP(I)/325.0)**1.5
  PREF(I)=0.707-(0.019)*(TEMP(I)-300.0)/100.0
100 CONTINUE
DO110I=2,NM1
  EMU(I)=0.5*(EMU(I)+EMU(I+1))
  PREF(I)=0.5*(PREF(I)+PREF(I+1))
110 CONTINUE
RETURN
END
```

C
C
C
C

SUBROUTINE FOR OUTPUT

```
SUBROUTINE OUTPUT(NTRIG)
COMMON/A/DUDY(75),EMU(75),HO(75),OM(75),PREF(75),RHO(75),RU(75),
C      TEMP(75),U(75),Y(75),EMURDY(75),TAU(75),R(75),UR(75),
C      BPI,OM1,PEI,TAUI,YI,R25,KRAD,IRAD
C /B/DPDX(75),P(75),CAIR,DX,HOINIT,IENTH,LT,N,NM1,NPOS,NSTEP,
C      PI,PR,RU3,TERAD,VISCL,X,DCURV,SLTX,SLTT,NSCAN,LAG
C /C/DISPT,SHAPE,TMTM
DISPTC=DISPT*1000.0
WRITE(2,100)NSTEP,X,DX,TAUI,DPDX(1),PI,SHAPE,DISPTC,PEI
100  FORMAT(' ',4X,I3,F11.6,F10.6,F8.4,F10.1,F11.1,F8.4,
1      F10.4,36X,F11.5)
C-----FULL OUTPUT EVERY 25 STEPS
IF(NTRIG.EQ.1)GOTO110
IF(FLOAT(NSTEP)/25.0.EQ.FLOAT((NSTEP)/25))GOTO110
105  RETURN
110  WRITE(2,115)
115  FORMAT('0',5X,'OMEGA',6X,'Y*1000',7X,'U',8X,'RHO',6X,'T',5X,
1      'EMU*10**6',3X,'PREF',6X,'DPDX',7X,'DUDY',7X,'PI',8X,
2      'TAU')
DO150I=1,N
YTTQ=Y(I)*1000.0
ETTQ=EMU(I)*1000000.0
120  WRITE(2,200)I,OM(I),YTTQ,U(I),RHO(I),TEMP(I),ETTQ,PREF(I),
1      DPDX(I),DUDY(I),P(I),TAU(I)
150  CONTINUE
200  FORMAT(' ',12,F9.5,F13.6,F9.3,F9.3,F8.1,F11.2,F9.4,
1      F11.2,F10.1,F10.1,F10.4)
RETURN
END
FINISH
```

FIGURES

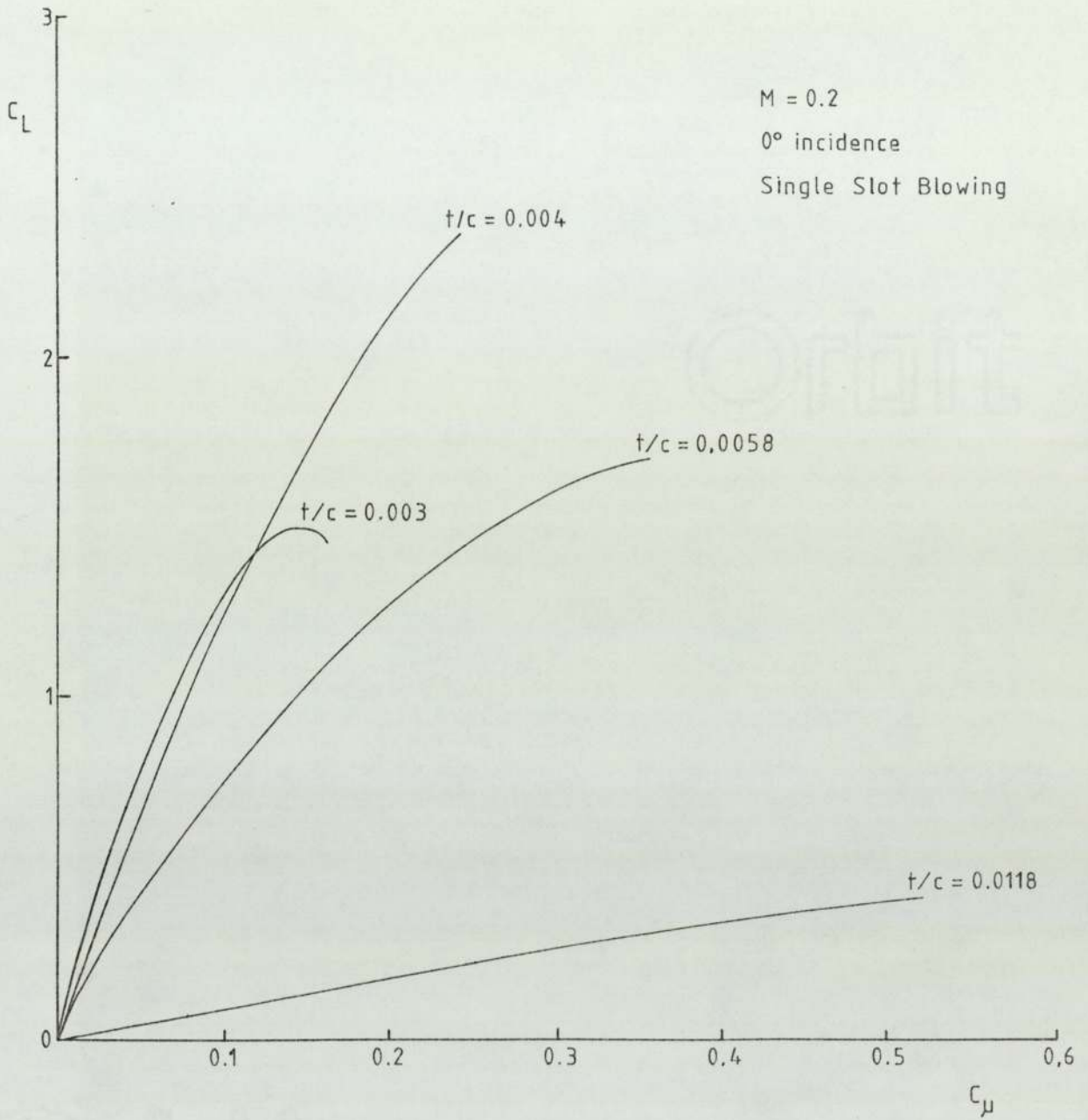


Figure 1
The Effect of Slot Width
on a 20% Ellipse
(Taken from Reference 32)

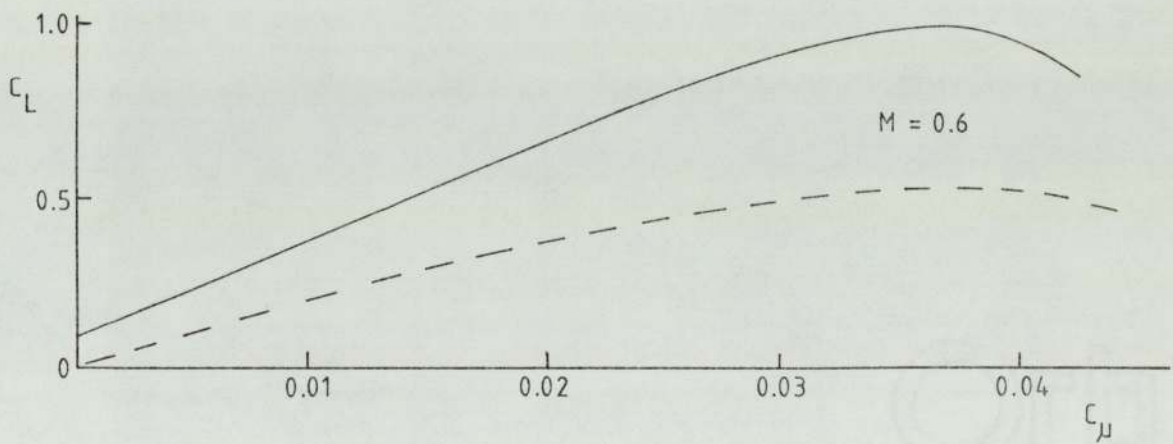
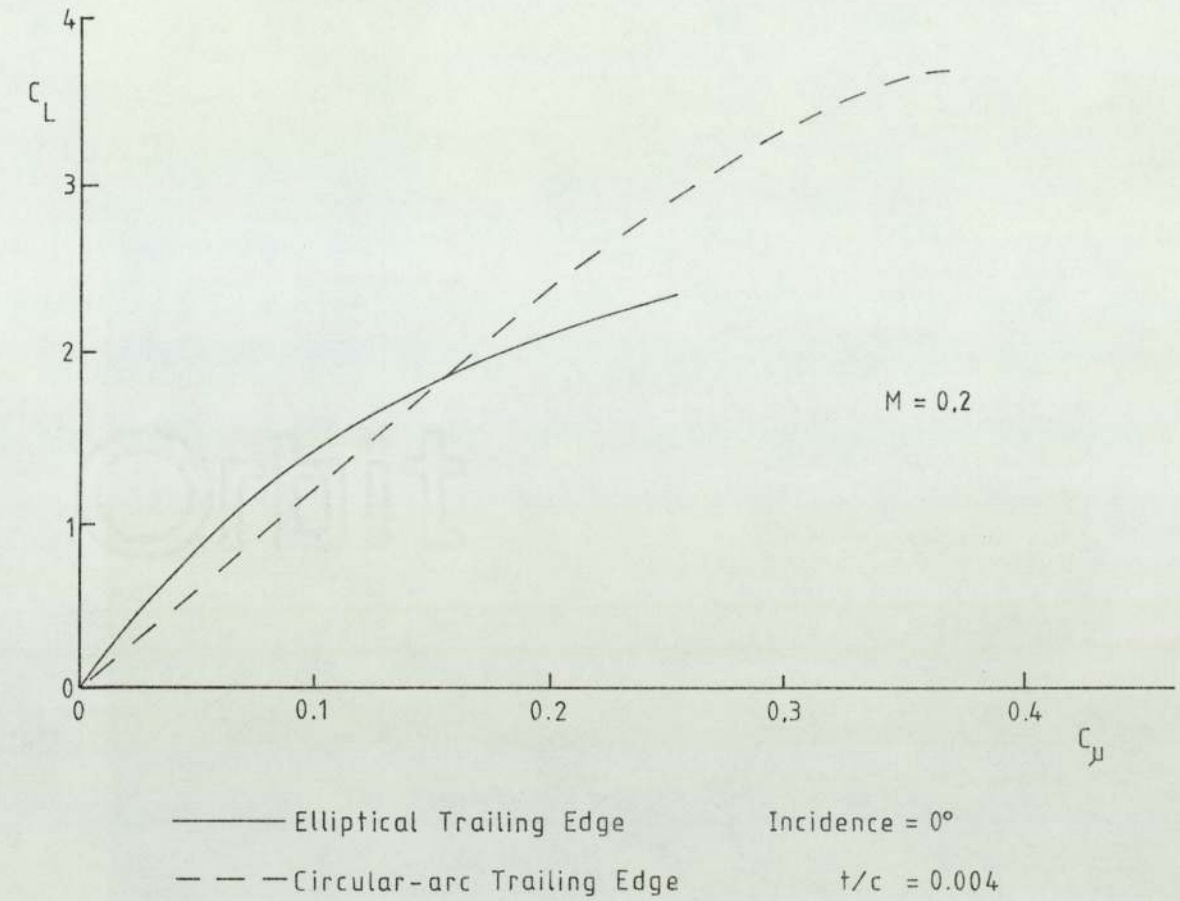


Figure 2
The Effect of Trailing Edge Shape
at Two Mach Numbers
on a 20% Ellipse
(Taken from Reference 32)

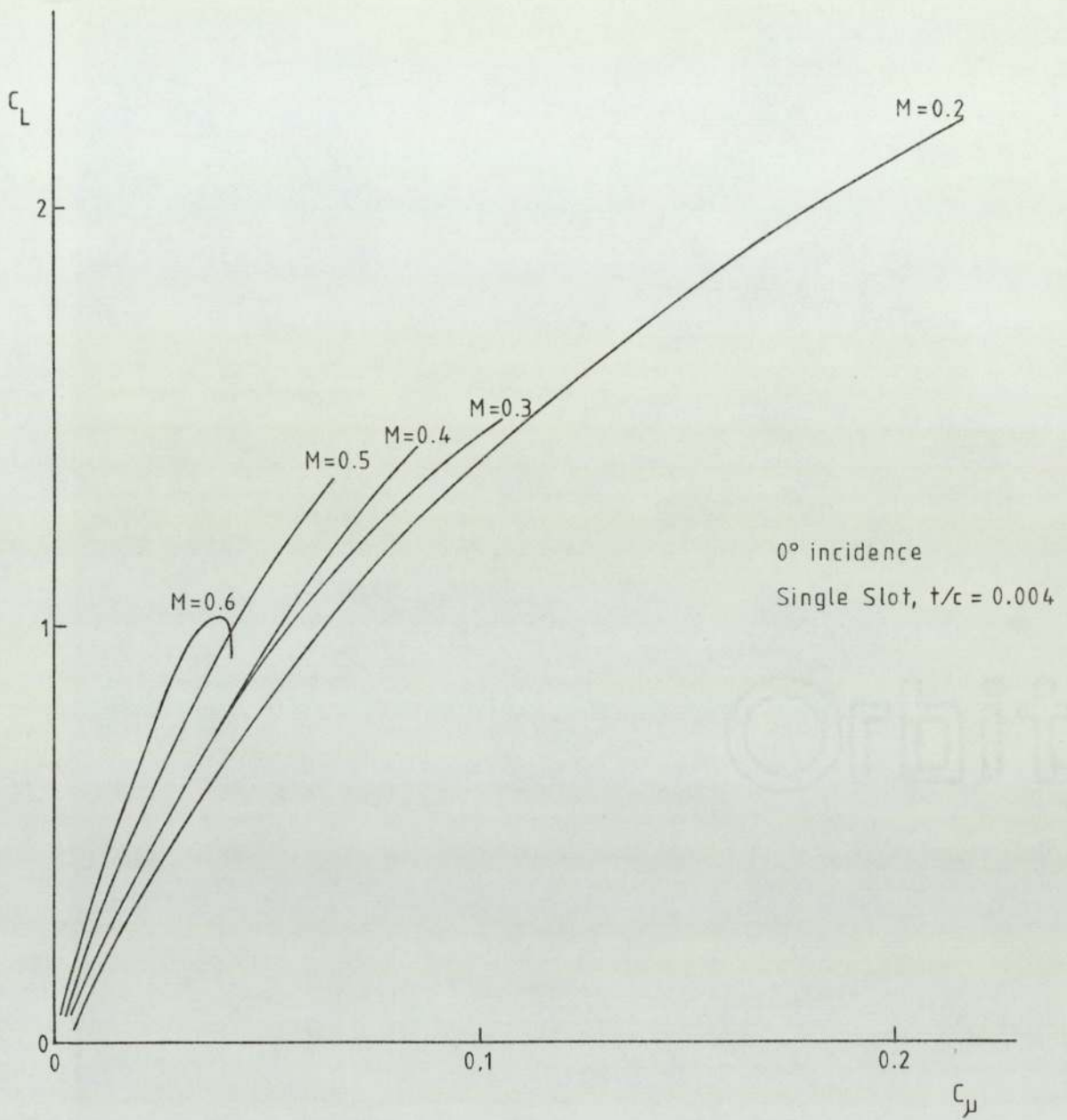
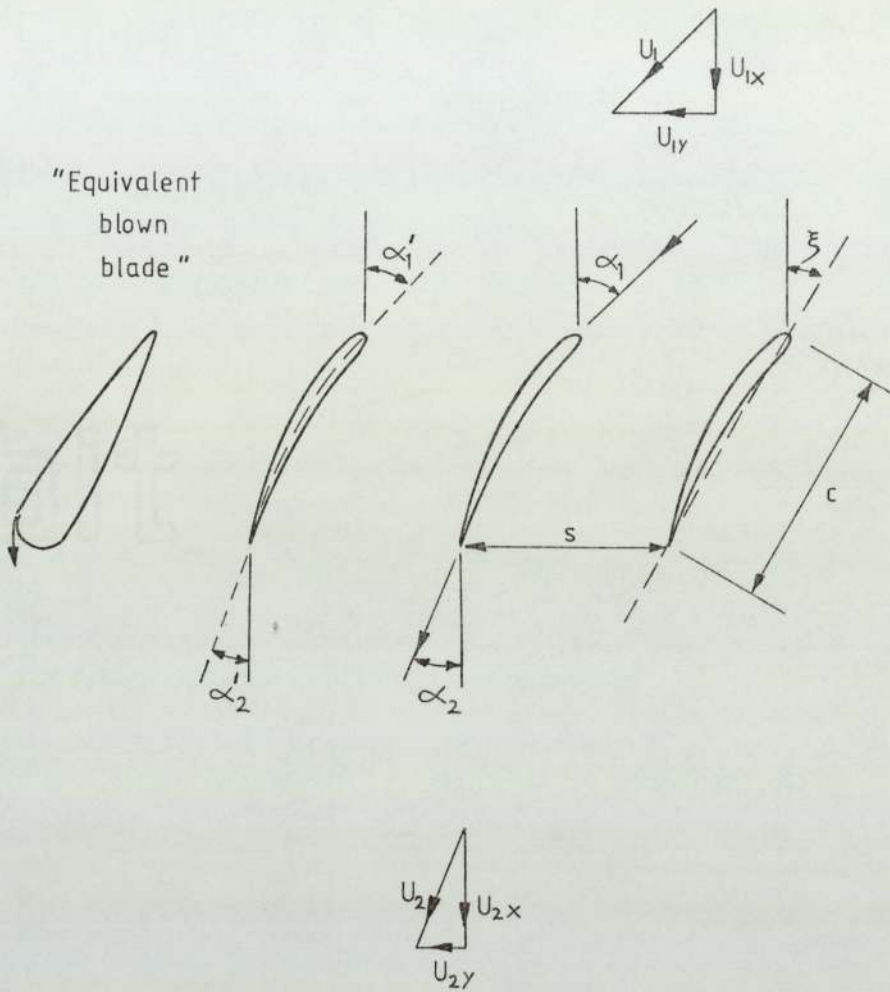


Figure 3
The Effect of Mach Number
on a 20% Ellipse
(Taken from Reference 32)



- α'_1 Blade inlet angle
- α'_2 Blade outlet angle
- α_1 Air inlet angle
- α_2 Air outlet angle
- ξ Stagger angle
- s Pitch
- c Chord

- U_1 Air inlet velocity
- U_2 Air outlet velocity

- $\frac{U_{1x}}{U_{2x}}$ Axial velocity ratio

Figure 4
Cascade Nomenclature

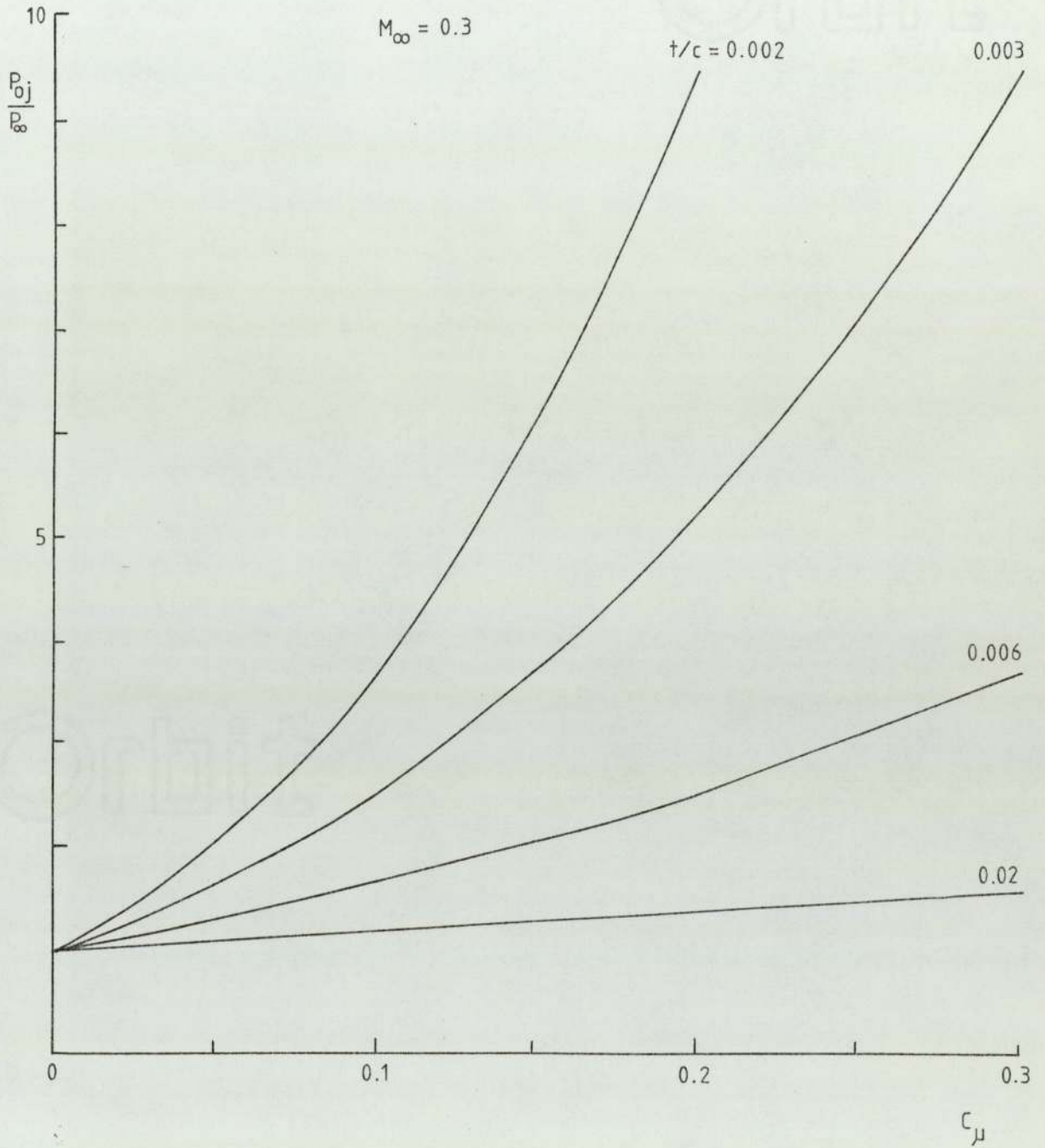
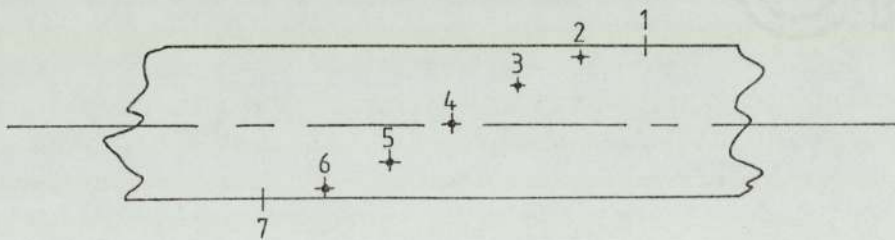
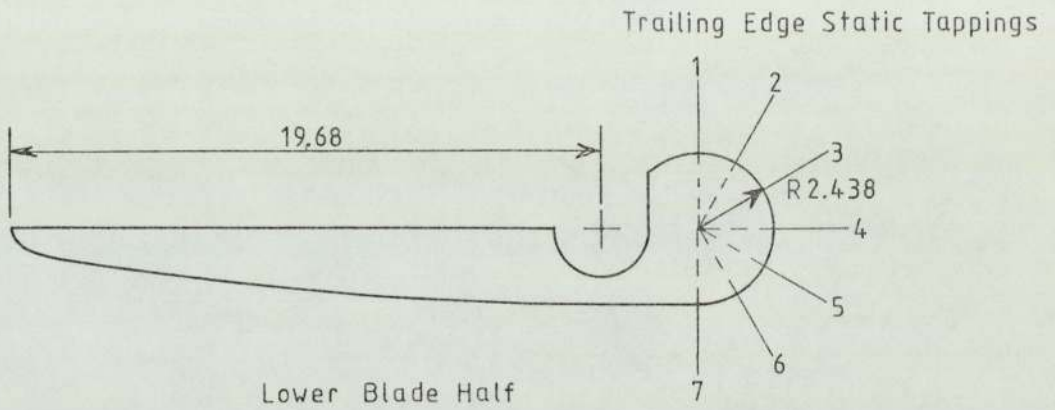
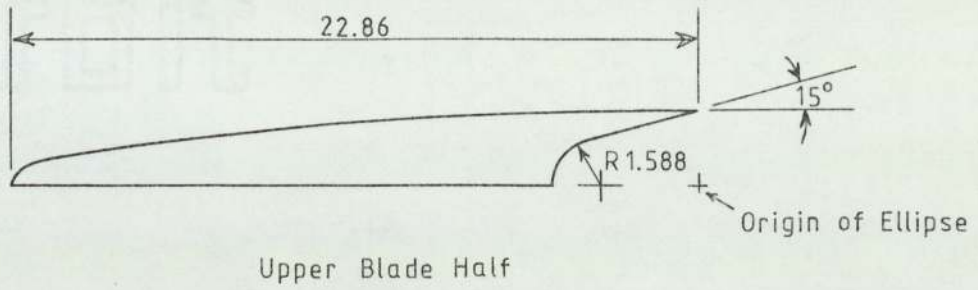


Figure 5
Slot Pressure Ratio
Required at a Given C_μ
for Various Slot Widths



Scale 4:1
Dimensions in mm.

Figure 6
Details of
Model Blades

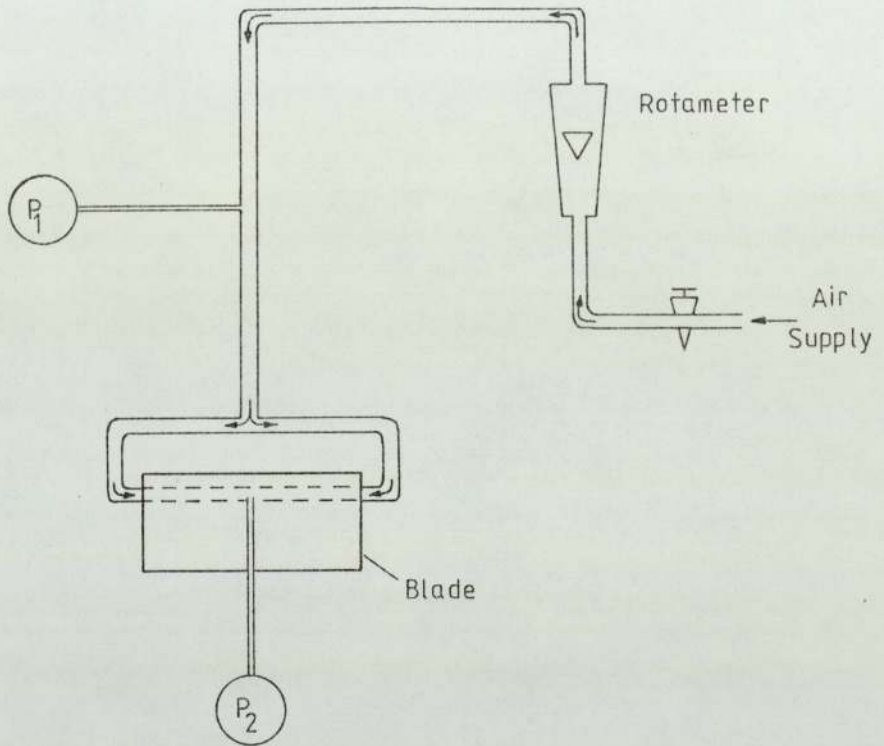
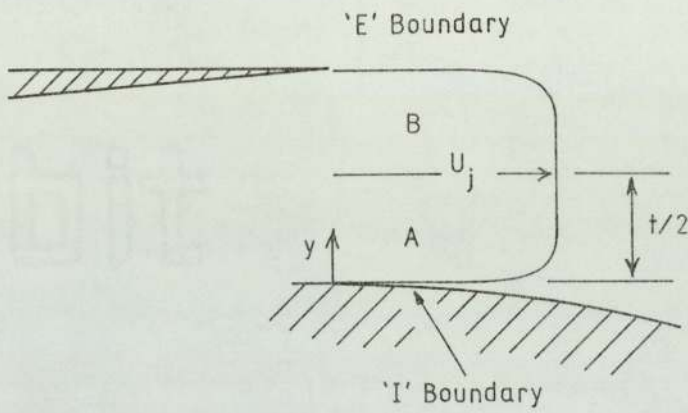


Figure 7
Blade Calibration
Arrangement



Region A: $\frac{u}{U_j} = \left(\frac{y}{t/2}\right)^{1/n}$

Region B: $\frac{u}{U_j} = \left(\frac{t-y}{t/2}\right)^{1/n}$

$$C_d = \frac{U_j \int_0^{t/2} \left(\frac{y}{t/2}\right)^{\frac{1}{n}} dy + U_j \int_{t/2}^t \left(\frac{t-y}{t/2}\right)^{\frac{1}{n}} dy}{U_j t}$$

Figure 8
Treatment of
Slot Velocity Profile

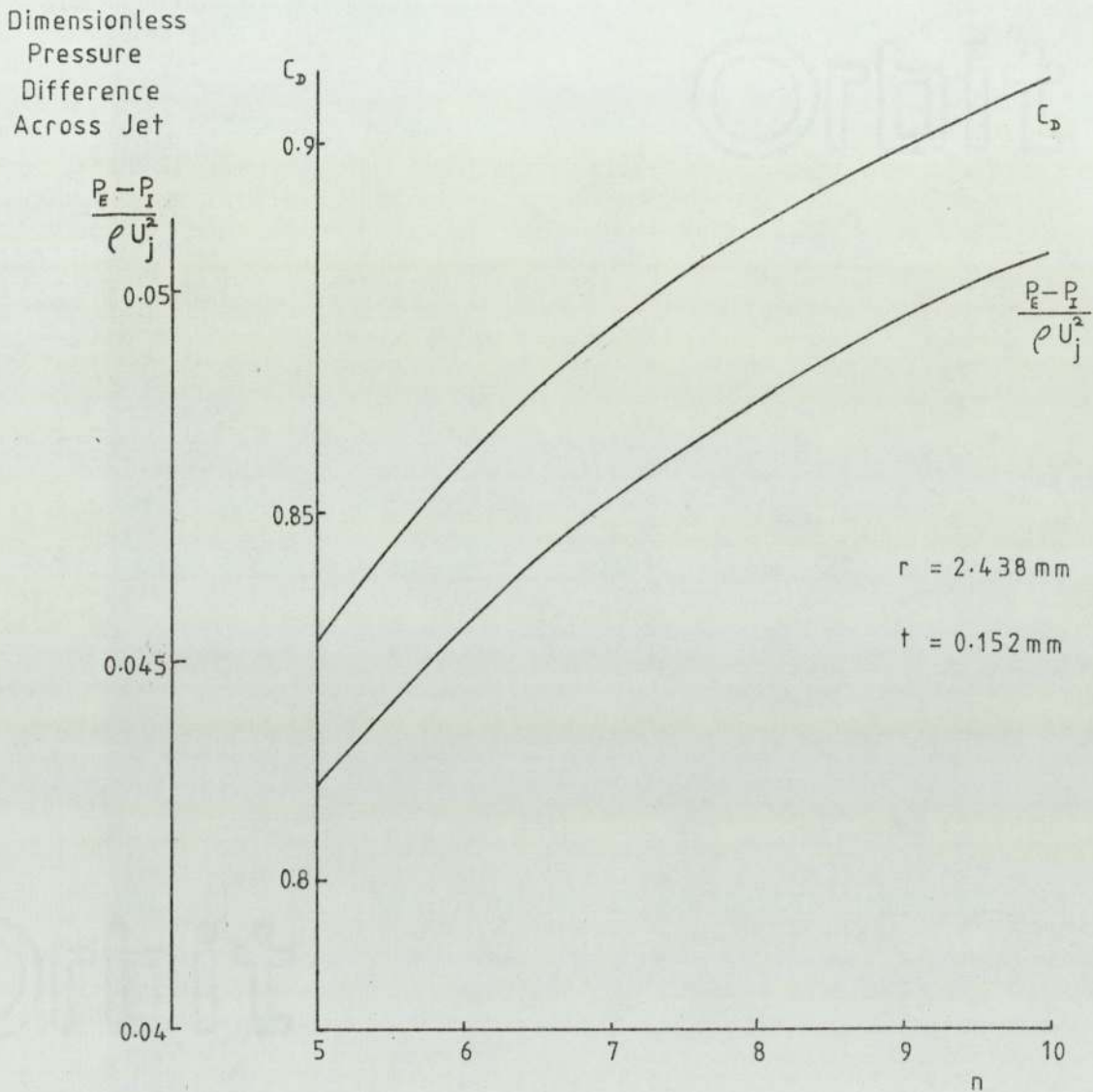


Figure 9
Variation of Discharge Coefficient
and Pressure Difference Across Jet
with Jet Shape Parameter n

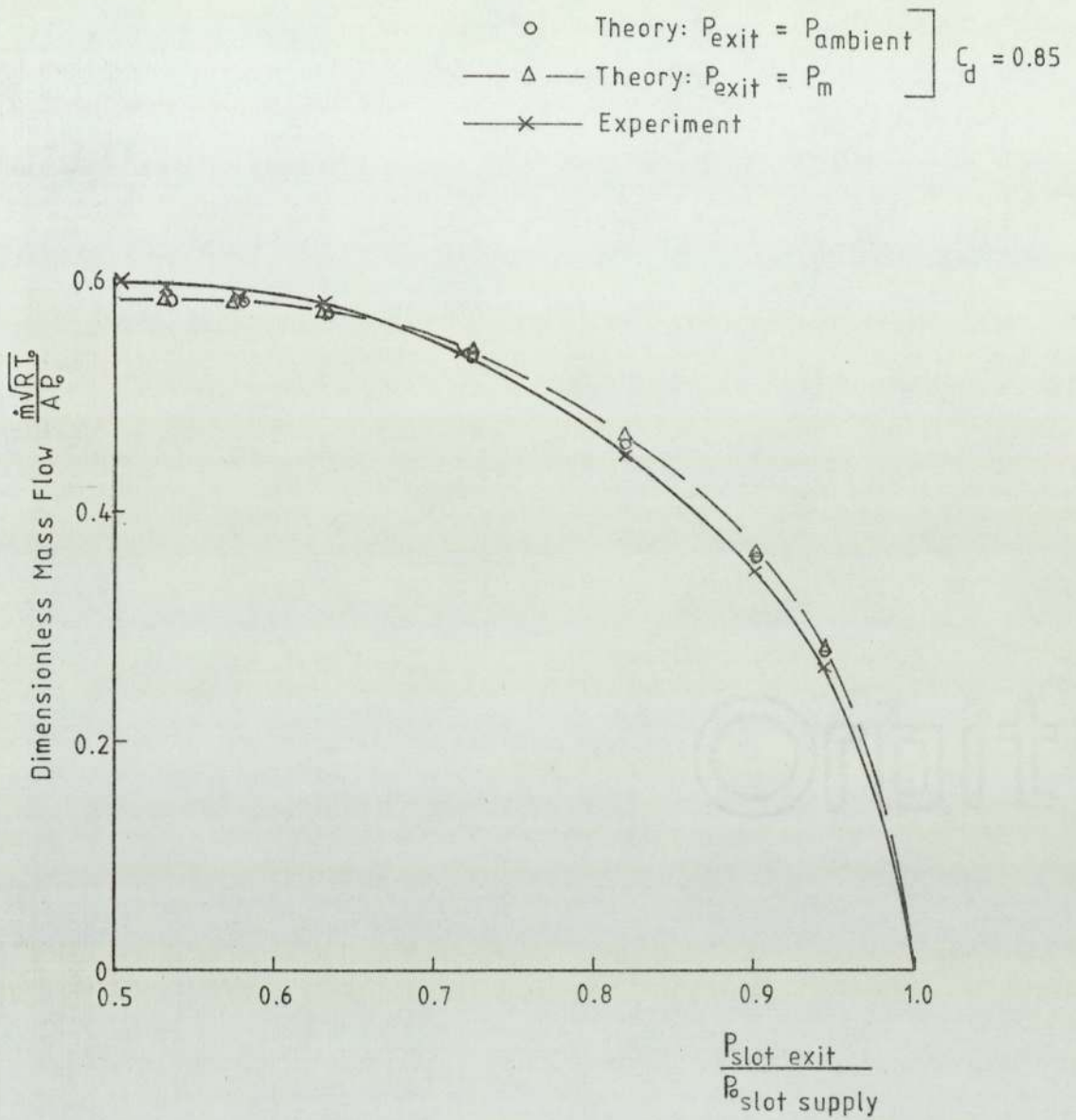


Figure 10
Blade Mass Flow
Calibration

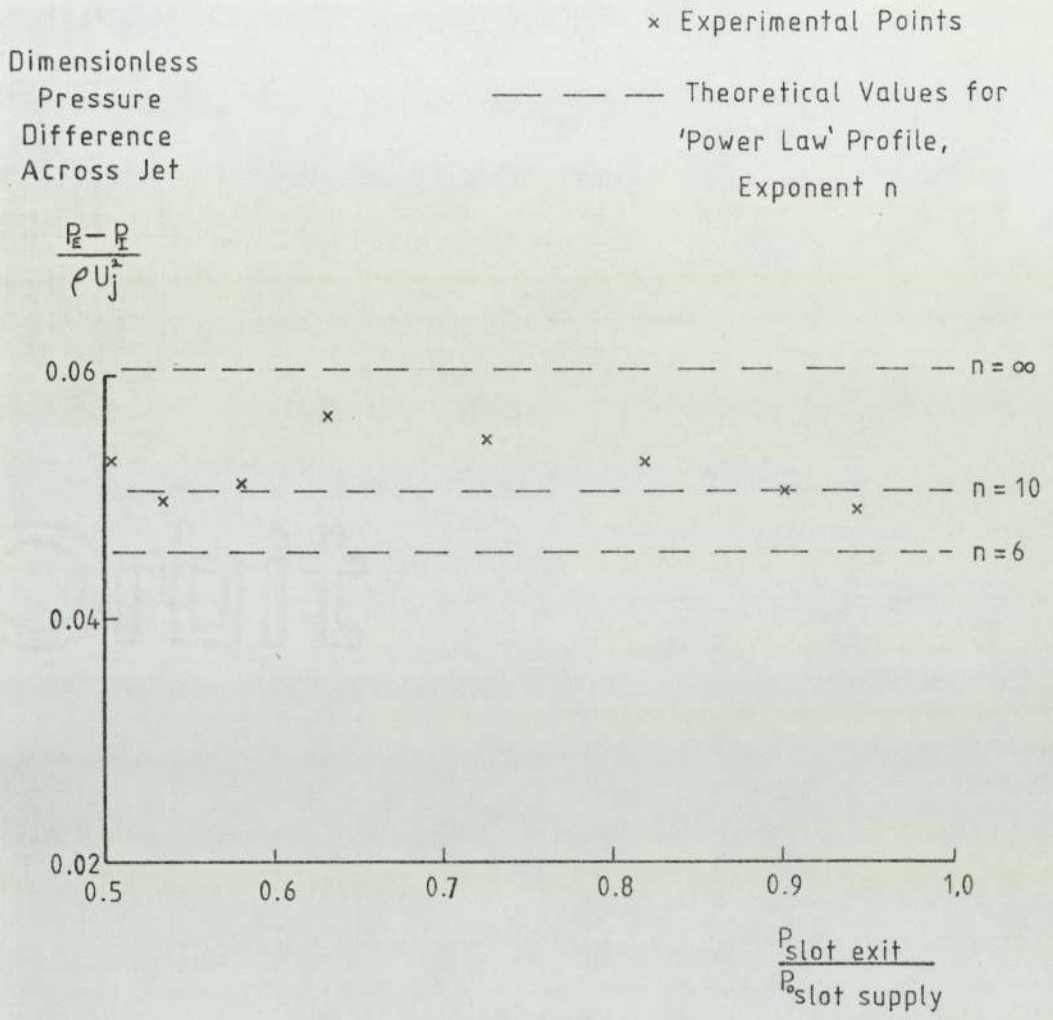


Figure 11
Measured
Pressure Difference
Across Jet



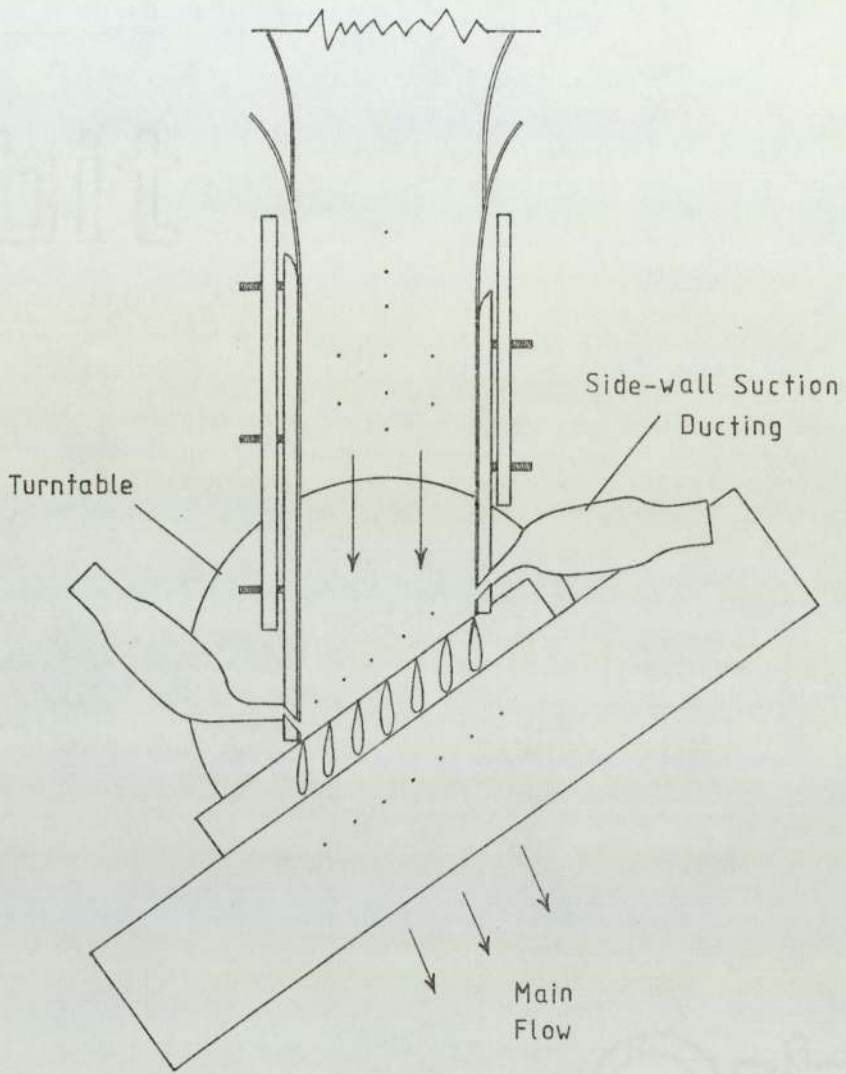


Figure 12
Sketch of the Cascade
Wind Tunnel

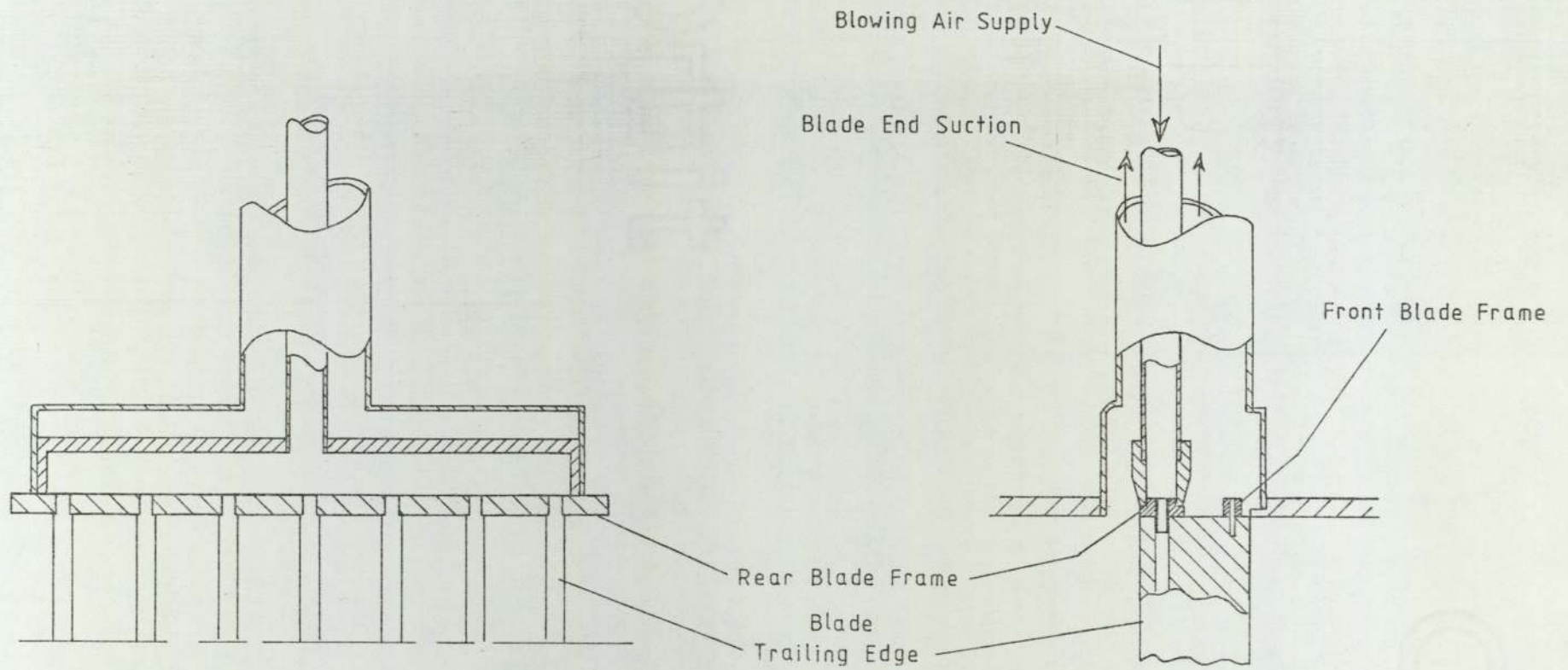
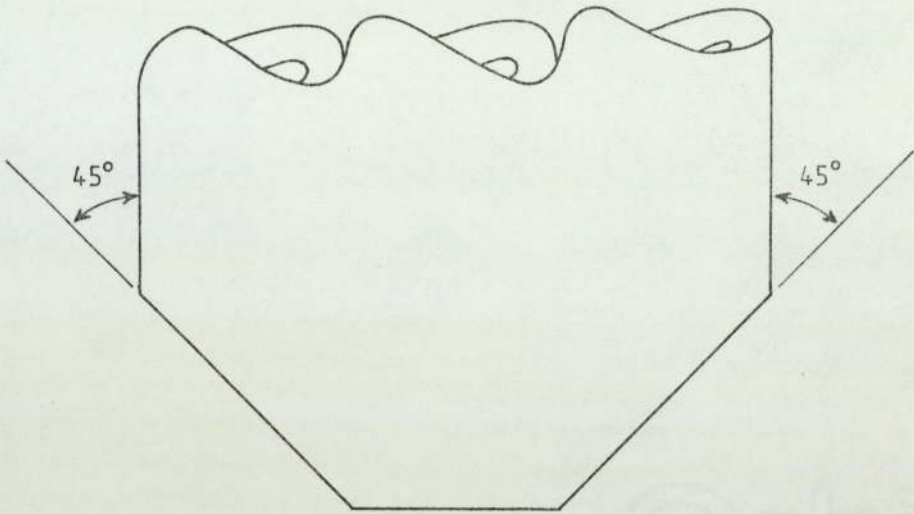


Figure 13
 Arrangement of Blowing Air Supply
 to Cascade



Tube Inner Diameter = 0.419mm
Outer Diameter = 0.712mm

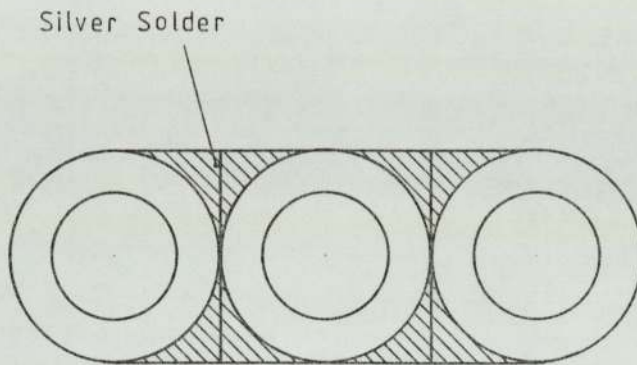


Figure 14
Tip of Probe
Used for Downstream
Total Pressure and Yaw Measurements

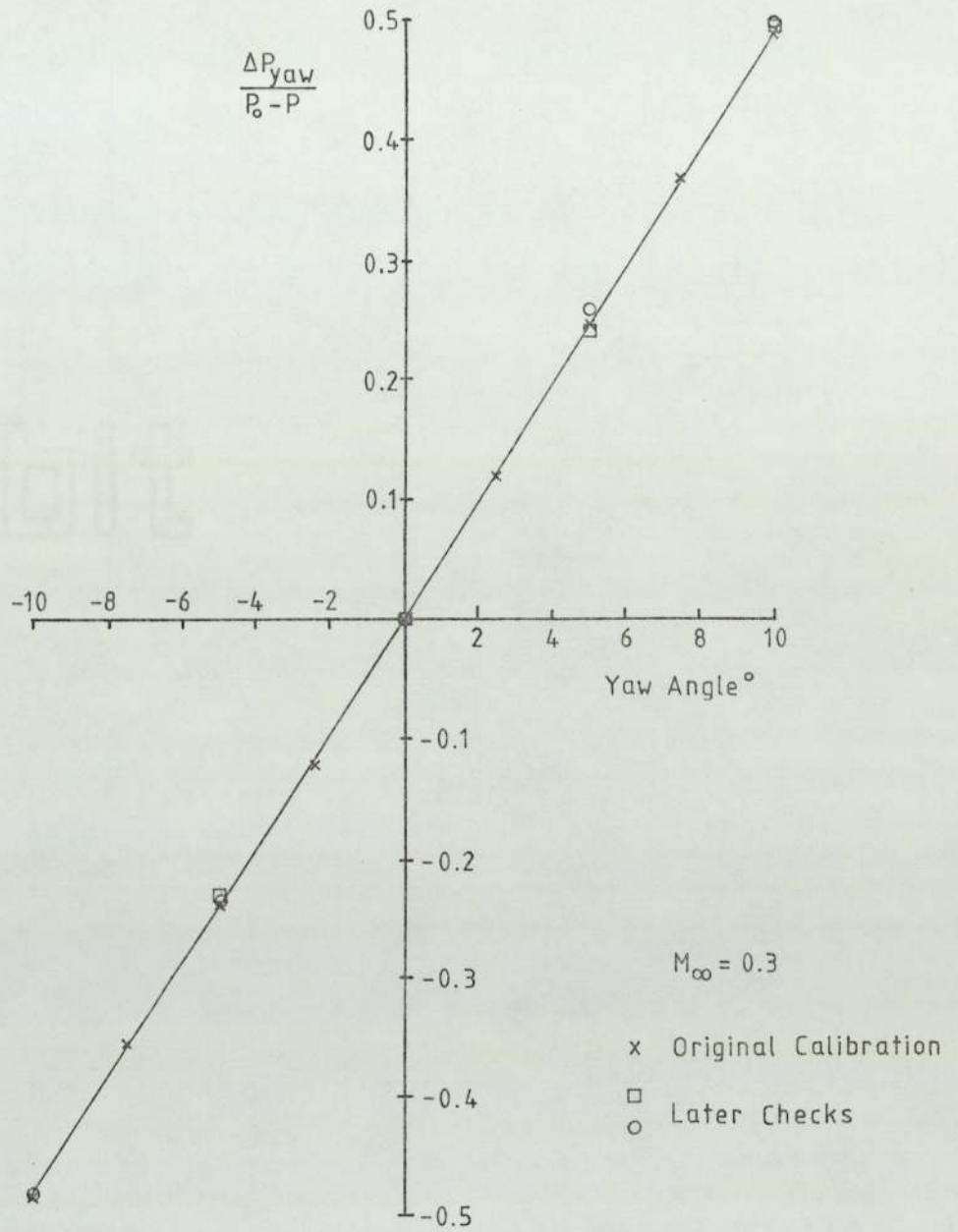


Figure 15
Yaw Probe
Calibration Curve

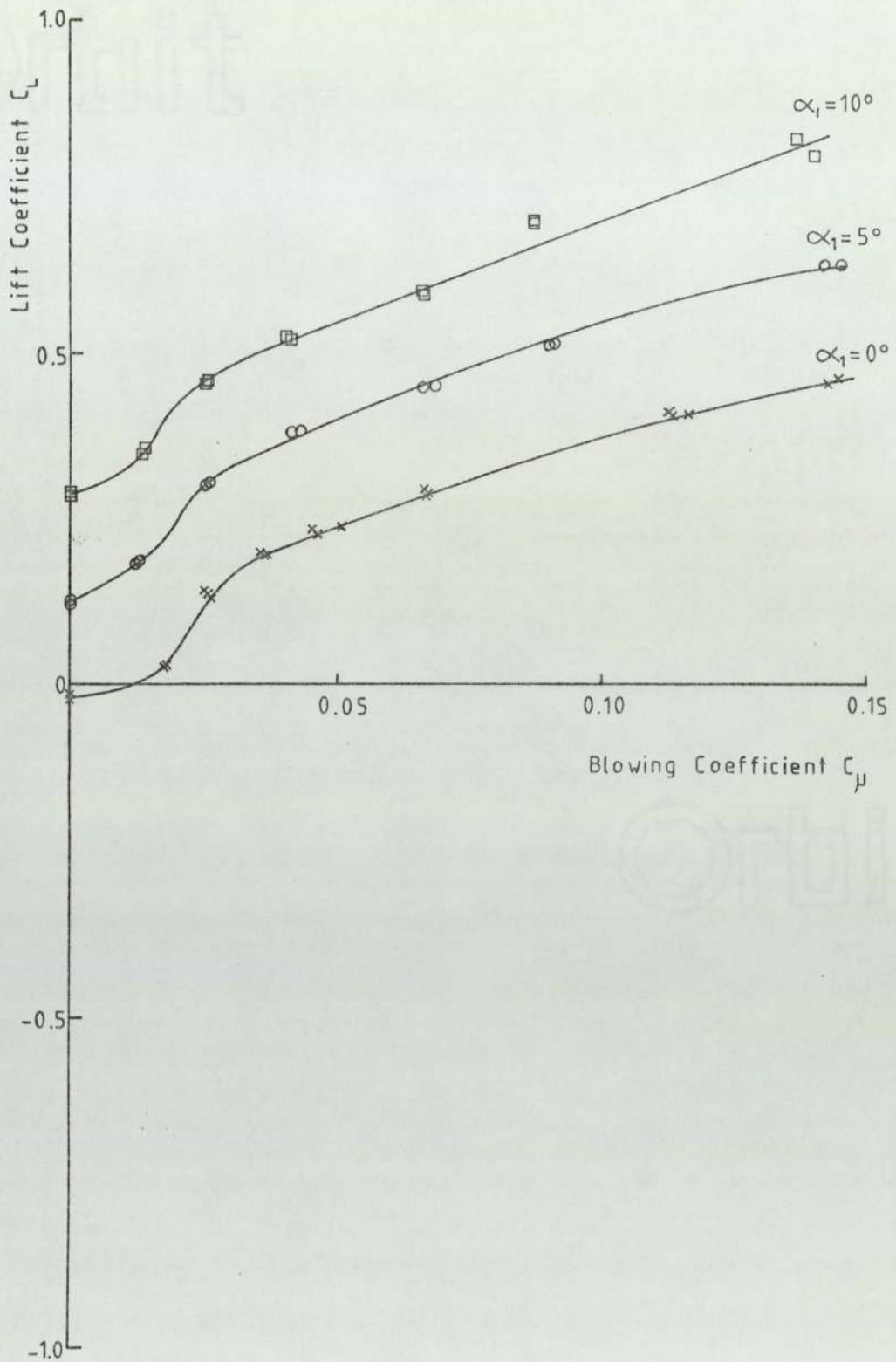


Figure 16
Variation of Lift Coefficient
with Momentum Coefficient
 $s/c = 1.0$, $\xi = 0^\circ$

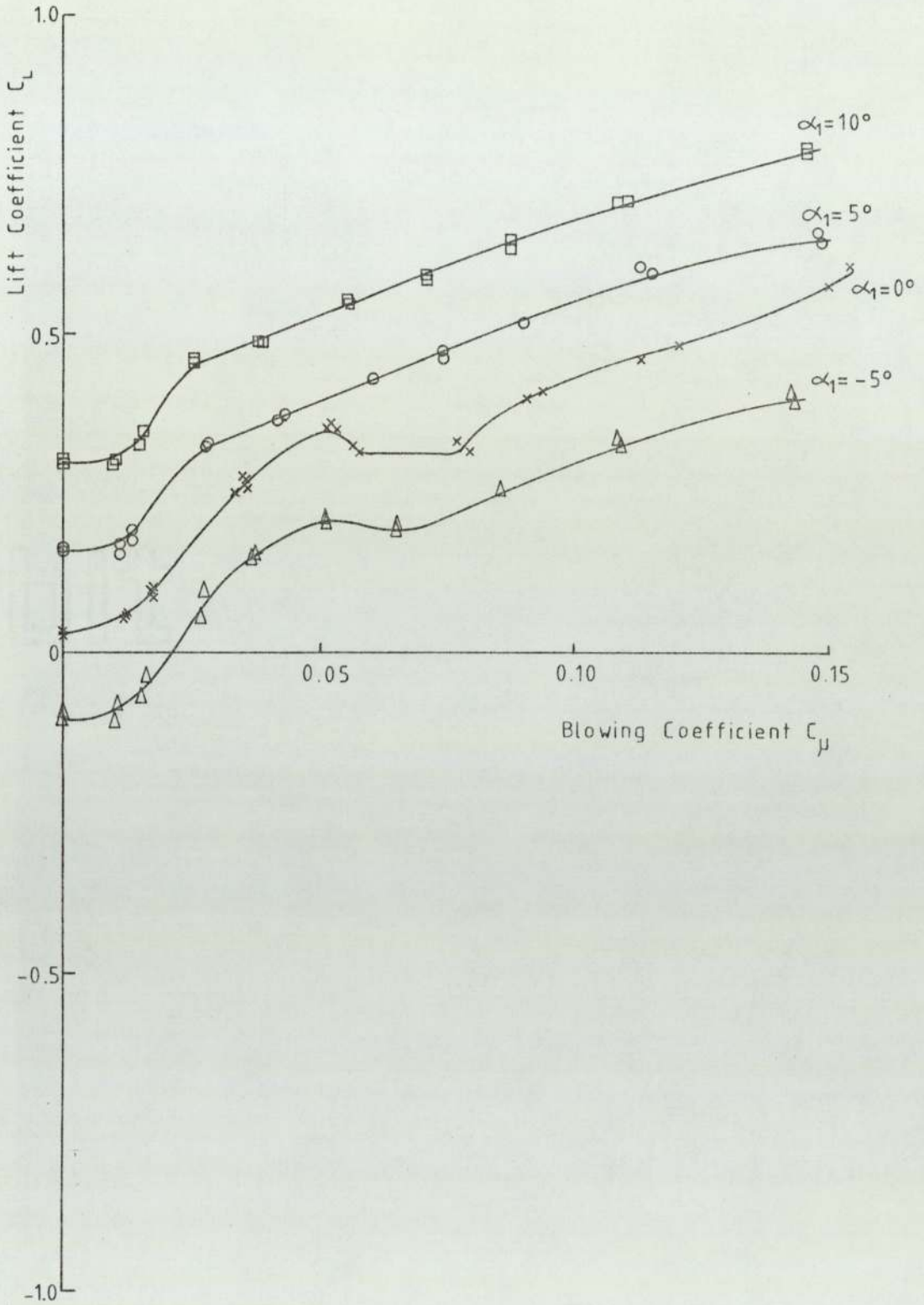


Figure 17
Variation of Lift Coefficient
with Momentum Coefficient
 $s/c = 0.75, \xi = 0^\circ$

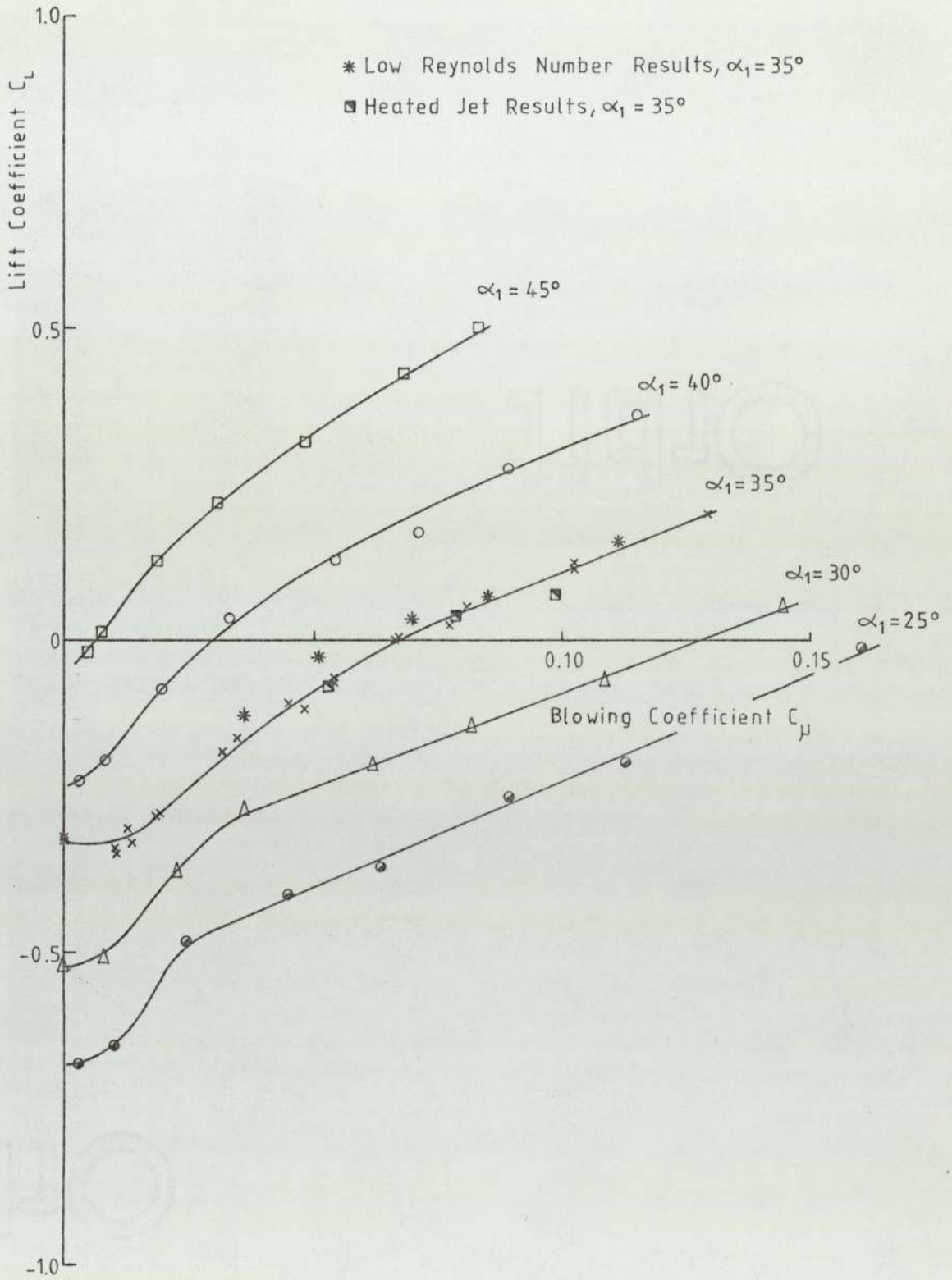


Figure 18
Variation of Lift Coefficient
with Momentum Coefficient
 $s/c = 0.75, \xi = 35^\circ$

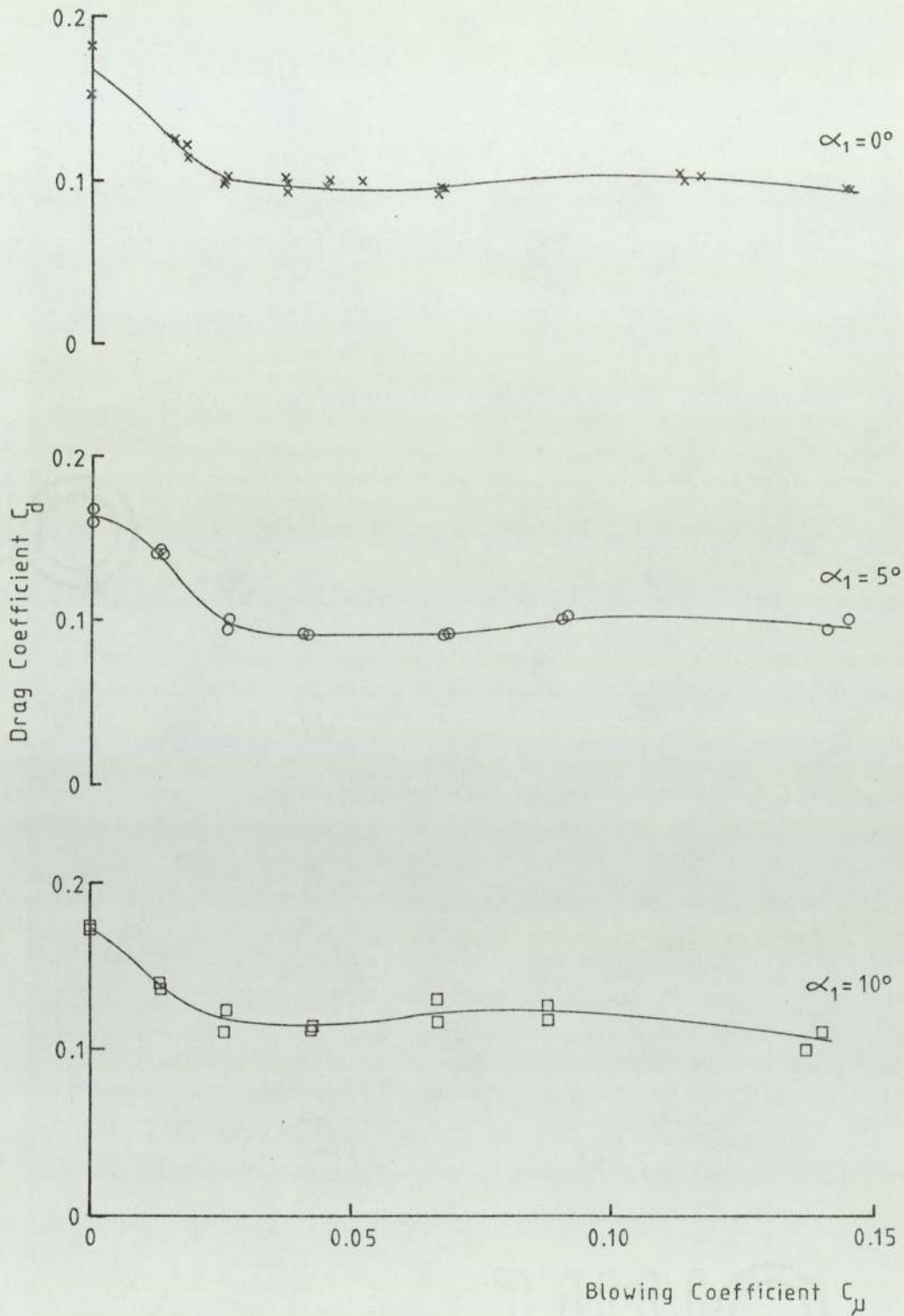


Figure 19
Variation of Drag Coefficient
with Momentum Coefficient
 $s/c = 1.0, \quad \xi = 0^\circ$

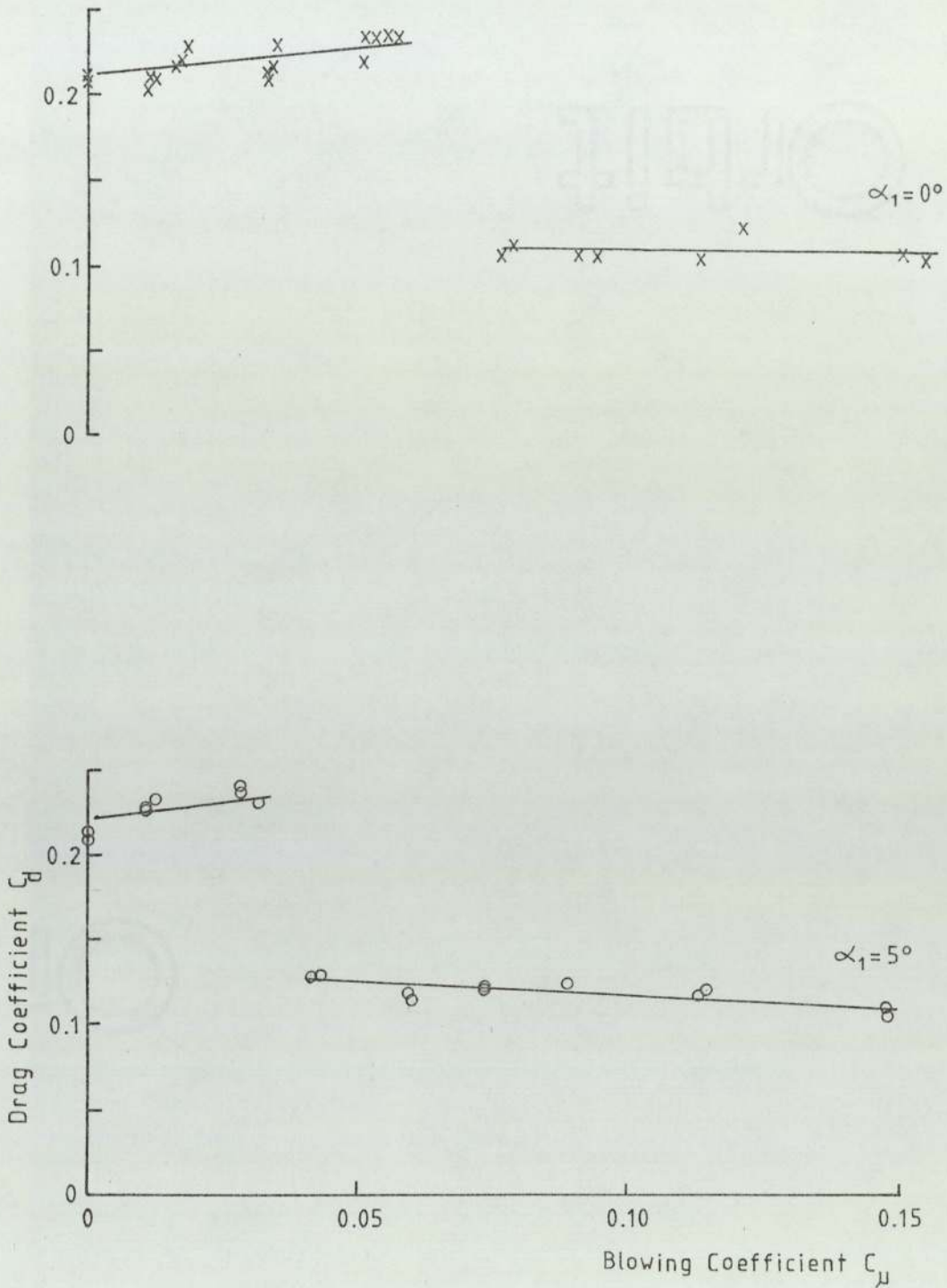


Figure 20
Variation of Drag Coefficient
with Momentum Coefficient
 $s/c = 0.75, \xi = 0^\circ$

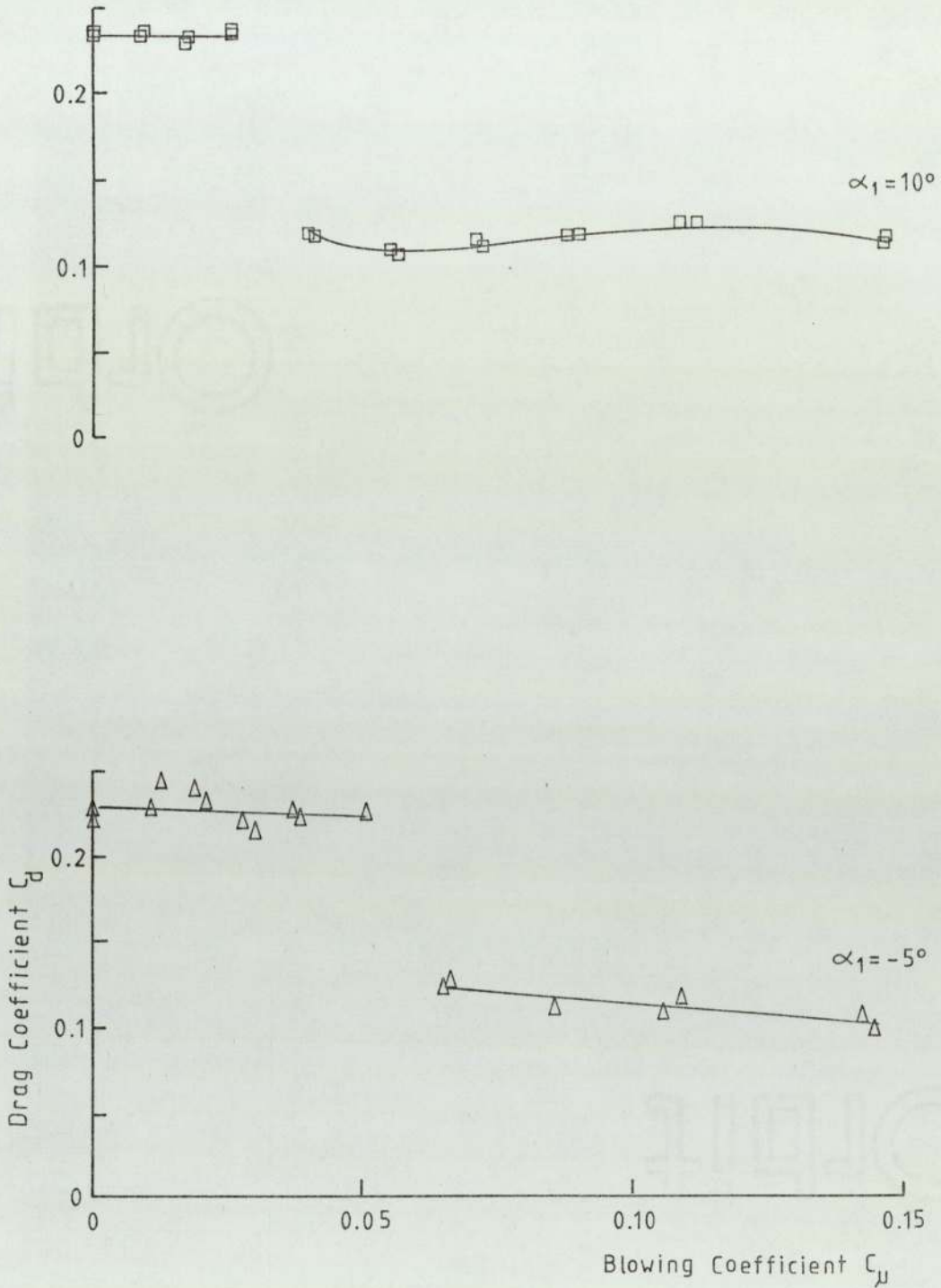


Figure 21
Variation of Drag Coefficient
with Momentum Coefficient
 $s/c = 0.75, \xi = 0^\circ$

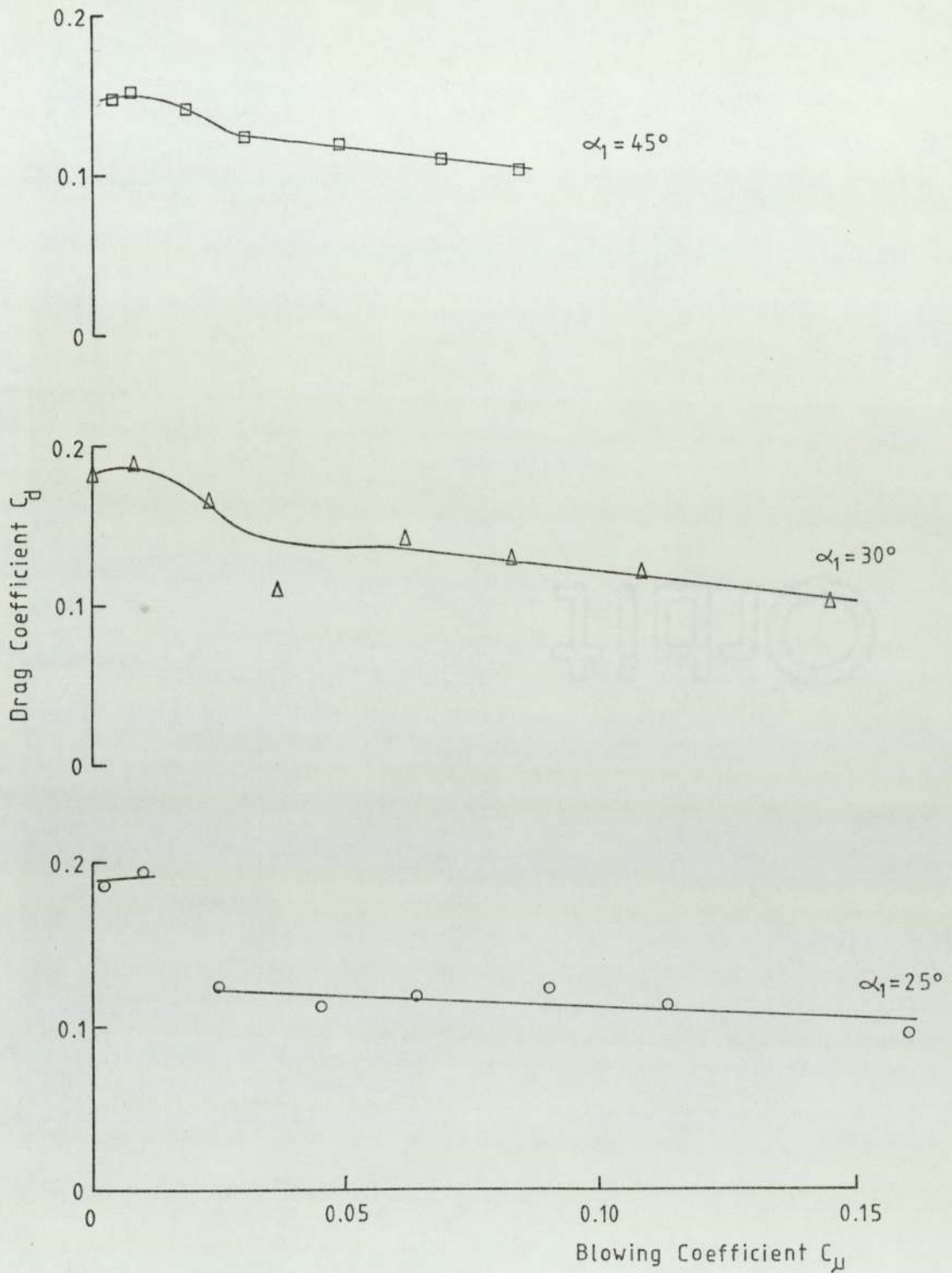


Figure 22
Variation of Drag Coefficient
with Momentum Coefficient
 $s/c = 0.75, \xi = 35^\circ$

- * Low Reynolds Number Results
- Heated Jet Results

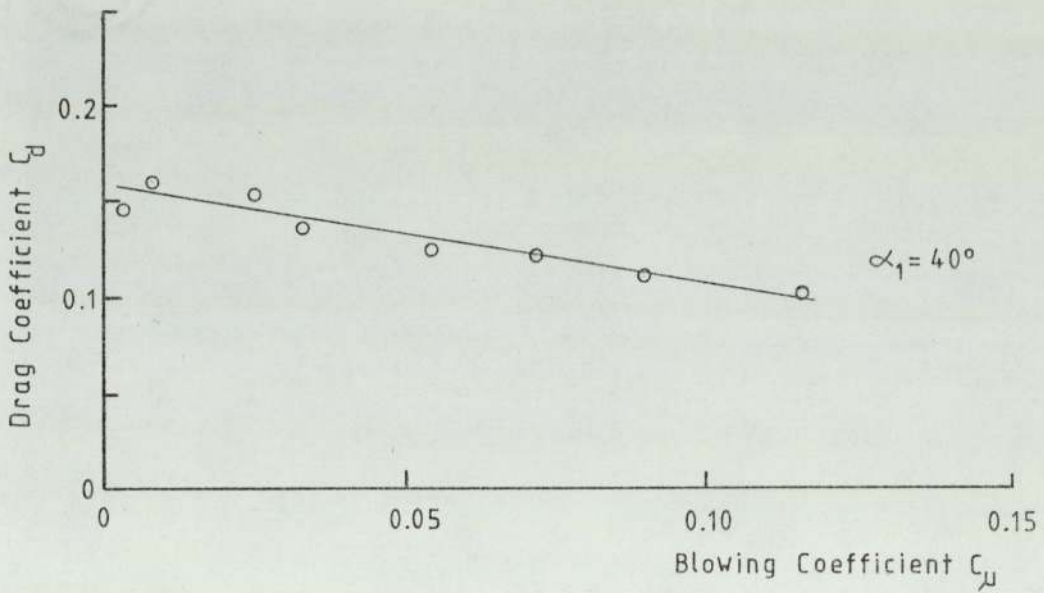
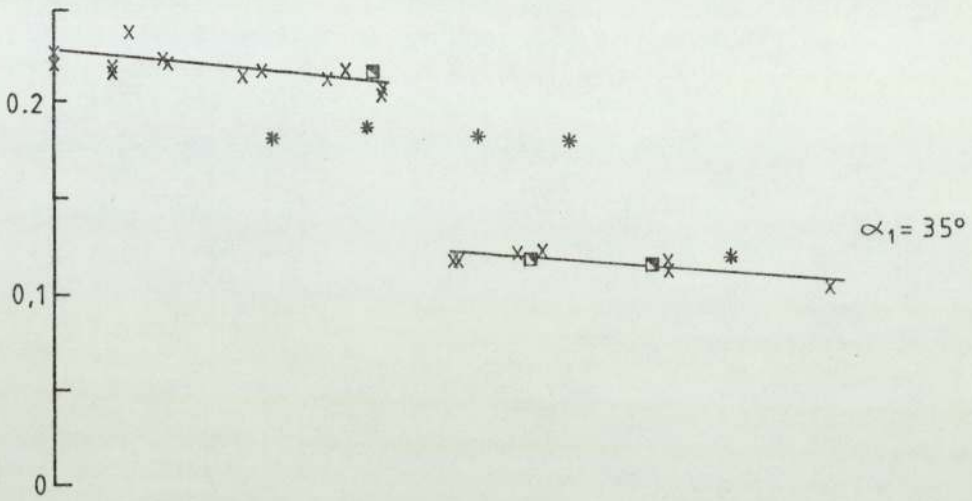


Figure 23
Variation of Drag Coefficient
with Momentum Coefficient
 $s/c = 0.75, \xi = 35^\circ$

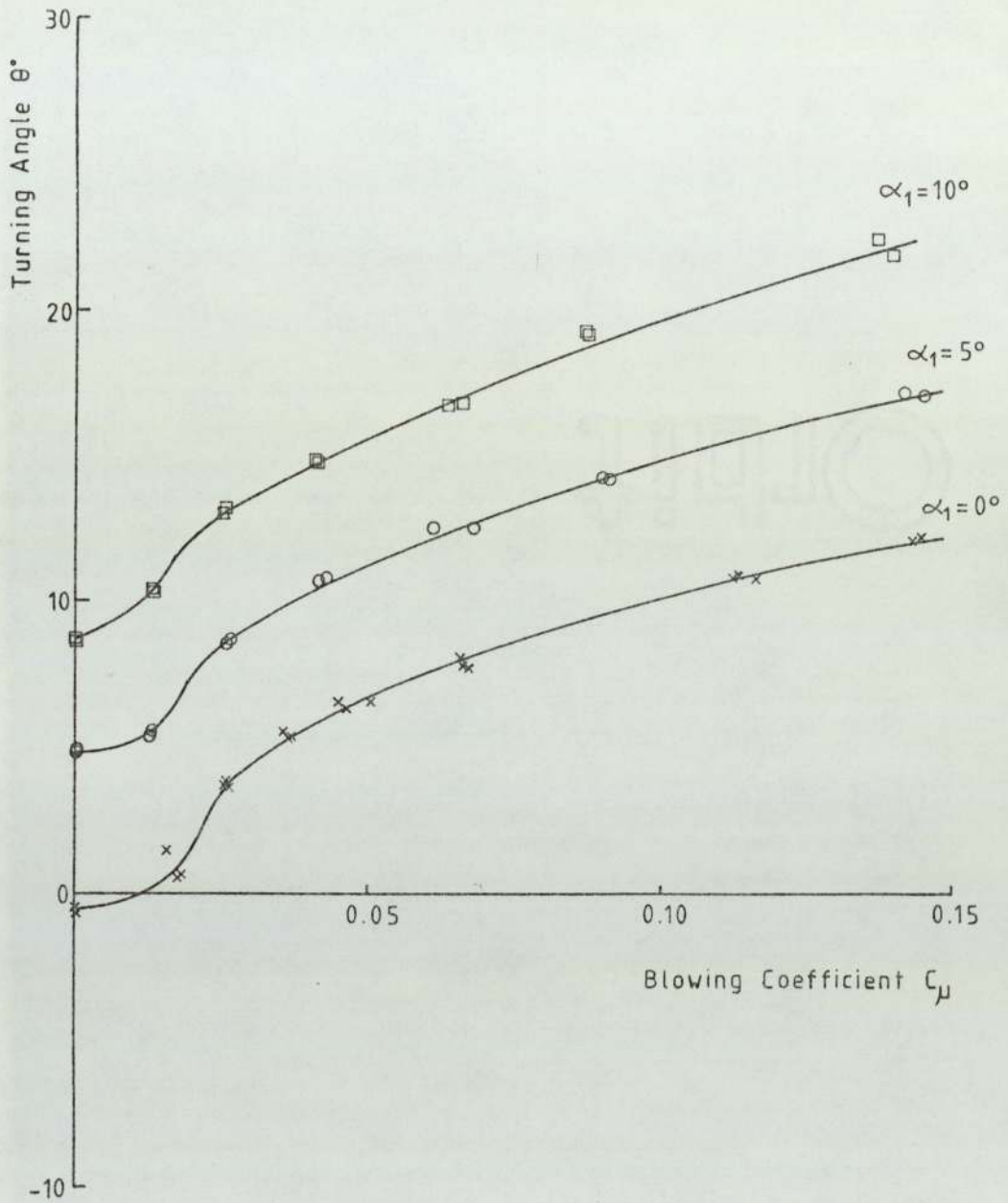


Figure 24
Variation of Turning Angle
with Momentum Coefficient
 $s/c = 1.0, \quad \xi = 0^\circ$

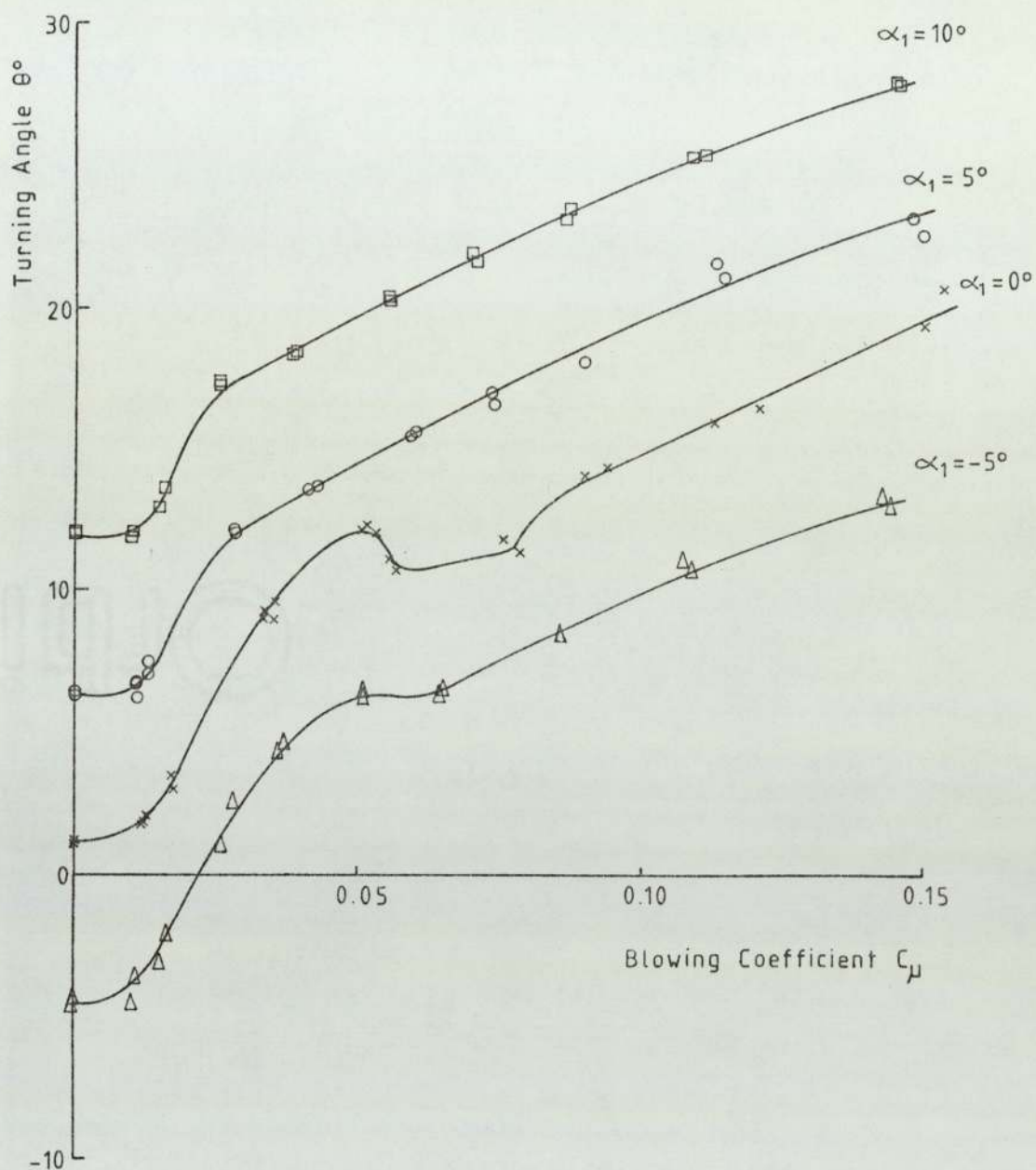


Figure 25
Variation of Turning Angle
with Momentum Coefficient
 $s/c = 0.75, \quad \xi = 0^\circ$

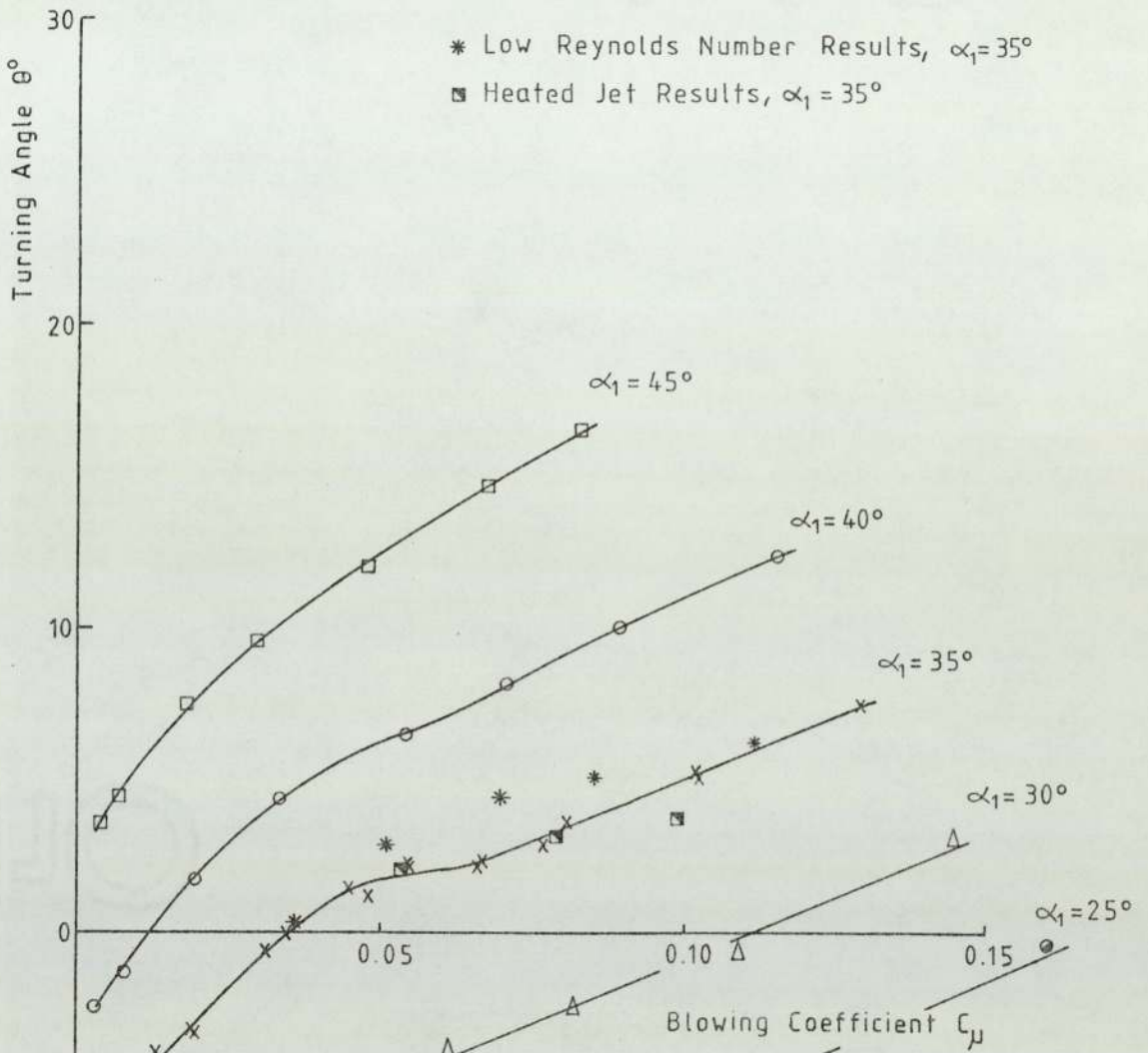
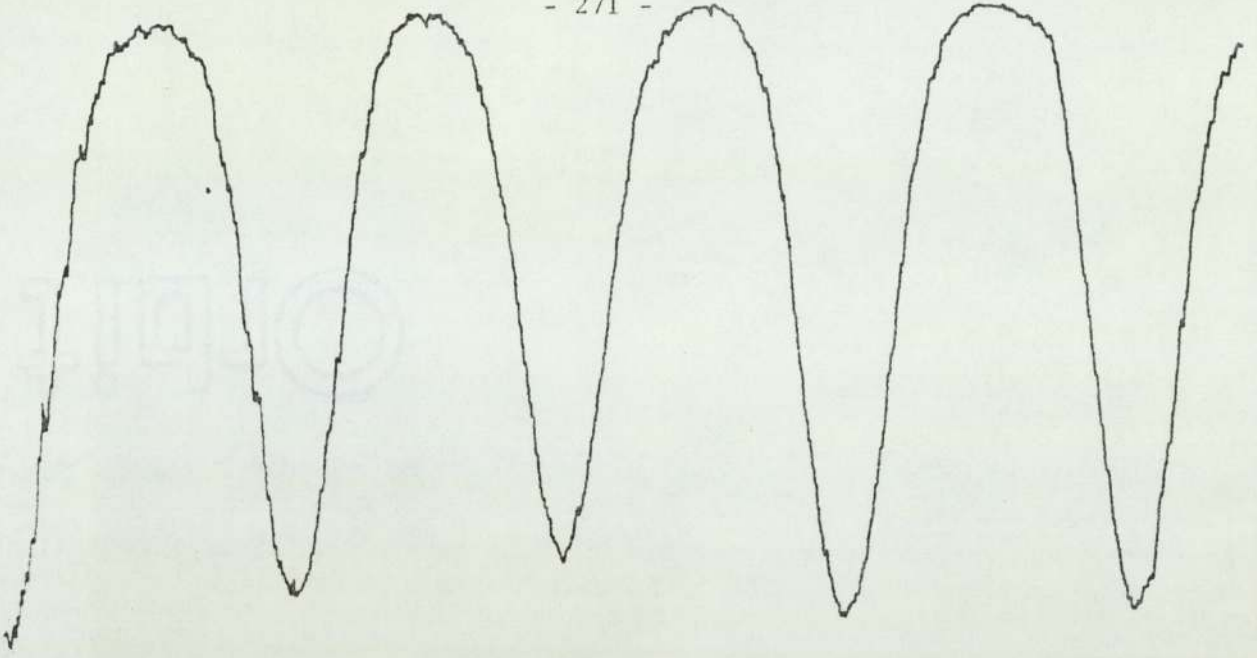
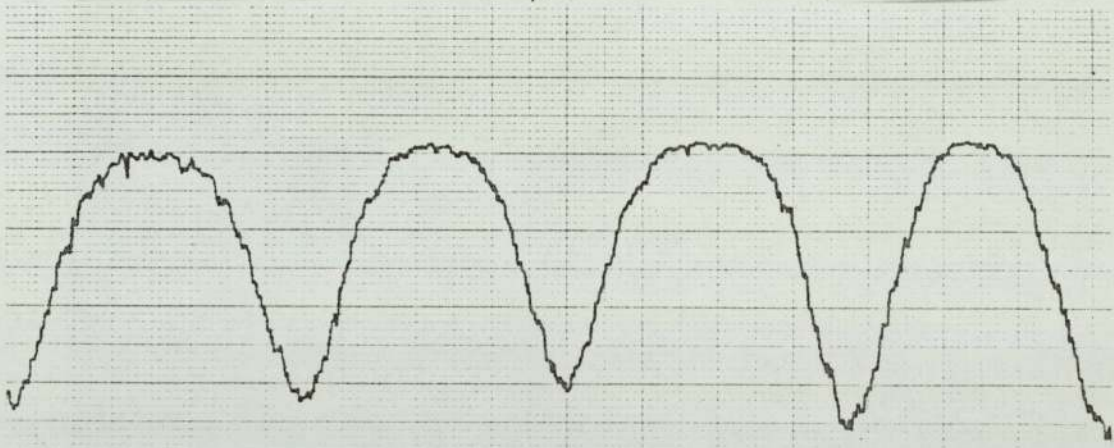


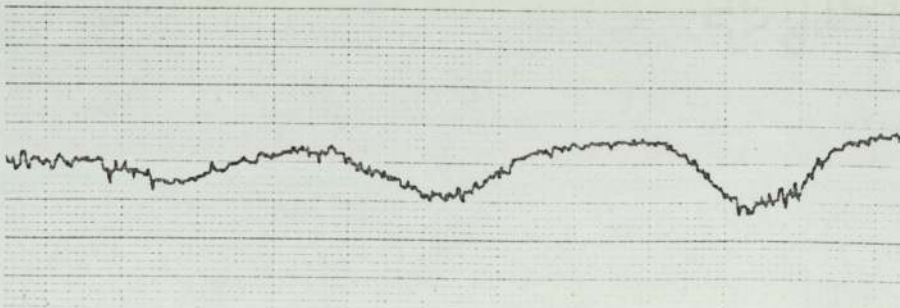
Figure 26
Variation of Turning Angle
with Momentum Coefficient
 $s/c = 0.75$, $\xi = 35^\circ$



(a) $C_{\mu} = 0.013$



(b) $C_{\mu} = 0.043$

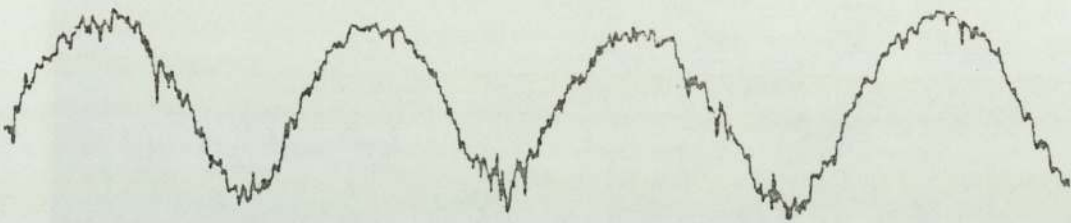


(c) $C_{\mu} = 0.149$

Figure 27
Variation of Downstream
Total Pressure Profile
with Blowing Coefficient
 $s/c = 0.75$, $\xi = 0^\circ$, $\alpha_1 = 5^\circ$



(a) $C_{\mu} = 0.0076$



(b) $C_{\mu} = 0.054$



(c) $C_{\mu} = 0.115$

Figure 28
Variation of Downstream
Total Pressure Profile
with Blowing Coefficient
 $s/c = 0.75$, $\xi = 35^\circ$, $\alpha_1 = 40^\circ$

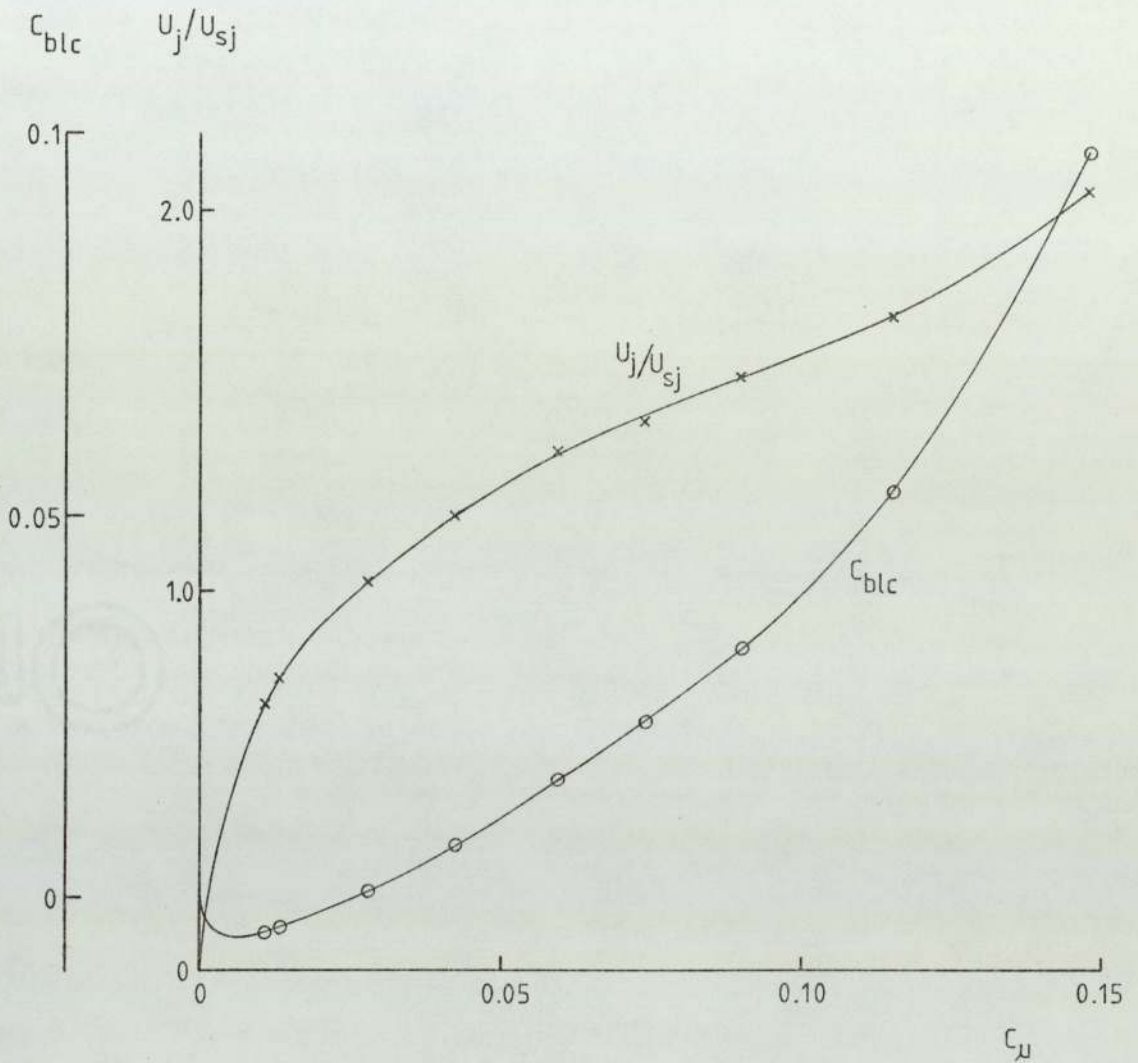


Figure 29
Relationships Between
Blowing Momentum Coefficient,
Slot Velocity Ratio
and
Boundary Layer Control Coefficient.
 $s/c = 0.75, \xi = 0^\circ, \alpha_1 = 5^\circ$

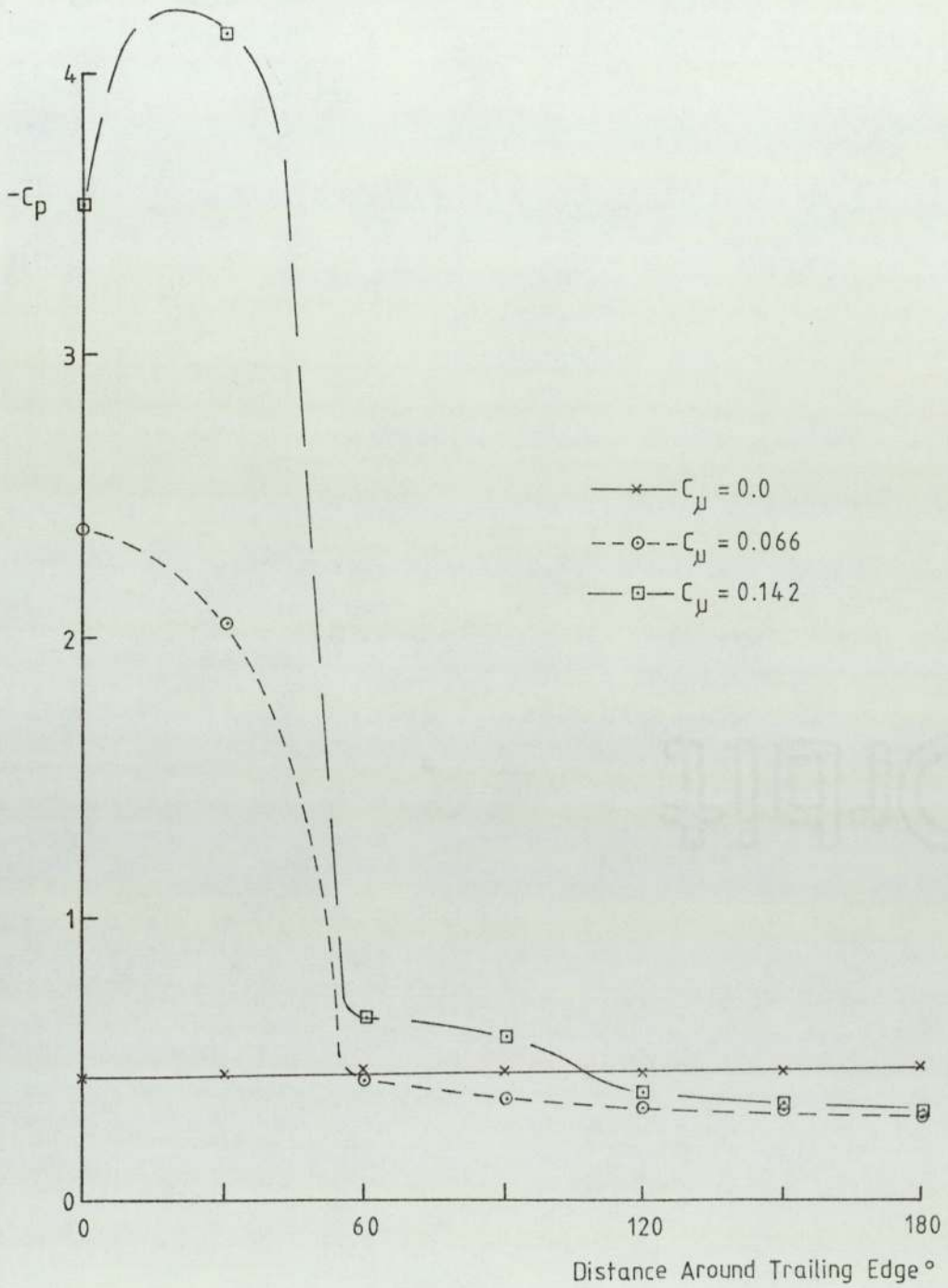


Figure 30
Pressure Distributions
Around Trailing Edge
 $s/c = 1.0, \xi = 0, \alpha_1 = 5^\circ$

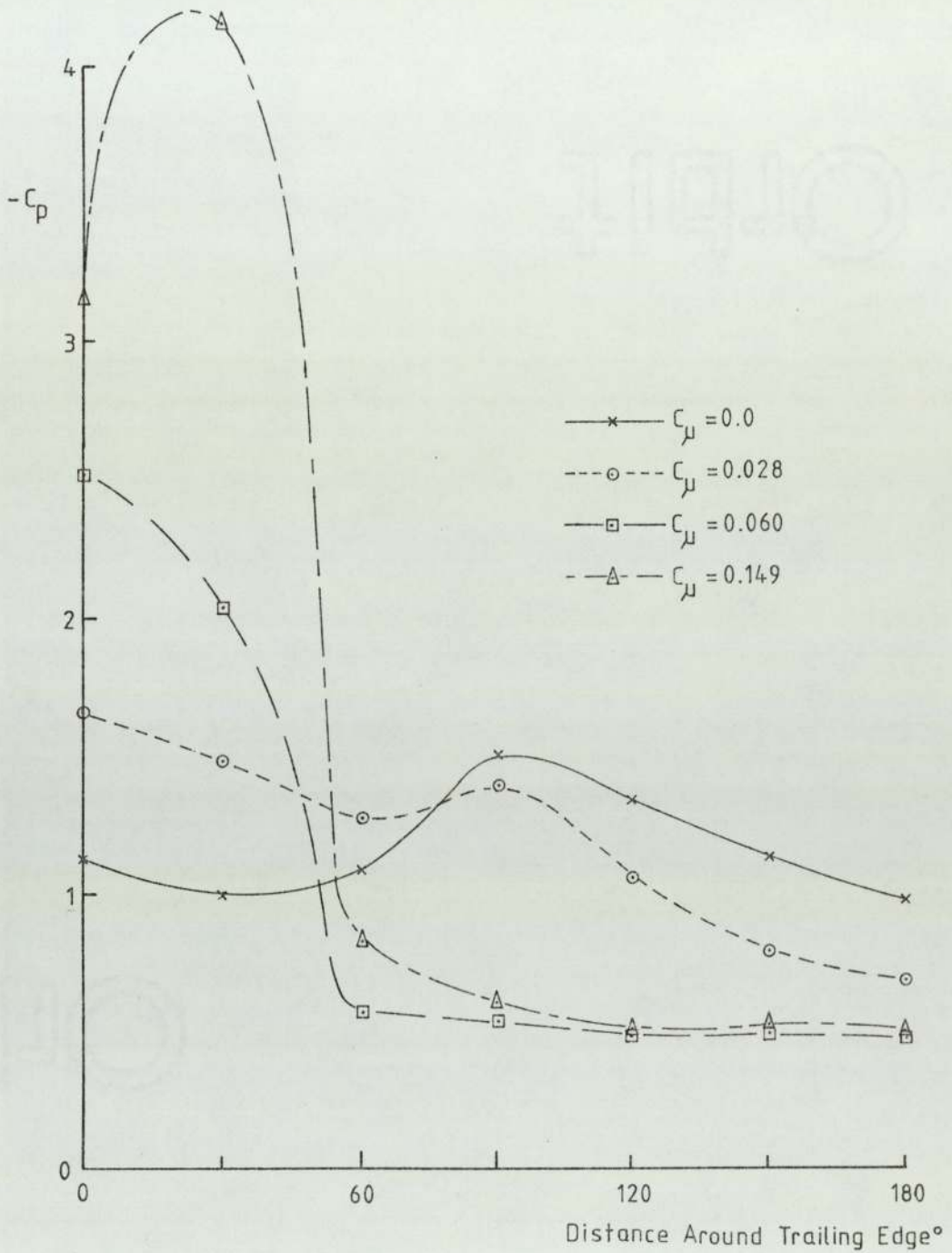
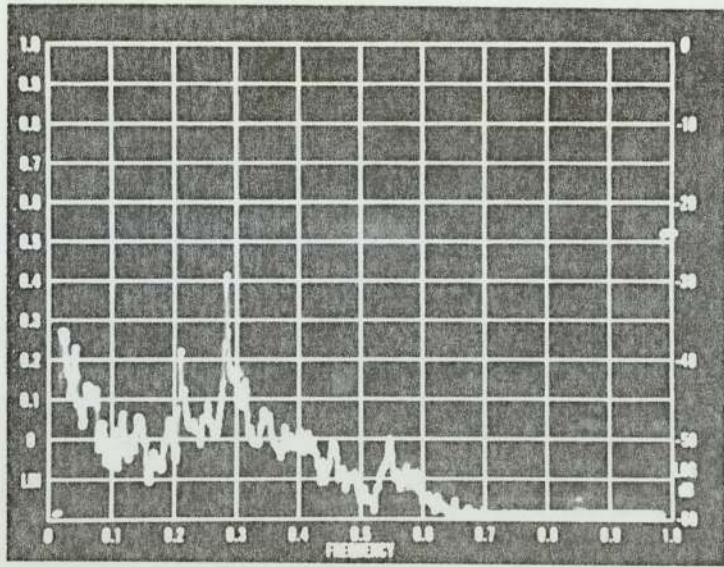
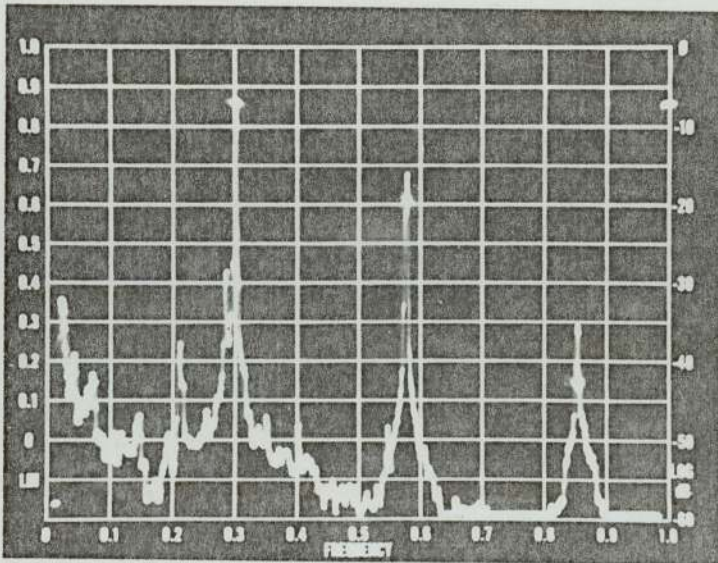


Figure 31
Pressure Distributions
Around Trailing Edge
 $s/c = 0.75, \xi = 0, \alpha_1 = 5^\circ$



Background Noise Only
(Frequency Scale = 20 kHz)



Background Noise with Whistle

Figure 32
Sound Intensity Spectra
Recorded Behind Cascade

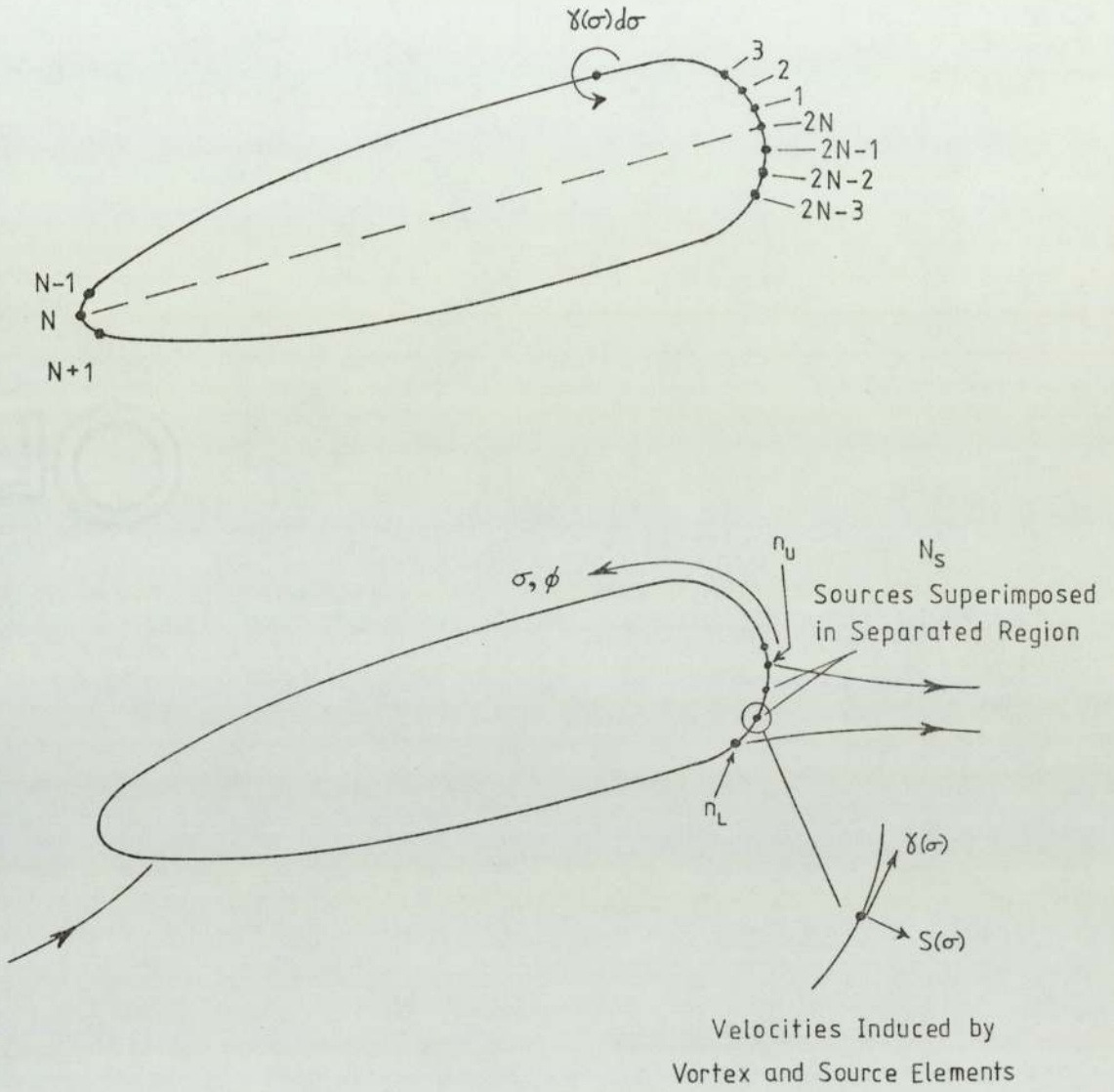


Figure 33
Pivotal Point Numbering System

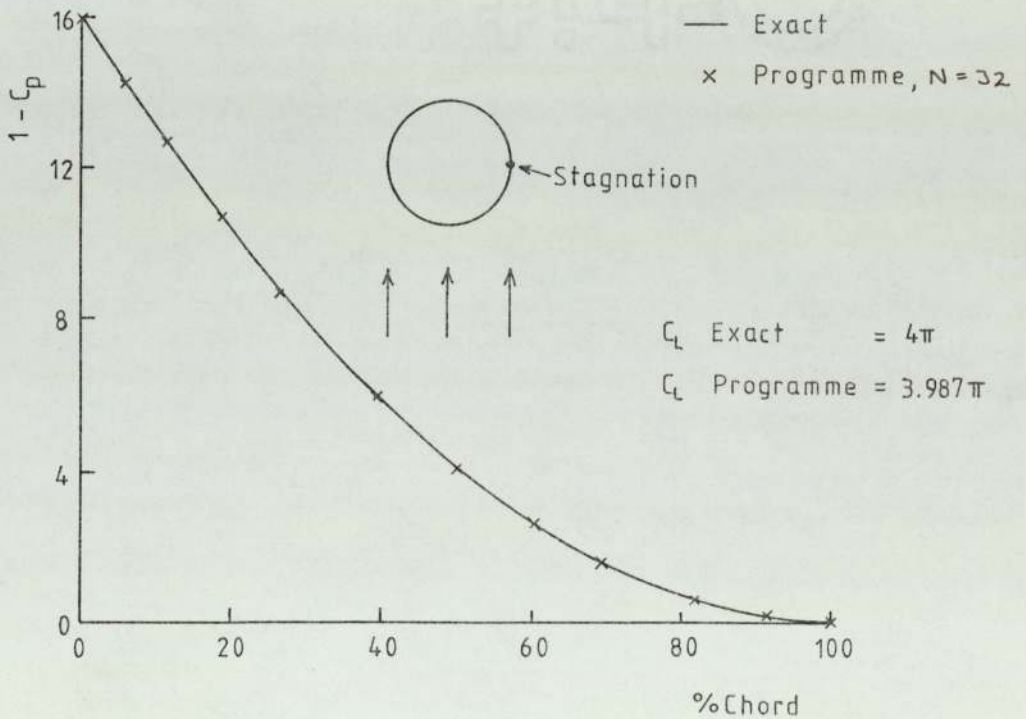
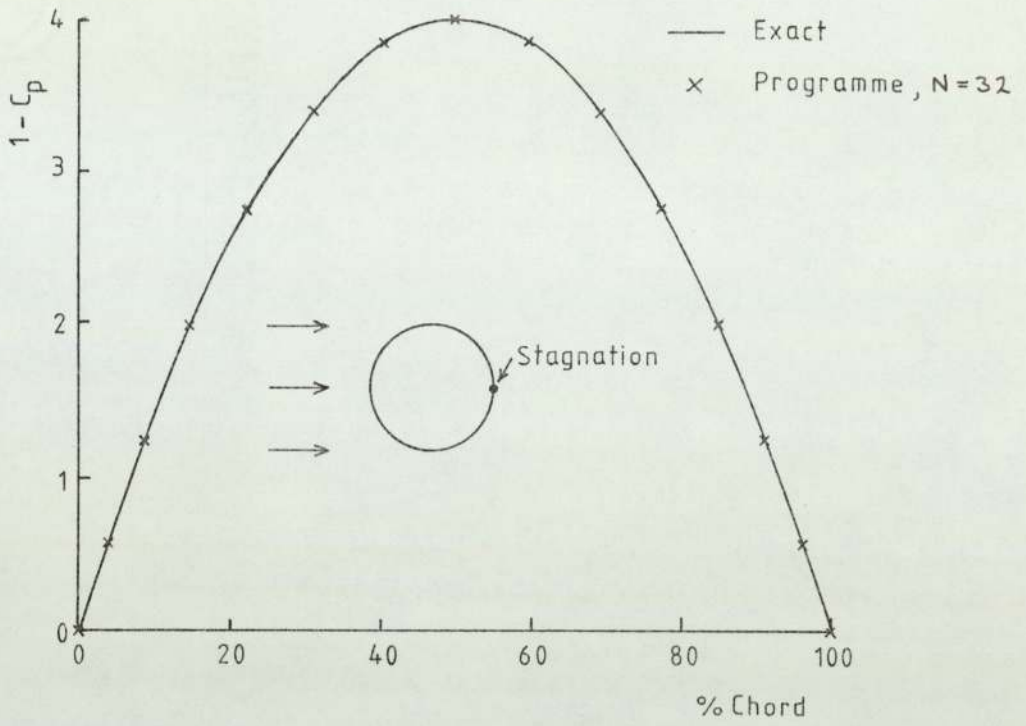


Figure 34
Comparison of Exact and Computed
Pressure Distributions about a
Circular Cylinder

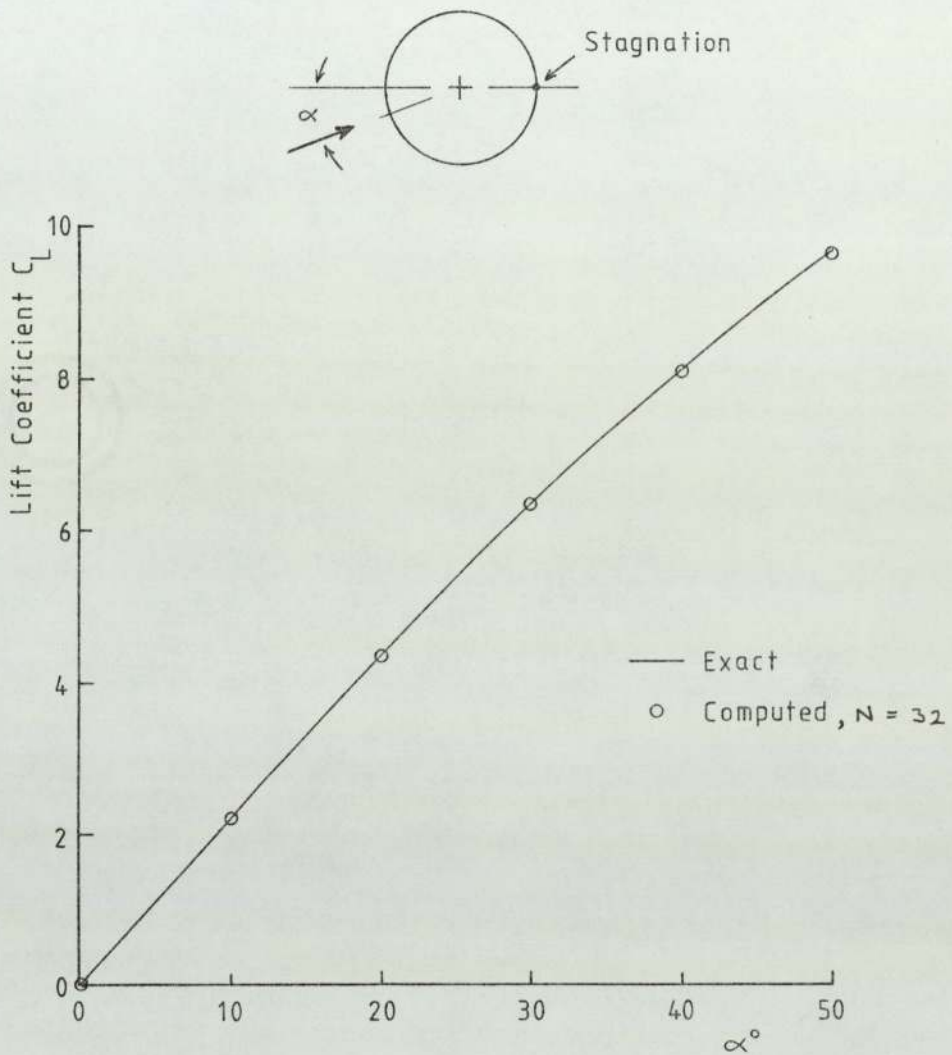


Figure 35
Comparison of Exact and Computed
Variation of Lift Coefficient with Incidence
for a Circular Cylinder

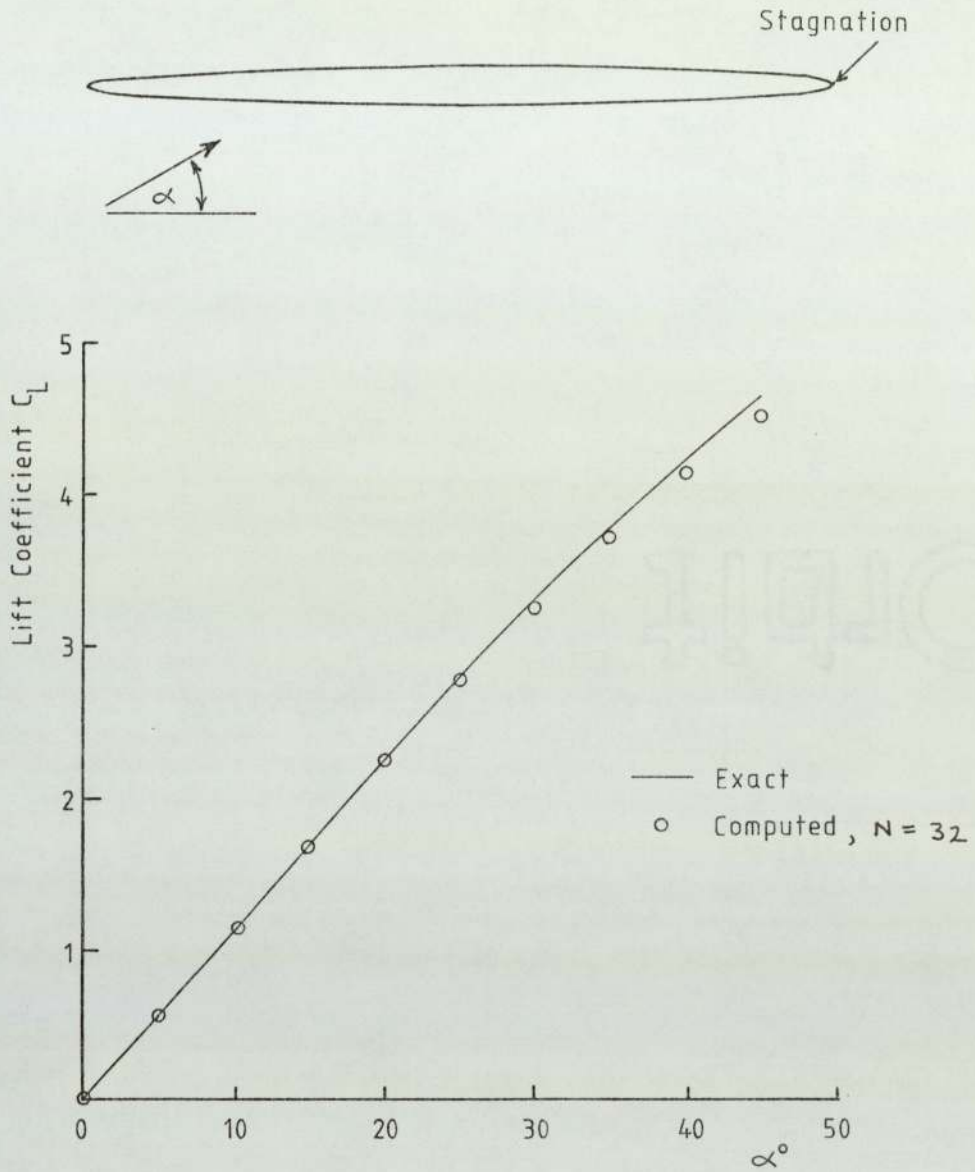
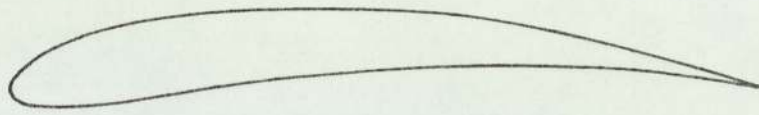


Figure 36
Comparison of Exact and Computed
Variation of Lift Coefficient with Incidence
for a 5% Ellipse



$S/C = 0.99016$, $\xi = 37.5^\circ$

$\alpha_1 = 53.5^\circ$

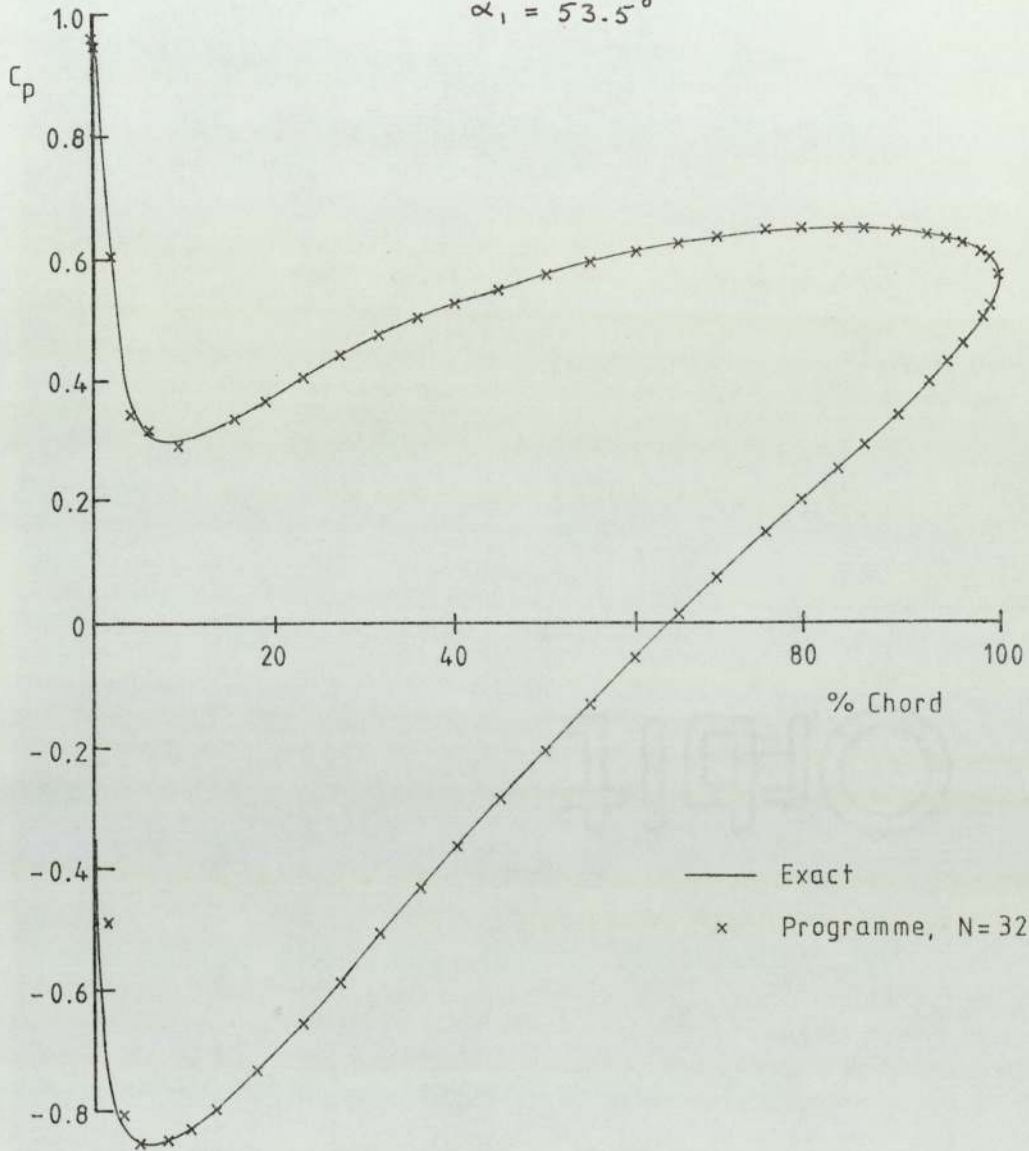


Figure 37
Comparison of Exact and Computed
Pressure Distributions about the
Cascade of Merchant and Collar

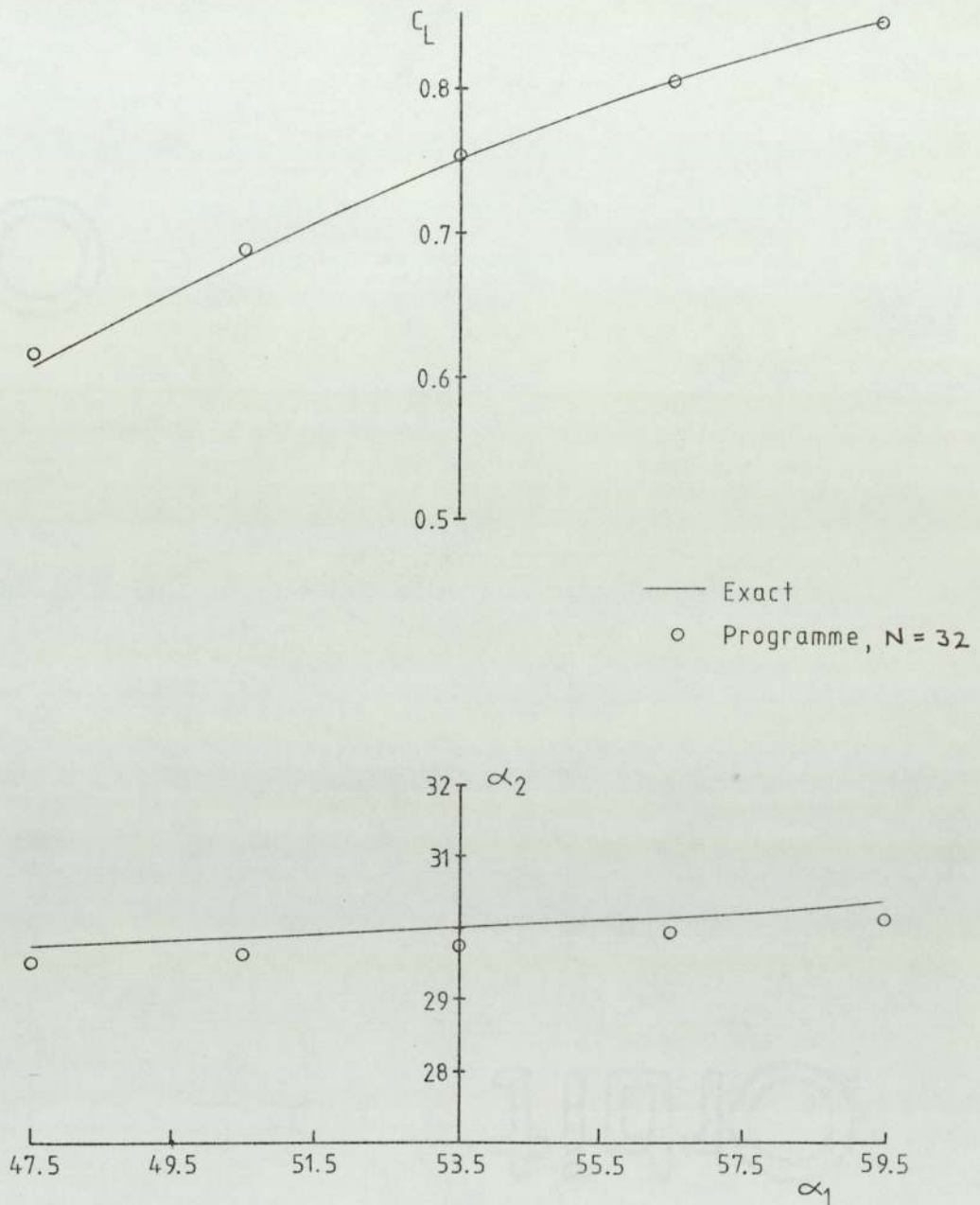
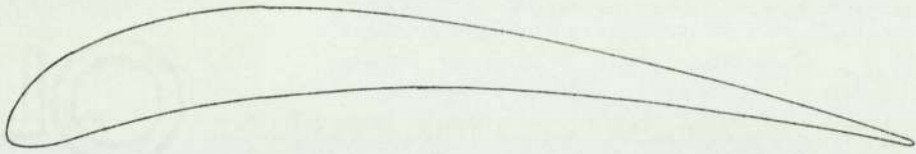


Figure 38
Comparison of Exact and Computed
Variations of Lift and Outlet Angle
with Inlet Angle.
Cascade of Merchant and Collar



S/C = 0.6667, Camber = 65°

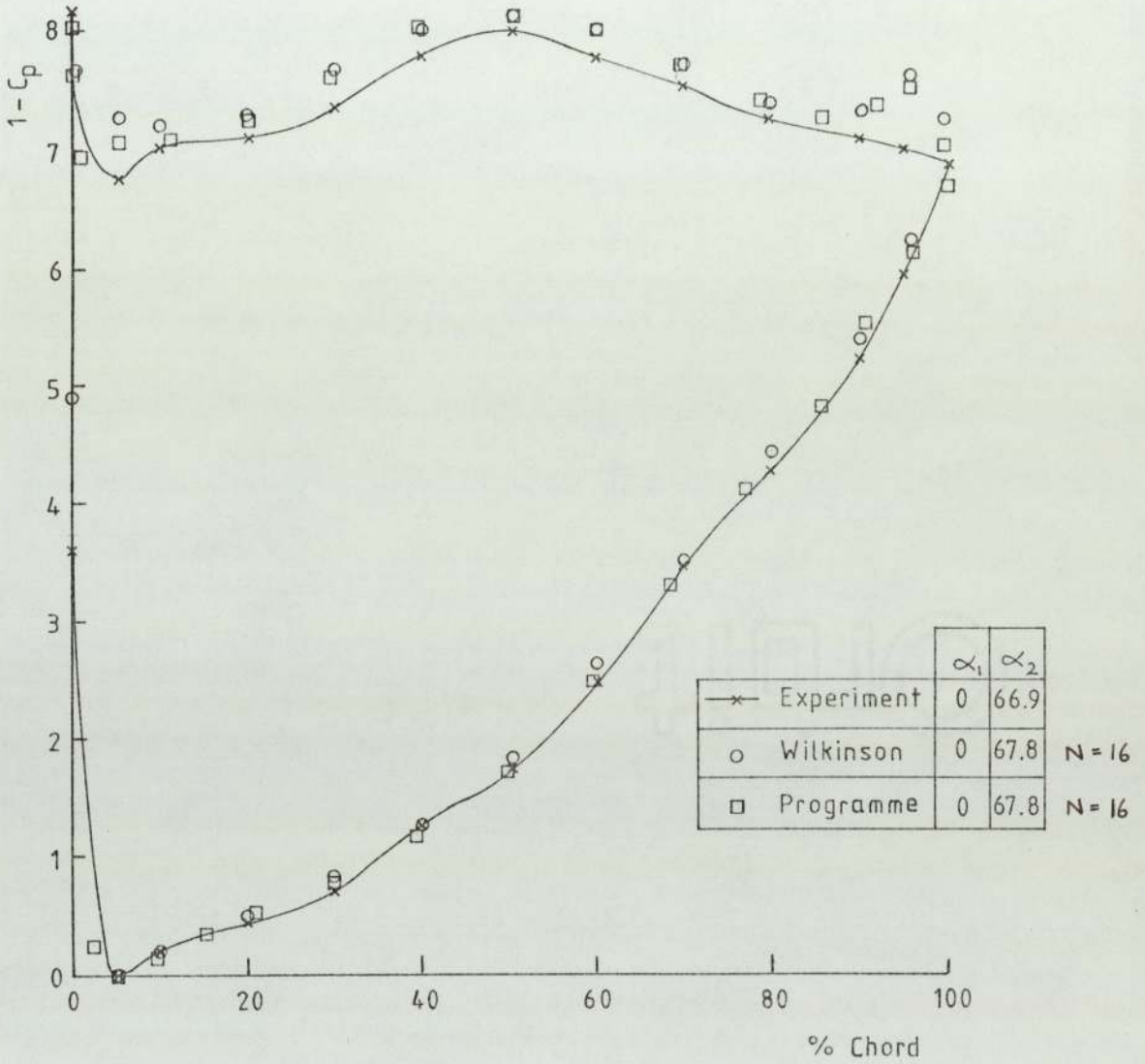


Figure 39

Comparison of Experimental and Computed
Pressure Distributions about a
Primary Turbine Cascade Blade

$$\xi = -53.2^\circ$$

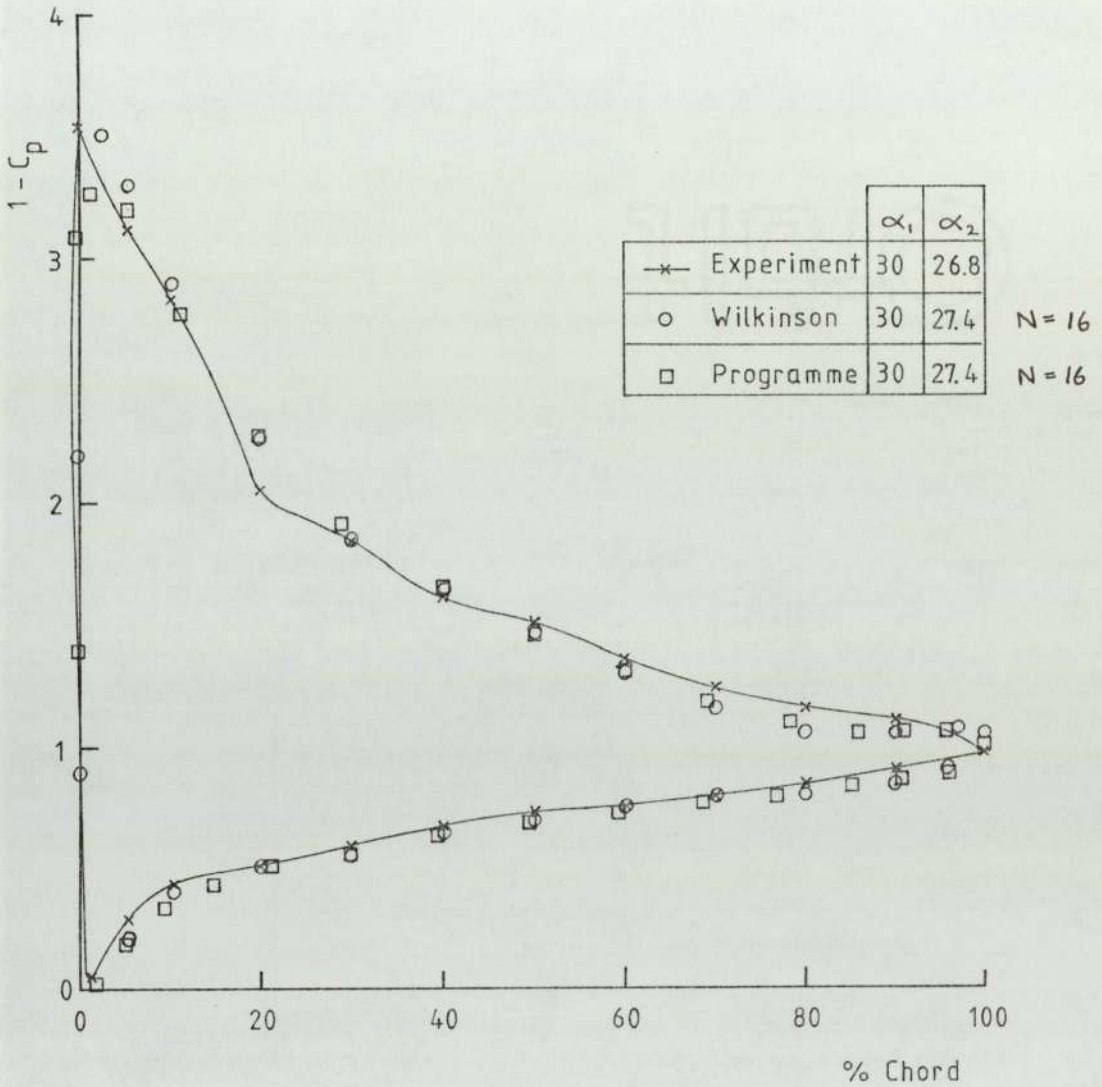


Figure 40
Comparison of Experimental and Computed
Pressure Distributions about a
Primary Turbine Cascade Blade
 $\xi = -13.8^\circ$

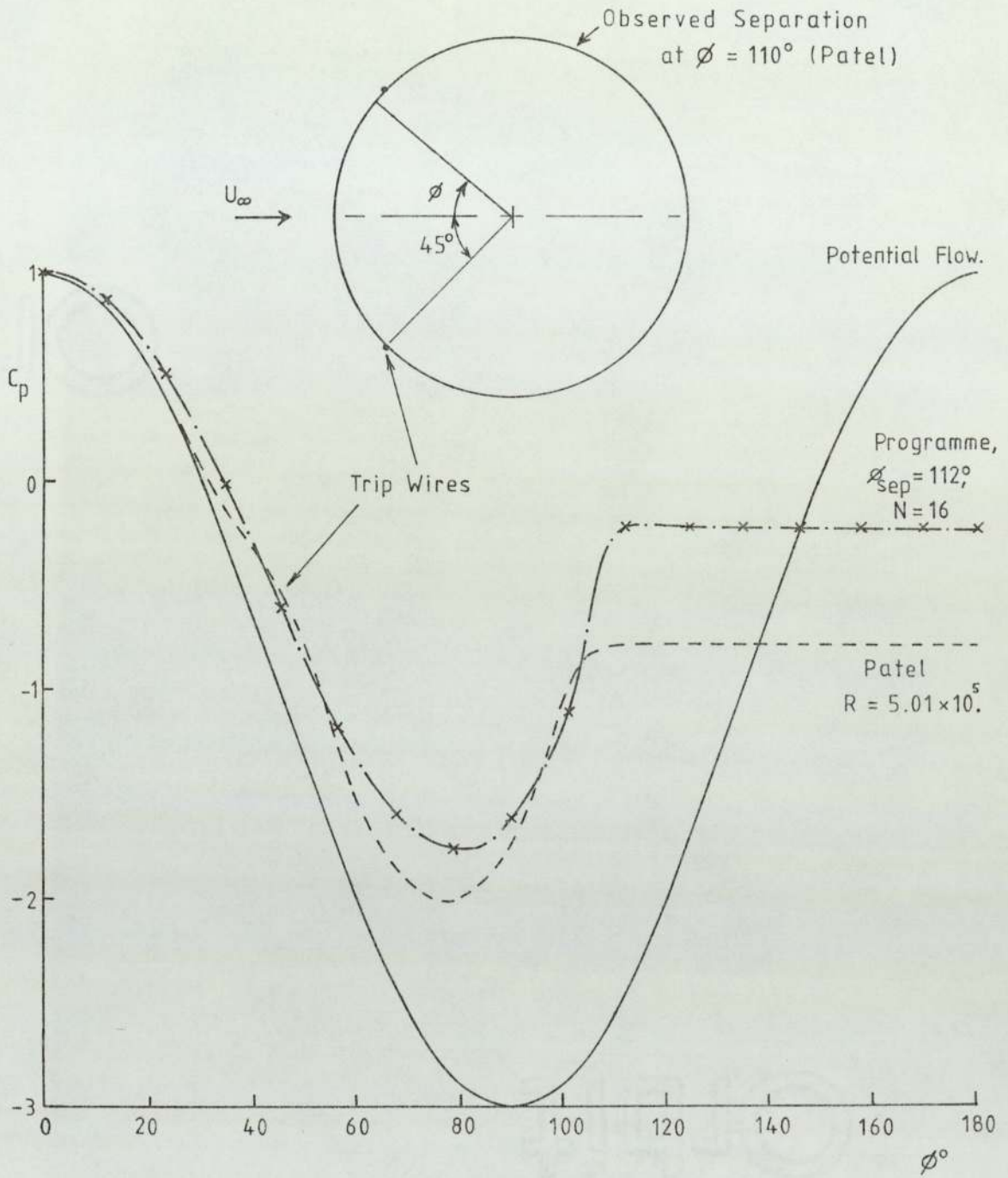


Figure 41
Comparison of Potential Flow,
Experimental and Predicted
Pressure Distributions About
a Circular Cylinder

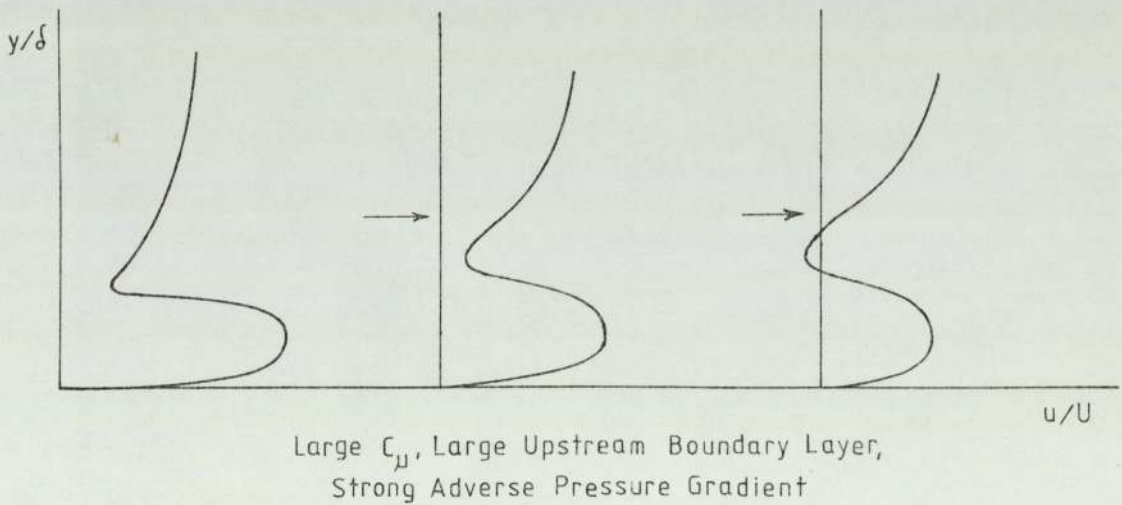
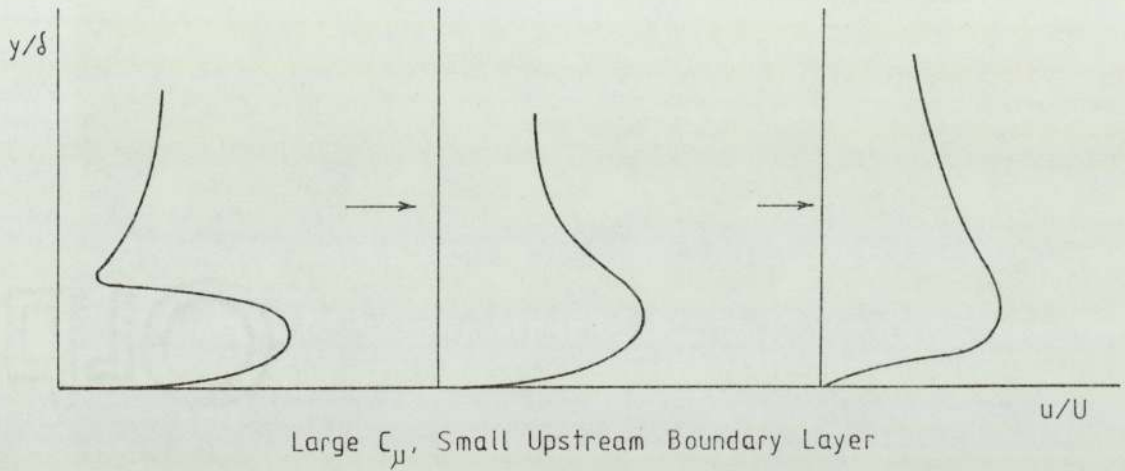
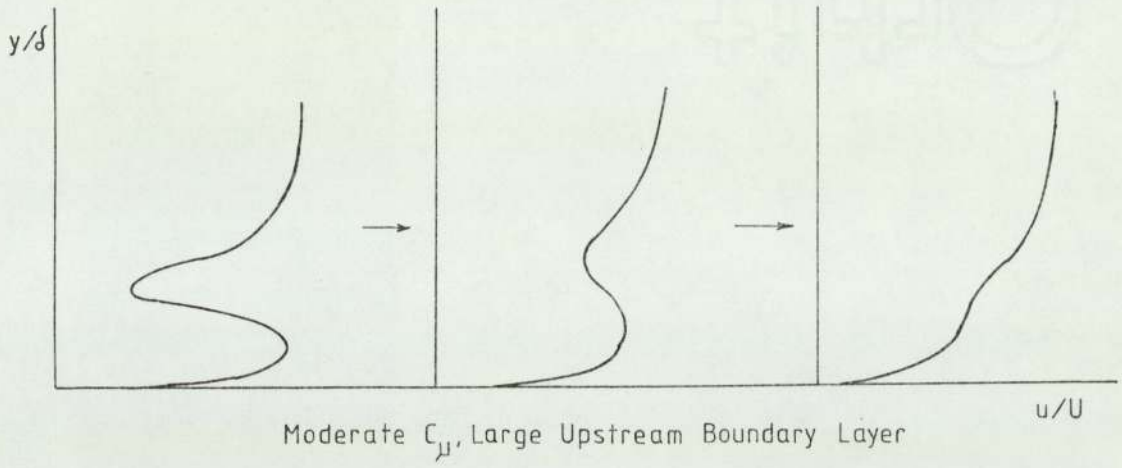


Figure 42
Possible Wall Jet Behaviour
in an Adverse Pressure Gradient

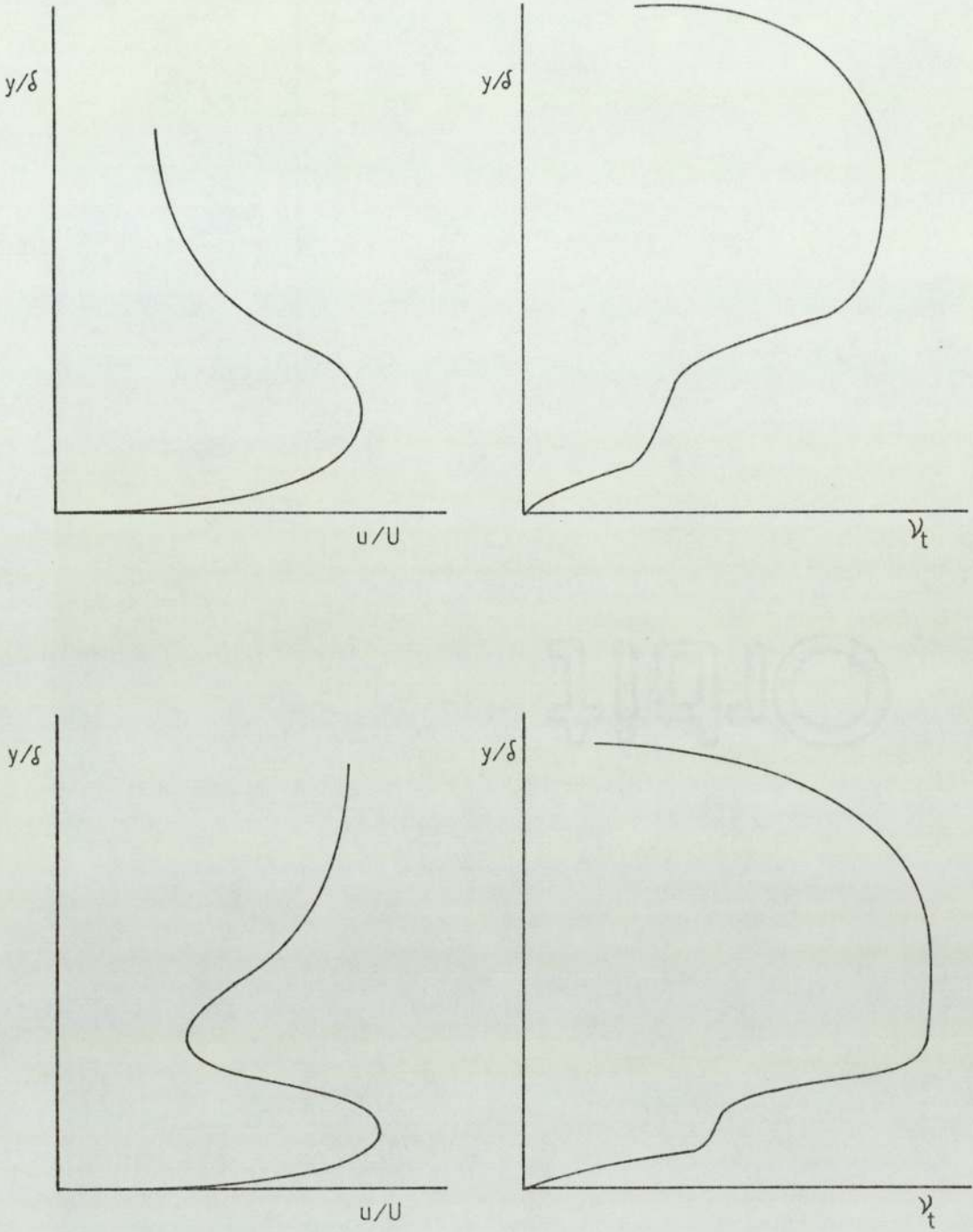


Figure 43
Wall Jet Eddy Viscosity
Profiles Proposed by Dvorak
(Ref 79)

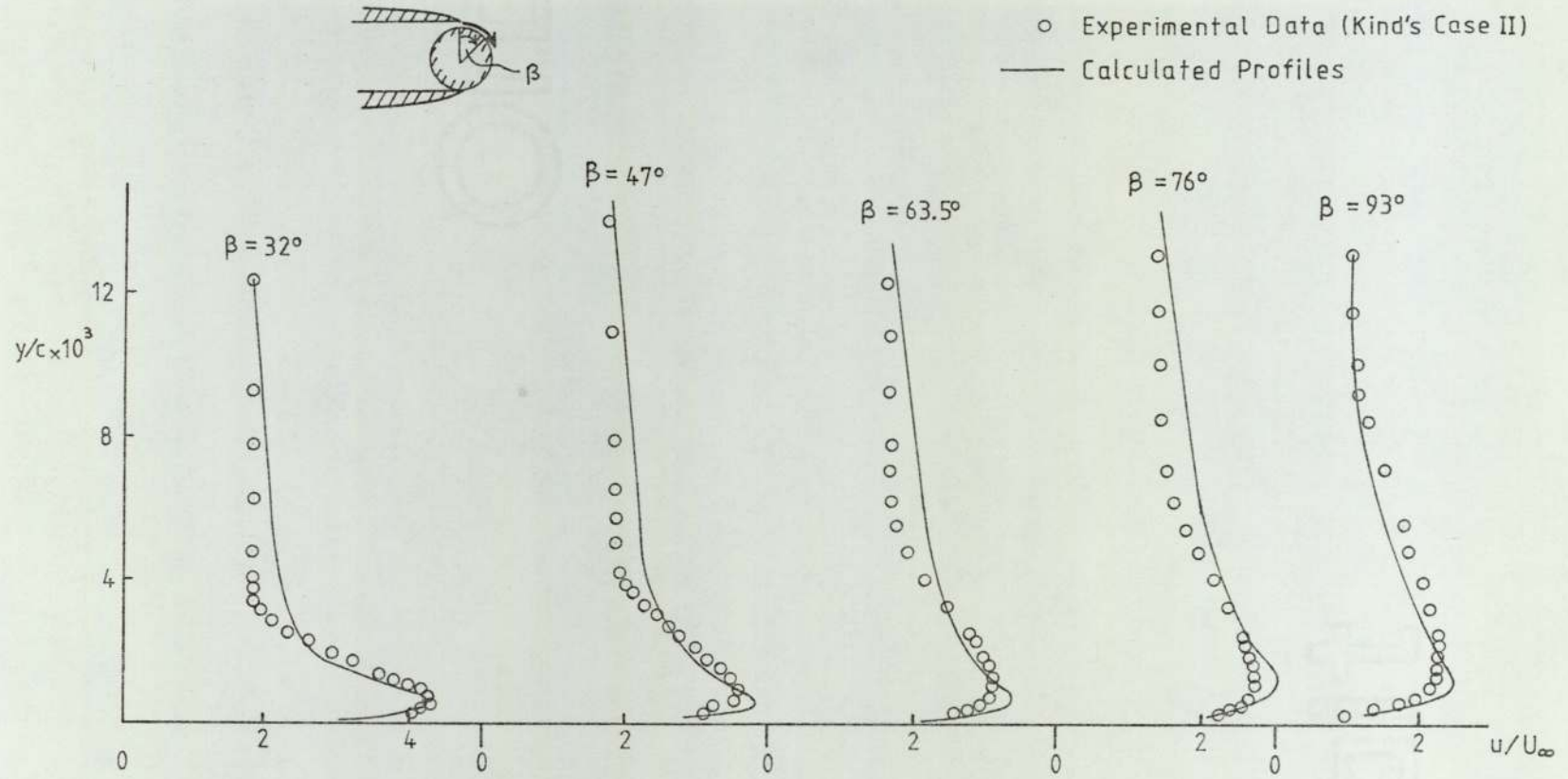


Figure 44
 Comparison of Calculated and Measured Velocity Profiles
 Downstream of a Blowing Slot
 (Kind's Case II)

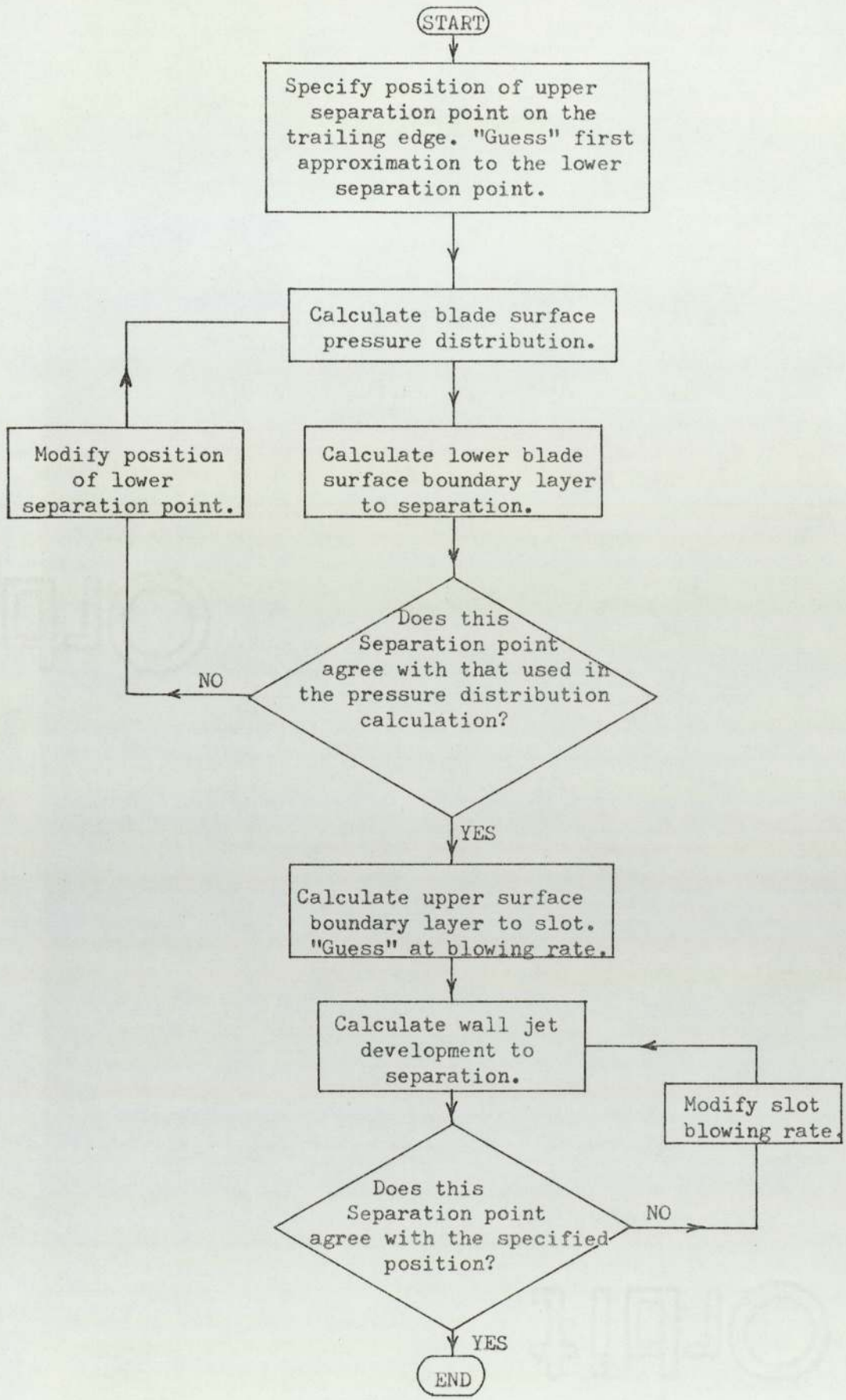


Figure 45
Outline Flowchart of Complete
Solution Procedure

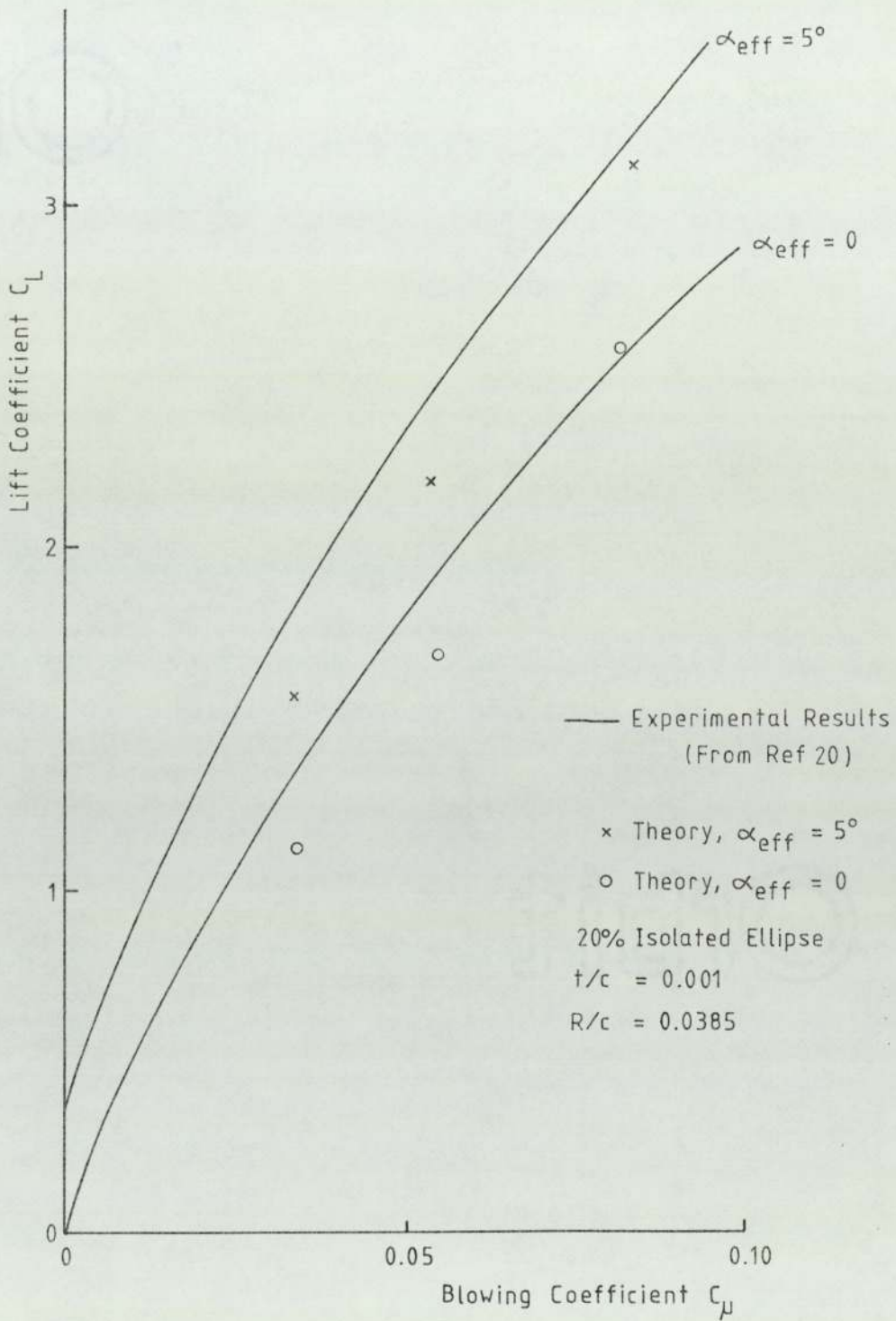


Figure 46
Comparison of Theoretical and Experimental
Variation of Lift with Blowing Coefficient.
Kind's Ellipse (Ref20) at
Constant Effective Incidence

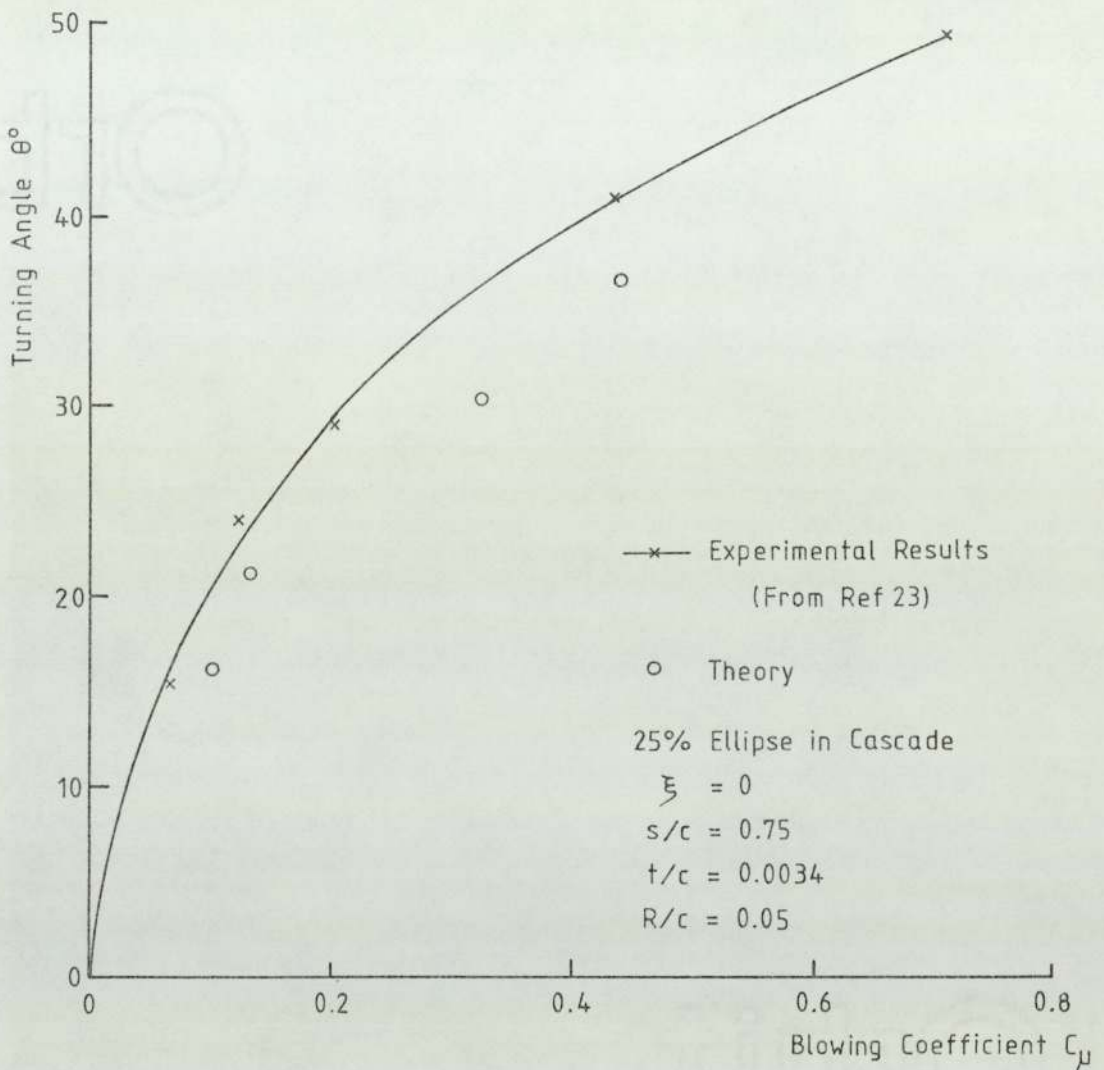


Figure 47
Comparison of Theoretical and Experimental
Variation of Turning Angle with
Blowing Coefficient.
Cascade of Landsberg and Krasnoff,
Test 8, (Ref 23)

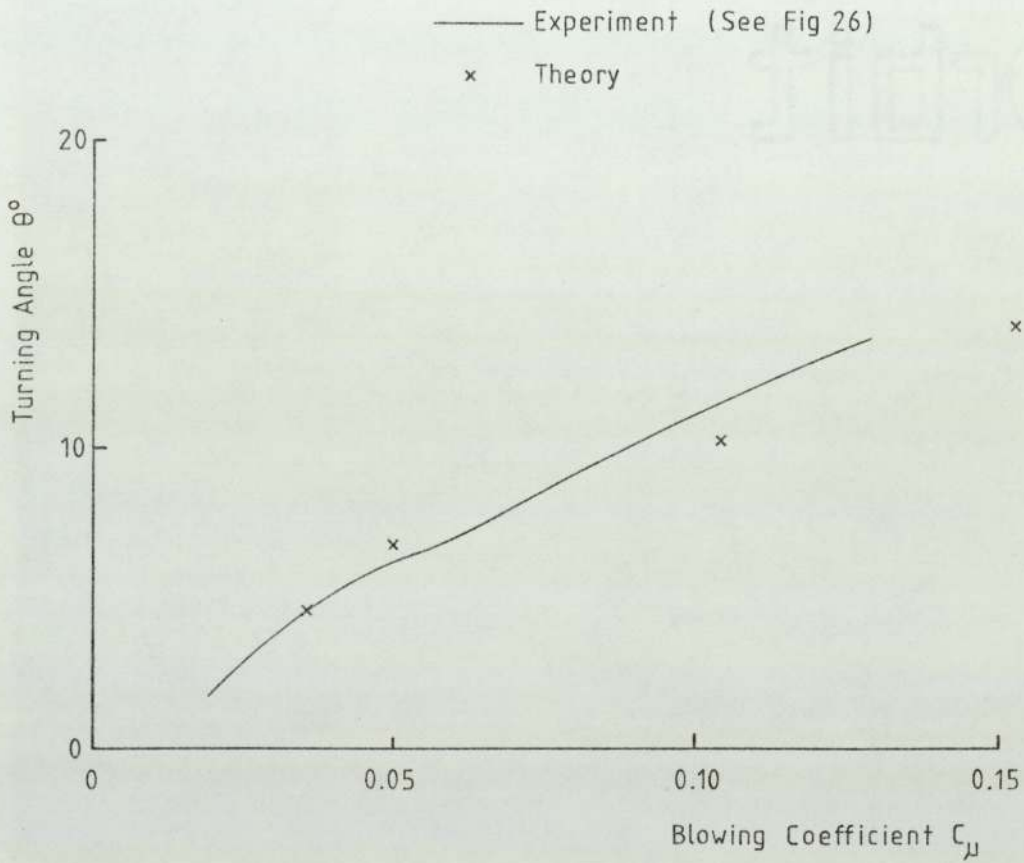


Figure 48

Comparison of Experimental and Theoretical
Variation of Turning Angle with
Blowing Coefficient.

Experimental Cascade,
 $s/c = 0.75$, $\xi = 35^{\circ}$, $\alpha_1 = 40^{\circ}$

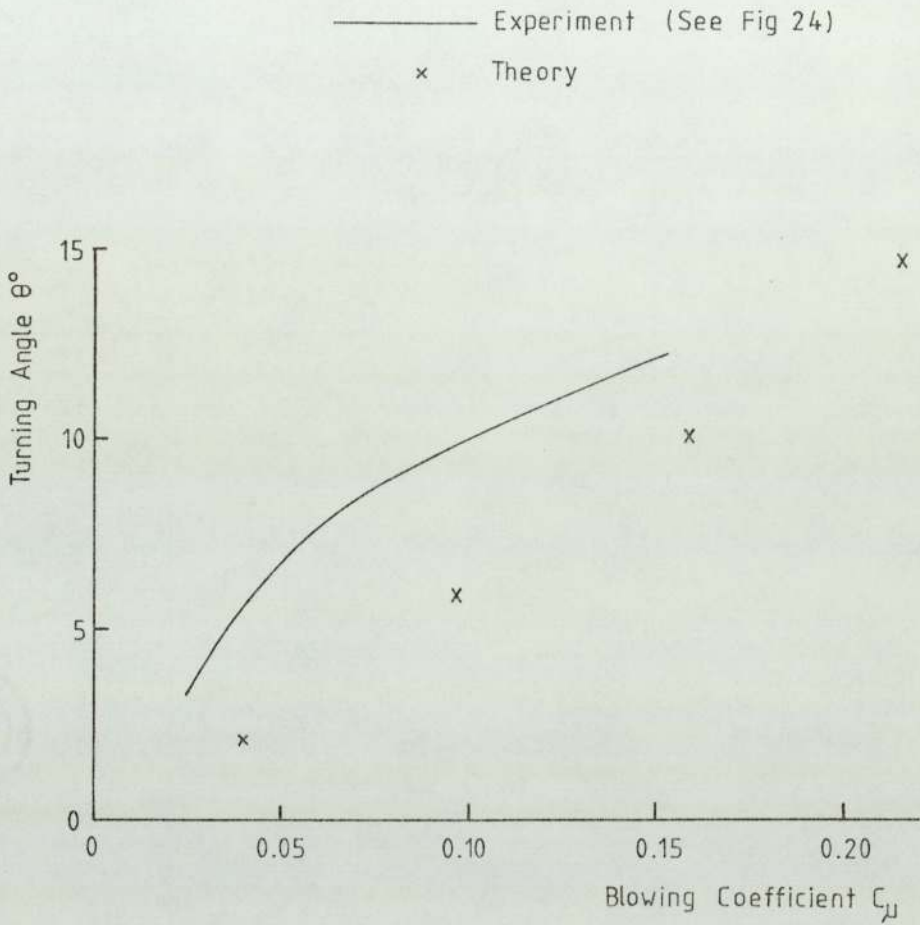


Figure 49

Comparison of Experimental and Theoretical
Variation of Turning Angle with
Blowing Coefficient.

Experimental Cascade,
 $s/c = 1.0$, $\xi = 0$, $\alpha_1 = 0$.

- × At Surface
 - At Outer Edge of Wall Jet
 - Theory, $\alpha = 0$, $C_{\mu} = 0.0815$, $C_L = 2.57$.
- Experiment, $\alpha_{\text{eff}} = -0.7^\circ$, $C_{\mu} = 0.083$,
(Ref 52) $C_L = 2.53$.

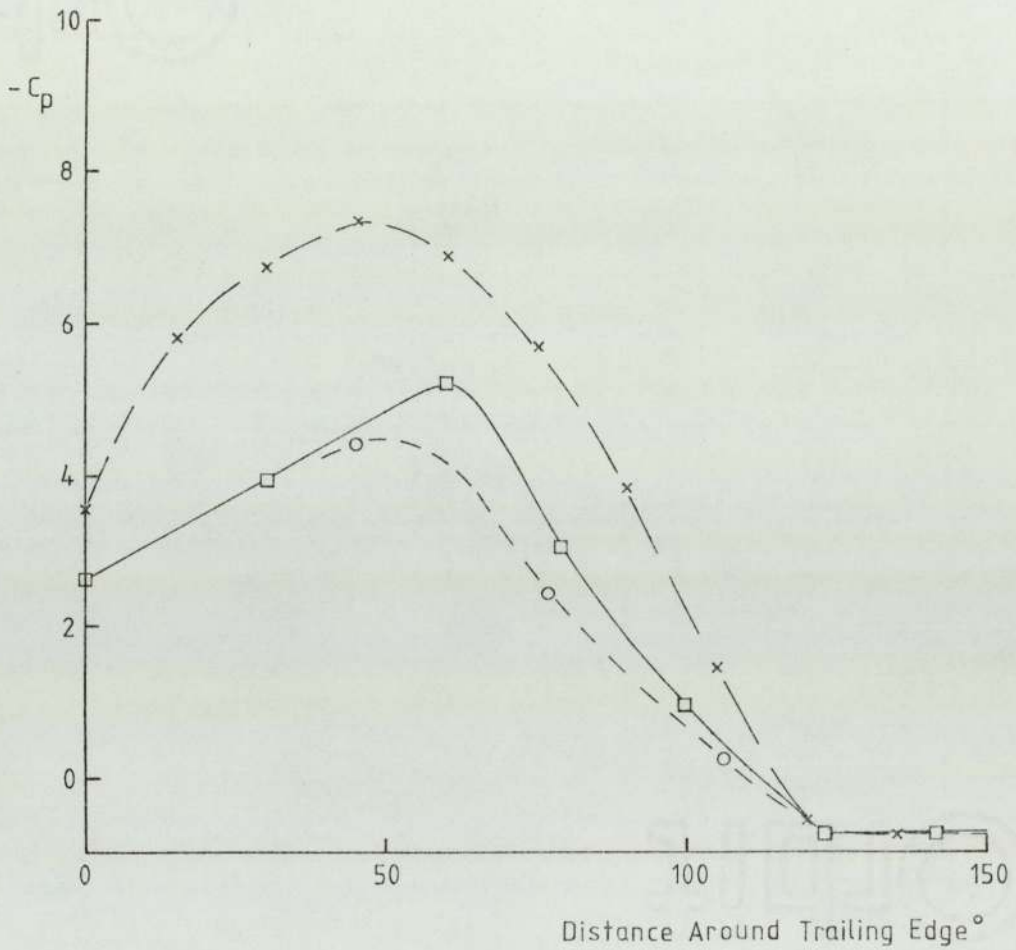


Figure 50
Comparison of Theoretical and Experimental
Trailing Edge Pressure Distributions.
Kind's Ellipse (Ref 52)

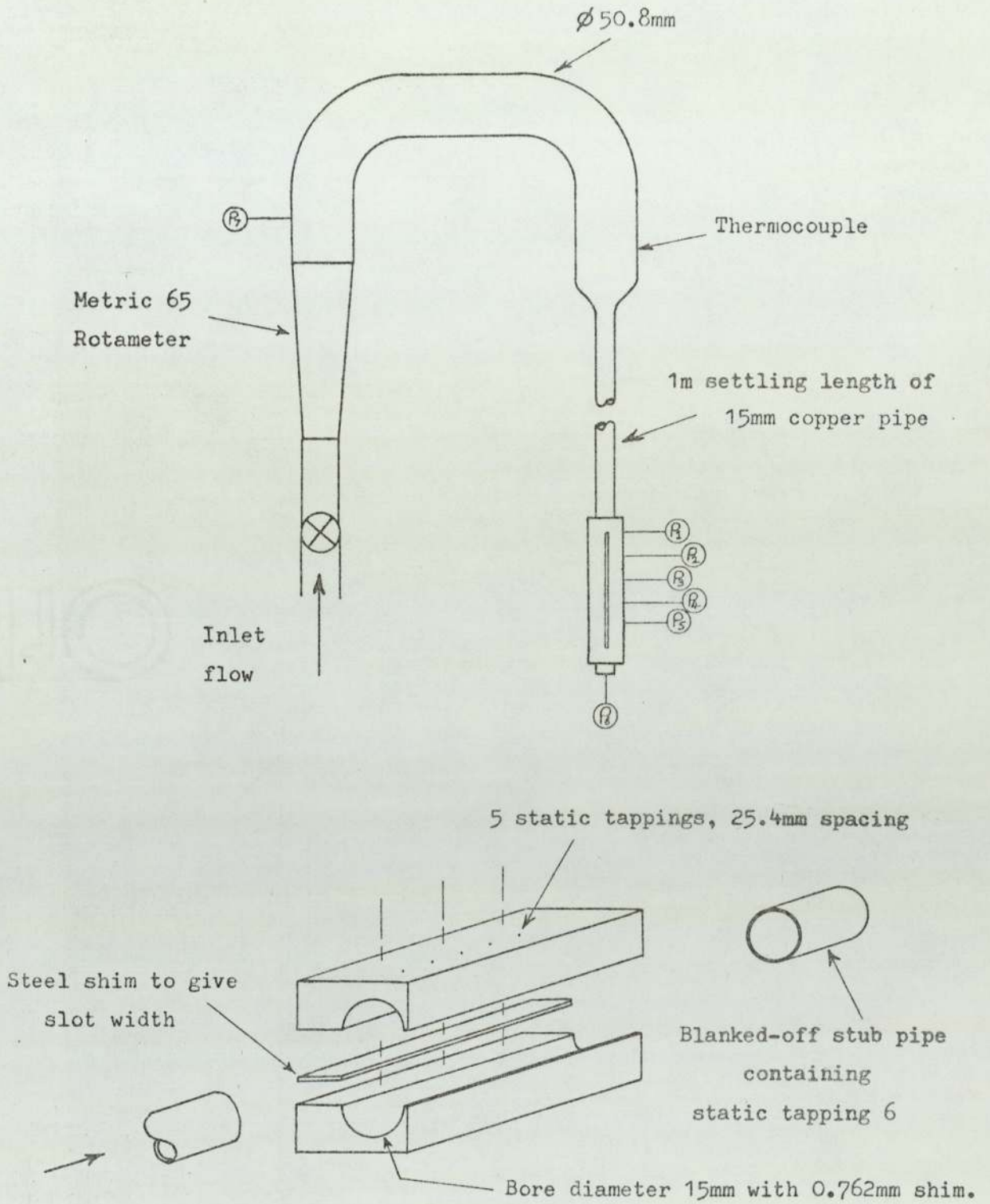


Figure 51
Apparatus Used for
Slotted Pipe Experiments

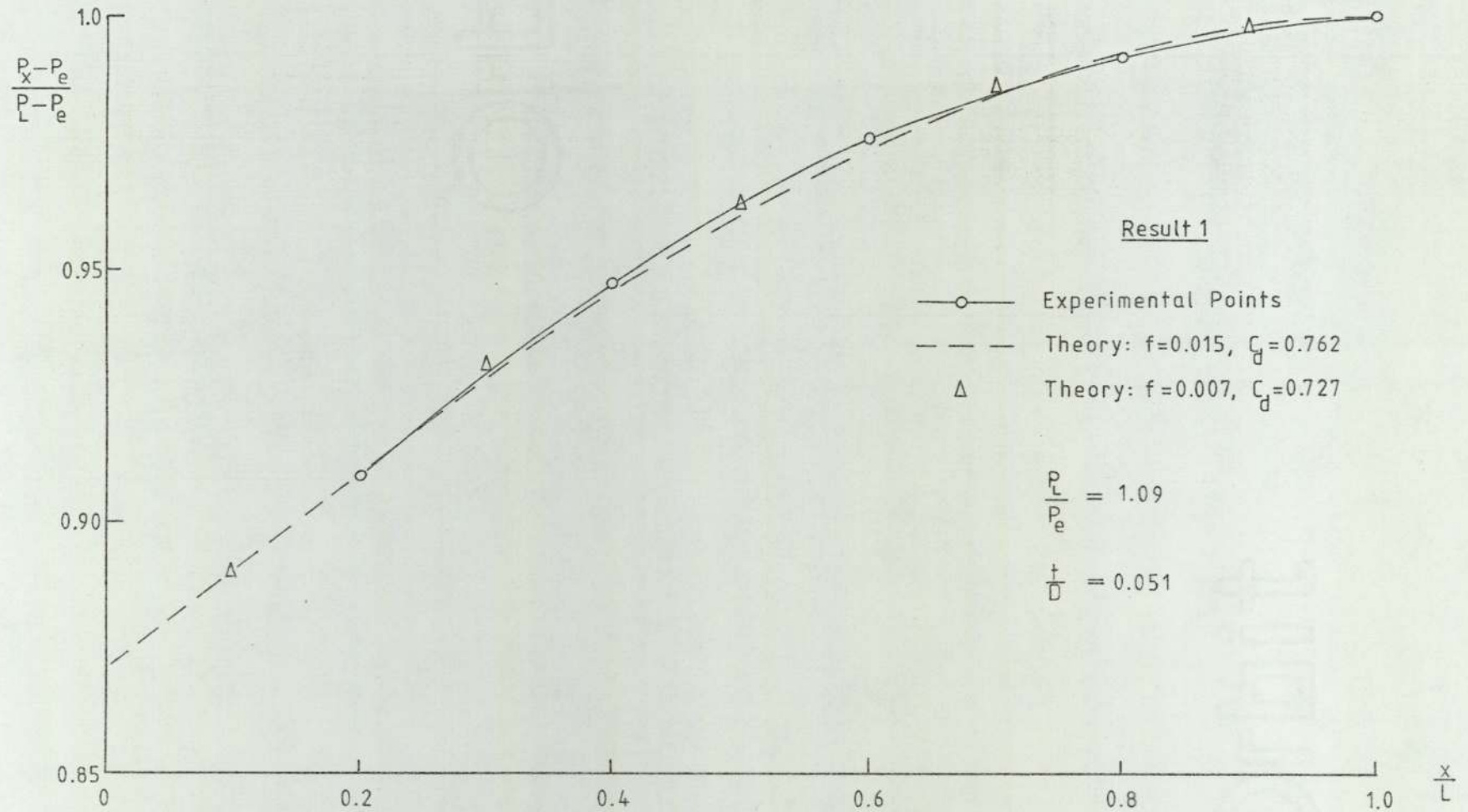


Figure 52 Measured and Theoretical Pressure Distributions along Slotted Pipe

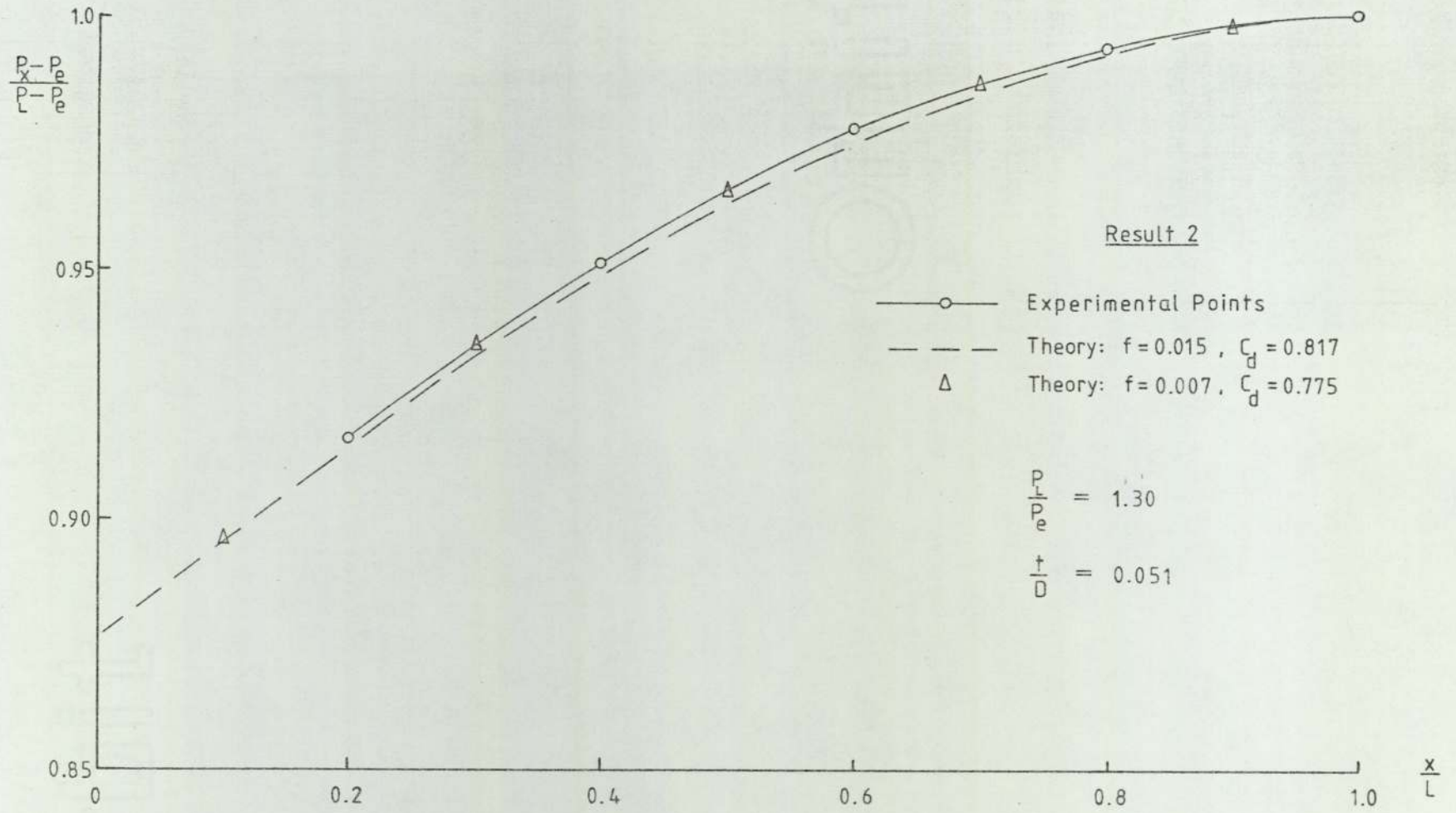


Figure 53 Measured and Theoretical Pressure Distributions along Slotted Pipe

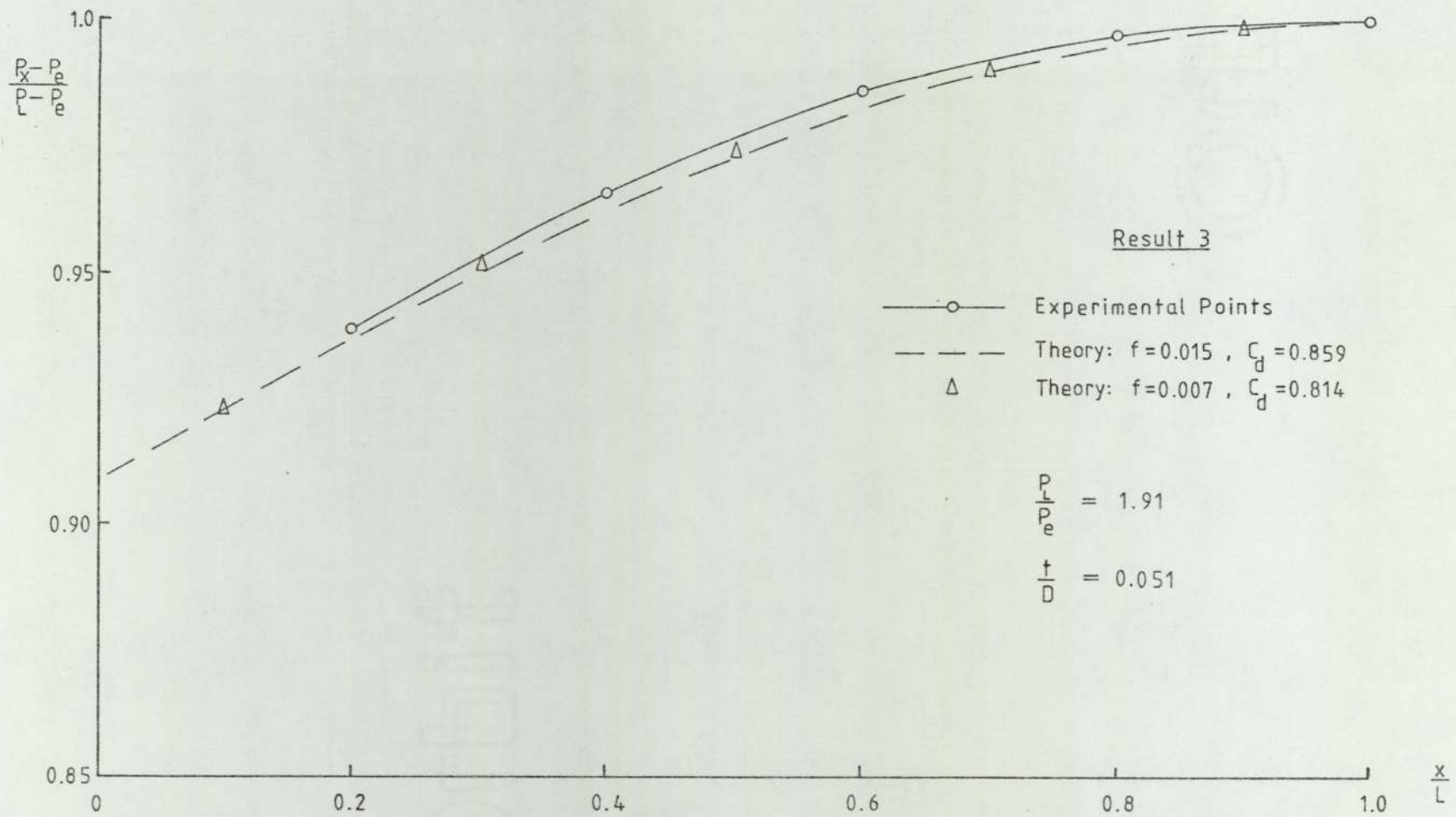


Figure 54 Measured and Theoretical Pressure Distributions along Slotted Pipe

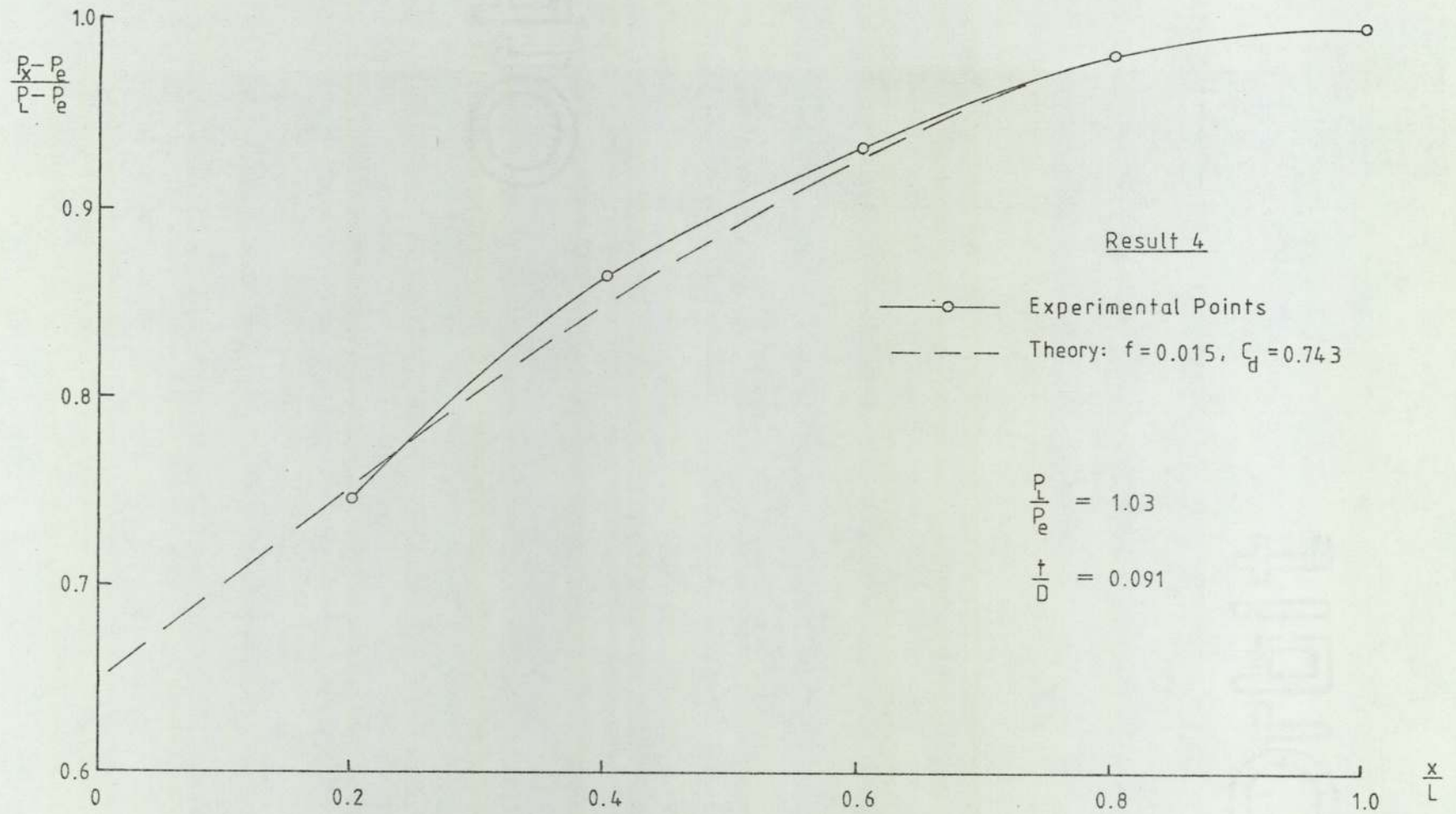


Figure 55 Measured and Theoretical Pressure Distributions along Slotted Pipe

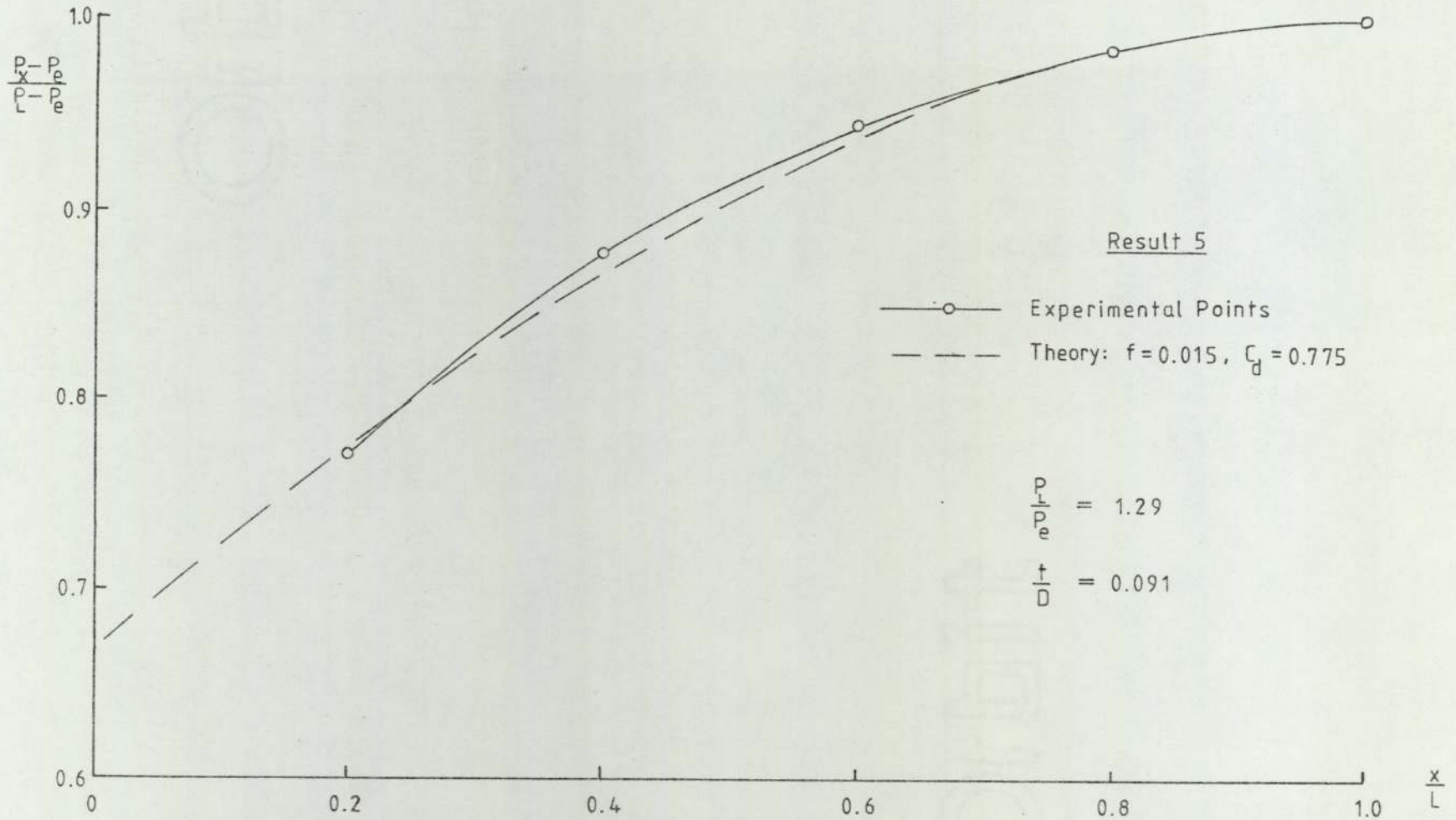


Figure 56 Measured and Theoretical Pressure Distributions along Slotted Pipe

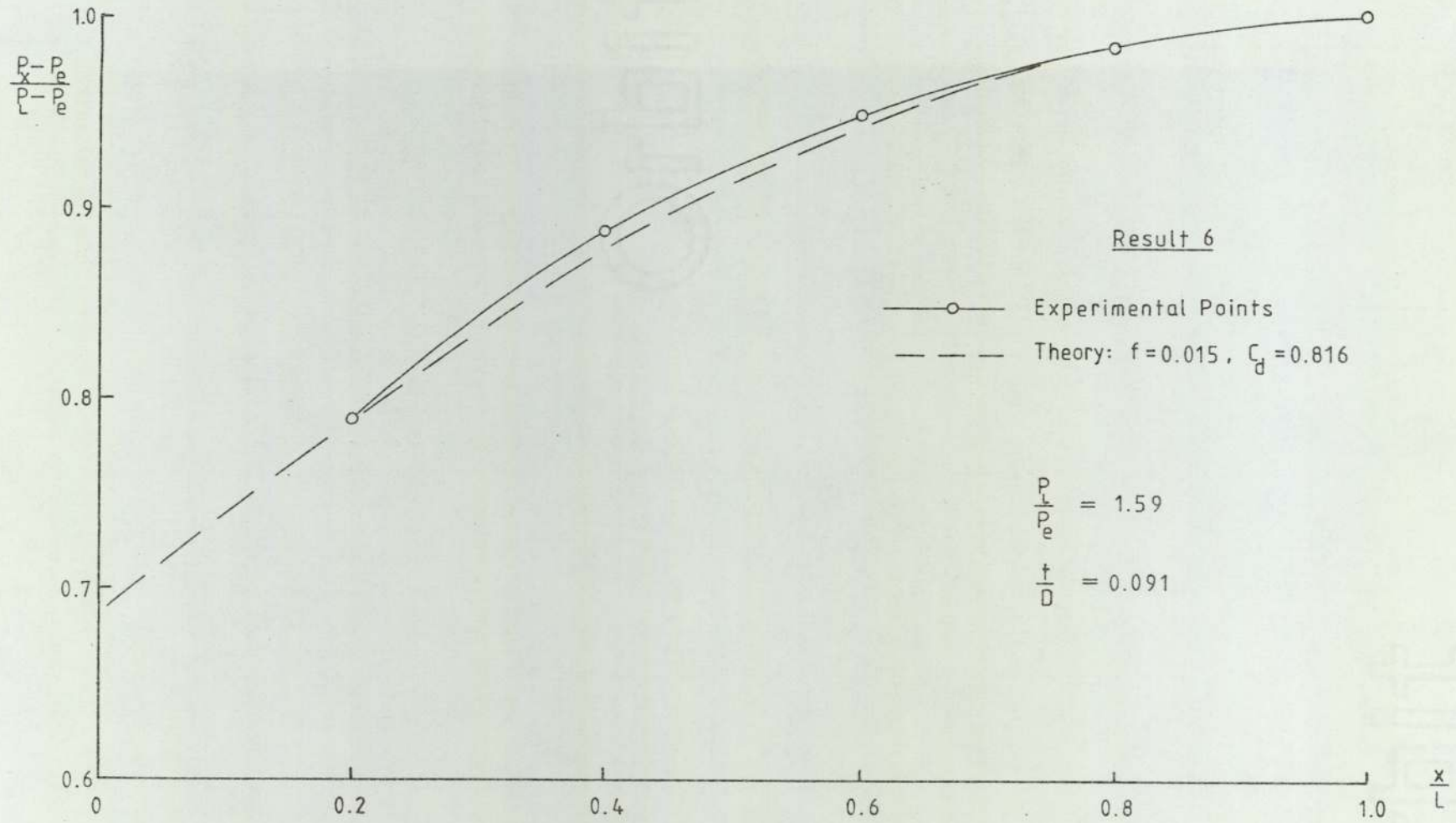


Figure 57 Measured and Theoretical Pressure Distributions along Slotted Pipe

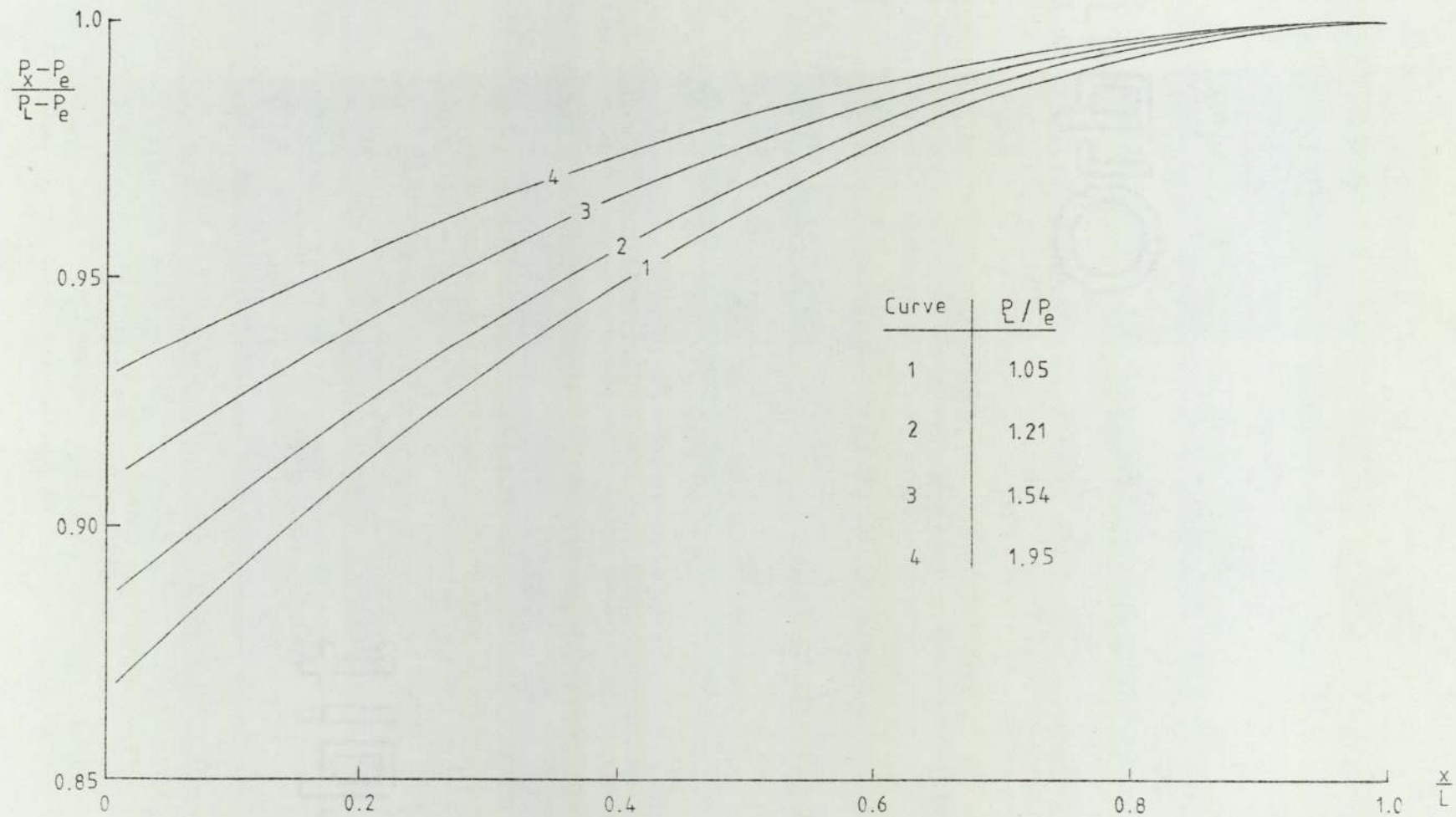


Figure 58 Predicted Pressure Distributions Along Slot Supply Duct of Cascade Blades

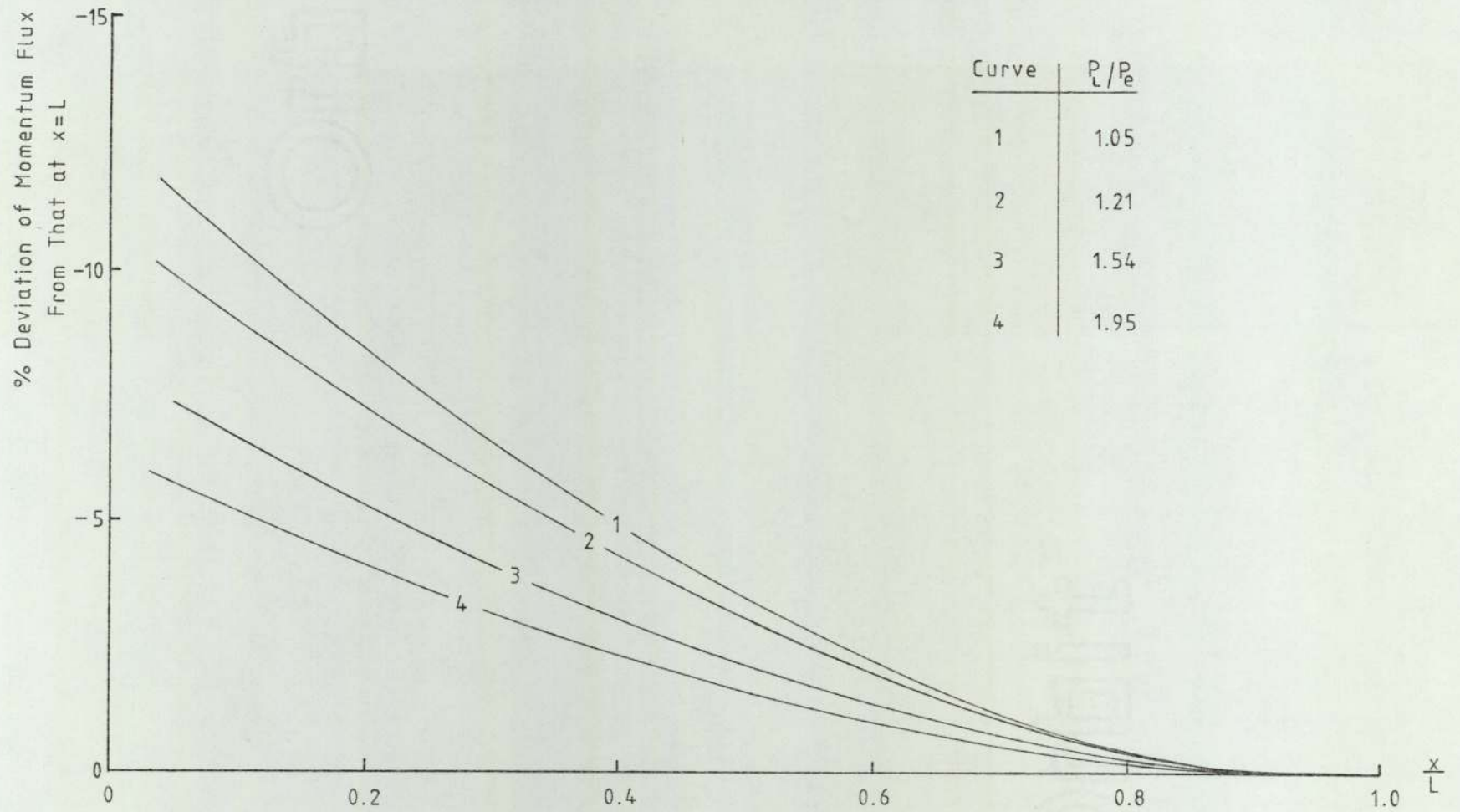
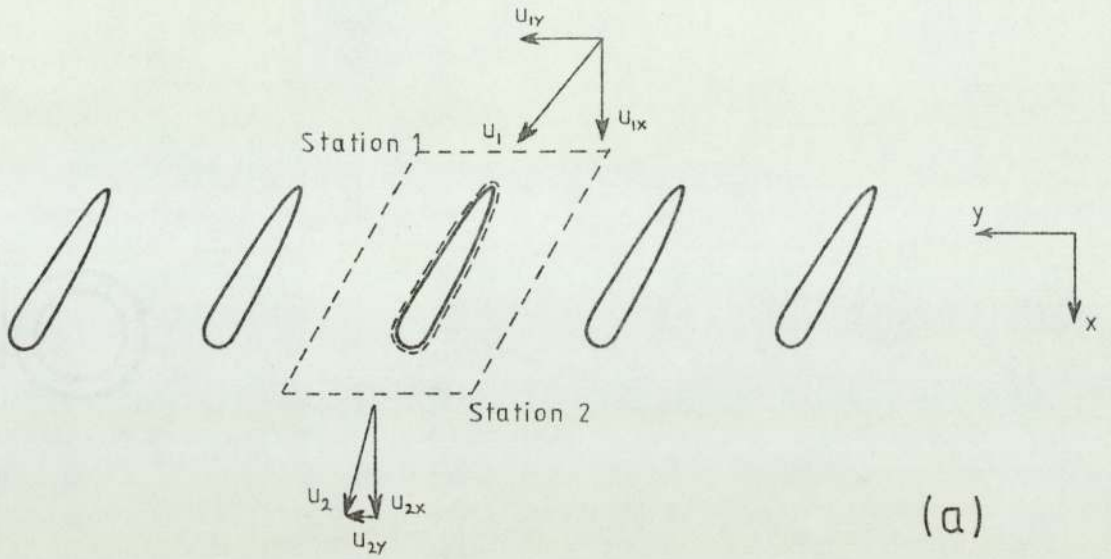
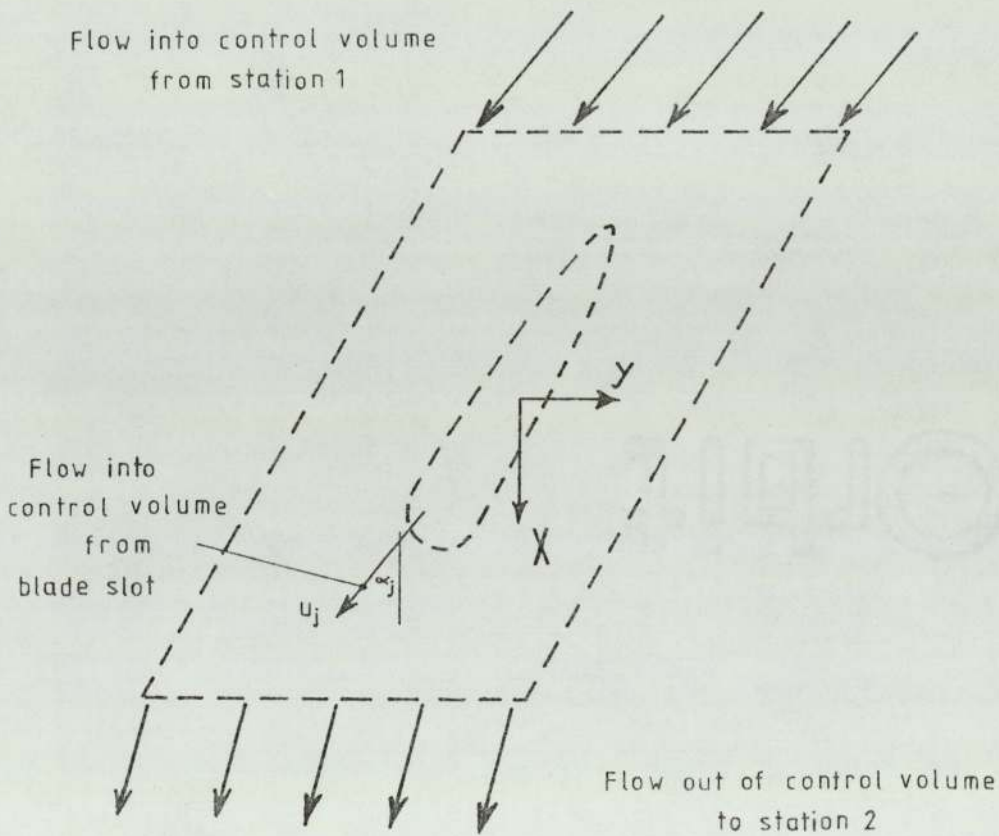


Figure 59 Predicted Variation of Slot Momentum Flux Along Span of Cascade Blades



(a)



(b)

Figure 60
Illustration of Control Volume
Used in Cascade Performance Analysis

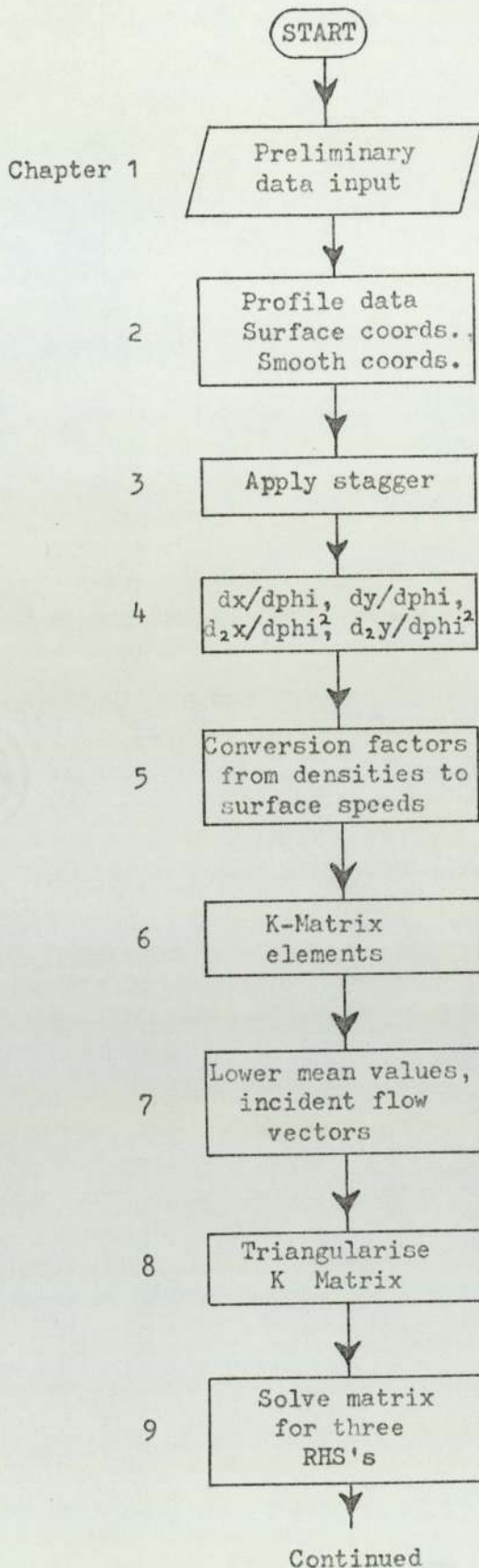
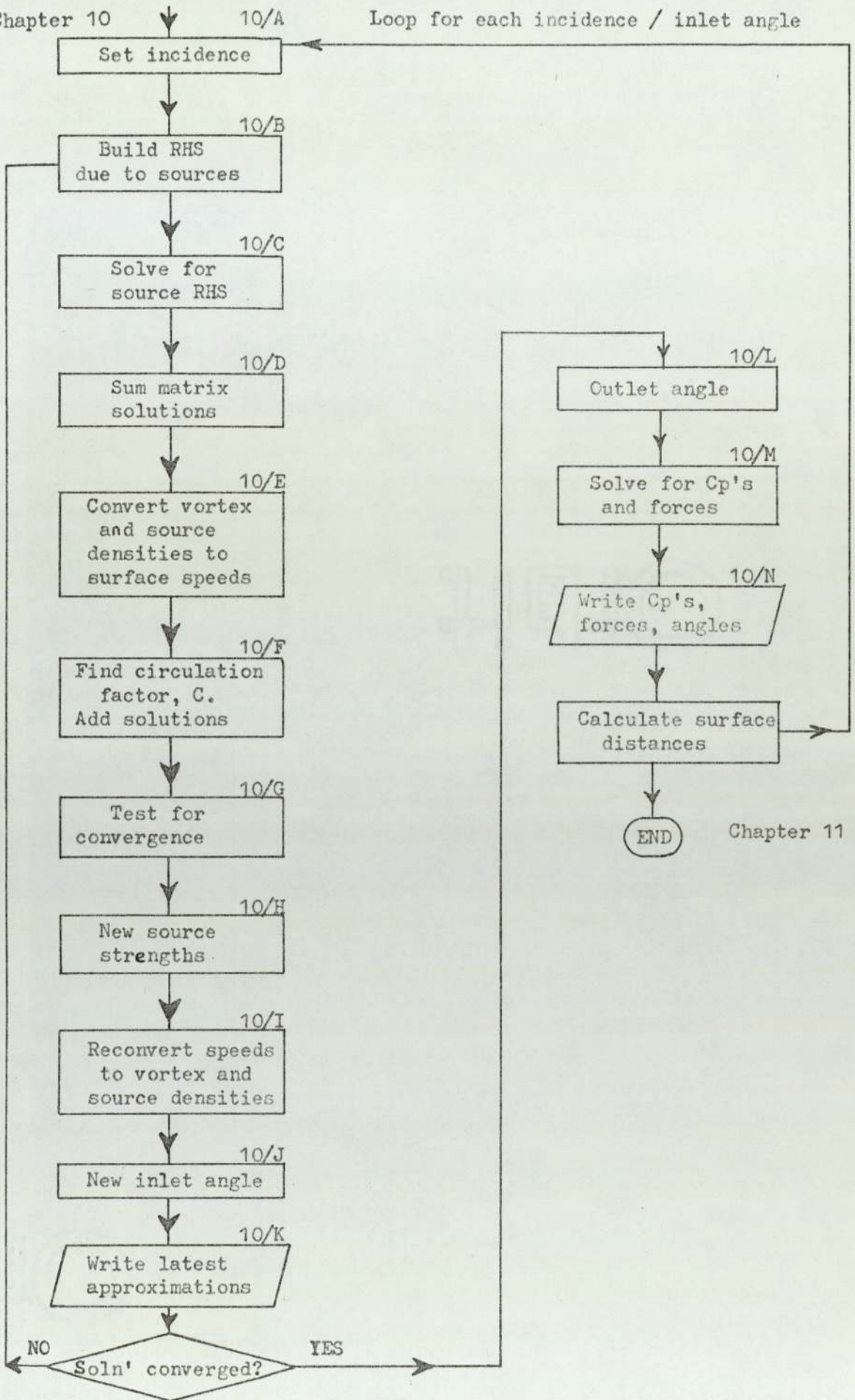


Figure 61
Flowchart of
Potential Flow Programme

Chapter 10

10/A

Loop for each incidence / inlet angle



Chapter 11

Figure 61
(Continued)

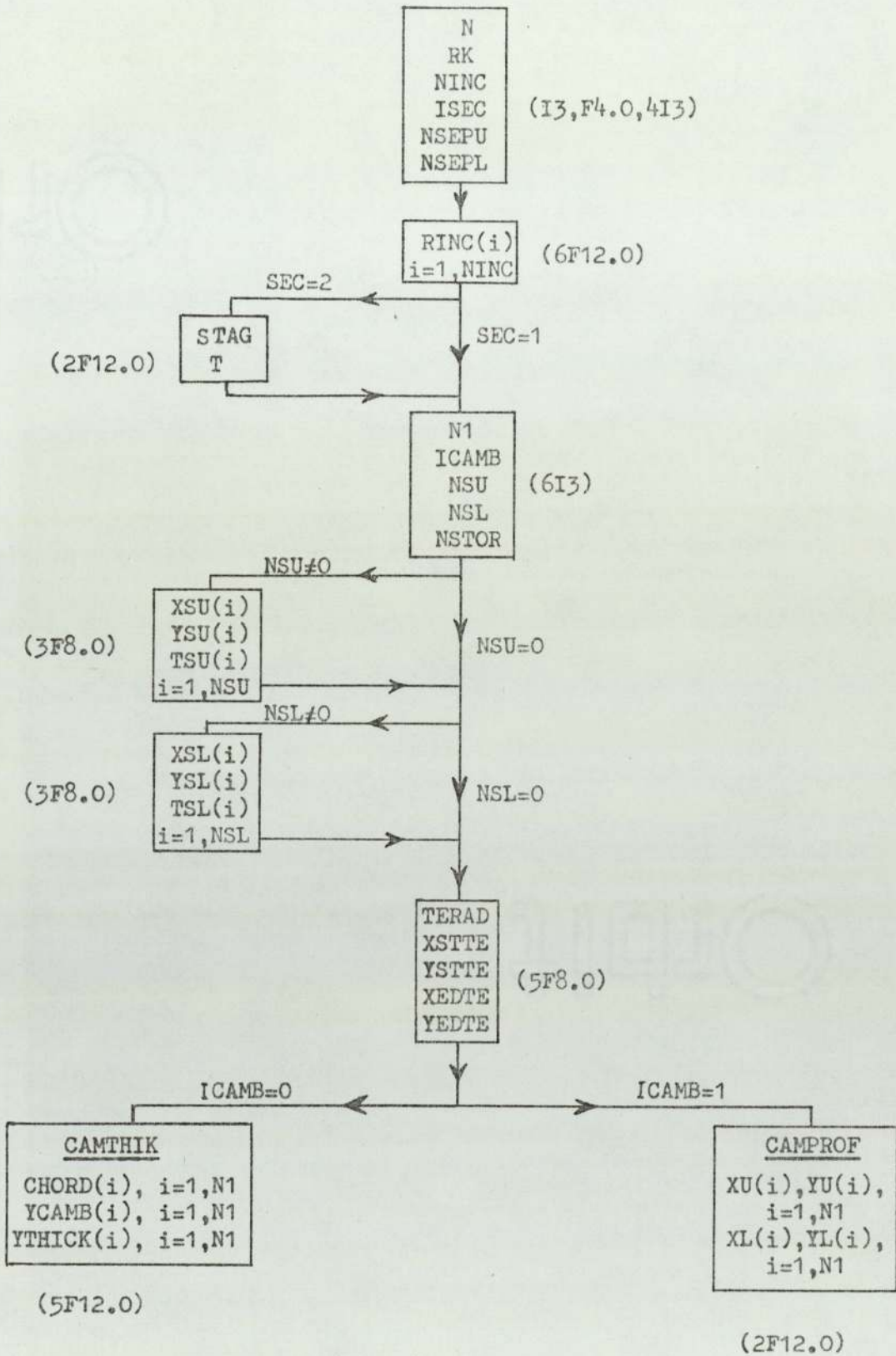


Figure 62
Data Input to
Potential Flow Programme

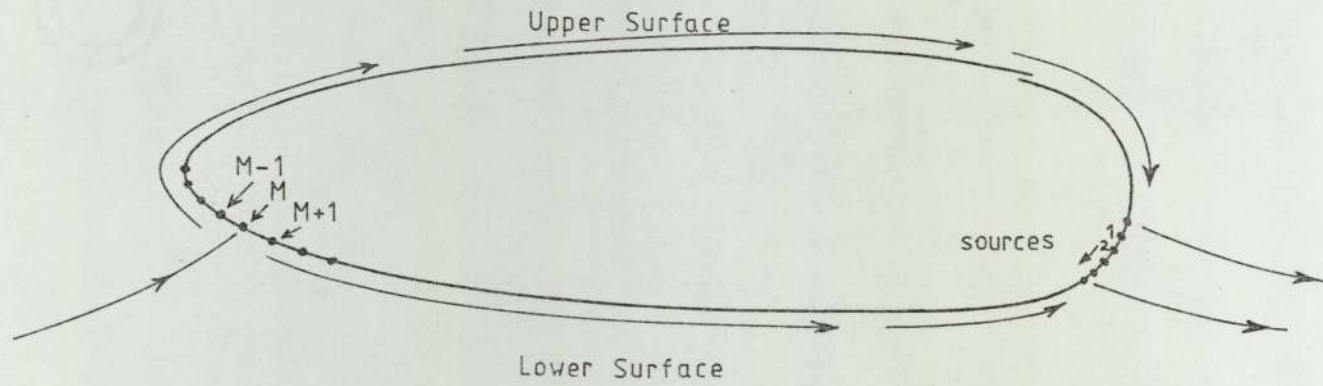


Figure 63
Illustration of Upper and Lower Surface
and Source Numbering Systems

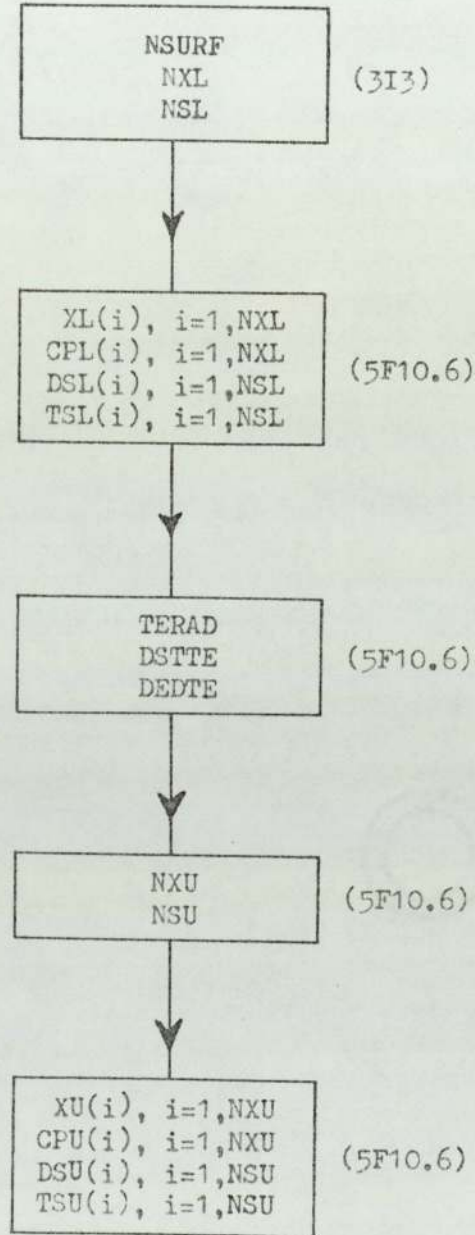


Figure 64
Data Output From
Potential Flow Programme

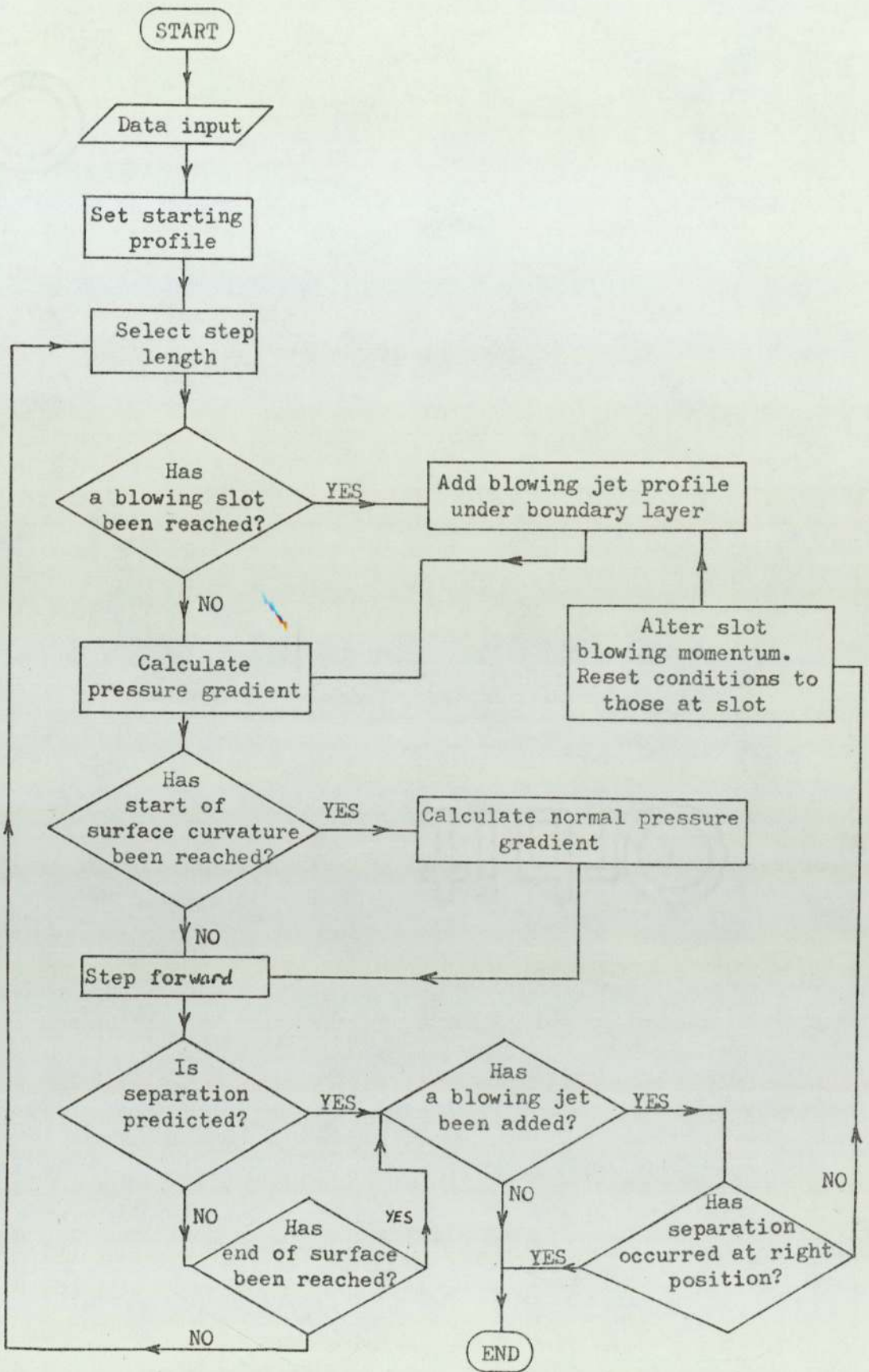


Figure 65
Outline Flowchart of Boundary Layer Programme

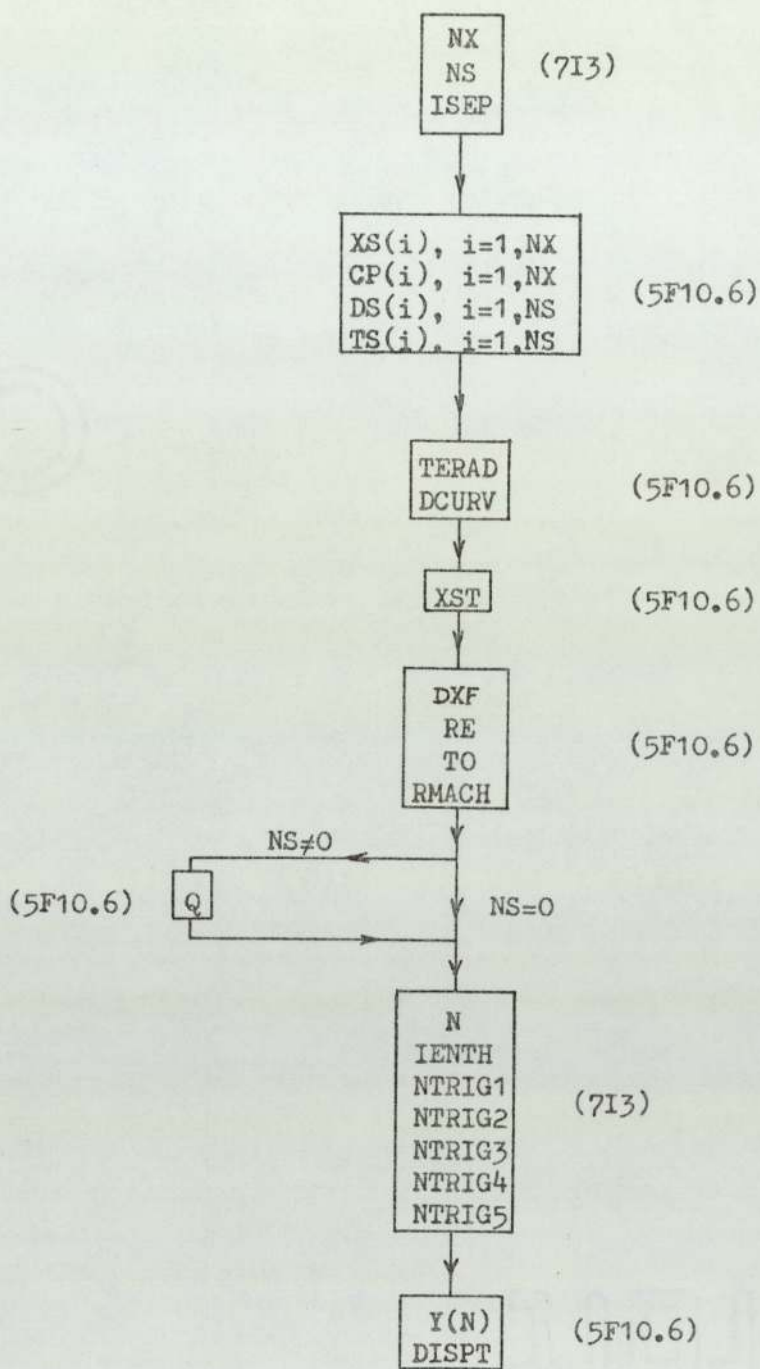


Figure 66
Data Input to
Boundary Layer Programme

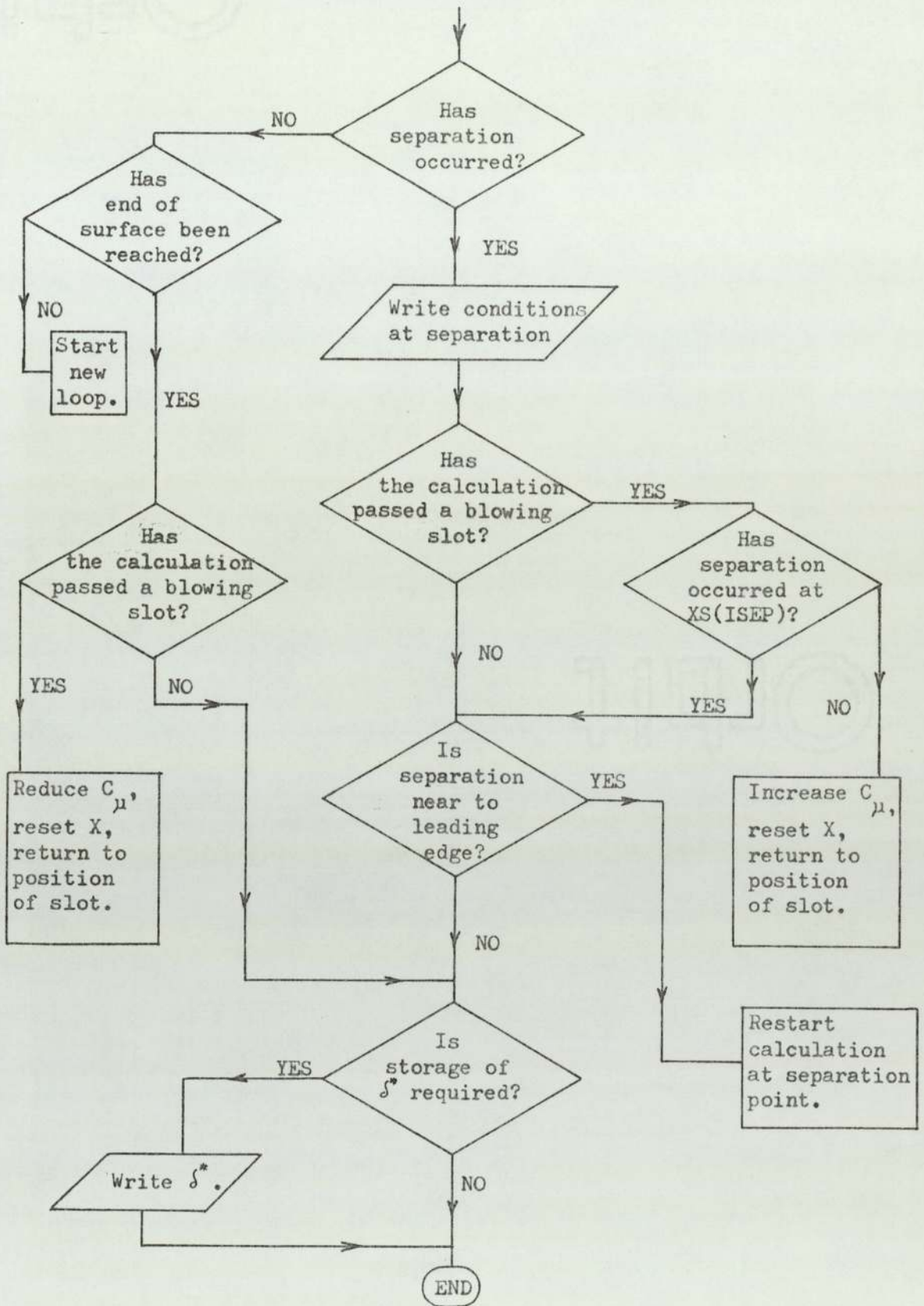


Figure 67
Final Section of
Boundary Layer Programme
Segment MAIN

BIBLIOGRAPHY

1. ARMSTRONG, F.W. "Gas Turbine Evolution", Paper in "Gas Turbines, Status and Prospects", Institute of Mechanical Engineers Conference Publications, 1976.
2. ARMSTRONG, F.W. "The Aero Engine and its Progress - Fifty Years After Griffith", Aeronautical Journal, Vol.82, pp499-520, 1976.
3. HOWELL, A.R. "Griffith's Early Ideas on Turbomachinery Aerodynamics", Aeronautical Journal, Vol.82, pp.521-529, 1976.
4. GOSTELOW, J.P. "Review of Compressible Flow Theories for Aerofoil Cascades", Journal of Engineering for Power, TASME, Vol.95, pp.281-292, 1973.
5. SCHOLZ, N. "Aerodynamics of Cascades", Translated by Klein, AGARD-AG-220, 1978.
6. YOUNG, T. "Outlines of Experiments and Enquiries Respecting Sound and Light", Lecture to the Royal Society, Jan 1800. (See Journal of the Royal Aeronautical Society, Vol.61, 1957, p.157).
7. REYNOLDS, O. "Suspension of a Ball by a Jet of Fluid", Proc.Manch. Lit. Phil.Soc., Vol.9, 1870.
8. NEWMAN, B.G. "The Deflection of Plane Jets by Adjacent Boundaries-Coanda Effect", Article in "Boundary Layer and Flow Control. Its Principles and Applications", Ed.Lachmann, Pergamon Press, 1961.
9. WILLIE, R. & FERNHOLZ, H. "Report on the First European Mechanics Colloquium on the Coanda Effect", Journal of Fluid Mechanics, Vol.23, Part 4, pp.801-809, 1965.
10. ATTINELLO, J.S. "Design and Engineering Features of Flap Blowing Installations", Article in "Boundary Layer and Flow Control. Its Principles and Applications", Ed.Lachmann, Pergamon Press, 1961.

11. KRUGER, R.A. et al., "The performance of a Cascade Fitted with Blown Flaps", Aeronautical Research Council, C.P.No.526, 1961.
12. MILLER, M.L. & CHAPMAN, D.C. "Single-Stage Experimental Evaluation of Boundary Layer Blowing Techniques for High Lift Stator Blades", Part 1, Compressor Design, NASA CR-54564, 1968.
13. SCHLICHTING, H. "Boundary Layer Theory", McGraw-Hill, 1960.
14. THWAITES, B. "Incompressible Aerodynamics", Oxford University Press, 1960.
15. MIKOLAJCZAK, A.A. et al., "Flow Through Cascades of Slotted Compressor Blades", Journal of Engineering for Power, TASME, Vol.92, pp.57-64, 1970.
16. ROCKENBACH, R.W. "Single-Stage Experimental Evaluation of Slotted Rotor and Stator Blading", Part IX, Final Report, NASA CR-53553, 1968.
17. BRENT, J.A. "Single-Stage Experimental Evaluation of Compressor Blading with Slots and Vortex Generators", Part V, Final Report, NASA CR-72793, 1973.
18. KEENAN, M.J. & BURDSALL, E.A. "High Loading, Low-Speed Fan Study", Part V, Final Report, NASA CR-121148, 1973.
19. SMITH, A.M.O. "High Lift Aerodynamics", Journal of Aircraft, Vol.12, No.6, pp.501-530, 1975.
20. KIND, R.J. & MAULL, D.J. "An Experimental Investigation of a Low Speed Circulation-Controlled Aerofoil", Aeronautical Quarterly, Vol.XIX, pp.171-182, 1968.
21. CHEESEMAN, I.C. "Circulation Control and its Application to Stopped Rotor Aircraft", Aeronautical Journal, Vol.72, pp.635-646, 1968.
22. DUNHAM, J. "Experiments Towards a Circulation-Controlled Lifting Rotor", Aeronautical Journal, Vol.74, pp.91-103 and pp.175-186, 1970.
23. LANDSBERG, T.J. & KRASNOFF, E. "An Experimental Study of Rectilinear Jet Flap Cascades", Journal of Basic Engineering, Vol.94, pp.97-104, 1972.

24. PAULON, J. "Application du Soufflage au bord de Fuite au Contrôle de la Déflexion des Grilles d'Aubes", Recherche Aérospatiales, No.67, pp.56-57, 1958.
25. STRATFORD, B.S. "Early Thoughts on the Jet Flap", Aeronautical Quarterly, Vol.7, pp.45-59, 1956.
26. STRATFORD, B.S. "Mixing and the Jet Flap", Aeronautical Quarterly, Vol.7, pp.85-105, 1956.
27. STRATFORD, B.S. "A Further Discussion on Mixing and the Jet Flap", Aeronautical Quarterly, Vol.7, pp.169-183, 1956.
28. SIESTRUNCK, R. "General Theory of the Jet Flap in Two-Dimensional Flow", Article in "Boundary Layer and Flow Control. Its Principles and Applications", Ed.Lachmann, Pergamon Press, 1961.
29. KRASNOFF, E. "Stream Deflection Produced by a Cascade of Jet Flap Aerofoils", Journal of Basic Engineering, TASME, Vol.91, pp.553-555, 1969.
30. SPENCE, D.A. "The Lift Coefficient of a Thin Jet-Flapped Wing", Proceedings of the Royal Society, Series A, Vol.238, pp.46-48, 1956.
31. STARKE, U. "A Theoretical Investigation of the Jet Flap Compressor Cascade in Incompressible Flow", Journal of Fluid Engineering, TASME, Vol.94, pp.249-260, 1972.
32. ALLCOCK, A.W.R. & DUNHAM, J. "The Aerodynamics of Circulation Control by Blowing", Lecture to the Royal Aeronautical Society, 1967.
33. KELLY, M.W. "Analysis of Some Parameters Used in Correlating Blowing Type Boundary Layer Control", NACA A56F12, 1956.
34. SIESTRUNCK, R. "General Theory of the Jet Flap in Two-Dimensional Flow", Article in "Boundary Layer and Flow Control! Its Principles and Applications", Ed.Lachmann, Pergamon Press, 1961.
35. NORTH, P. "The Suppression of Flow Separation by Sequential Wall Jets", Journal of Fluids Engineering, TASME, Vol.98, pp.447-454, 1976.

36. NEWMAN, B.G. "The Prediction of Turbulent Jets and Wall Jets", Canadian Aeronautics and Space Journal, Vol.15, No.8, pp.447-454, 1976.
37. RHODEN, H.G. "Effects of Reynolds Number on the Flow of Air Through a Cascade of Compressor Blades", Aeronautical Research Council Rep. and Memor. 2919, 1956.
38. HORLOCK, J.H. et al., "Reynolds Number Effects in Cascades and Axial Flow Compressors", Journal of Engineering for Power, TASME, Vol.86, pp.236-242, 1964.
39. POLLARD, D. & GOSTELOW, J.P. "Some Experiments at Low Speed on Compressor Cascades", Journal of Engineering for Power, TASME, Vol.89, pp.427-436, 1967.
40. HORLOCK, J.H. et al. "Wall Stall in Compressor Cascades", Journal of Basic Engineering, TASME, Vol.88, pp.637-648, 1966.
41. HORLOCK, J.H. "Some Recent Research in Turbo-Machinery", Proceedings of the Institution of Mechanical Engineers, Vol.182, Part 1, 1967-1968.
42. ROBERTS, W.B. "The Effect of Reynolds Number and Laminar Separation on Axial Cascade Performance", Journal of Engineering for Power, TASME, Vol.97, pp.261-273, 1975.
43. NASH, J.F. et al., "Experiments on Two-Dimensional Base Flow at Subsonic and Transonic Speeds", N.P.L. Aero. Rept., ARC 25070, 1963.
44. HANLEY, W.T. "A Correlation of End Wall Losses in Plane Compressor Cascades", Journal of Engineering for Power, TASME, Vol.90, pp.251-257, 1968.
45. STRATFORD, B.S. "The Prevention of Separation and Flow Reversal in the Corners of Compressor Blade Cascades", Aeronautical Journal, Vol.77, pp.249-256, 1973.
46. FELIX, A.R. & EMERY, J.C. "A Comparison of Typical NGTE and NACA Axial Flow Compressor Blade Sections in Cascade at Low Speed", NACA TN 3937, 1957.

47. ERWIN, J.R. & EMERY, J.C. "Effect of Tunnel Configuration and Testing Technique on Cascade Performance", NACA Rep. No.1016, 1951.
48. HORLOCK, J.H. "Axial Flow Compressors", Butterworths Scientific Publications, 1958.
49. BRYER, D.W. & PANKHURST, R.C. "Pressure Probe Methods for Determining Wind Speed and Flow Direction", National Physical Laboratory, H.M.S.O.Publication, 1971.
50. DUDZINSKI, J.T. & KRAUSE, L.N. "Flow Direction Measurement with Fixed Position Probes", NACA TM X-1904, 1969.
51. LARCOMBE, M.J. & PETRO, J.W. "The Response Time of Typical Transducer-Tube Configurations for the Measurement of Pressures in High Speed Wind Tunnels", Aeronautical Research Council CP 913, 1966.
52. KIND, R.J. "A Proposed Method of Circulation Control", Ph.D.Thesis, Clare College, Cambridge, 1967.
53. KRUKA, V. & ESKINAZI, S. "The Wall Jet in a Moving Stream", Journal of Fluid Mechanics, Vol.20, Part 4, pp.555-580, 1964.
54. BAKER, A.J. & MANHARDT, D. "Numerical Prediction of Mean and Fluctuating Velocities for Jet Flap Flows", AIAA Journal, Vol.16, No.8, 1978.
55. CHANG, P.K. "Separation of Flow", Pergamon Press, 1970.
56. ROSHKO, A. "On the Drag and Shedding Frequency of Two-Dimensional Bluff Bodies", NACA TN 3169, 1954.
57. MUIR, W.A. & MAULL, D.J. "Bluff Bodies and Vortex Shedding - A Report on Euromach 17", Journal of Fluid Mechanics, Vol.45, Part 2, pp.209-224, 1971.
58. MODI, V.S. & WILAND, E. "Unsteady Aerodynamics of Stationary Elliptic Cylinders in Sub-Critical Flow", AIAA Journal, Vol.8, No.10, pp.1814-1821, 1970.

59. GOSTELOW, J.P. "Potential Flow Through Cascades"- A Comparison Between Exact and Approximate Solutions", Aeronautical Research Council, CP 807, 1964.
60. MERCHANT, W. & COLLAR, A.R. "Flow of an Ideal Fluid Past a Cascade of Blades", Aeronautical Research Council RM 1893, 1941.
61. SCHLICHTING, H. "Berechnung der Reibungslosen Inkompressiblen Strömung für ein Vorgegebenen ebenes Schaufelgitter", VDI Forschungsheft 447, 1955.
62. MARTENSEN, E. "Berechnung der Druckverteilung an Gitterprofilen in ebener Potentialströmung mit einer Fredholmschen Integral-gleichung", Arch. Rat. Mech. Anal., Vol.3, pp.235-270, 1959.
63. POLLARD, D. & WORDSWORTH, J. "A Comparison of two Methods of Predicting the Potential Flow around Arbitrary Airfoils in Cascade", Aeronautical Research Council C.P.No.618, 1963.
64. LEWIS, R.I. & PENNINGTON, G.A. "Theoretical Investigation of Some Basic Assumptions of Schlichting's Singularity Method of Cascade Analysis", Aeronautical Research Council C.P.No.813, 1964.
65. GELLER, W. "Calculation of the Turning Angle of Two-Dimensional Incompressible Cascade Flow", AIAA Journal, Vol.14, No.3, pp.297-298, 1976.
66. JACOB, K. & REIGELS, F.W. "The Calculation of the Pressure Distribution over Aerofoil Sections of Finite Thickness with and without Flaps and Slats", Royal Aircraft Establishment Library Translation No.1101, 1965.
67. MINASSIAN, L.M. "A Study of Multielement Cascades and Airfoils", Journal of Fluids Engineering, TASME, Vol.98, pp.208-215, 1976.
68. SEEBOHM, T. & NEWMAN, B.G. "A Numerical Method for Calculating Viscous Flow Round Multiple-Section Aerofoils", Aeronautical Quarterly, Vol.26, pp.176-188, 1975.

69. WILKINSON, D.H. "A Numerical Solution of the Analysis and Design Problems for the Flow Past One or More Aerofoils or Cascades", Aeronautical Research Council RM.3545, 1967.
70. PATEL, V.C. "The Effects of Curvature on the Turbulent Boundary Layer", Aeronautical Research Council RM 3599, 1968.
71. SCHWARTZ, W.H. & CODART, W.P. "The Two-Dimensional Wall Jet", Journal of Fluid Mechanics, Vol.10, pp.481-495, 1961.
72. GORADIA, S.H. & COLWELL, G.T. "Parametric Study of a Two-Dimensional Turbulent Wall Jet in a Moving Stream with Arbitrary Pressure Gradient", AIAA Journal, Vol.9, No.11, pp.2156-2165, 1971.
73. KACKER, S.C. & WHITELAW, J.H. "The Turbulence Characteristics of Two-Dimensional Wall Jet and WallWake Flows", Journal of Applied Mechanics, Vol.38E, pp.239-252, 1971.
74. BRADSHAW, P. & GEE, M.T. "Turbulent Wall Jets with and without an External Stream", Aeronautical Research Council RM 3252, 1960.
75. PATEL, R.P. "Turbulent Jets and Wall Jets in Uniform Streaming Flow", Aeronautical Quarterly, Vol.72, pp.311-326, 1971.
76. SPALDING, D.B. "A Unified Theory of Friction, Heat Transfer and Mass Transfer in the Turbulent Boundary Layer and Wall Jet", Aeronautical Research Council CP 829, 1964.
77. KIND, R.J. "A Calculation Method for Circulation Control by Tangential Blowing Around a Bluff Trailing Edge", Aeronautical Quarterly, Vol.XIX, pp.205-223, 1968.
78. GARTSHORE, I.S. & NEWMAN, B.G. "The Turbulent Wall Jet in an Arbitrary Pressure Gradient", Aeronautical Quarterly, Vol.20, pp.25-56, 1969.
79. DVORAK, F.A. "Calculation of Turbulent Boundary Layers and Wall Jets over Curved Surfaces", AIAA Journal, Vol.11, No.4, pp.517-524, 1973.

80. LAUNDER, B.E. et al., "The Calculation of Turbulent Boundary Layers on Spinning and Curved Surfaces", Journal of Fluids Engineering, TASME, Vol.99, pp.231-239, 1977.
81. FIEDLER, H. & HEAD, M.R. "Intermittency Measurements in the Turbulent Boundary Layer", Journal of Fluid Mechanics, Vol.25, pp.719-738, 1966.
82. GARTSHORE, I.S. "An Experimental Examination of the Large-Eddy Equilibrium Hypothesis", Journal of Fluid Mechanics, Vol.24, pp.89-98, 1966.
83. CORRSIN, S. & KISTLER, A. "The Free Stream Boundaries of Turbulent Flows", NACA Rept. 1244, 1954.
84. VAN DRIEST, E.R. "On Turbulent Flow Near a Wall", Journal of the Aeronautical Sciences, Vol.23, No.11, p.1007, 1956.
85. WYGNANSKI, I. & FIEDLER, H.E. "Jets and Wakes in Tailored Pressure Gradients", The Physics of Fluids, Vol.11, No.12, pp.2513-2523, 1968.
86. BRADSHAW, P. & FERRISS, D.H. "The Response of a Retarded Equilibrium Boundary Layer to the Sudden Removal of Pressure Gradient", NPL Aero Rept.1145, 1965.
87. RAYLEIGH, J.W.S. "On the Dynamics of Revolving Fluids", Proceedings of the Royal Society of London, Vol.6A, p.148-154, 1916.
88. BRADSHAW, P. "The Analogy Between Streamline Curvature and Buoyancy in Turbulent Shear Flow", Journal of Fluid Mechanics, Vol.36, pp.177-191, 1969.
89. BRADSHAW, P. "Effects of Streamline Curvature on Turbulent Flow", AGARDograph No.169, 1973.
90. SO, R.M.C. & MELLOR, G.L. "Experiments on Turbulent Boundary Layers on a Concave Wall", Aeronautical Quarterly, Vol.XXVI, pp.35-40, 1975.
91. RAMAPRIAN, B.R. & SHIVAPRASAD, B.G. "Mean Flow Measurements in Turbulent Boundary Layers along a Mildly Curved Surface", AIAA Journal, Vol.15, No.2, pp.189-197, 1977.

92. IRWIN, H.P.A.H. & ARNOT SMITH, P. "Prediction of the Effects of Streamline Curvature on Turbulence", *The Physics of Fluids*, Vol.18, No.6, pp.624-630, 1975.
93. SAWYER, R.A. "Two-Dimensional Reattaching Jet Flows Including the Effect of Curvature on Entrainment", *Journal of Fluid Mechanics*, Vol.17, pp.481-499, 1963.
94. SCHAUBER, G.B. & KLEBANOFF, P.S. "Investigation of Separation of the Turbulent Boundary Layer", NACA TN 2133, 1950.
95. JOHNSTON, J.P. & EIDE, S.A. "Turbulent Boundary Layers on Centrifugal Compressor Blades: Prediction of the Effects of Surface Curvature and Rotation", *Journal of Fluids Engineering*, TASME, Vol.98, pp.374-381, 1976.
96. SCOTT, C.J. & RASK, D.R. "Turbulent Viscosities for Swirling Flow in a Stationary Annulus", *Journal of Fluids Engineering*, TASME, Vol.95, p.557, 1973.
97. WILSON, D.J. & GOLDSTEIN, R.J. "Turbulent Wall Jets with Cylindrical Streamwise Surface Curvature", *Journal of Fluids Engineering*, TASME, pp.550-557, 1976.
98. RAMAPRIAN, B.R. & SHIVAPRASAD, B.G. "Mean Flow Measurements in Turbulent Boundary Layers Along Mildly Curved Surfaces", *AIAA Journal* Vol.15, No.2, pp.189-196, 1977.
99. PATANKAR, S.V. & SPALDING, D.B. "Heat and Mass Transfer in Boundary Layers", Intertext Books, London, 1970.
100. HUFFMAN, G.D. & BRADSHAW, P. "A Note on Von Kármán's Constant in Low Reynolds Number Turbulent Flows", *Journal of Fluid Mechanics*, Vol.53, pp.45-60, 1972.
101. CEBECI, T. "Kinematic Eddy Viscosity at Low Reynolds Numbers", *AIAA Journal*, Vol.11, No.1, pp.102-104, 1973.

102. HORTSMAN, C.C. "Turbulence Model for Nonequilibrium Adverse Pressure Gradient Flows", AIAA Journal, Vol.15, No.2, pp.131-132, 1977.
103. KREYSZIG, E. "Advanced Engineering Mathematics", Third Edition, John Wiley and Sons, 1972.
104. LEUDERS, H.G. & ROELKE, R.J. "Some Experimental Results of Two Concepts Designed to Increase Turbine Blade Loadings", Journal of Engineering for Power, TASME, Vol.92, pp.198-206, 1970.
105. MILNE-THOMPSON, L.M. "Theoretical Aerodynamics", MacMillan, 1966.
106. LABRUJERE, T.E. et al., "An Approximate Method for the Determination of the Pressure Distribution on Wings in the Lower Critical Speed Range", Advisory Group for Aerospace Research and Development (NATO) Conference Proceedings No.35, September 1968.
107. COLES, D.E. "The Law of the Wake in the Turbulent Boundary Layer", Journal of Fluid Mechanics, Vol.1, pp.191-226, 1956.

<u>Upper Surface</u>		<u>Lower Surface</u>	
X	Y	X	Y
1.00000000	0.00000000	1.00000000	0.00000000
0.99447180	0.00161910	0.99859530	0.00038560
0.99120430	0.00259680	0.99459300	0.00144330
0.98710930	0.00383300	0.98807240	0.00308600
0.98213630	0.00534480	0.97908210	0.00522830
0.96929630	0.00927480	0.96764540	0.00778450
0.95199030	0.01457820	0.95376360	0.01066760
0.94133570	0.01782590	0.93741890	0.01378790
0.92908740	0.02153070	0.91857500	0.01705230
0.91496040	0.02575490	0.89717650	0.02036310
0.89854450	0.03058510	0.87314690	0.02361690
0.87921220	0.03615040	0.84638460	0.02670360
0.85591170	0.04266140	0.81675640	0.02950500
0.82660450	0.05051860	0.78408640	0.03189260
0.78605960	0.06073350	0.74813840	0.03372410
0.76302550	0.06618070	0.70858670	0.03483890
0.71052680	0.07759100	0.69165900	0.03504320
0.65007920	0.08893400	0.66496460	0.03504860
0.59419250	0.09763750	0.61656780	0.03412030
0.56850420	0.10104010	0.56225440	0.03174200
0.52114490	0.10628240	0.49995700	0.02744010
0.45415810	0.11128010	0.42513580	0.02033000
0.40305550	0.11302860	0.32198010	0.00778400
0.38089100	0.11318610	0.27085270	0.00079470
0.32317760	0.11173870	0.24721250	-0.00250690
0.28998890	0.10958550	0.23203190	-0.00462580
0.25991260	0.10671430	0.17849290	-0.01187220
0.20698670	0.09928160	0.16536600	-0.01353410
0.18403670	0.09499300	0.14643930	-0.01579150
0.16161290	0.09009090	0.14513260	-0.01594000
0.12235070	0.07954040	0.11098210	-0.01935450
0.08843710	0.06791480	0.09500000	-0.02052480
0.05953180	0.05544740	0.07500000	-0.02142290
0.03562750	0.04235830	0.05758230	-0.02149150
0.02563970	0.03565360	0.03089410	-0.01922260
0.01705840	0.02888680	0.01519040	-0.01509780
0.00999730	0.02209790	0.00598570	-0.00992540
0.00461490	0.01533480	0.00124780	-0.00410090
0.00113160	0.00865750	0.00006310	-0.00039360
-0.00014140	0.00214370	-0.00014140	0.00214370

TABLE 1

Surface Coordinates of Merchant and Collar Cascade Blade

Used in Computer Programme POTFLOI to Generate Results of

Figure 37.

X	CAMBER	1/2-THICKNESS
1.000000	0.000000	0.000000
0.950000	0.014130	0.005510
0.900000	0.026190	0.006040
0.850000	0.037620	0.009150
0.800000	0.048430	0.012030
0.750000	0.058700	0.015440
0.700000	0.068250	0.019240
0.650000	0.077020	0.023310
0.600000	0.084900	0.027500
0.550000	0.091710	0.031700
0.500000	0.097230	0.035760
0.450000	0.101460	0.039570
0.400000	0.104000	0.042970
0.350000	0.104690	0.045530
0.300000	0.103210	0.048070
0.250000	0.099170	0.049500
0.200000	0.092010	0.050000
0.150000	0.081080	0.049140
0.100000	0.065060	0.045040
0.050000	0.041610	0.034590
0.025000	0.025190	0.024860
0.012500	0.014740	0.017350
0.000000	0.000000	0.000000

TABLE 2

Camber and Half-thickness Values of Primary Turbine Blade
Used in Computer Programme POTFLO1 to Generate Results of
Figures 39 and 40.